An experimental and numerical study of confined non-reacting and reacting turbulent jets to facilitate homogeneous combustion in industrial furnaces

by

Insu Lee

A dissertation submitted in partial fulfillment
of the requirements for the degree of
Doctor of Philosophy
(Mechanical Engineering)
in the University of Michigan
2015

Doctoral Committee:

Professor Arvind Atreya, Co-Chair
Associate Professor Claus Borgnakke, Co-Chair
Professor James F. Driscoll
Professor Margaret S. Wooldridge

To my beloved my parents and all of my family member;

Specially to my wife (Youngju An), son (Yungeun Lee) and

외할머니 (민남출)

Acknowledgements

During my studies I over these past several years I have interacted with and benefitted from many people. First of all, I am thanking for my co-advisor, Prof. Arvind Atreya. He gave me the chance to finish Ph.D. with his guidance. I am thanking for Prof. James Driscoll as being cognate committee member as well as his valuable feedback. I am also special thankful of Prof. Margaret Wooldridge's consideration, she makes great office condition where I have a chance to meet her excellent students. I am thanking so much for my co-advisor, Prof. Claus Borgnakke. If he was not here, I think that I will never finish my Ph.D. thesis. He gave me enough motivation and valuable guidance whenever I had troubles in doing research. I never forget his help and his advice during my life. Also, I want to say thank for continuous funding and career counselling from previous and current graduate chairs, Prof . Steve Skerlos and Prof. Kevin pipe during study.

I am thanking for my current and previous office mates as well as lab and department staffs, Dr. Paul, Dr. Siamak, Dr. Darshan, Dr. Ethan, Dr. Mohammad, Dr. Pawel, Dr. Andrew, Dr. Scot, Dimitris, Eric, Steve, Peter, Cesar, Edward and Charlie. They helped me many times while I was studying and working. I think that I can finish my work due to their helps.

I specially want to thank for my alumni, previous lab alumni and great mentor, Prof. Jaesung Bae, Dr. Heeseok Roh, Dr. Seil Chun, Princial Engineer Youngguk Kim, Dr. Kilsoo Kim, Dr. Jaeheon Sim and Dr. Myung Kim. I was big indebt to them. I do not know how I can compensate it. Whenever I was in troubles, they were always near me and were ready to be good

mentor for me. Also, I am thanking for my friends in South Korea and previous colleagues in Renault Samsung motors.

Finally, I am thankful for my relatives. Also, I want to say thank for my parents (**Youngran Kim** and **Jongik Lee**) and my younger brother's (**Jinsu Lee**) family. They are always waiting and praying for my success with patience. Also, I want to say sorry to my younger brother due to giving him huge responsibilities. 거의 8 년 가까운 시간동안 언제나 저를 기달려 주시고, 마지막 돌아가시는 순간까지 손자의 성공을 기원하신 정말 보고 싶은 할머니, 할머니(**민남출**)!. 죄송하고, 정말 많이 사랑했고 영원히 사랑하겠습니다. Finally, I am really thank for my wife (**Youngju An**) and my son (**Yungeun Lee**) due to their love and patience. From now, I want to be good husband and good father. I try to do best in order to make better life for them.

TABLE OF CONTENTS

LIST OF FIGURES

LIST OF TABLES

LIST OF APPENDICES

LIST OF ABBREVIATIONS

Φ	Equivalence ratio
C_t	Craya-Curtet number
U	Velocity
C	Concentration
D	Diameter
ρ	Density
r	Radius
u_k	Kinematic mean velocity
u_d	Dynamic mean velocity
C_{tni}	Non-isothermal Craya-Curtet number
ρ_M	Mean density of the exit fluid
X	Coordinate in the X direction
Y	Coordinate in the Y direction
Z	Coordinate in the Z direction
M	Mach number
T	Temperature
Re	Reynolds number
M_{sqrt}	Modified momentum ratio
d	Nozzle diameter
t	Time
S_m	Mass increment by the evaporation of the droplet
D_{ij}	Species diffusion coefficient

Y_i	Mass fraction of species *i*
α	Thermal diffusion coefficient
S_i	Production of species *i* by chemical reaction
S_h	Production of enthalpy by the chemical reaction
h	Enthalpy
p_{ref}	Standard pressure
p	Pressure
M_i	Molecular weight of species *i*
k	Turbulent kinetic energy
ε	Turbulent dissipation rate
Mw	Molar mass
σ_{12}	Average collision diameter
$\boldsymbol{\Omega}$	Temperature-dependent collision integral
Φ_e	Entrainment ratio
$\dot{V}$	Volumetric flow rate
E_a	Activation of energy
S	Separation distance
D_a	Damköhler number

Subscripts

∞	Free stream
O	Original or initial properties at jet exit
t	Properties at duct
j or *jet*	Original or initial properties at jet exit
co	Properties at co-flow
count	Properties at counter-flow
c	centerline
m	Average

ex	Properties at duct exit
air	Oxidizer
fuel	Fuel
max	max properties

Abstract

Confined non-reacting turbulent jets are ideal for recirculating the hot flue gas back into the furnace from an external exhaust duct. Such jets are also used inside the furnace to internally entrain and recirculate the hot flue gas to preheat and dilute the reactants. Both internal and external implementation of confined turbulent jets increase the furnace thermal efficiency. For external implementation, depending on the circumstances, the exhaust gas flow may be co- or counter-flow relative to the jet flow. Inside the furnaces, fuel and air jets are injected separately. To create a condition which can facilitate near homogeneous combustion, these jets have to first mix with the burned gas inside the furnace and simultaneously being heated and diluted prior to combustion. Clearly, the combustion pattern and emissions from reacting confined turbulent jets are affected by jet interactions, mixing and entrainment of hot flue gas. In this work, the flow and mixing characteristics of a non-reacting and reacting confined turbulent jet are investigated experimentally and numerically. This work consists of two parts:

(i) A study of flow and mixing characteristics of non-reacting confined turbulent jets with co- or counter-flowing exhaust/flue gas. Here the axial and radial distributions of temperature, velocity and ***NO*** concentration (used as a tracer gas) were measured. ***FLUENT*** was used to numerically simulate the experimental results. This work provides the basic understanding of the flow and mixing characteristics of confined turbulent jets and develops some design

considerations for recirculating flue gas back into the furnace as expressed by the recirculation zone and the stagnation locations.

(ii) Numerical calculations of near homogeneous combustion are performed for the existing furnace. The exact geometry of the furnace in the lab is used and the real dimensional boundary conditions are considered. The parameters such as air nozzle diameter ($\boldsymbol{d_{air}}$), fuel nozzle diameter ($\boldsymbol{d_f}$), equivalence ratio ($\boldsymbol{\Phi}$), oxygen concentration, gravity, different bottom temperature and separation distance as well as soot radiation that influence the establishment of homogeneous combustion to improve combustion efficiency and reduce pollutant emissions will be numerically studied. These results will help to understand the influence from the selected parameters on the main large scale flow characteristics and provide some insight to the conditions that can facilitate near homogeneous combustion in furnaces.

CHAPTER 1

Introduction

1.1. Literature Review

There are considerable experimental and numerical investigations of free turbulent jets. Although previous experimental results of free turbulent jets are useful to understand the confinement effect, the study of confined turbulent jet must be needed to predict the flow and mixing characteristics of confined turbulent jet reasonably. Thring et al. [1] found the occurrence of recirculation in the duct with confined turbulent jet. Later, Craya and Curtet [2][3] proposed a Craya-Curtet number (C_t) by using the theory of an isothermal, incompressible confined jet flow.

Craya-Curtet number:

$$C_t = \frac{(U_o - U_\infty)\left(\frac{r_o}{r_t}\right)^2 + U_\infty}{\sqrt{\left(U_o^2 - U_\infty^2\right)\left(\frac{r_o}{r_t}\right)^2 + 0.5\left(U_\infty^2 - \left((U_o - U_\infty)\left(\frac{r_o}{r_t}\right)^2 - U_\infty\right)^2\right)}} \quad (1)$$

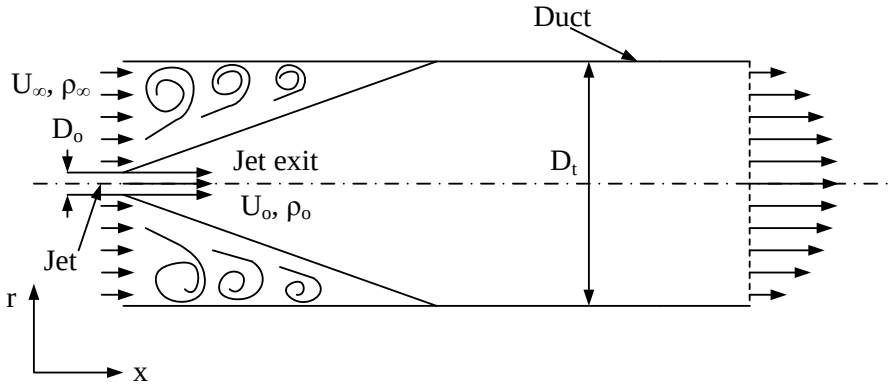

Figure 1.1 Confined turbulent jet in a co-flowing stream

C_t is defined as the ratio of mean velocity inlet to excess of momentum flux at inlet in equation (1). The Craya-Curtet number (C_t) is the indicator of the onset of recirculation under certain flow conditions. If C_t is 0 ($U_o >> U_\infty$), confined flow is considered to be in total recirculation. On the other hand, if the flow is uniform parallel motion or no recirculation in the duct (($U_o = U_\infty$), the Craya-Curtet number is at $C_t = \infty$. Curtet and Ricou [4] did experiments on isothermal axis-symmetric confined jets to verify the theoretical approach of the Craya-Curtet number (C_t). Experimental studies of measured mean velocity and concentration by Becker et al. [5] have proven that flow and the mixing characteristics of constant-density confined jets are only functions of the Craya-Curtet number (C_t) and flow recirculation (if $C_t \leq 0.75$). Exley [6] analytically investigated the effect of the separation and the recirculation on mixing characteristics of confined jet flow. He also verified that the Craya-Curtet number (C_t) properly estimates the flow conditions in terms of specified inlet conditions. In the study of a jet mixing at higher ratios of jet radius to tube radius, Hill [7][8] evaluated the characteristics of the mean velocity field in an isothermal homogeneous-confined turbulent jet flow by considering differential integral methods. He suggested that the mean velocity profiles in self-similar regions of the confined turbulent jets should correspond to the results of a circular free turbulent jet flow. Nickels [9] studied the mean flow behavior and compared to self-similar asymptotic expressions of velocities and stresses in order to find self-similar region in a family of axisymmetric co-flowing turbulent jet with different size of nozzle. Dealy [10][11] found that Curtet's similarity analysis may not evaluate the flow and the mixing characteristics of the confined turbulent jet flow accurately because flow inlet conditions have a significant effect on the mixing. Moeller et al. [12] investigated a macroscopic approach of confined circular jet flow with and without recirculating flows or back flows. They studied the correlation between mixing characteristics

and the Craya-Curtet number (C_t) in order to confirm the effect of recirculation. Also, they found that mixing characteristics of confined turbulent jet flow depends on the ratio of the injector diameter to the mixing duct diameter. Razinsky et al. [13] found the details of the mixing mechanism in confined turbulent jet flow without separating conditions (when the Craya-Curtet number, C_t, was below 0.9) and checked the transition status to the fully developed confined jet flow. G. Singh et al. [14] did mixing studies for variable density confined jets. They demonstrated that entrainment and mixing phenomena depend on the effect of various parameters such as: aspect ratio, density ratio, jet Reynolds number and jet location. For the study of variable density jets, Steward and Guruz [15] proposed the non-isothermal Craya-Curtet number (C_{tni}) from a logical extension of the Craya-Curtet number (C_t) of a uniform density confined jet. They validated that recirculation will not occur for $C_{tni} \geq 0.8$. Figure 1.1 shows the flow structure to explain the definition of the non-isothermal Craya-Curtet number (C_{tni}). The non-isothermal Craya-Curtet number (C_{tni}) is defined by the kinematic mean velocity (u_k) and the dynamic mean velocity (u_d),

$$C_{tni} = \frac{u_k}{\sqrt{\left(u_d^2 - \frac{1}{2}u_k^2\right)}} \tag{2}$$

The kinematic mean velocity (u_k) and the dynamic mean velocity (u_d) are defined as

$$u_k = \frac{\rho_o U_o D_o^2 + \rho_\infty U_\infty (D_t^2 - D_o^2)}{D_t^2 \rho_M} \tag{3}$$

$$u_d^2 = \frac{\rho_o U_o^2 D_o^2 + \rho_\infty U_\infty^2 (D_T^2 - D_o^2)}{D_T^2 \rho_M} - \frac{1}{2}\frac{\rho_\infty U_\infty^2}{\rho_M} \tag{4}$$

Here, ρ_M, the mean density of the exit fluid, is derived from the mass conservation equation as,

$$\rho_M = \frac{\rho_o U_o D_o^2 + \rho_\infty U_\infty (D_t^2 - D_o^2)}{D_o^2 U_o + (D_t^2 - D_o^2) U_\infty} \tag{5}$$

The physical meaning of denominator of the non-isothermal Craya-Curtet number (C_{tni}) is considered as the available excess inlet momentum for mixing the two flows in equation (2). A critical value of the non-isothermal Craya-Curtet number ($C_{tni,cri}$) was found by Steward and Guruz; If an actual non-isothermal Craya-Curtet number (C_{tni}) is greater than a critical non-isothermal Craya-Curtet number ($C_{tni,cri}$), some momentum loss of the jet occurs when the jet interacts with the co-flow. The rest of the jet momentum is dissipated completely at the duct wall. Thus, the recirculation zone is not found inside the duct. If the flow Craya-Curtet (C_{tni}) number is lower than the critical Craya-Curtet number ($C_{tni,cri}$), jet momentum is not destroyed completely by the interaction of co-flow and by the duct wall. Accordingly, the residue of jet momentum causes the formation of recirculation in the duct. Several studies of the entrainment in a turbulent flow into co-flow have been performed. Shear stress is generated in the boundary layer between the jet and co-flow or stagnant conditions due to the velocity gradient. The shear stress causes the formation of turbulent eddies which enhances in the entrainment of the surrounding fluid into the jet flow. Ricou et al. [16] studied the entrainment of axi-symmetrical turbulent jets by considering the effect of buoyancy. Pritchard et al. [17] proposed an analytical expression for R_q (entrainment ratio), $R_q = \frac{Q_\infty}{Q_o} = \frac{-(1+\sigma)}{2} + \sqrt{\frac{\sigma A_T}{A_o(1+C_L)}}$, expressed in terms of the density ratio (σ), the area ratio (A_T/A_o) and the friction loss coefficient of the flow in the duct (C_L) through the use of simple momentum and energy balances. Singh et al. [18] performed an experimental study of the entrainment and the spread characteristics of confined/semi-confined circular and noncircular confined jets in a circular tube. The similarity solutions by Becker et al. [5] are applicable to the spread characteristics of circular jet and noncircular jet as well as to the entrainment ratio, which generally depends on the diameter of the duct.

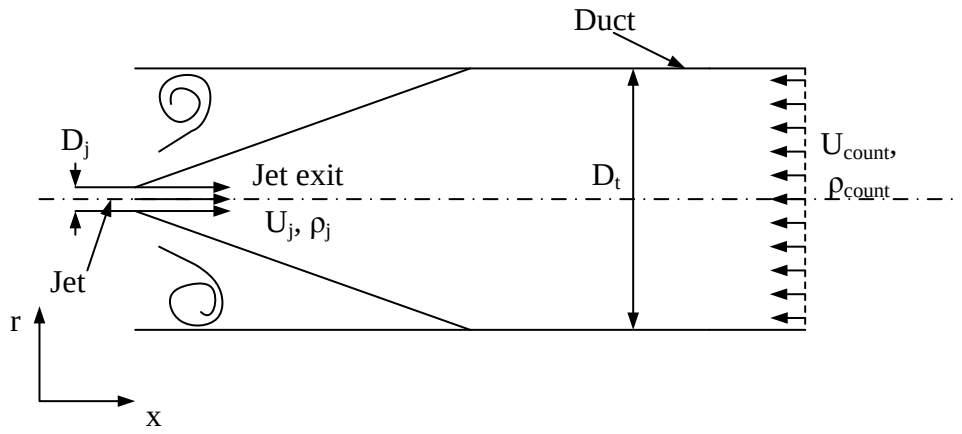

Figure 1.2 Confined turbulent jet into counter-flow

Relatively few studies of ***confined*** turbulent jet in counter-flow were performed previously in the near jet region and not further downstream because of highly complicated flow and mixing characteristics by the recirculation zone and the flow instability as shown in figure 1.2. Most previous studies of counter-flow were considered as unconfined flow condition. Arendt J. et al., was the first research group, [19] to study a turbulent jet in counter-flow. Oron et al. [20] studied unconfined turbulent jets theoretically using a flow similarity solution. The experimental studies by Beltaos et al. [21], Sekunkov [22], Morgan et al. [23] and Saghravani et al. [24] described an upstream penetration length of a turbulent jet in counter-flow condition as a linear function of a momentum ratio (a velocity ratio) between jet and counter-flow. Lam et al. [25] demonstrated that the penetration length is shorter but the spreading angle of a circular jet into a counter-flow condition is wider as the counter-flow velocity increases. Yoda et al. [26] found that the flow becomes more unstable with significant fluctuations along the radial direction as well as in the downstream direction as counter-flow velocity increases. Bernero et al. [27][28] used Particle image velocimetry (PIV) experiments to measure the dynamics of vorticity structures and chaotic fluctuations of the jet to get some additional understanding of its behavior.

They [29-32] assessed an analytical solution in a Lagrangian frame and determined an empirical equation of a mean velocity field, jet width of single turbulent jet and penetration length in counter-flow at various velocity ratios (jet velocity/counter-flow velocity). Also, Lam et al. [33] studied mixing characteristics of turbulent jet into counter-flow from a jet exit up to ***X/d***=18 as the velocity ratio (jet velocity/counter-flow velocity) changes from 3 to 15. Tsunoda et al. [34] focused on the characteristics of velocity fields and concentration fields as velocity ratios (jet velocity/counter-flow velocity: 2.9, 4 and 5.1) change. The mean concentration of a jet into counter-flow decays much faster than that of a free turbulent jet in ambient condition, as jet flow moves downstream. Luis A. et al [35] show the concentration profile as measured along axial and radial directions in water by using planar laser induced fluorescence, but only for a limited axial distance. Sivapragasam et al. [36] investigated a single confined turbulent jet into a uniform counter-flow numerically.

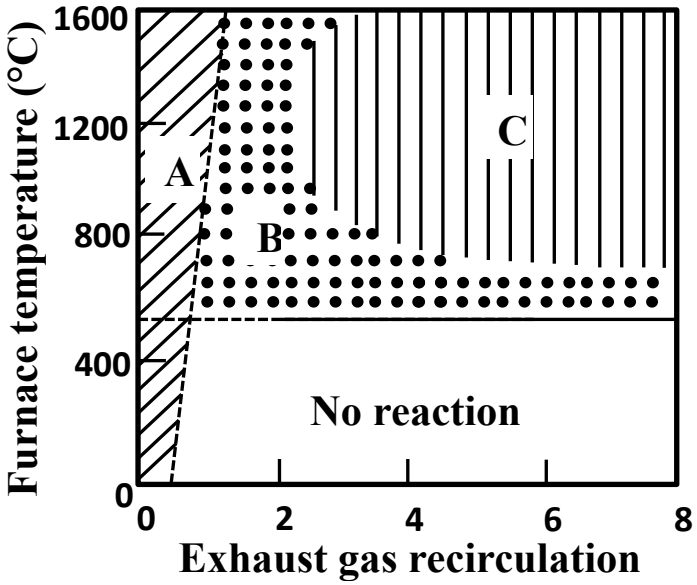

Figure 1.3 The schematic of stability limit as $K_v = \frac{\dot{m}_e}{\dot{m}_a + \dot{m}_f}$ for a furnace[26]

$\dot{m}_e$: exhaust gas mass flow rate, $\dot{m}_a$: air mass flow rate, $\dot{m}_f$: fuel mass flow rate

Homogeneous combustion is an advanced technology to control $\boldsymbol{NO_x}$ emission efficiently as well as improve thermal energy efficiency significantly by using an exhaust gas recirculation. Homogeneous combustion is referred to by different acronyms such as flameless oxidation (***FLOX***) [37], high temperature air combustion (***HiTAC***) [38] or moderate intense low oxygen dilution (***MILD***) [39]. Figure 1.3 shows the schematic of stability limit of a furnace. '***A***' is a stable combustion, '***B***' is an unstable combustion while ***C*** is a flameless oxidation or homogeneous combustion. For larger K_v values the combustion can become unstable and have no reaction (not shown in figure) as the dilution lowers the reaction rate and the heat transfer loss becomes larger than the energy released by the reaction.

From the previous literature[37]-[41], the characteristics of homogenous combustion can be summarized as follows:

- Stable volumetric reaction creates near uniform temperature and species concentration distributions.
- The reactant mixture is highly diluted (lowers the reaction rate) done by a high rate of mixing (leading to a low Damköhler number)
- The exhaust gas recirculation enables a high enough temperature ($T > T_{autoignition}$)
- $\boldsymbol{NO_x}$ emission is decreased due to low, uniform and stable temperature distribution.
- Less combustion noise due to low fluctuations of temperature temporally and spatially.
- Reduction of ***UV*** emission and visible spectral range because of less ***OH*** radical, $\boldsymbol{C_2}$ species and soot concentration in the volumetric reaction zone.

1.2. Motivation and Objectives

Many industrial applications such as furnaces or combustors use confined turbulent jets. Mixing and entrainment in confined turbulent jets are different from free turbulent jets because the jet momentum is not conserved due to an adverse pressure gradient caused by the confinement. Confined turbulent jets have the benefits of fast mixing and fast dilution without fans needed to drive an internal/external EGR flow. However, very few investigations have been conducted on flow characteristics of ***confined*** turbulent jets due to their complicated flow structure. Therefore, an analysis of flow and mixing characteristics of confined turbulent jets is necessary. Previous research on the fundamental aspects of flow and mixing characteristics of confined turbulent jet flow into co- or counter-flow are very limited. All of previous studies usually focused on velocity fields under isothermal conditions even though mixing is very important to create working regime of homogeneous combustion (because these jets have to first mix with the burned gas inside the furnace and simultaneously heat and dilute prior to combustion). The combustion pattern and emissions from reacting confined turbulent jets are affected by jet interactions and mixing. Also, typically the previous investigators used only low jet velocity and measured the velocity near the jet exit due to the limitation of the measurement of high jet velocity and complexity of the flow structure of the confined turbulent jet. Therefore, there is still insufficient information about how much flow and mixing characteristics are changed by the effect of high jet velocity up to transonic condition ($\boldsymbol{M}$=0.9) in a confined environment.

To study the flow and mixing characteristics of confined non-reacting and reacting turbulent jets for creating homogenous combustion in industrial furnaces numerically and experimentally, the first part of this thesis is to show an experimental and numerical

investigation of the resulting concentration fields and temperature field as well as velocity field in the ***confined***, non-reacting, ***non-isothermal***, high velocity turbulent jet flow for practical applications such as furnaces as well as any application which has confined turbulent jet conditions. In the second part of this thesis, the limit of ranges of important furnace and flow parameters that can enable a near homogenous combustion will be investigated numerically by using the current existing furnace based on previous works. To find the variables that effect the stability limit of homogenous combustion, air nozzle diameter ($\boldsymbol{d_{air}}$), fuel nozzle diameter ($\boldsymbol{d_f}$), equivalence ratio ($\boldsymbol{\Phi}$), oxygen concentration, gravity, different bottom temperature and separation distance as well as soot radiation are included in the investigation. Finally, the range limits and some design considerations for working domain of homogeneous combustion as influenced by the chosen parameters are examined and explained by the analysis.

CHAPTER 2

Experimental and numerical setup of a confined non-reacting turbulent jet in co- and counter-flowing streams

2.1. Experimental Setup

To investigate confined jet flow, a large circular duct for confined jet test is selected to a 2ft outer diameter and 6ft vertical height and shown schematically in figure 2.2 and 2.3. The inside 2" insulation is used to prevent heat loss through the duct wall. For measuring the flow and mixing characteristics of confined jets inside the duct such as velocity, concentration, temperature and entrainment ratio, the duct has 15 access holes on the duct wall. The distance between each hole is 4″. Measurement device slides into the hole (in order to measure flow and mixing characteristics of the flow inside the duct) and when not used the hole is covered in figure 2.4. To ensure the axisymmetric flow, six holes are placed at 0° and along the same vertical line. The remaining nine holes are placed at 90° angular direction to the vertical line of six holes. The center jet is created by a circular nozzle of 0.25″ exit diameter and it is installed in the center of the duct vertically. The nozzle is designed on the basis of Masahiro et al. [42]. The range of the discharge coefficient value of this type of nozzle varies from 0.984 (at $\boldsymbol{M}$=0.3) to 0.99 (at $\boldsymbol{M}$=0.9) depending on each velocity. The jet flows are injected upward from the nozzle inside the duct. The setup of the hot co- and counter-flow is aligned and opposed to the jet flow. For simulating the exhaust gas as hot co- and counter-flow, co- and counter-flow velocity is calculated from 1 to 10 MMBtu (Generated) industrial-scale burners' exhaust gas flow rate and

induced by four fans. These co- or counter-flow was calibrated at room temperature (296.65K). Then, the fan's law, Bernoulli's equation (***M***<0.3) and compressed flow velocity equation was considered in order to find the mean co- and counter-velocity at ***T***=328.15K. The calculation is found in figure 2.1 as shown below.

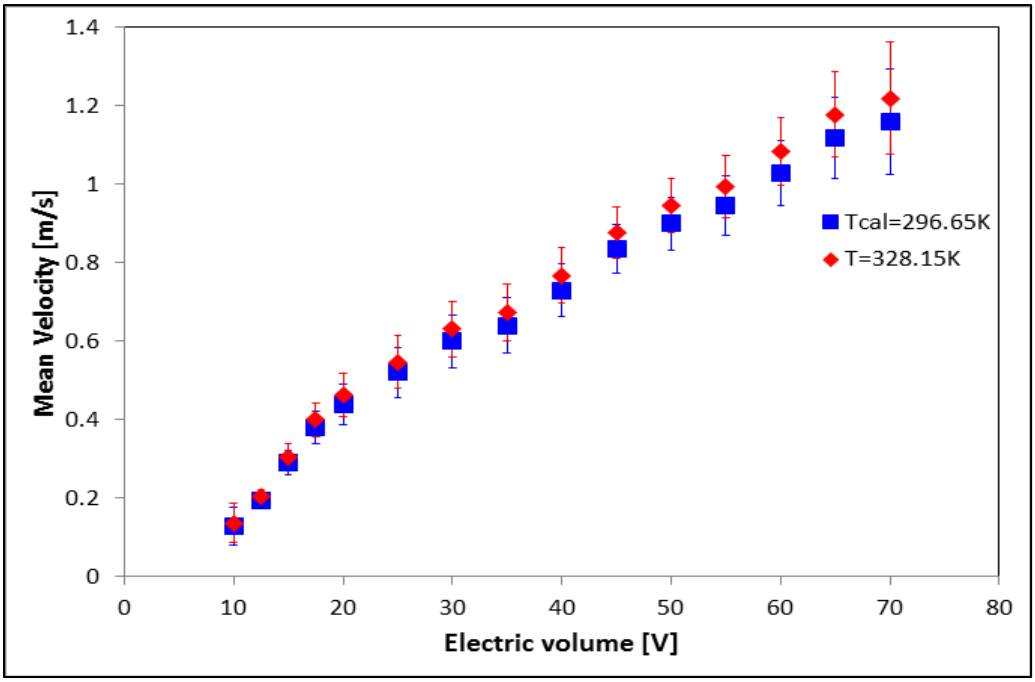

Figure 2.1 The calibration of co- or counter-velocity as function of the power setting of the fan

The turbulent flow velocity from the nozzle is maintained nearly constant during the experiment by two compressed air tank supply units. For obtaining the concentration profiles of the jet flow, ***NO*** gas is used as a tracer gas into the compressed air before out through a nozzle. A 3m long pipe is used in order to ensure well-mixed flows between the compressed air and the ***NO*** gas before entering the nozzle. The compressed air jet (containing the tracer gas ***NO*** for measuring the concentration profile) is regulated by a flow-meter. To measure the turbulent jet velocity correctly, this flow meter is calibrated. To obtain velocity profiles, temperature profiles and

concentration profiles, the measuring device is used as a flow intrusion method. To reduce a disturbance against the flow for measuring, the cross section of the measuring device is designed in a shape of an airfoil. The Pitot tube, the sampling tube and the thermocouple are installed inside the measuring device. To measure different ranges of the velocity, the pair of absolute pressure transducers (***COOPER PTG404*** Series) for M>0.3 and four different differential pressure transducers (***SETRA C239*** series & ***TESTO***) are used below M=0.3. The sampling gas is driven by the vacuum pump through the sampling tube. The sampling line is connected to a NO_x Gas analyzer (***Siemens***) after removing H_2O inside the sampling gas. The entire data to be converted as the pressure, the ***NO*** concentration and the temperature inside the duct are connected to a ***NI DAQ*** system. Finally, the velocity, the concentration of ***NO*** and the temperature are calculated in ***LABVIEW***.

To analyze flow and mixing characteristic of a non-reacting confined turbulent jet into co- or counter-flow in detail, the experimental apparatus of the confined turbulent jet in co- or counter-flow was designed as shown figure 2.2 and 2.3 respectively. The range of the Reynolds number of the confined turbulent jet in this experimental study is $0.39\times10^5 < \mathrm{Re} < 1.2\times10^5$. The jet nozzle diameter and the mean jet velocity at the nozzle exit are used to calculate the Reynolds number. A compressed air tank enables a high jet velocity at the nozzle. To simulate the exhaust gas as hot co- or counter-flow, the co- or counter-flow air is heated and maintained at 55°C by a heater (***ADH***-10KW, ***Chromalox***). The turbulent air jet with the nitric oxide (***NO***) tracer gas is injected through a 1/4″ circular nozzle in hot air co- or counter-flow. While the tracer gas, ***NO***, is injected through the nozzle into co- or counter-flow, the measurement device will move vertically through turbulent jet flow. In order to calculate turbulent jet velocity, the pressure, the temperature and the concentration of ***NO*** need to be measured and averaged for 30sec after

stabilizing a fully developed turbulent flow. In the initial stage of the test, the experimental setup and the procedure was calibrated and validated by checking the axisymmetric velocity and concentration characteristics of a single turbulent jet without any co- or counter-flow in the duct. To study the effect of the non-isothermal Craya-Curtet number ($\boldsymbol{C_{tni}}$), the velocity ratio between jet and co-flow is only changed at the fixed jet nozzle diameter. Four jet velocity conditions such as 96.12m/s ($\boldsymbol{M}$=0.3), 160.19m/s ($\boldsymbol{M}$=0.5), 224.26m/s ($\boldsymbol{M}$=0.7) and 304.37m/s ($\boldsymbol{M}$=0.9) are chosen for these experiments. Co-flow velocities of 0.612m/s, 0.913m/s, 1.856m/s and 3.123m/s are used and they are calculated on the basis of the amount of the exhaust gas from a 1MMBtu to 10MMBtu combustor. Also, to prove the correction between the non-isothermal Craya-Curtet numbers ($\boldsymbol{C_{tni}}$) and flow/mixing characteristics of confined turbulent jet flow in co-flow, the non-isothermal Craya-Curtet number ($\boldsymbol{C_{tni}}$) is determined in these experiments. The range of the non-isothermal Craya-Curtet number ($\boldsymbol{C_{tni}}$) is from 0.17 to 2.53. For the study of a confined turbulent jet into counter-flow, the modified momentum ratio ($\boldsymbol{M_{sqrt}}$) is used in equation (6).

$$M_{sqrt} = \sqrt{\frac{\dot{m}_j U_j}{\dot{m}_{count} U_{count}}} = \sqrt{\frac{\rho_j A_j U_j^2}{\rho_{count} A_{count} U_{count}^2}} \tag{6}$$

The same set of velocities, 0.612m/s, 0.913m/s, 1.856m/s and 3.123m/s are used for the counter-flow velocities of the amount of the exhaust gas from a 1MMBtu to 10MMBtu combustor. Flow and mixing characteristics of the confined turbulent jet in counter-flow is demonstrated by using modified momentum ratio from 0.40 to 3.43. The physical relation between modified momentum ratio ($\boldsymbol{M_{sqrt}}$) and flow/mixing characteristics of confined turbulent jet flow into counter-flow will be verified. In the experimental studies, the measurements will be made up to $\boldsymbol{X/d}$=19 from jet nozzle exit because of the spatial limitations in the test duct.

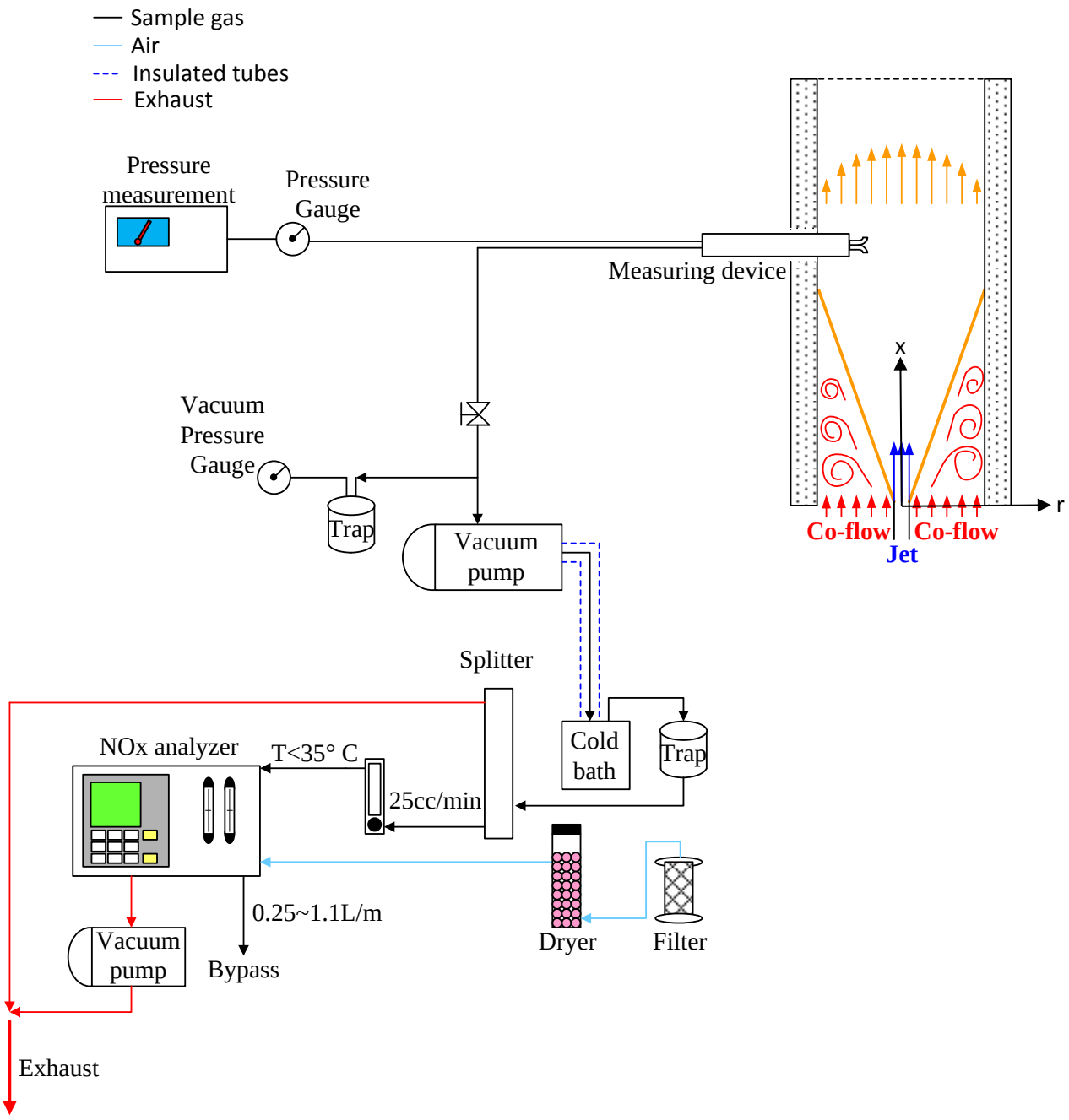

Figure 2.2 The experimental schematics of a confined turbulent jet in co-flowing streams

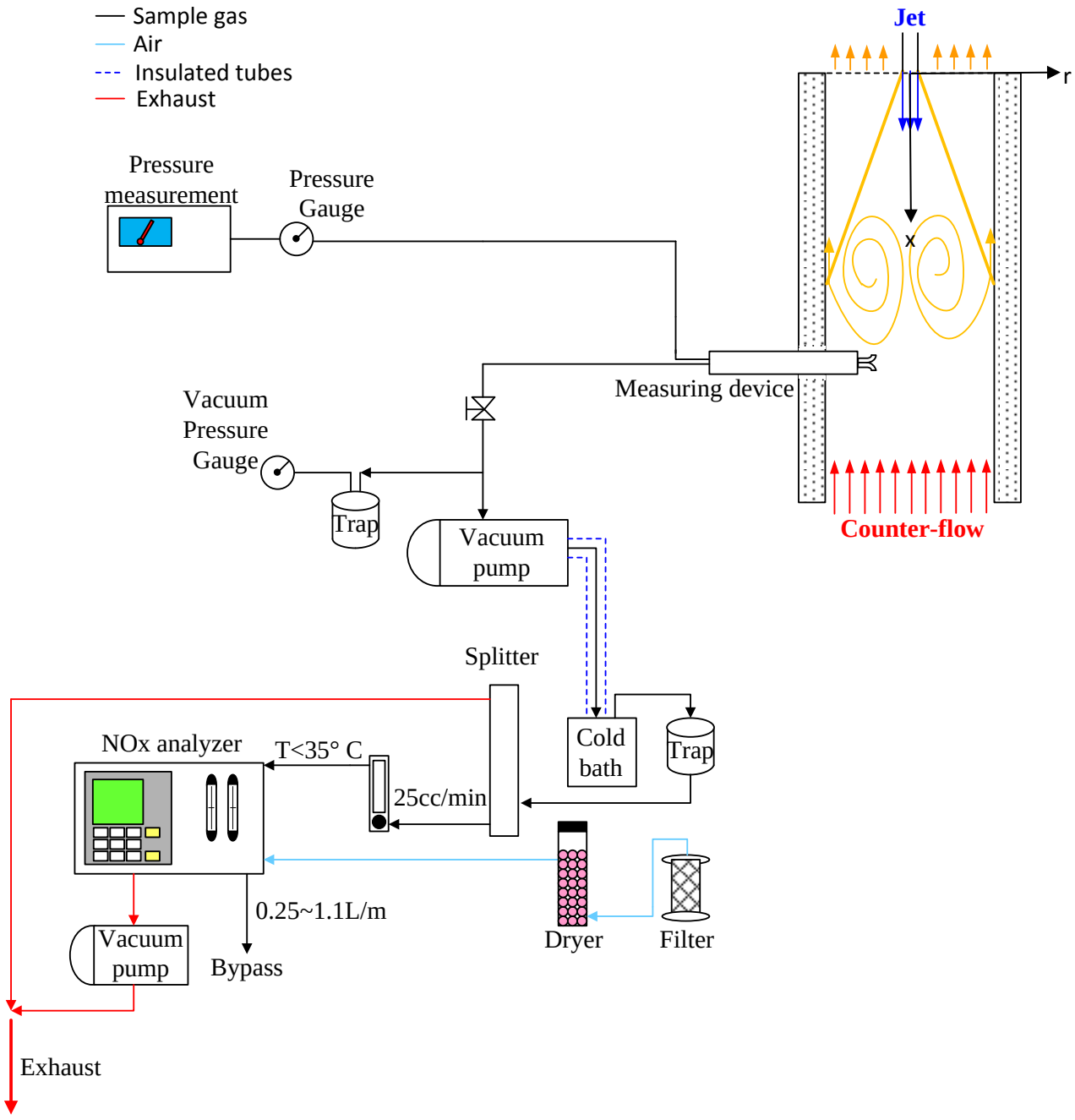

Figure 2.3 The experimental schematics of a confined turbulent jet in counter-flowing streams

(a) Duct for confined turbulent jet test

(b) Jet nozzle inside the duct

(c) Measurement device

Figure 2.4 The picture of test facility for the study of confined turbulent jet

2.2. The setup of numerical calculation

Numerical simulations are performed by using ***FLUENT*** among several commercial programs. To analyze flow and mixing characteristics of a confined non-reacting turbulent jets in this research, the conservation equations of mass, species, momentum, energy as well as equation of state for the fluid are used as follows [43],

$$\frac{\partial \rho}{\partial t} + \frac{\partial}{\partial x_i}(\rho u_i) = S_m \tag{7}$$

$$\frac{\partial}{\partial t}(\rho Y_i) + \frac{\partial}{\partial x_i}(\rho u_i Y_i) = \frac{\partial}{\partial x_i}\left(\rho D_{ij}\frac{\partial Y_i}{\partial x_i} + \alpha\left(\frac{1}{T}\right)\left(\frac{\partial T}{\partial x_i}\right)\right) + S_i \tag{8}$$

$$\frac{\partial}{\partial t}(\rho u_i) + \frac{\partial}{\partial x_i}(\rho u_i u_j) = \frac{\partial p}{\partial x_i} + \frac{\partial}{\partial x_j}\left(\mu\left(\frac{\partial u_i}{\partial x_j} + \frac{\partial u_j}{\partial x_i}\right) - \frac{2}{3}\mu\frac{\partial u_i}{\partial x_i}\delta_{ij}\right) + \rho g_i \tag{9}$$

$$\frac{\partial}{\partial t}\left(\rho\sum_i Y_i h_i\right) + \frac{\partial}{\partial x_i}\left(\rho u_i \sum_i Y_i h_i\right) = -\frac{\partial}{\partial x_i}\left(\kappa\frac{\partial T}{\partial x_i}\right) + \frac{\partial}{\partial x_i}\sum_i h_i\left(\rho D_{ij}\frac{\partial Y_i}{\partial x_i} + \alpha\left(\frac{1}{T}\right)\left(\frac{\partial T}{\partial x_i}\right)\right)$$
$$+\frac{\partial p}{\partial t} + u_i\frac{\partial p}{\partial x_i} + \left(\mu\left(\frac{\partial u_i}{\partial x_j} + \frac{\partial u_j}{\partial x_i}\right) - \frac{2}{3}\mu\frac{\partial u_i}{\partial x_i}\delta_{ij}\right)\frac{\partial u_i}{\partial x_i} + S_h \tag{10}$$

$$\rho = \frac{p_{ref} + p}{\bar{R}T\sum_i \frac{m_i}{M_i}} \tag{11}$$

Where x_i is the spatial coordinate, t is time, u_i is the velocity, ρ is the density, S_m is mass increment by the evaporation of the droplet, Y_i is the mass fraction of species i, D_{ij} is the species diffusion coefficient, α is the thermal diffusion coefficient, T is temperature, S_i is the production

of species ***i*** by chemical reaction, ***k*** is the thermal conductivity coefficient, S_h is the production of enthalpy by the chemical reaction, radiation and heat transfer between two phase fluid, ***h*** is the enthalpy, p_{ref} is the standard pressure, ***p*** is the pressure and M_i is the molecular weight of species ***i***.

FLUENT has several turbulent models. For this research, the standard ***K-ε*** model and realizable ***K-ε*** model are considered. The equations of standard ***K-ε*** model[44] are

$$\frac{\partial}{\partial t}(\rho k)+\frac{\partial}{\partial x_i}(\rho k u_i)=\frac{\partial}{\partial x_i}\left(\left(\mu+\frac{\mu_t}{\sigma_k}\right)\frac{\partial k}{\partial x_j}\right)+G_k+G_b-\rho\varepsilon-Y_M+S_k \tag{12}$$

$$\frac{\partial}{\partial t}(\rho \varepsilon)+\frac{\partial}{\partial x_i}(\rho \varepsilon u_i)=\frac{\partial}{\partial x_j}\left(\left(\mu+\frac{\mu_t}{\sigma_\varepsilon}\right)\frac{\partial \varepsilon}{\partial x_j}\right)+C_{1\varepsilon}\frac{\varepsilon}{k}(C_{3\varepsilon}G_b+G_k)-\rho C_2\frac{\varepsilon^2}{k}+S_\varepsilon \tag{13}$$

$$\mu_t=\rho C_\mu\frac{k^2}{\varepsilon} \tag{14}$$

The model constants of the ***K-ε*** turbulence model are $C_{1\varepsilon}$=1.44, $C_{2\varepsilon}$=1.92, C_μ=0.99, σ_k=1.0 and σ_ε=1.3.

The realizable ***K-ε*** model was proposed by Shih et al.[45] to resolve the limitation of traditional ***K-ε*** model. The transport equations for the realizable ***K-ε*** model are

$$\frac{\partial}{\partial t}(\rho k)+\frac{\partial}{\partial x_i}(\rho k u_i)=\frac{\partial}{\partial x_i}\left(\left(\mu+\frac{\mu_t}{\sigma_k}\right)\frac{\partial k}{\partial x_j}\right)+G_k+G_b-\rho\varepsilon-Y_M+S_k \tag{15}$$

$$\frac{\partial}{\partial t}(\rho \varepsilon)+\frac{\partial}{\partial x_j}(\rho \varepsilon u_j)=\frac{\partial}{\partial x_j}\left(\left(\mu+\frac{\mu_t}{\sigma_\varepsilon}\right)\frac{\partial \varepsilon}{\partial x_j}\right)+\rho C_1 S\varepsilon-\rho C_2\frac{\varepsilon^2}{k+\sqrt{\nu\varepsilon}}+C_{1\varepsilon}\frac{\varepsilon}{k}C_{3\varepsilon}G_b+S_\varepsilon \tag{16}$$

$$C_1 = \max\left[0.43, \frac{\eta}{\eta+5}\right], \eta = S\frac{k}{\varepsilon} \tag{17}$$

$$G_k = -\rho\overline{u_i'u_j'}\frac{\partial u_j}{\partial x_i},\ G_b = -\frac{g_i}{\rho}\frac{\mu_t}{\mathrm{Pr}_t}\left(\frac{\partial \rho}{\partial T}\right)_p\frac{\partial T}{\partial x_i},\ Y_M = 2\rho\varepsilon\left(\frac{k}{\gamma RT}\right) \tag{18}$$

Where $\boldsymbol{G_k}$ means the generation of mean turbulent kinetic energy by the mean velocity gradient, $\boldsymbol{G_b}$ represents the production of turbulent kinetic energy due to the buoyancy, $\boldsymbol{Y_M}$ is the contribution of the fluctuating dilatation. To manipulate this turbulence model, $\boldsymbol{Pr_t}$ (Turbulent Prandtl number)=0.85, $\boldsymbol{C_2}$=1.9, $\boldsymbol{C_{1\varepsilon}}$=1.44, $\boldsymbol{\sigma_k}$=1.1, $\boldsymbol{\sigma_\varepsilon}$=1.2, $\boldsymbol{C_\mu}$=0.09, $\boldsymbol{S_k}$ and $\boldsymbol{S_\varepsilon}$ (user defined source terms) are used as default values.

Enhanced wall function is considered to estimate the effect by wall. Enhanced wall function is called near wall modeling that uses a two-layer model [43]. The whole domain for numerical calculation is subdivided into a near wall region (viscosity-dominant region, $\boldsymbol{Re_y}$<$\boldsymbol{Re_y^*}$) and a fully turbulent region ($\boldsymbol{Re_y}$ >$\boldsymbol{Re_y^*}$, $\boldsymbol{Re_y^*}$=200).

$$\mathrm{Re}_y = \frac{\rho y\sqrt{k}}{\mu} \tag{19}$$

where $\boldsymbol{y}$ is the normal distance of wall at the cell centers. The $\boldsymbol{y}$ is calculated as:

$y \equiv \min_{\vec{r}_w \in \Gamma_w}\left\|\vec{r} - \vec{r}_w\right\|$, $\vec{r}$ and $\vec{r}_w$:position vector of the field and wall respectively (20)

Figure 2.5 shows the schematic diagram of the computational domain used in this study. The computational domain is one-quarter of the size of the real main cylindrical test duct for a confined turbulent jet into co- or counter-flow. The domain is $40D \times 264D$ (radial direction and

axial direction) of the configuration based on the center jet nozzle diameter (***D***). The domain consists of 2.8 million grid points to be made up of tetrahedrons meshes for adapting real shape properly. The number of grid points leads to typical average cell dimensions of (x: 3mm, y: 3mm z: 3.3mm) which is a resolution that is sufficient to describe the flow and mixing characteristics by considering the accuracy and required computation time. Also, initial value of K, ε or turbulence intensity for turbulence model such as the standard ***K-ε*** model and realizable ***K-ε*** model are estimated by the initial jet velocity and co- or counter-flow velocity condition.

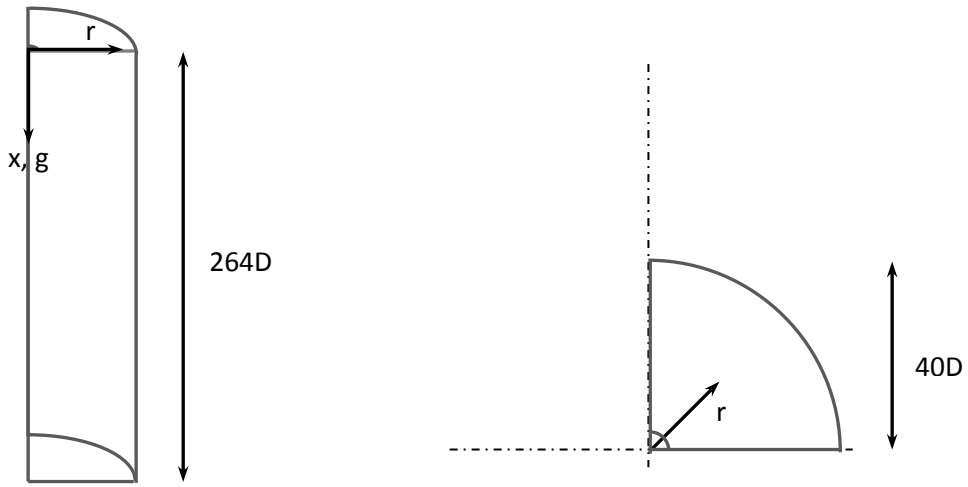

Figure 2.5 The schematic diagram of the computational domain and coordinate

2.2.1. The selection of turbulence model

To find the optimal model for this study, the standard ***K-ε*** model and realizable ***K-ε*** model are investigated in this section through the comparisons between experimental results and each numerical calculation. The comparisons are described at confined non-reacting turbulent jet into co-flowing streams in figure 2.6. Generally, the standard ***K-ε*** model shows the better agreement with experimental results of flow and mixing characteristics of confined non-reacting turbulent. Therefore, the standard ***K-ε*** turbulence model will be used to calculate the confined non-reacting turbulent jet into co- and counter-flowing streams.

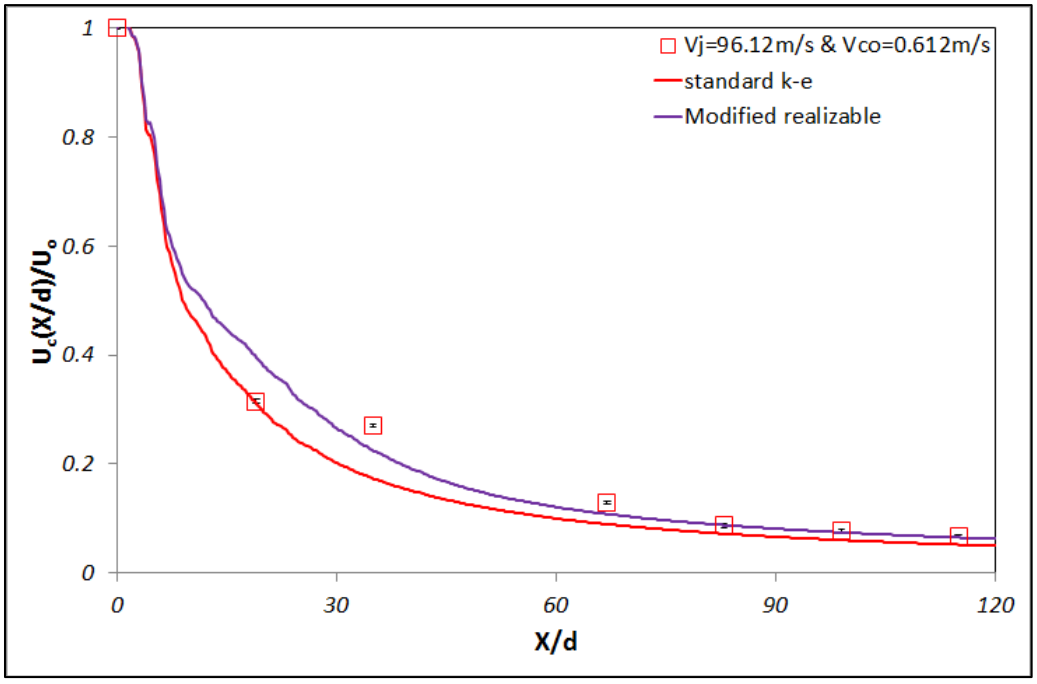

(a) Normalized center velocity in axial axis

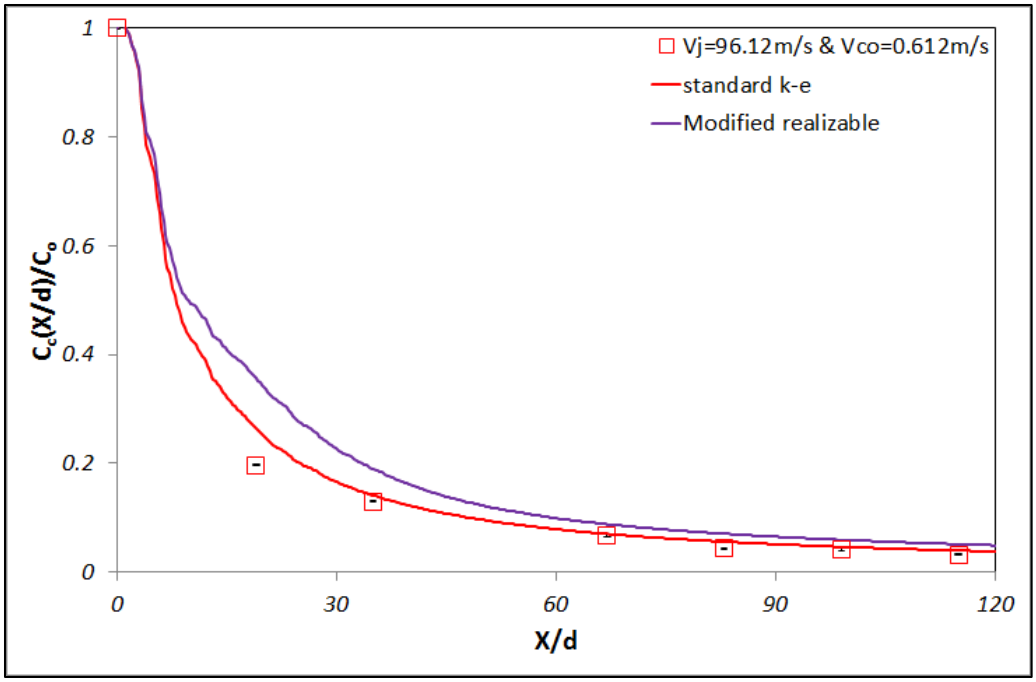

(b) Normalized center concentration in axial axis

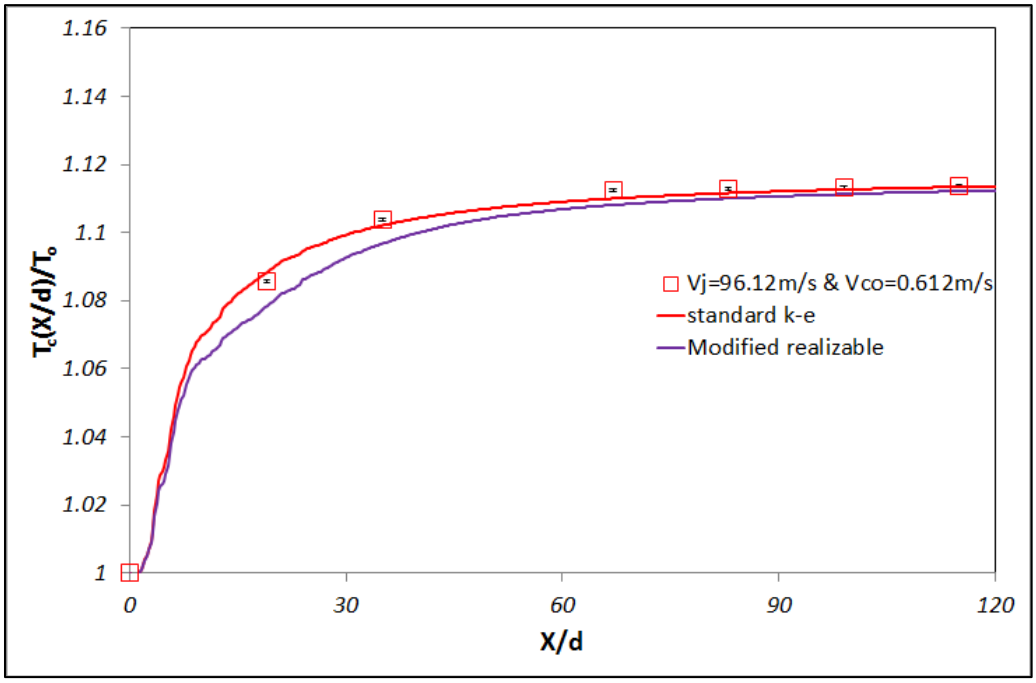

(c) Normalized center temperature in axial axis

Figure 2.6 The verification of the turbulence models

2.2.2. The effect of turbulence coefficients and turbulent quantities in turbulence model

It is well known that the standard ***K-ε*** turbulence model over-predict the decay rate and the spreading rate of a round jet. There are found in the following modification of the $C_{\varepsilon 1}$ constant in the dissipation equation [46][47][48].

$$C_{\varepsilon 2} = 1.92 - 0.667\left\{\frac{y_{1/2}}{2U_{cl}}\left(\left|\frac{dU_{cl}}{dx}\right| - \frac{dU_{cl}}{dx}\right)\right\}^{0.2} \quad (21)^{[46]}$$

$$C_{\varepsilon 1} = 1.14 - 5.31\frac{y_{1/2}}{U_{cl}}\frac{dU_{cl}}{dx} \quad (22)^{[47]}$$

$$C_{\varepsilon 1} = 1.4 - 3.4\left(\frac{\kappa}{\varepsilon}\frac{\partial U}{\partial x}\right)_{cl}^{3} \quad (23)^{[48]}$$

Where $y_{1/2}$ is a normal distance, U_{cl} is a velocity at center, x is an axial distance, k is a turbulent kinetic energy and ε is a turbulent dissipation.

The adjustment of the turbulence quantities such as turbulent kinetic energy provide better agreement of jet spread and decay rates of turbulent jet flow [49][50]. To check these effects, several numerical calculations were performed. There were no significant effects found in the range of conditions in my study. Therefore, in this dissertation, the effect of different turbulent coefficients and changed turbulence quantities are not considered.

2.2.3. The effect of mass diffusivity and dilute of approximation

To validate mass diffusivity in given values of ***FLUENT***, the mass diffusivity was calculated on the basis of the test condition of confined non-reacting turbulent jet flow. The dependence of the mass diffusion coefficient on temperature for gases is able to be defined in the ***Chapman-Enskog*** theory.

$$D = \frac{1.858\times10^{-3}T^{\frac{3}{2}}\sqrt{\frac{1}{Mw_1}+\frac{1}{Mw_2}}}{P\sigma_{12}^2\Omega} \qquad (24)^{[50]}$$

Where ***T*** is a temperature, ***Mw*** is a molar mass, ***P*** is a pressure, σ_{12} is an average collision diameter and ***Ω*** is a temperature-dependent collision integral. There is the difference between a given value (***D***=0.288cm^2/s) in ***FLUENT*** and a calculated value (***D***=0.235cm^2/s) by ***Chapman-Enskog*** theory. However, there is no any difference of concentration distribution between dilute approximation and ***Chapman-Enskog*** theory. Also, a dilute approximation was checked because of the low concentration used in the test conditions. Dilute approximation is found in [43],

$$D_{i.m} = \frac{1-\chi_i}{\sum_{j,j\neq i}\left(\chi_j D_{i,j}\right)} \qquad (25)$$

Where $D_{i,m}$ is mass diffusivity as a constant or as a polynomial function of temperature and χ_i is mass faction of ***i*** species.

Figure 2.7 shows the effect of dilute approximation. It does not see any difference by the effect of dilute approximation.

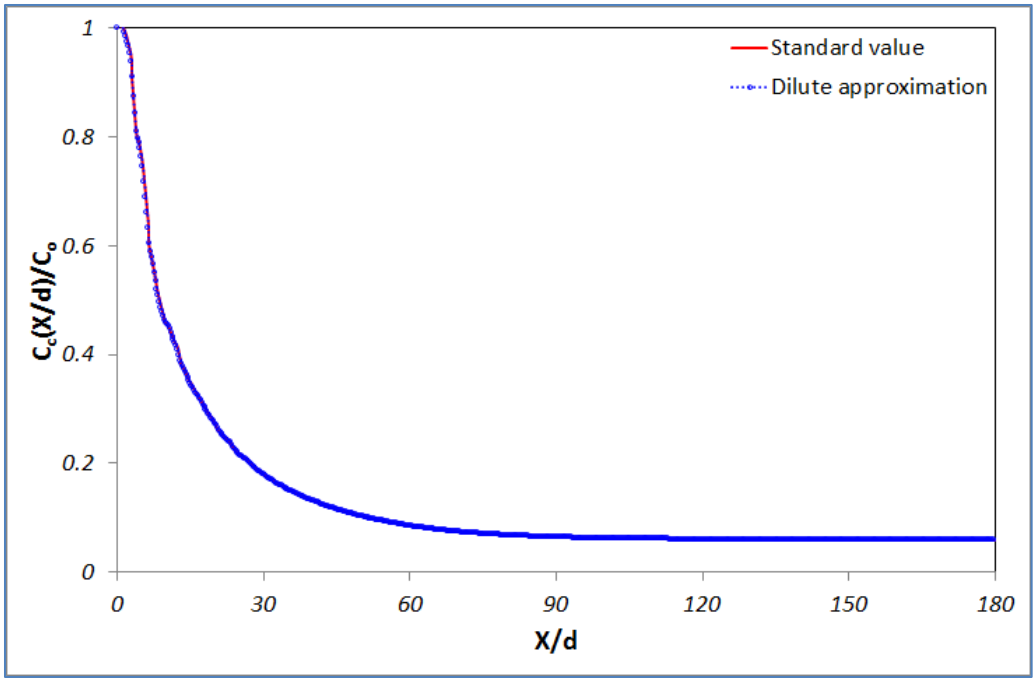

Figure 2.7 The verification of the effect of dilute of approximation

As a result, the study of confined non-reacting turbulent jet in co- and counter-flow in this dissertation, the standard ***K-ε*** turbulence model with given value (***D***=0.288cm^2/s) in ***FLUENT*** is used.

CHAPTER 3

Experimental and numerical results of a confined non-reacting turbulent jet in co-flow and counter-flow

3.1. Experimental and numerical results of a confined non-reacting turbulent jet in co-flow

In this section, the experimental results of the velocity, the concentration and the temperature field as well as the entrainment ratio in the confined turbulent jet into co-flow is studied. To maintain a fully developed turbulence condition, the jet Reynolds number is kept above 10^4 as proposed by Dimotakis [52].

3.1.1. The verification of the non-isothermal Craya-Curtet number for the flow and the mixing characteristics of the confined turbulent jet in co-flow

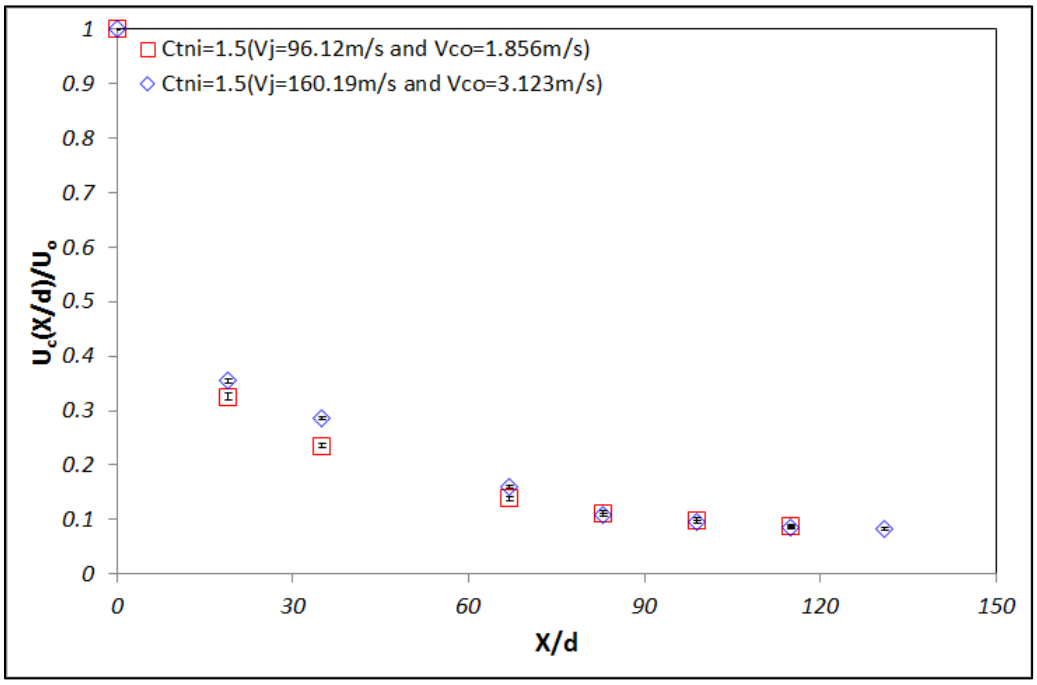

(a) Normalized velocity

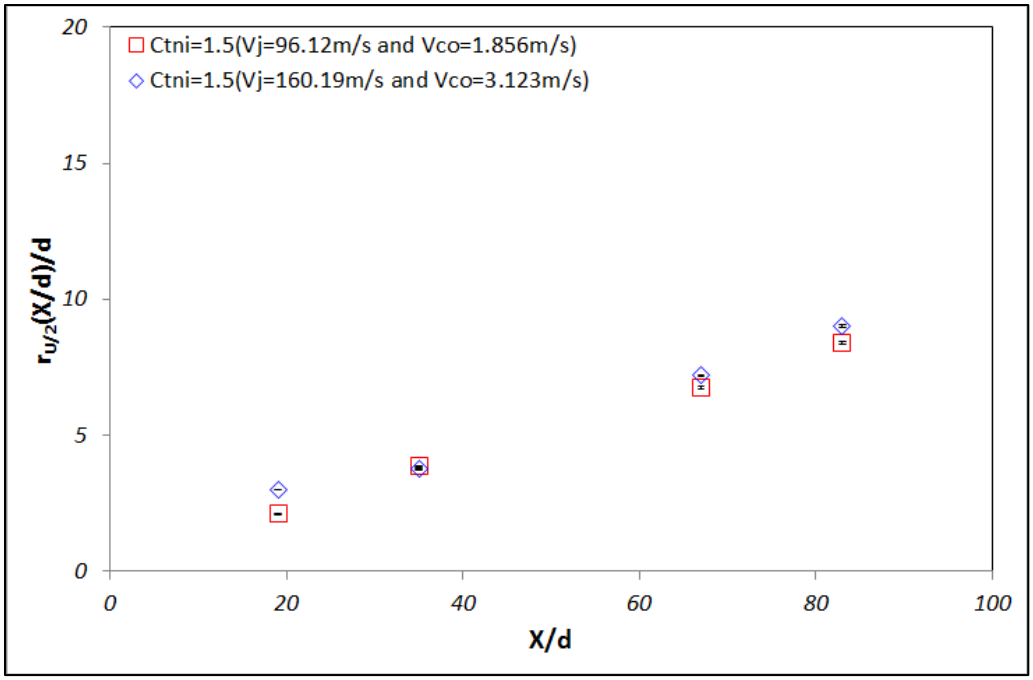

(b) Width of half jet velocity

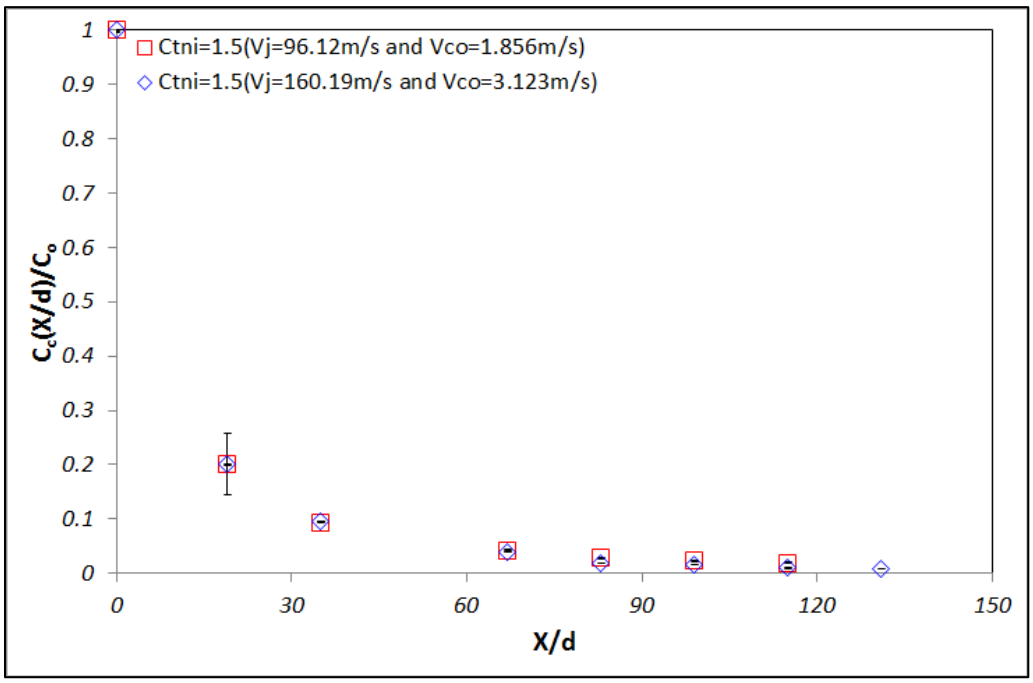

(c) Normalized concentration

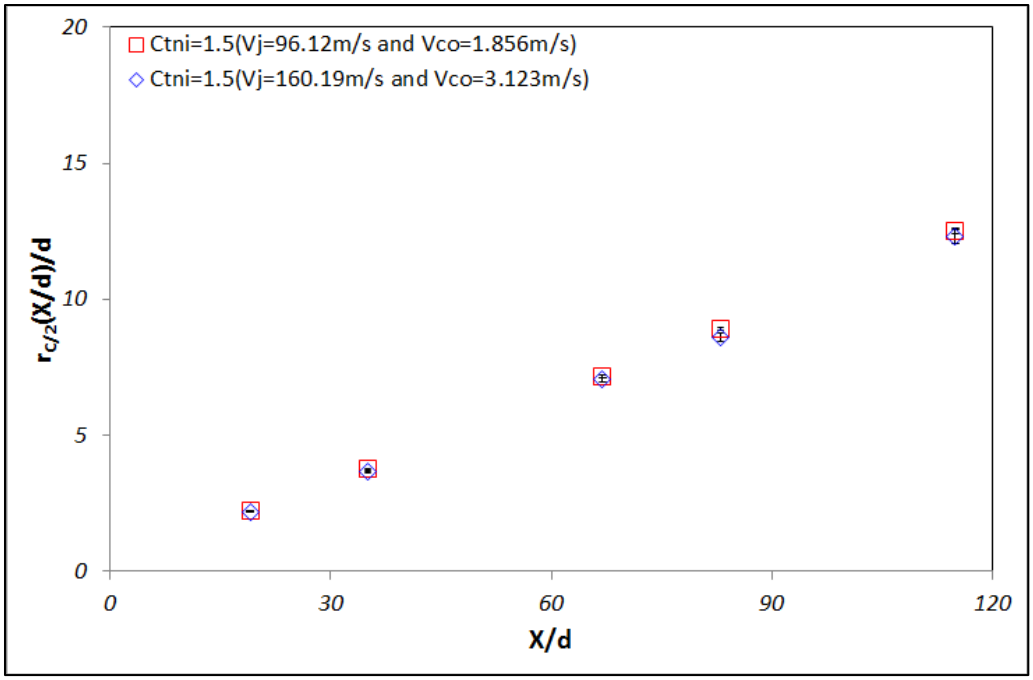

(d) Width of half concentration

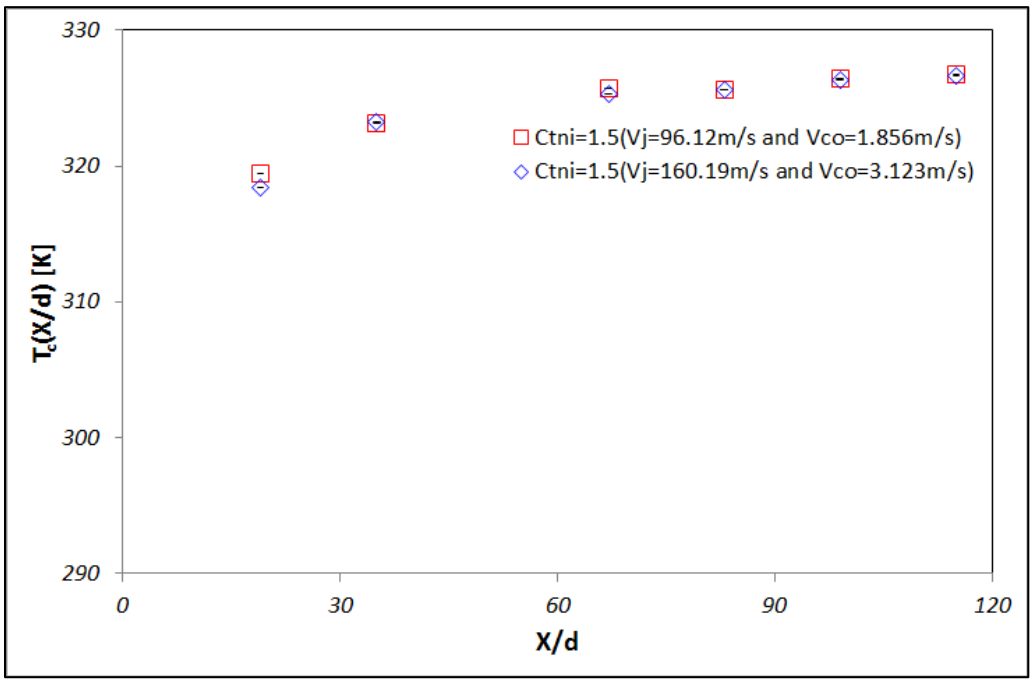

(e) Normalized temperature

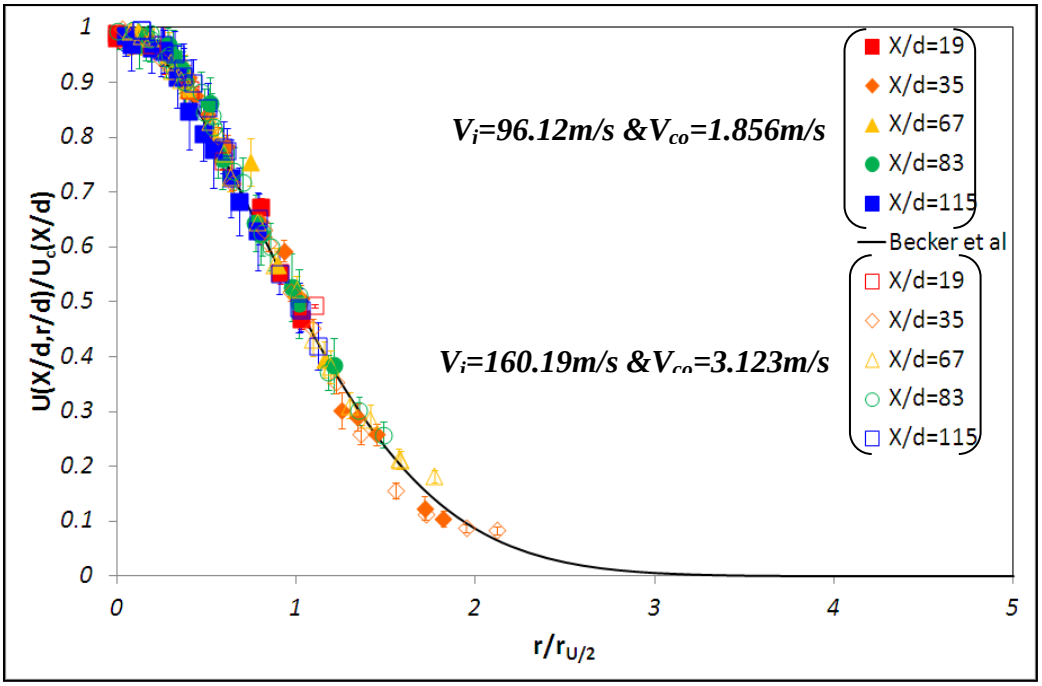

(f) Normalized velocity in radial axis

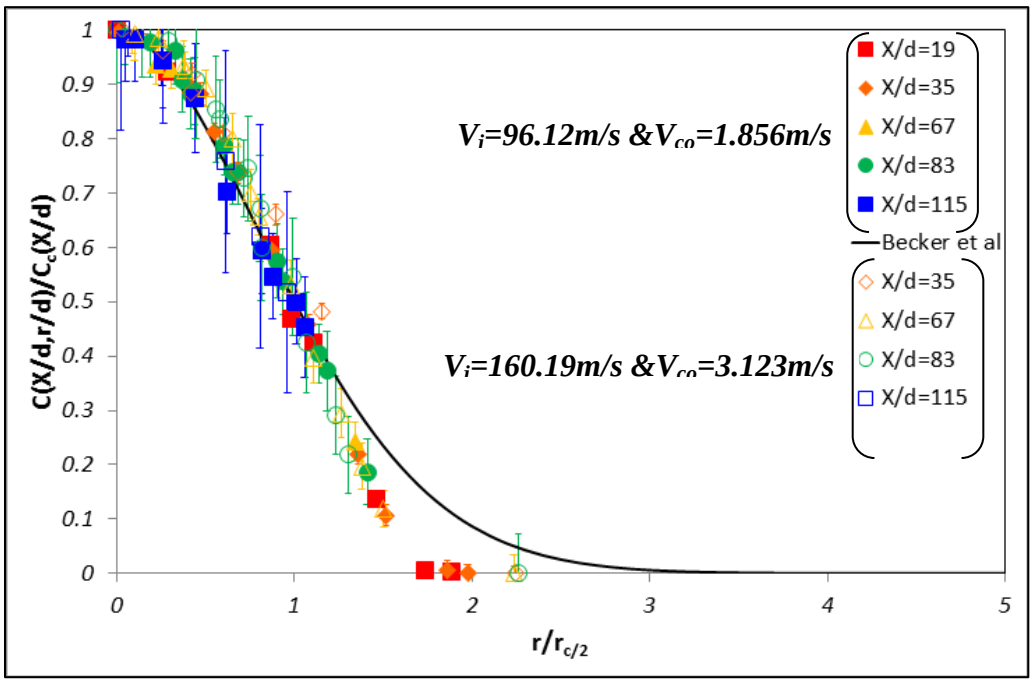

(g) Normalized concentration in radial axis

Figure 3.1 The verification of the non-isothermal Craya-Curtet number

The non-isothermal Craya-Curtet number is widely used to explain the recirculation zone in the confined turbulent jet. In this paper, the possibility of the non-isothermal Craya-Curtet

number to validate the flow and the mixing characteristics in a non-isothermal confined turbulent jet is assessed. Figure 3.1 shows that the velocity, the temperature and the width of jet velocity/concentration are mostly the same at the same non-isothermal Craya-Curtet number in spite of different jet and co-flow velocity (***X***: axial direction, ***d***: jet nozzle diameter, ***r***: radial direction, $\boldsymbol{r_{U/2}}$: width of the half jet velocity and $\boldsymbol{r_{C/2}}$: width of the half ***NO*** concentration). Therefore, the non-isothermal Craya-Curtet number can be used to analyze the flow and the mixing characteristics as well as study the recirculation zone of the non-isothermal confined turbulent jet.

3.1.2. The experimental and numerical conditions of a confined non-reacting turbulent jet in co-flow

Jet velocity(m/s)	Coflow velocity(m/s)	Craya Curtet number
96.12	0.612	0.50
	0.913	0.74
	1.856	1.50
	3.123	2.53
160.19	0.612	0.30
	0.913	0.45
	1.856	0.90
	3.123	1.50
224.26	0.612	0.22
	0.913	0.32
	1.856	0.65
	3.123	1.08
304.37	0.612	0.17
	0.913	0.24
	1.856	0.48
	3.123	0.80

Table 3.1 The experimental and numerical conditions of co-flow

To study the characteristics of the flow and mixing of the confined turbulent jet into co-flow, the profiles of the velocity, the concentration, the temperature, the width and the entrainment are determined experimentally and numerically. In this section, the effect of the non-isothermal Craya-Curtet number is investigated. The experimental and numerical conditions that have been chosen for this study are listed in table 3.1. To identify the distribution of ***NO*** concentration in the jet flow, the ***NO*** gas is used as the tracer gas into the jet flow.

3.1.3. The velocity distribution

The characteristics of the velocity are investigated along the axial and the radial direction. To check the effect by different co-flow velocities, the axial velocity profiles are plotted by changing the velocity of co-flow at fixed jet velocity. The initial jet velocity ($\boldsymbol{U_o}$) is normalized by using the centerline velocity ($\boldsymbol{U_c}$). The location of normalized velocity is also normalized by a jet nozzle diameter ($\boldsymbol{d}$).

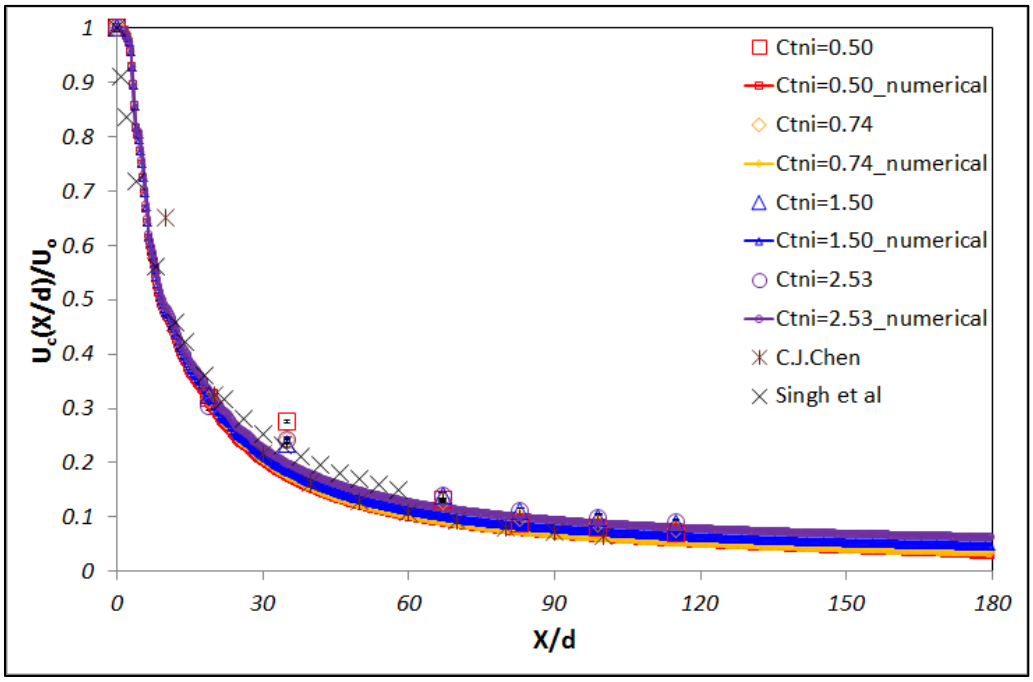

(a) U_{jet}=96.12m/s at each different co-flow

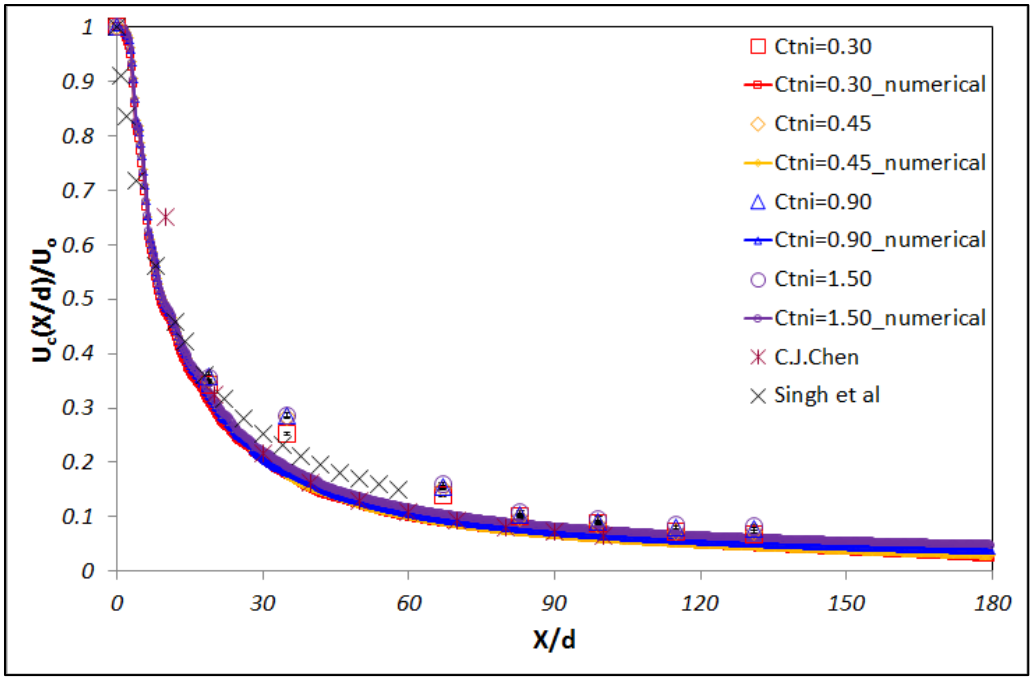

(b) U_{jet}=160.19m/s at each different co-flow

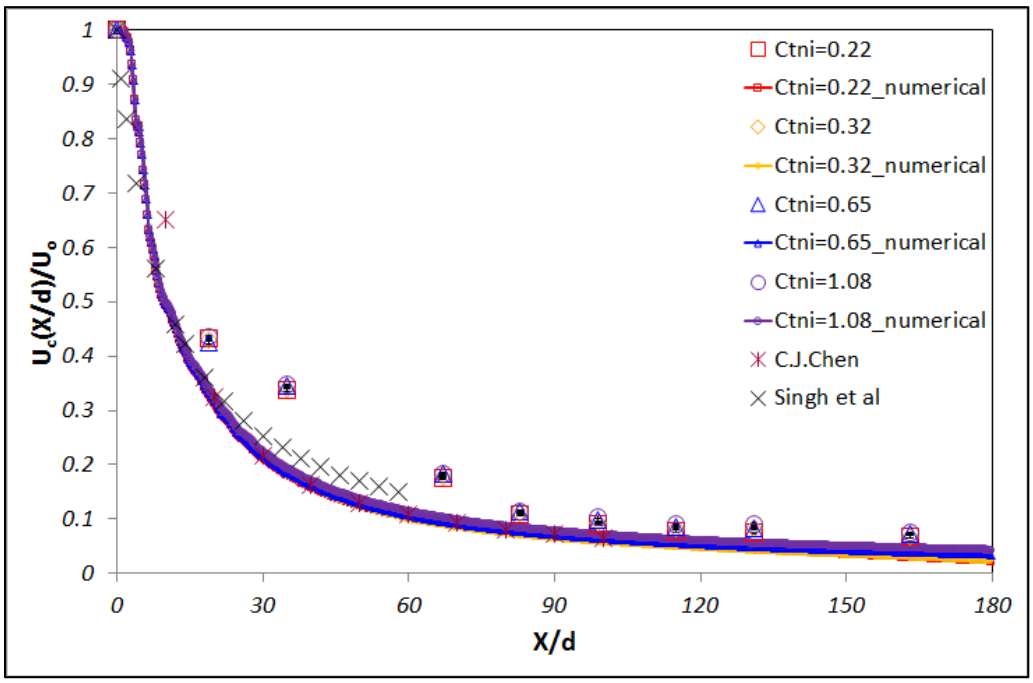

(c) U_{jet}=224.26m/s at each different co-flow

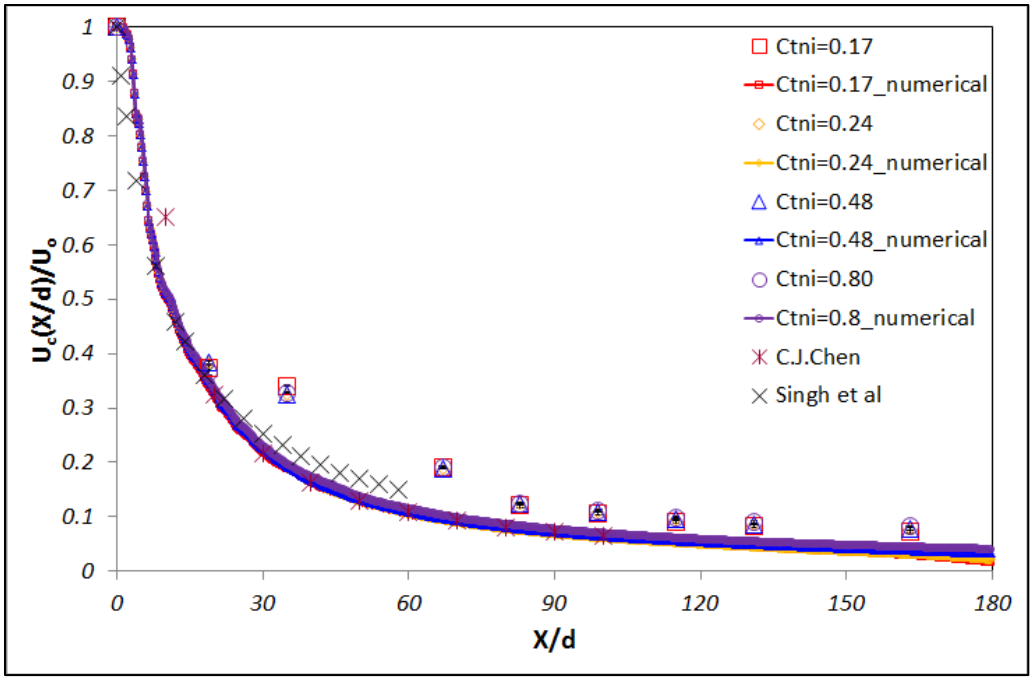

(d) U_{jet}=304.37m/s at each different co-flow

Figure 3.2 The decay of normalized axial centerline velocity

The velocity conditions are expressed as the non-isothermal Craya-Curtet number (C_{tni}) in each plot of figure 3.2. U_o is the initial jet velocity and U_c is the centerline velocity. Previous results of C.J Chen [53] from free turbulent jet and Singh et al. [54] from confined turbulent jet were plotted for the comparison between my data and previous results. First of all, experimental and numerical results are well matched along the axial direction. Usually the numerical results are over-estimated as compared with the experimental results. Also, the comparison shows that my experimental and numerical results are reasonable close to those corresponding to Singh's results at U_{jet}=96.12 and 160.19m/s. However, there is a deviation at high jet velocity (U_{jet}=224.26 and 304.37m/s) because Singh's data were measured at very low velocity (U_{jet}=0.2m/s) and not able to explain the expansion phenomena by high compressible flow (to produce high jet velocity at nozzle). The centerline velocity decays as the flow moves along the axial direction. The centerline velocity decays slower relatively as the non-isothermal Craya-

Curtet number increases. This means that the condition of high co-flow causes the slow decay of the centerline velocity because of less confinement effect by recirculation zone to the zone of center jet. The recirculation zone is formed easily at low non-isothermal Craya-Curtet number because of the high excess momentum at inlet condition between jet and co-flow. The recirculation zone will be much smaller by increasing non-isothermal Craya-Curtet number due to decrease in the excess momentum. Finally, there is not formed any recirculation zone at some critical non-isothermal Craya-Curtet number. Therefore, the interacting zone between the center jet and the recirculation zone is decreased. The decay of centerline velocity is slowed as the $\boldsymbol{C_{tni}}$ increases. Experimental and numerical results show that the different slope of velocity decay is found after ***X/d*** (***X***: axial direction, ***d***: jet nozzle diameter) is 60 approximately in all of cases due to the confinement effect. Also, at higher jet velocity ($\boldsymbol{U_{jet}}$=224.26 and 304.37m/s), high jet velocities are able to be measured at further downstream because high jet velocity has high momentum and then jet flow moves further downstream by resisting the viscous interaction of two flows. From these results, the decay of the normalized centerline velocity is inversely proportional to the normalized axial location (***X/d***). Therefore, the result of the velocity decay of a free turbulent jet can be used to estimate the velocity decay of confined turbulent jet flow reasonably well.

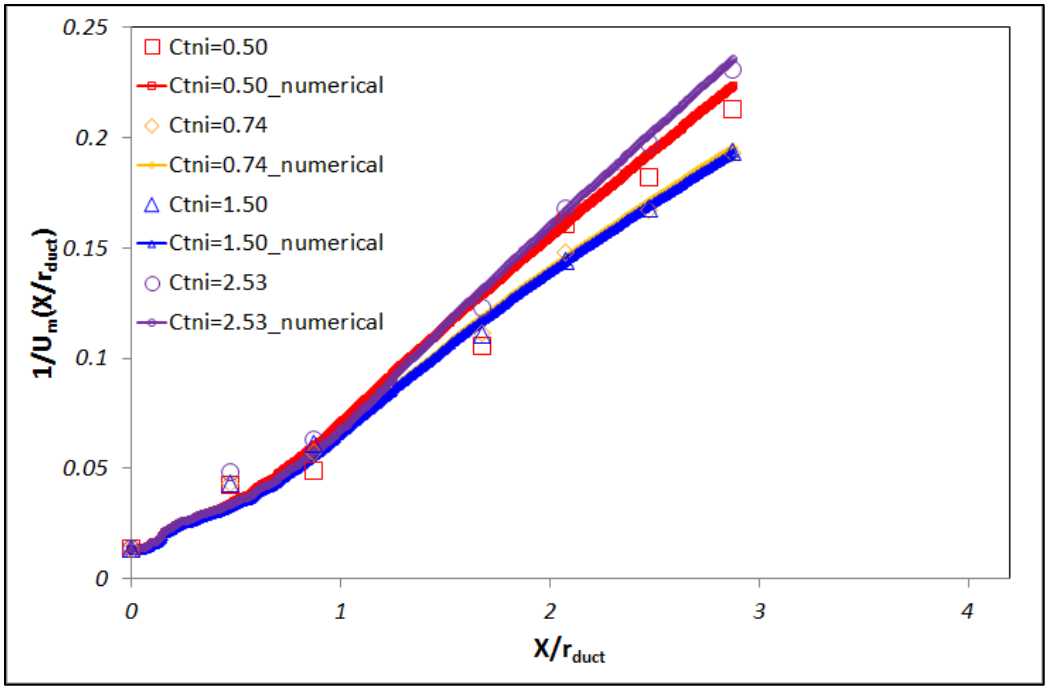

(a) U_{jet}=96.12m/s at each different co-flow

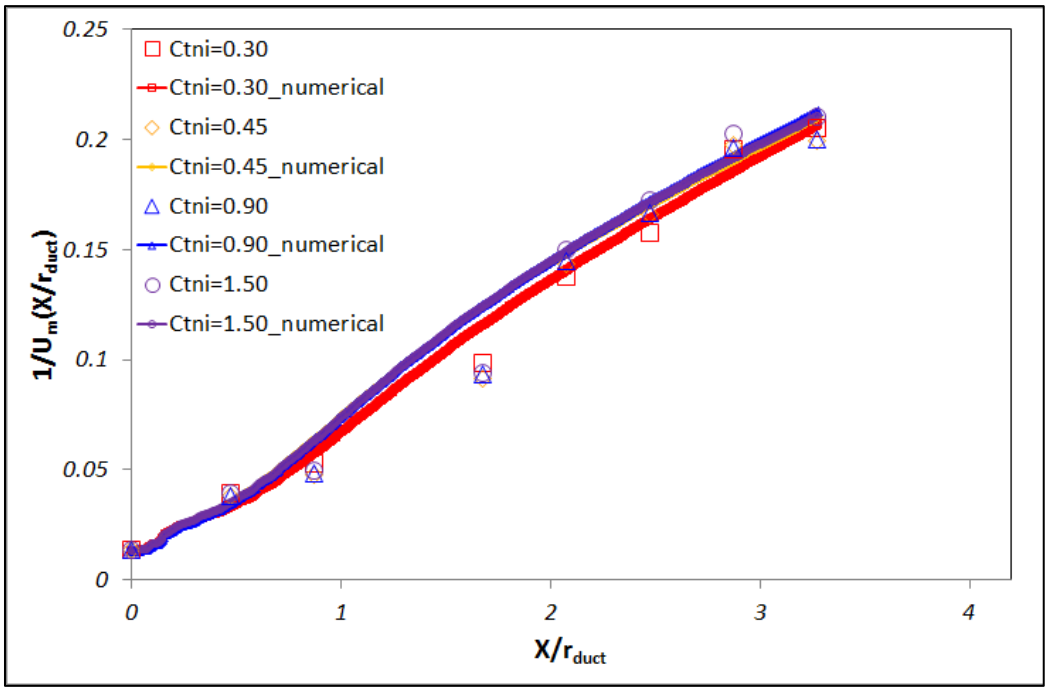

(b) U_{jet}=160.19m/s at each different co-flow

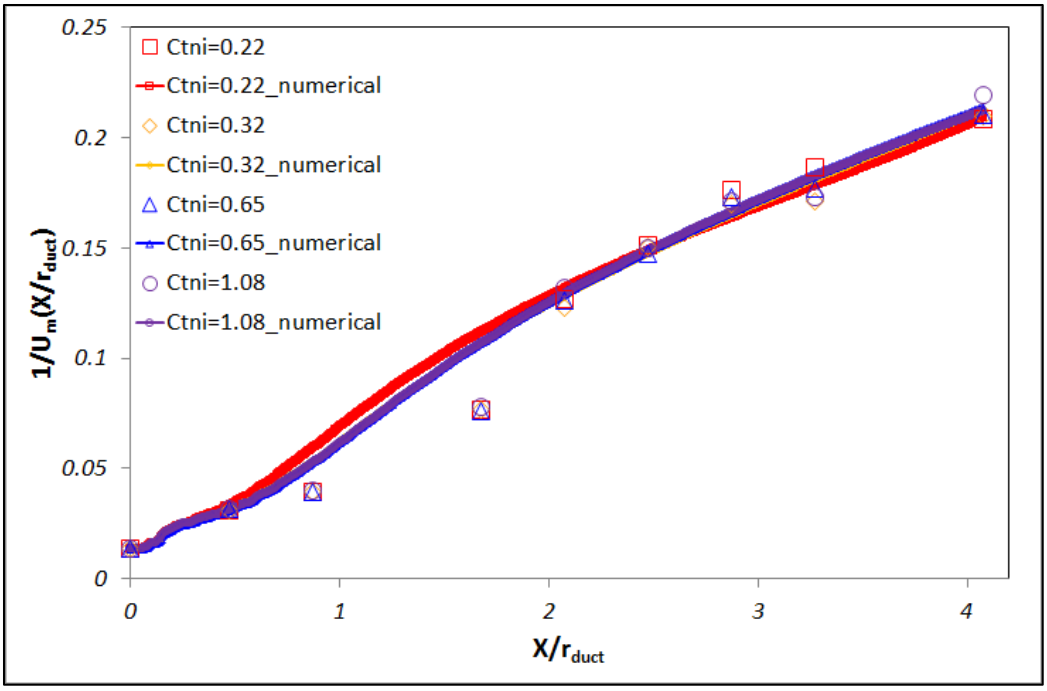

(c) U_{jet}=224.26m/s at each different co-flow

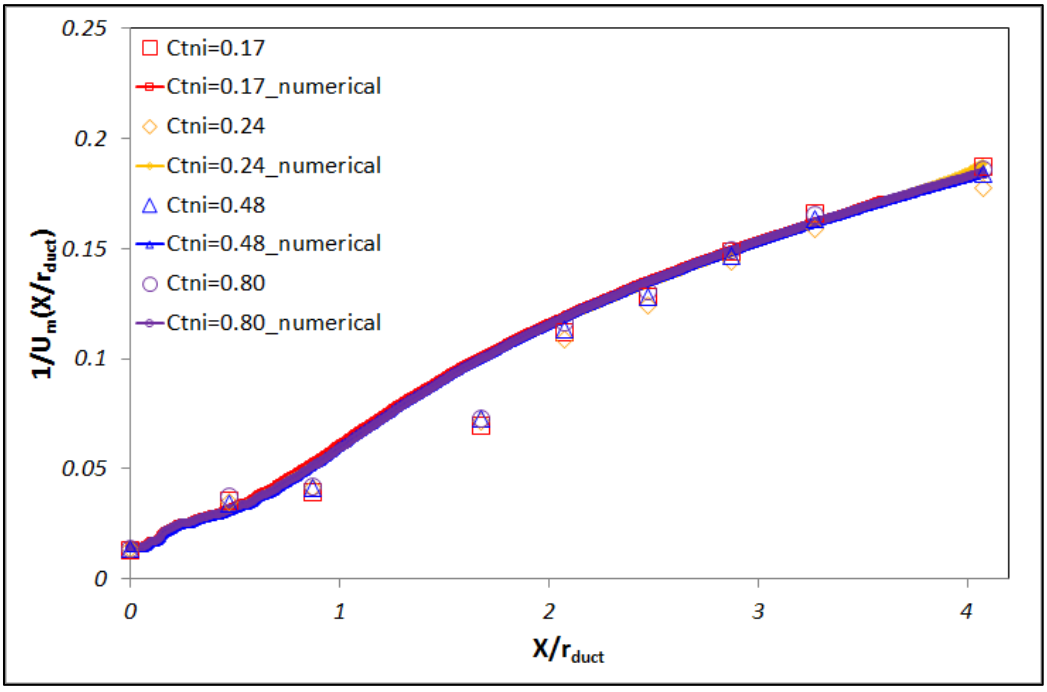

(d) U_{jet}=304.37m/s at each different co-flow

Figure 3.3 The decay of inversely normalized mean excess centerline velocity

To study the axial decay of the centerline velocity at different angle, The inversely normalized maximum excess centerline jet velocity, $1/U_m$, is used by defining the characteristic system velocity (u_o^*) defined by Becker et al. [5].

$$\frac{u_o^*}{U_{\max,o} - U_\infty} = \frac{1}{U_m} \text{ , where } u_o^* = \frac{u_k}{C_{tni}} \tag{26}$$

The velocity conditions are expressed as the non-isothermal Craya-Curtet number in each plot of figure 3.3. This value is described as the function of $\boldsymbol{X/r_{duct}}$ (***X***: axial direction, $\boldsymbol{r_{duct}}$: the radius of main test duct). Experimental and numerical results show that the inversely normalized maximum excess centerline jet velocity is decayed as the flow moves along the axial direction. Also, the inversely normalized maximum excess centerline jet velocity decays faster as the non-isothermal Craya-Curtet number increases. This means that the normalized maximum excess centerline jet velocity decays slowly. Also, the condition of high co-flow results in the slow decay of the excess centerline velocity because of reduced recirculation zones. Physically, the high excess momentum difference at inlet condition between jet and co-flow (at a low non-isothermal Craya-Curtet number) causes the recirculation zone to be earlier and bigger. However, there is no large recirculation zone at high non-isothermal Craya-Curtet number due to less excess momentum. Therefore, the interacting zone between the center jet and the recirculation zone is decreased and the decay of centerline velocity is slower. Also, the value of inverse normalize maximum excess centerline jet velocity is almost same values at high $\boldsymbol{X/r_{duct}}$ but the average slope of the decay of normalized mean excess centerline velocity is decreased as a jet velocity increases because of initial high centerline jet velocity. Therefore, the jet flow move further in the cases of high jet velocity by overcoming the viscous interaction between two flows.

Figure 3.4 shows that the normalized axial centerline velocity has the function of ***X/d*** (***X***: axial direction, ***d***: jet nozzle diameter) in order to analyze the different jet velocities at fixed co-flow velocity respectively. These graphs are plotted at fixed co-flow and different jet velocities. Also, $\boldsymbol{U_o}$ is the initial jet velocity and $\boldsymbol{U_c}$ is the centerline velocity. To compare our experimental and numerical data, previous results (Chen's [53] and Singh's [54]) were plotted in each graph. From these comparisons, the currently obtained results and Singh's results are reasonably close. The centerline velocity decays slowly further downstream as the non-isothermal Craya-Curtet number increases. There are no any significant differences between the effect of different jet velocity and previous case (the effect of different co-flow velocities) once we are considering the normalized velocities. Also, the results of free turbulent jet are predicted well to the results of confined turbulent jet. From these results, the non-isothermal Craya-Curtet numbers are used to explain the decay of velocity. After ***X/d*** (***X***: axial direction, ***d***: jet nozzle diameter) is 60 approximately in all of cases, the different slop of velocity decay is identified due to the confinement effect. This result shows the inversely linear relation between the normalized centerline velocity and the normalized axial location (***X/d***).

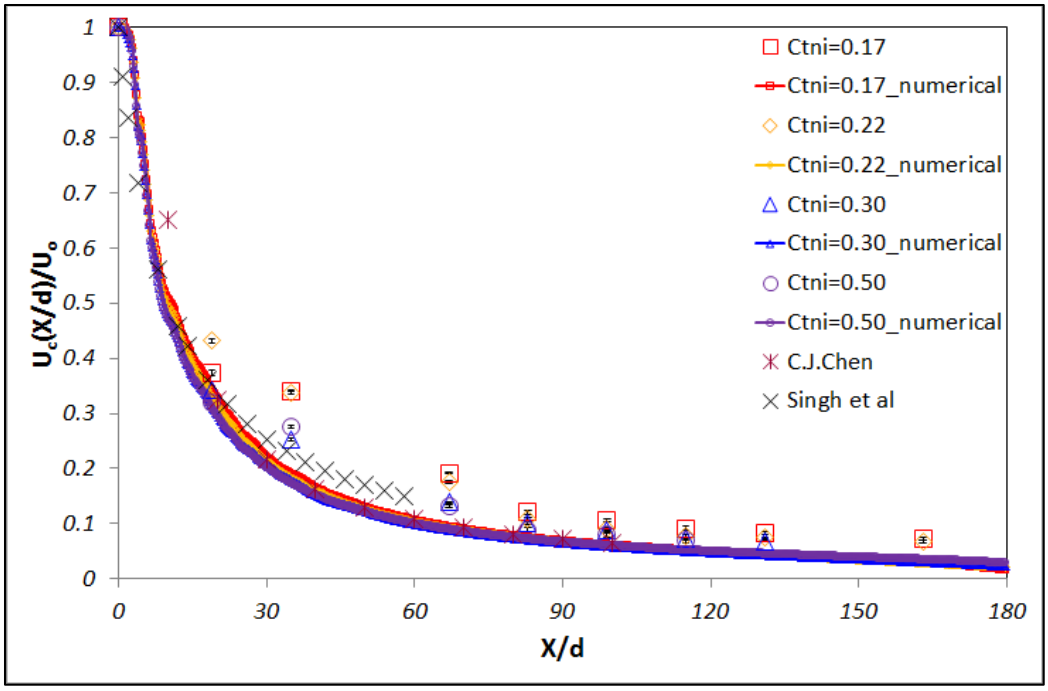

(a) U_{co}=0.612m/s at each different jet velocity

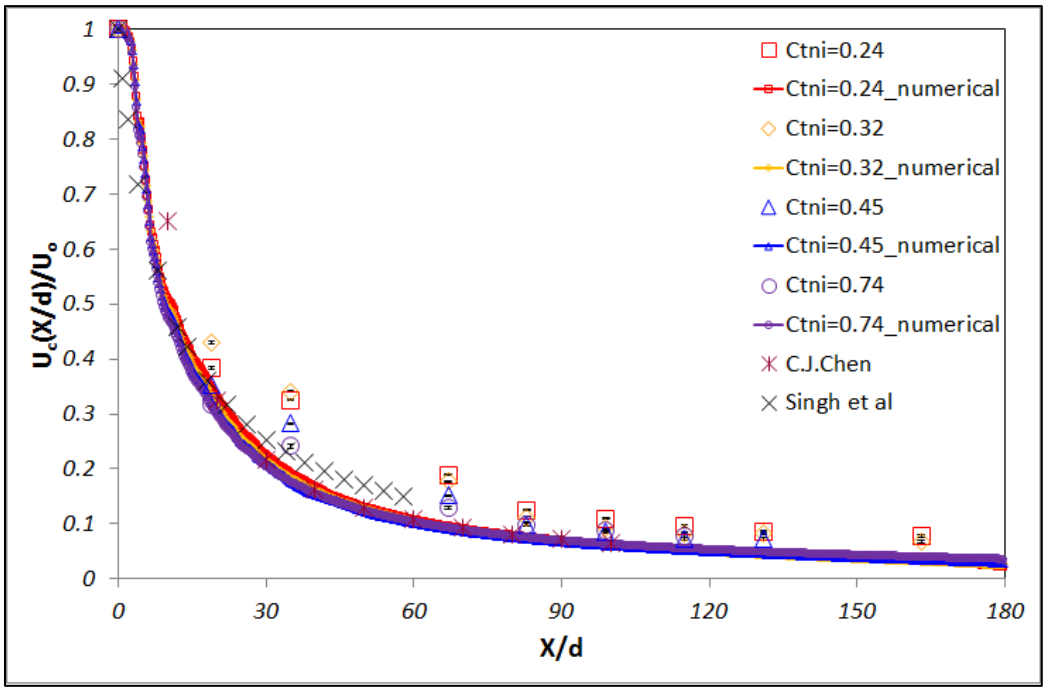

(b) U_{co}=0.913m/s at each different jet velocity

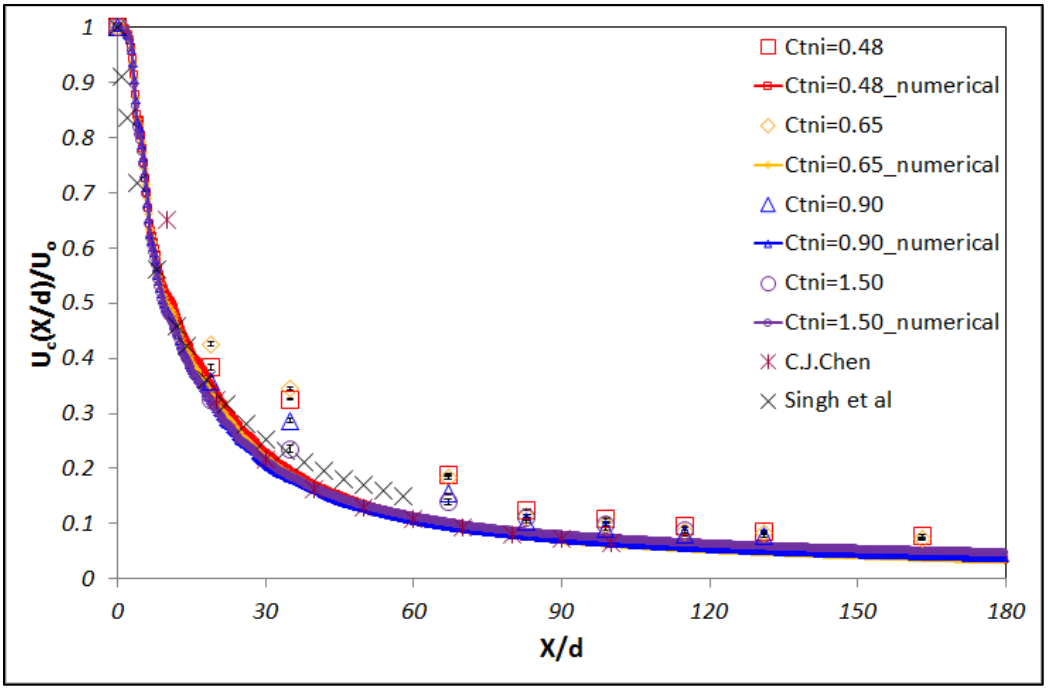

(c) U_{co}=1.856m/s at each different jet velocity

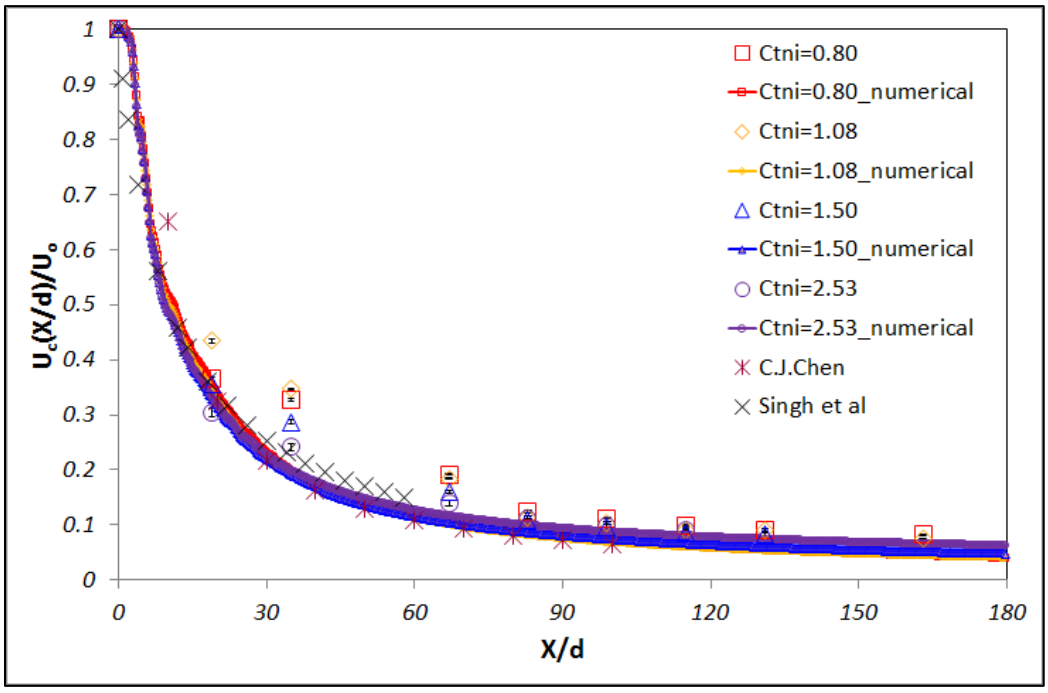

(d) U_{co}=3.123m/s at each different jet velocity

Figure 3.4 The decay of normalized axial centerline velocity

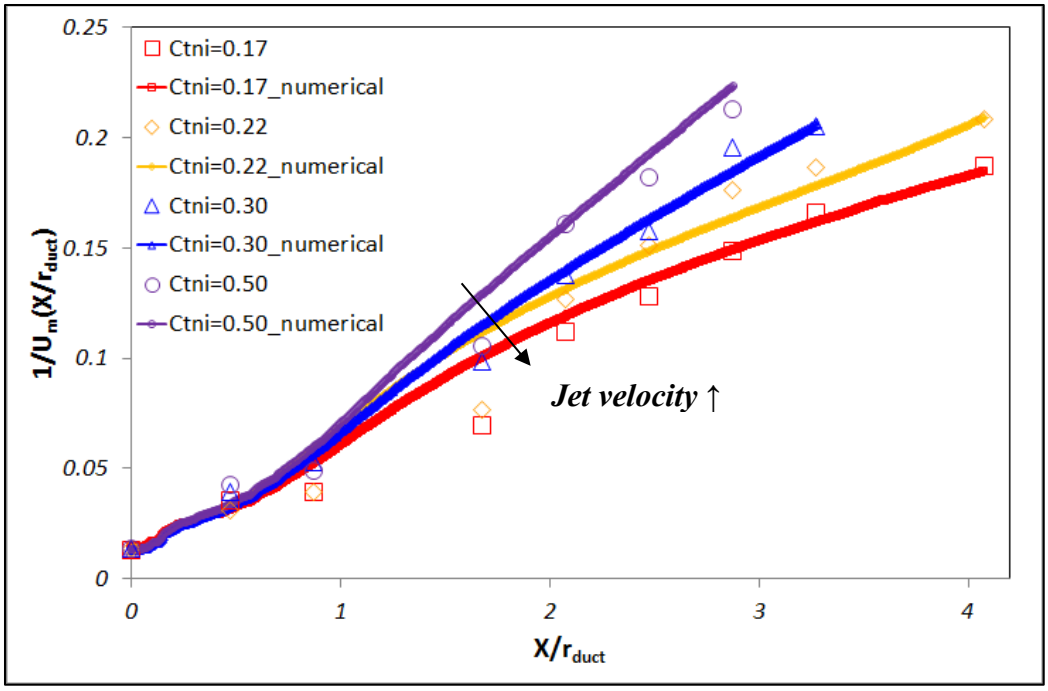

(a) U_{co}=0.612m/s at each different jet velocity

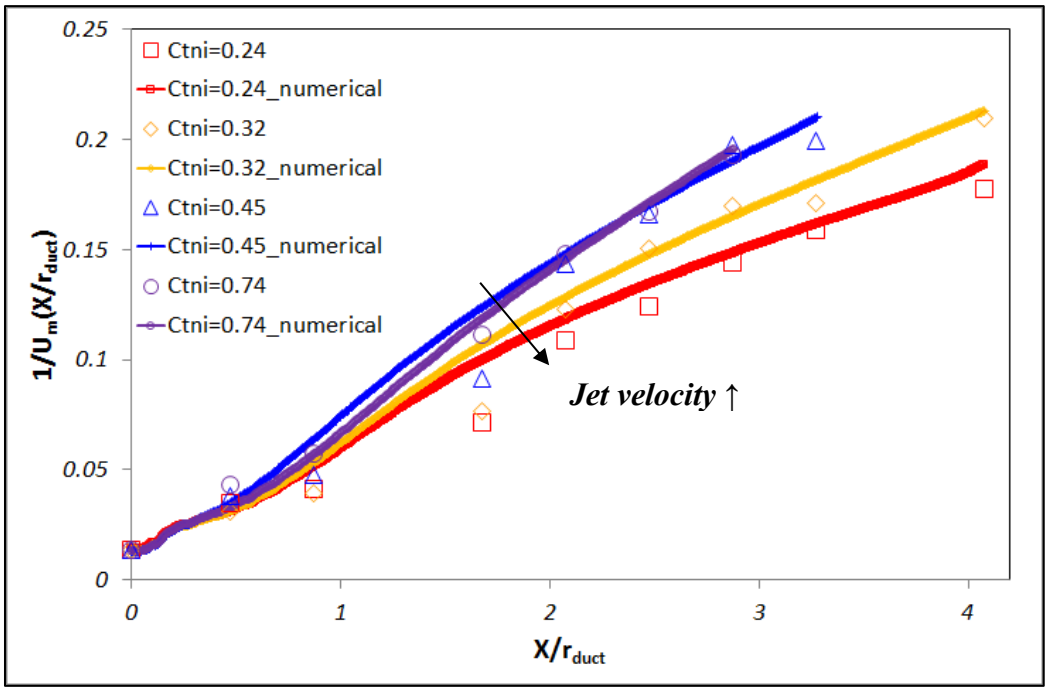

(b) U_{co}=0.913m/s at each different jet velocity

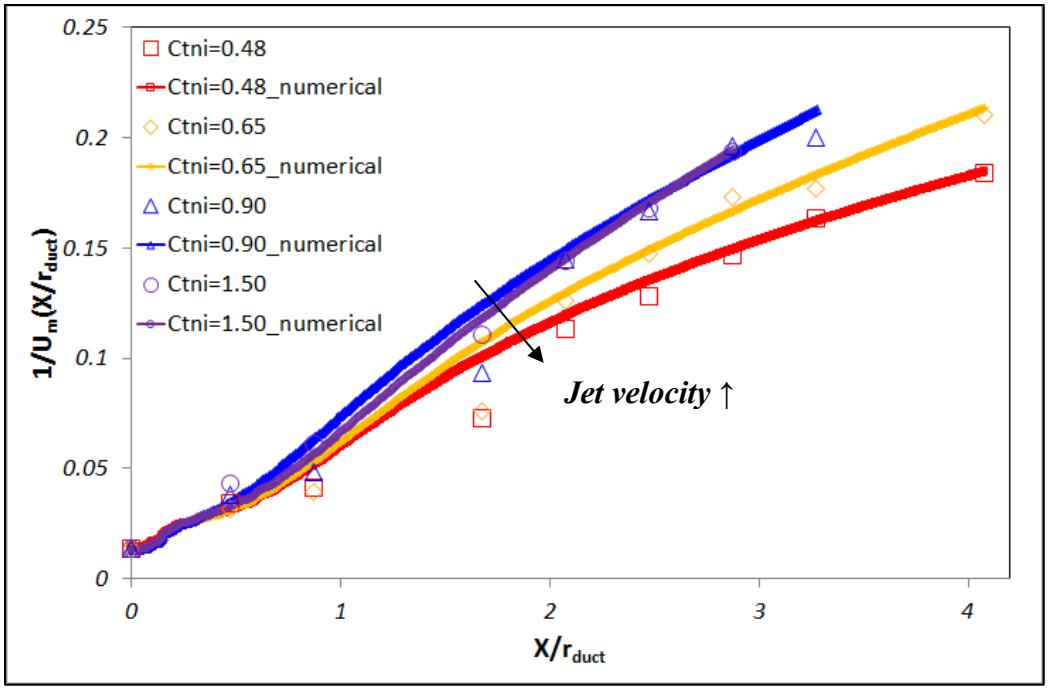

(c) U_{co}=1.856m/s at each jet velocity

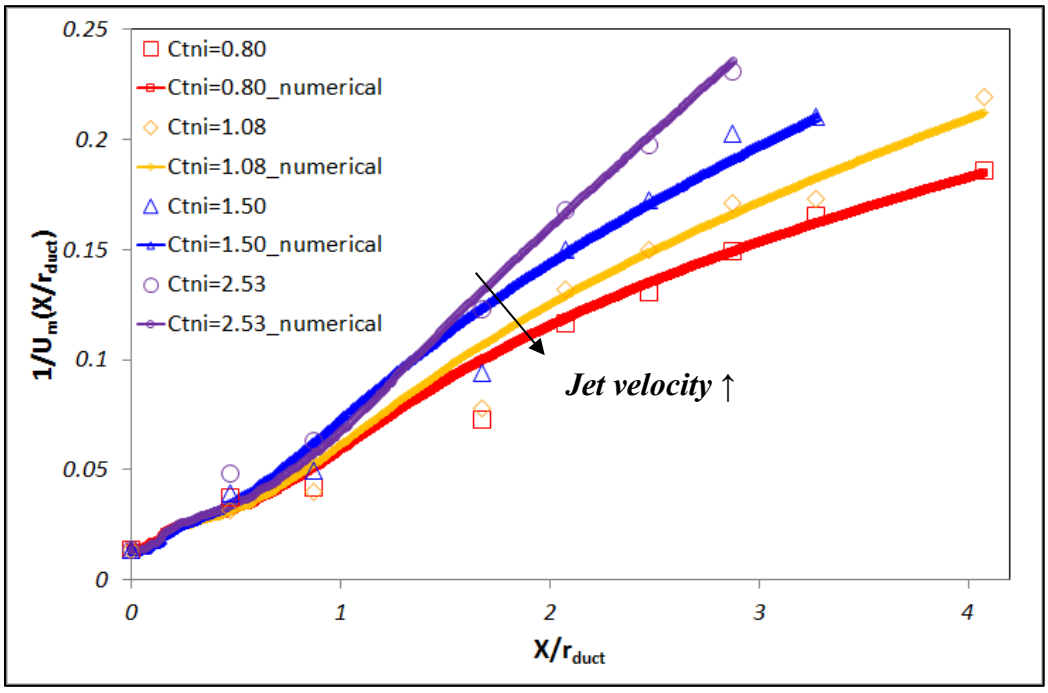

(e) U_{co}=3.123m/s at each jet velocity

Figure 3.5 The decay of inversely normalized mean excess centerline velocity

Also, the inversely normalized maximum excess centerline jet velocity is investigated at fixed co-flow and different jet velocities in Figure 3.5. Figure 3.5 also shows that the inversely

normalized centerline jet velocity decreases faster at high non-isothermal Craya-Curtet number. As a result, normalized mean excess centerline velocity is decaying slower as non-isothermal Craya-Curtet number increases. This means that the recirculation zone or the confinement effect has significant influence on the centerline velocity. Accordingly, although the results of free turbulent jet flow estimate reasonably the velocity decay of confined turbulent jet flow, these results will not be useful at low non-isothermal Craya-Curtet number because of the recirculation zone. The value of inversely normalized maximum excess centerline jet velocity is spread at high X/r_{duct} and the range of slope value of the decay of normalized mean excess centerline velocity is decreased at high jet velocity. The figure shows that the normalized mean excess centerline velocity has the fastest decrement at C_{tni}=1.50 and 2.53 among all the test conditions.

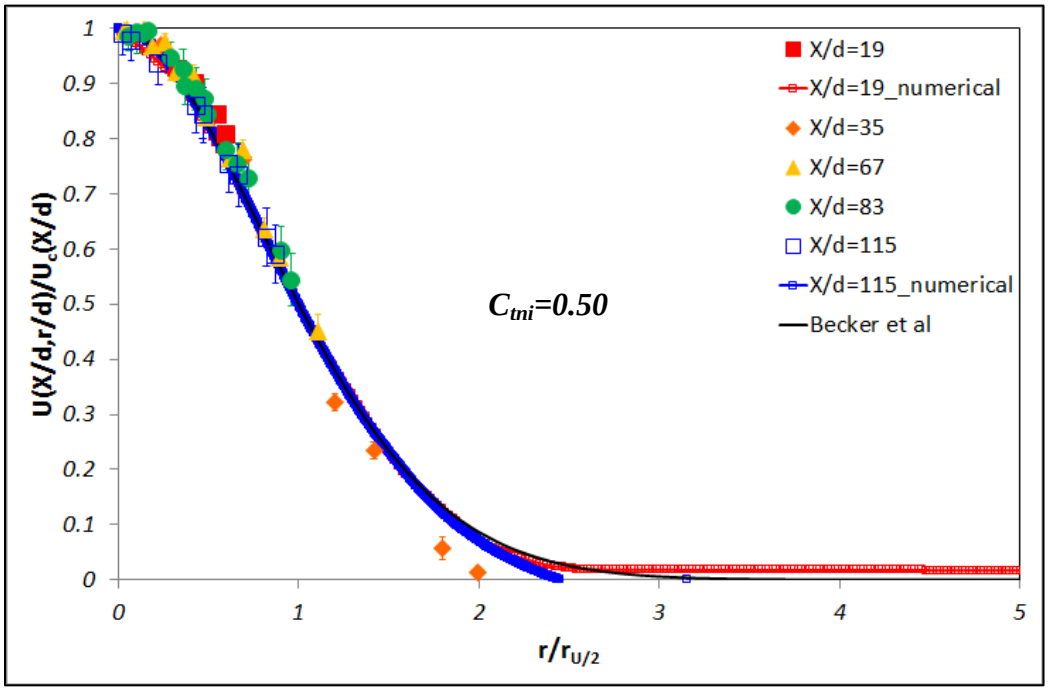

(a) U_{jet}=96.12m/s and U_{co}=0.612m/s

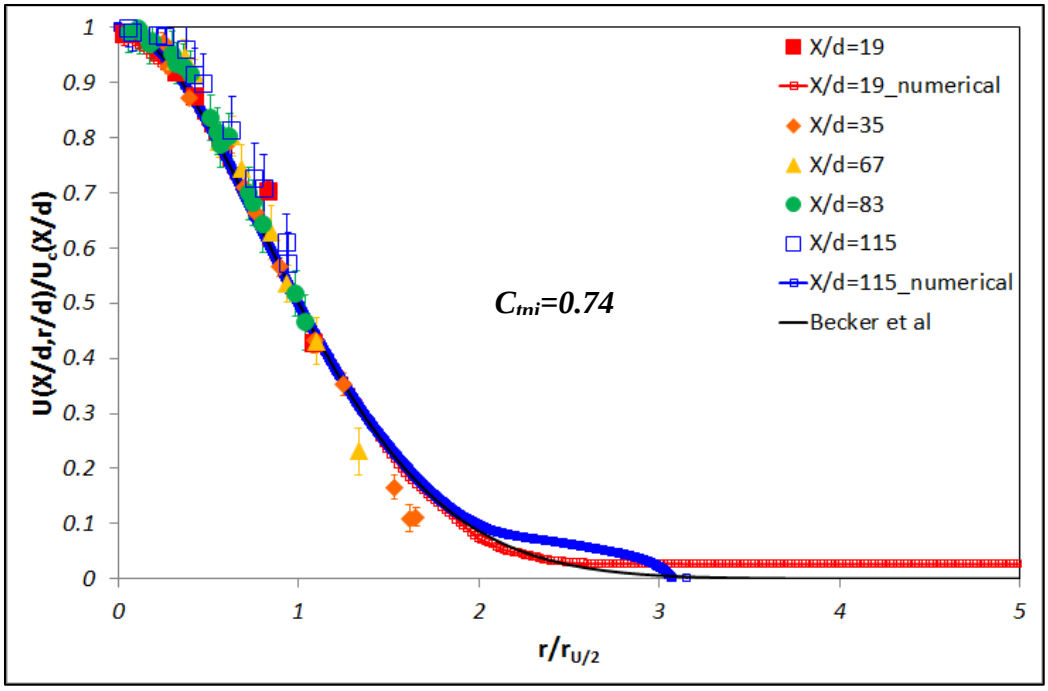

(b) U_{jet}=96.12m/s and U_{co}=0.913m/s

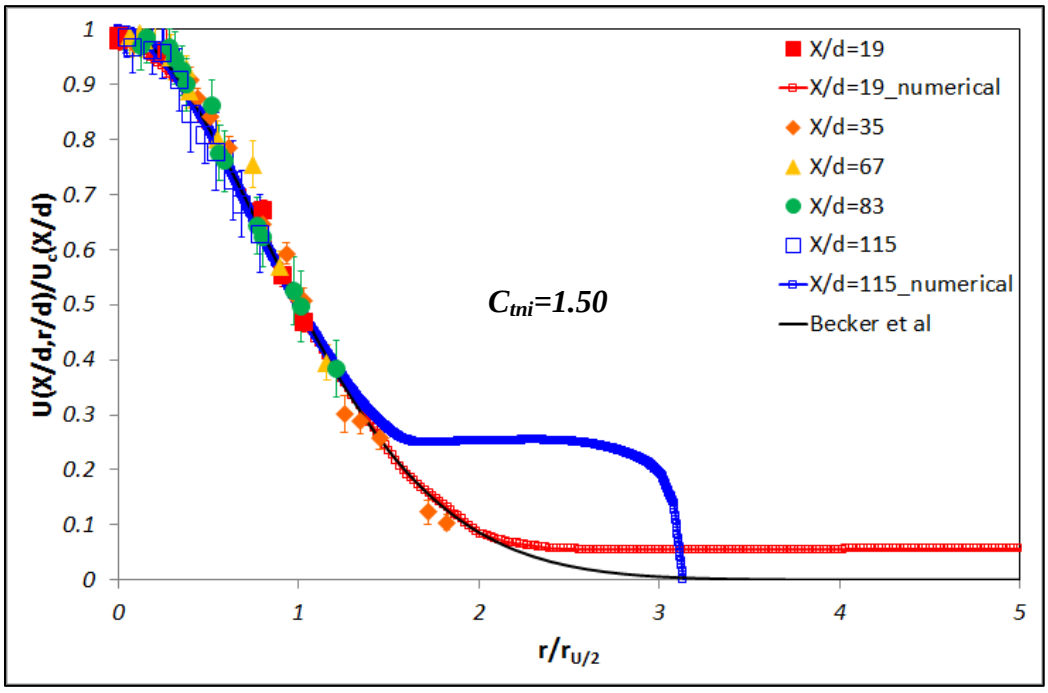

(c) U_{jet}=96.12m/s and U_{co}=1.856m/s

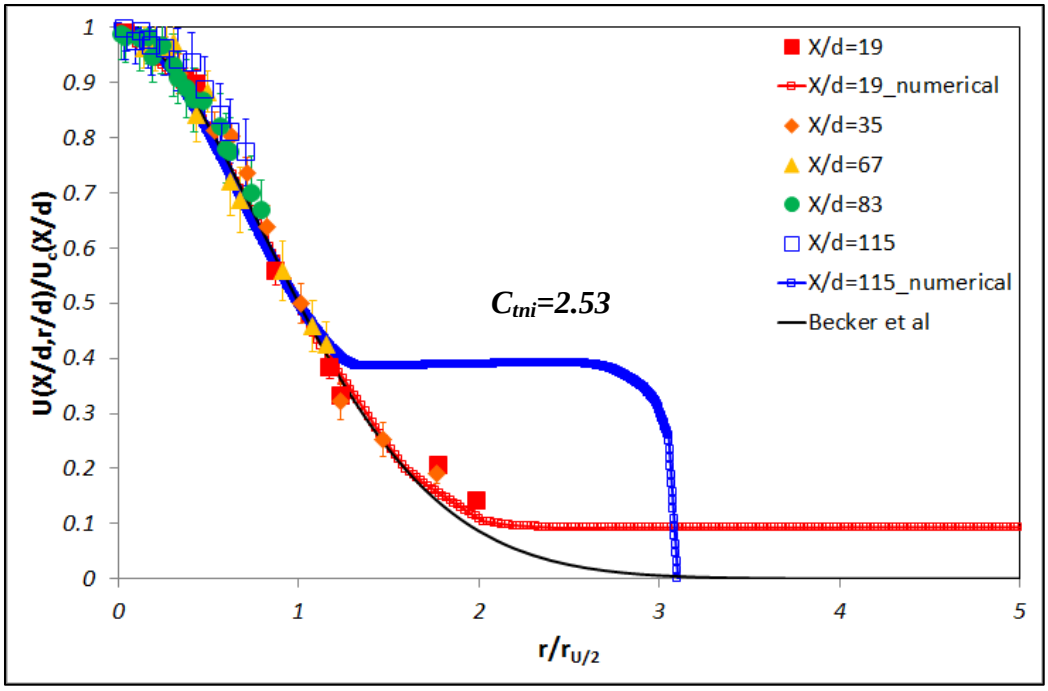

(d) U_{jet}=96.12m/s and U_{co}=3.123m/s

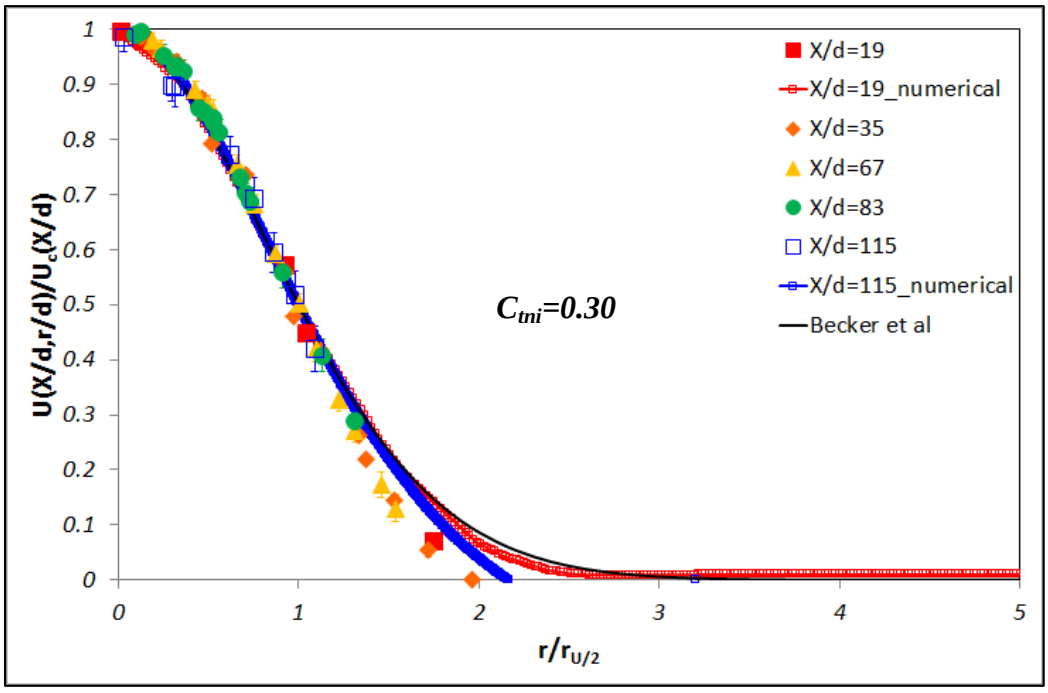

(e) U_{jet}=160.19m/s and U_{co}=0.612m/s

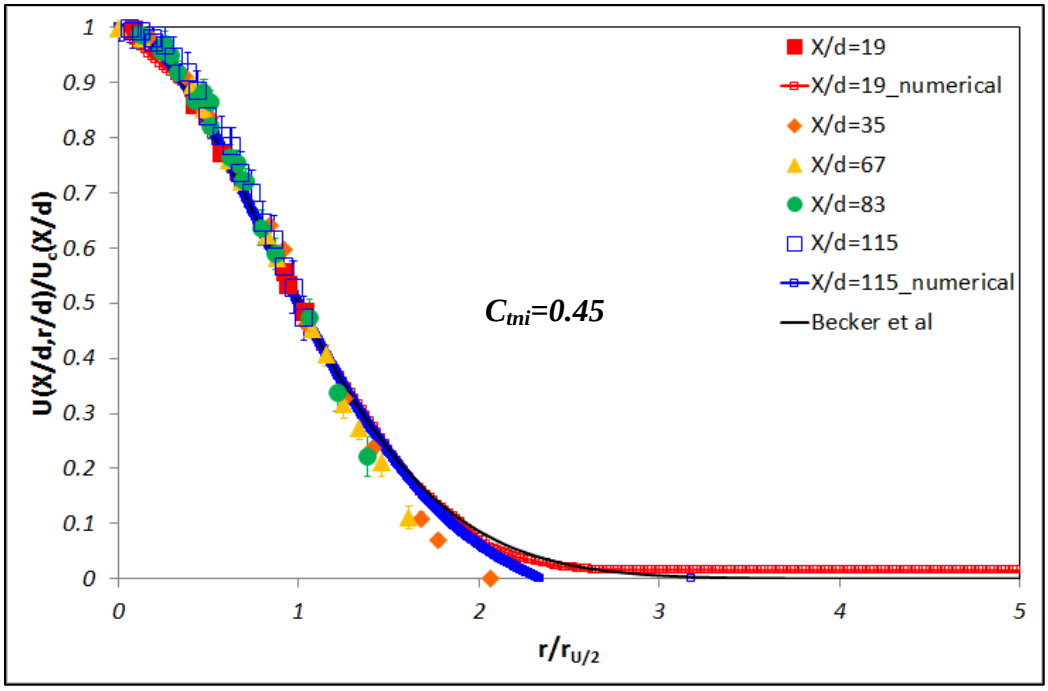

(f) U_{jet}=160.19m/s and U_{co}=0.913m/s

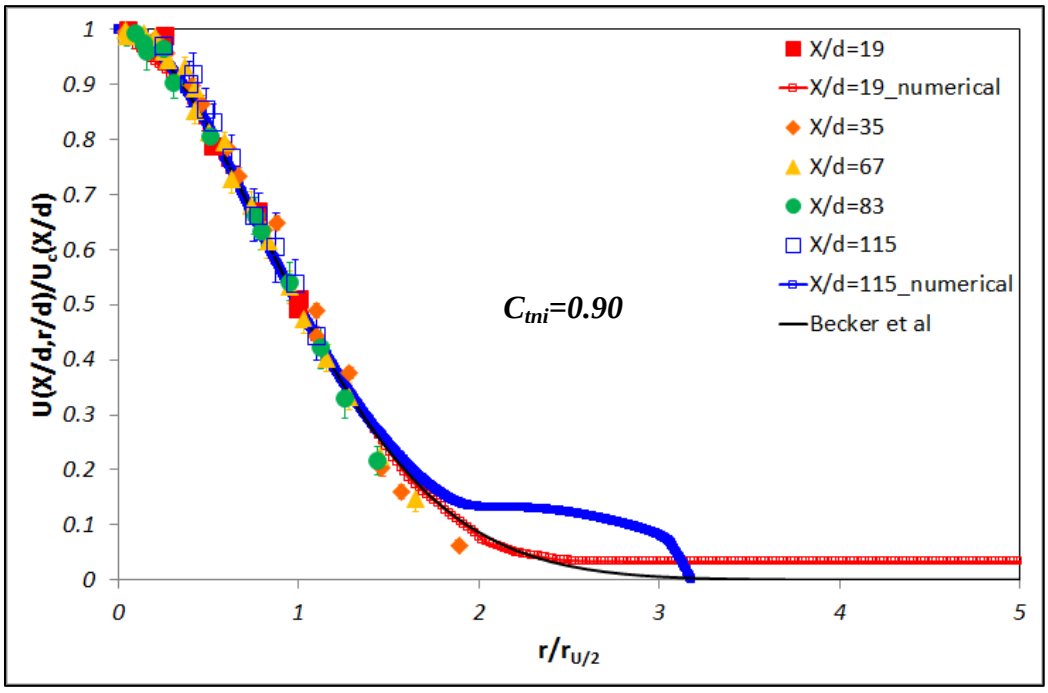

(g) U_{jet}=160.19m/s and U_{co}=1.856m/s

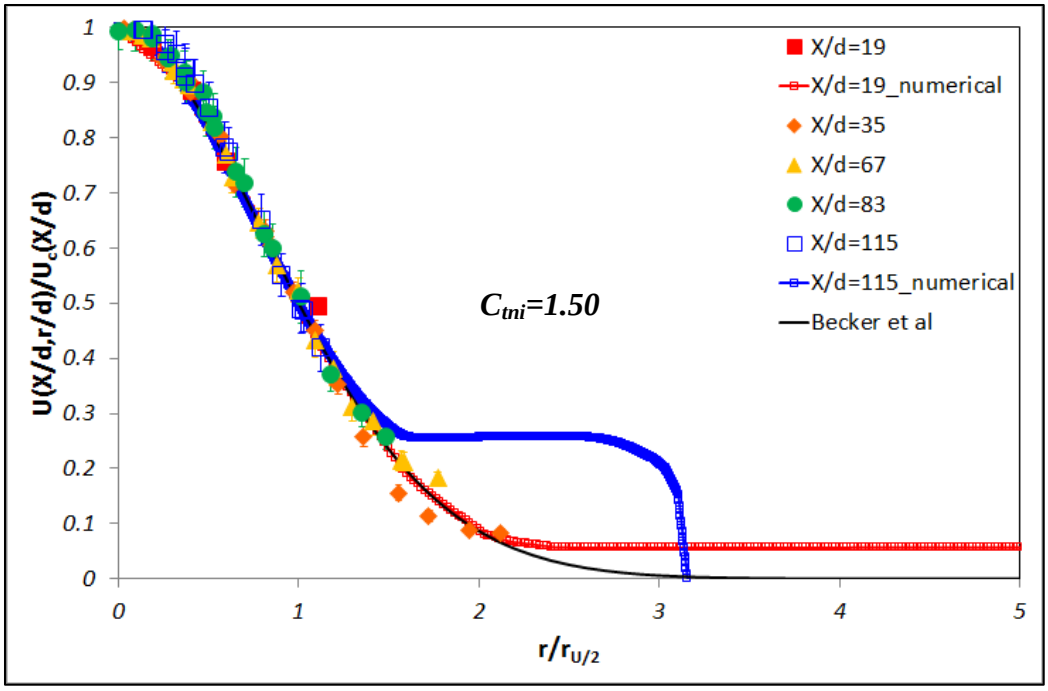

(h) U_{jet}=160.19m/s and U_{co}=3.123m/s

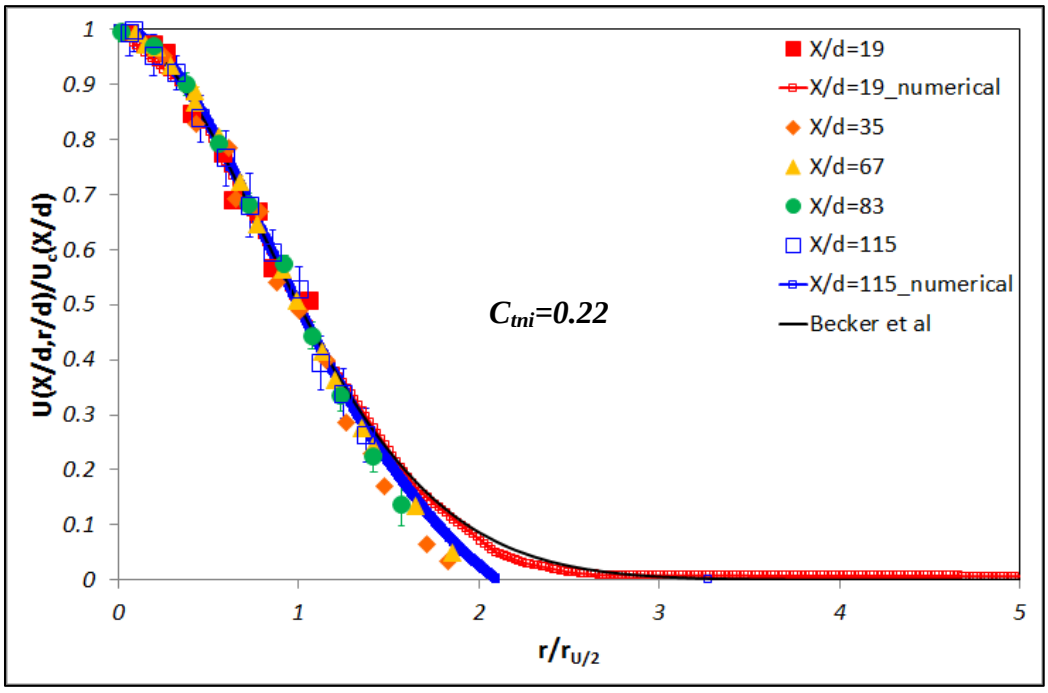

(i) U_{jet}=224.26m/s and U_{co}=0.612m/s

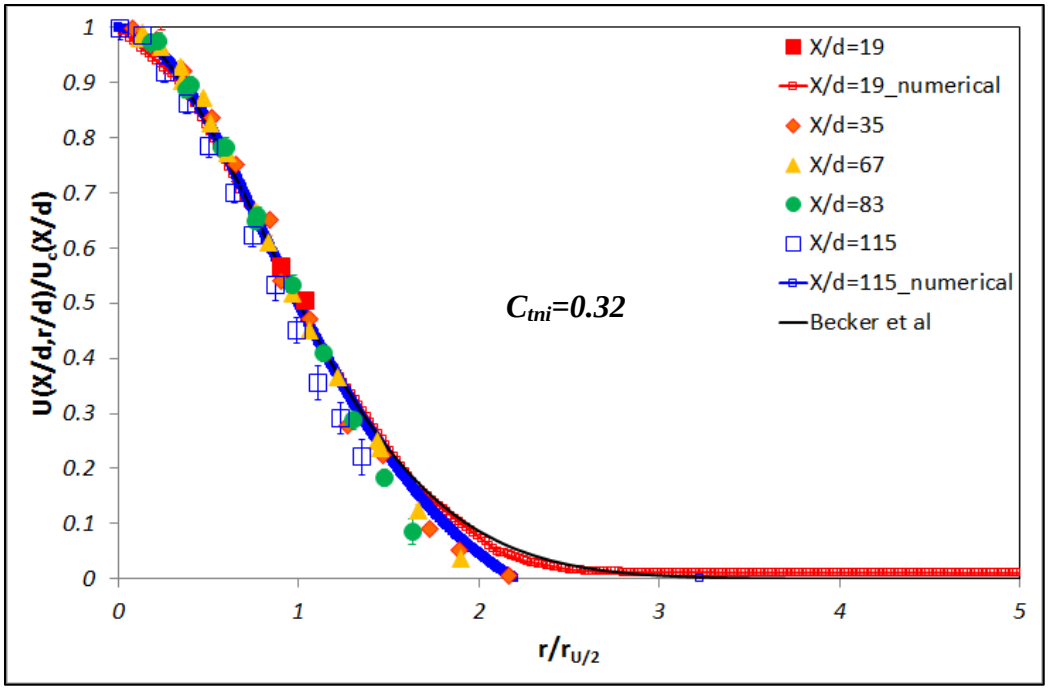

(j) U_{jet}=224.26m/s and U_{co}=0.913m/s

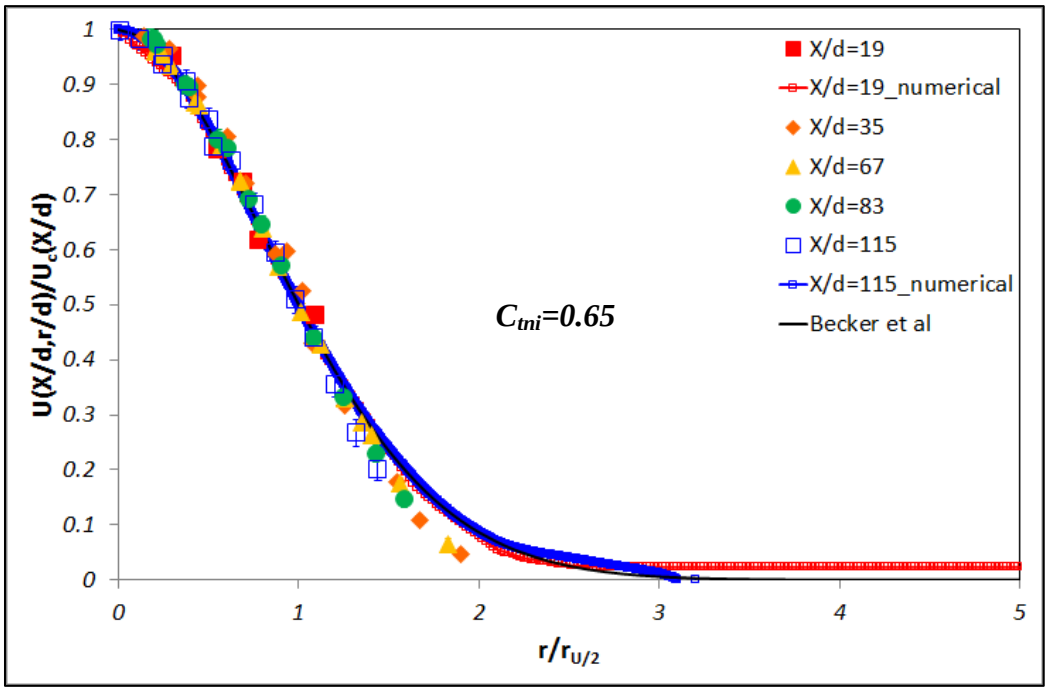

(k) U_{jet}=224.26m/s and U_{co}=1.856m/s

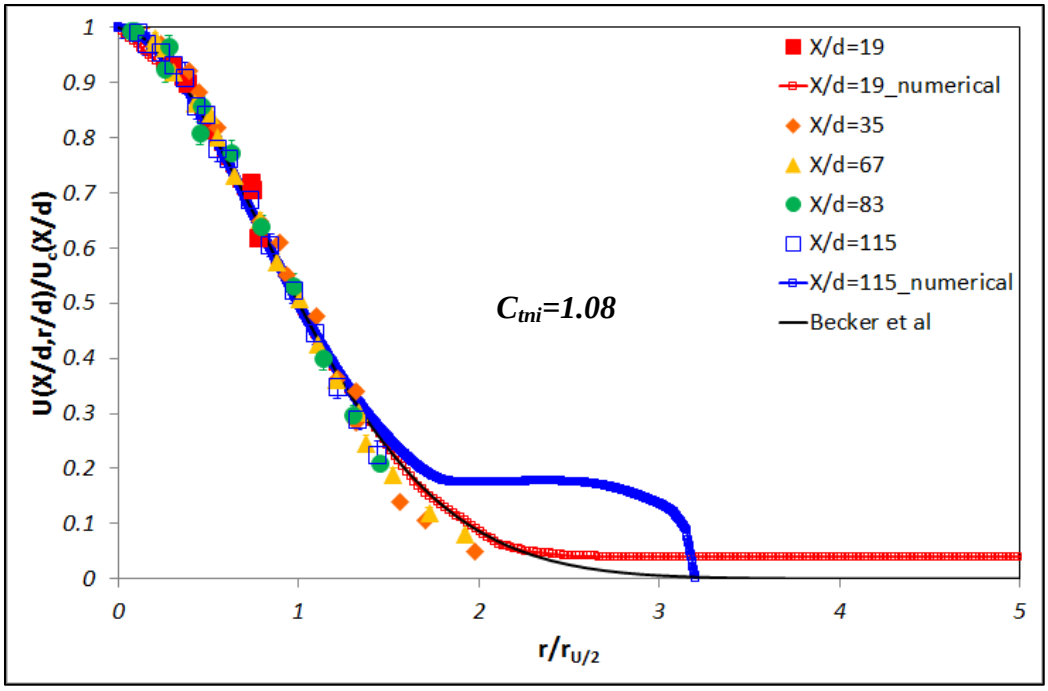

(l) U_{jet}=224.26m/s and U_{co}=3.123m/s

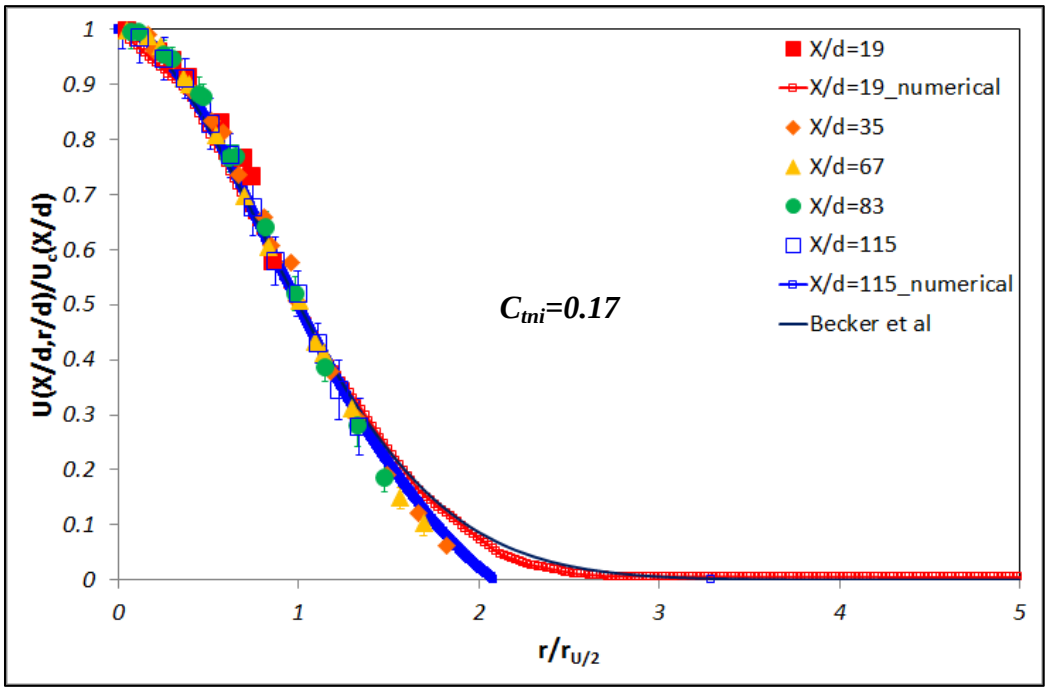

(m) U_{jet}=304.37m/s and U_{co}=0.612m/s

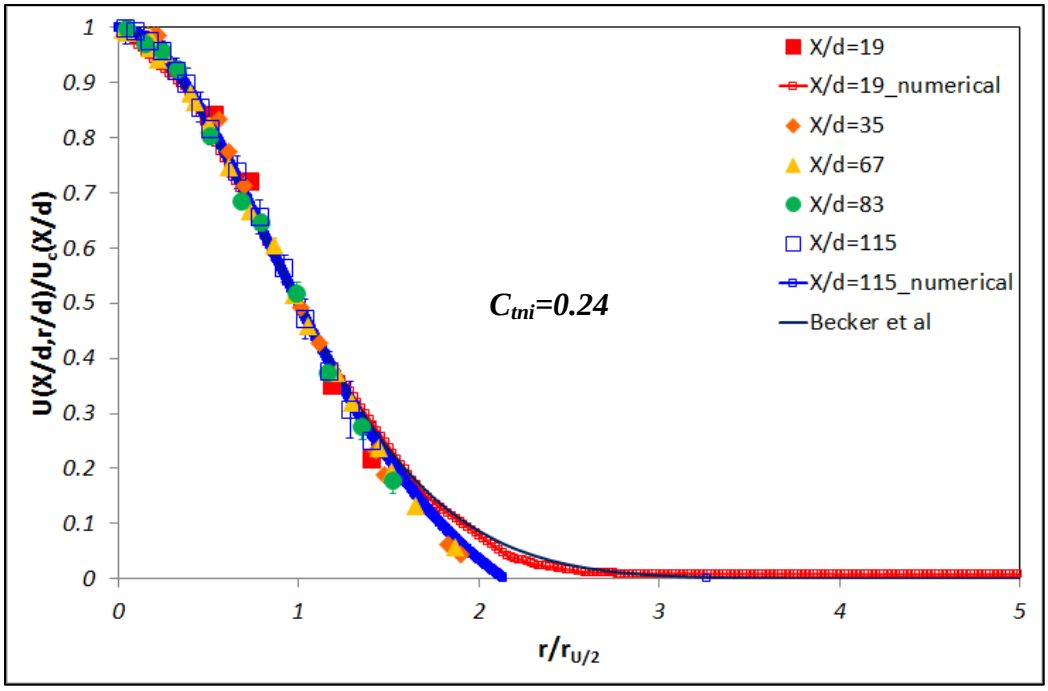

(n) U_{jet}=304.37m/s and U_{co}=0.913m/s

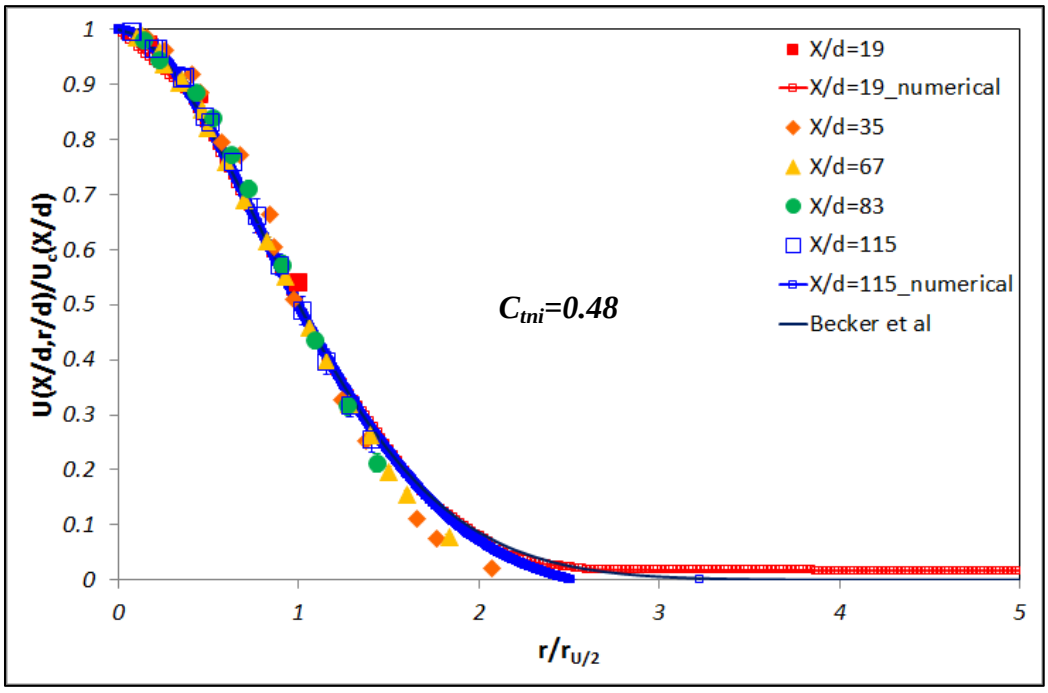

(o) U_{jet}=304.37m/s and U_{co}=1.856m/s

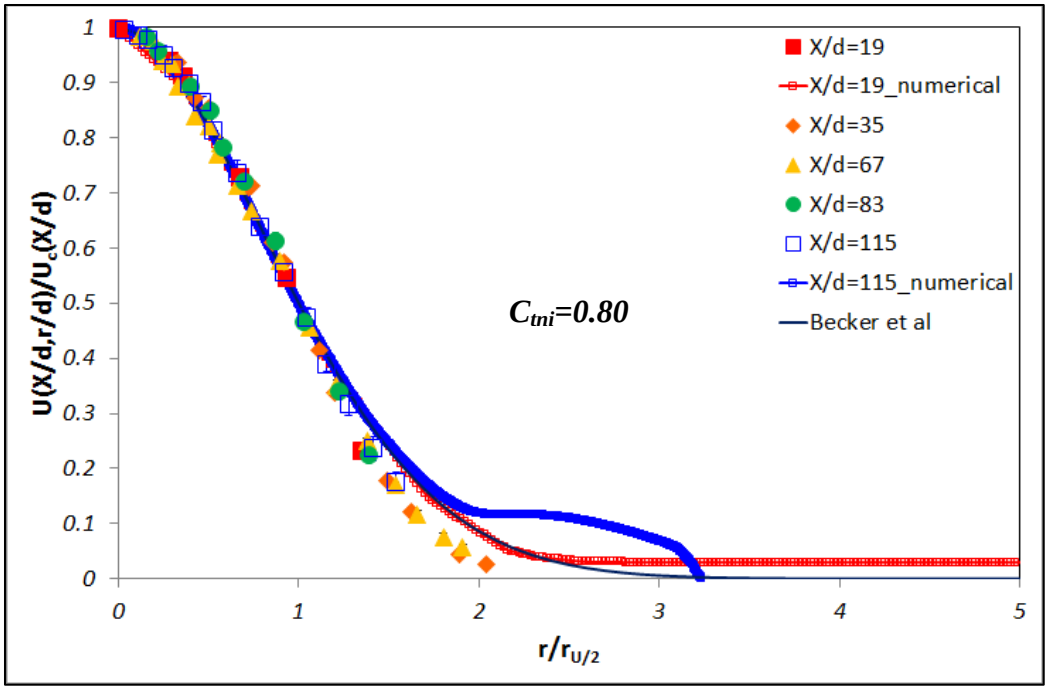

(p) U_{jet}=304.37m/s and U_{co}=3.123m/s

Figure 3.6 The radial velocity distribution

Figure 3.6 shows the radial velocity distribution at different jet velocities and different co-flow conditions. Different colored rhombuses and colored lines are indicating the experimental and numerical results of the different location of ***X/d*** (***X***: axial direction, ***d***: jet nozzle diameter) respectively. Equation (27) for the black solid line is found in Becker et al. [5] as,

$$\overline{U} = \frac{U}{U_c} = \exp\left[-0.693\left(r \Big/ r_{\frac{U}{2}}\right)^{1.82}\right] \tag{27}$$

U is the radial velocity at the different location of ***X/d***, U_c is the centerline velocity and $r_{U/2}$ is the width of the half jet velocity. The computed and the measured profiles collapse fairly well on a single curve to be represented by a Gaussian function from equation (27), except for the mean

scalar fraction at the position far downstream near the near edge ($r/r_{U/2}$>1). This means that the good agreement is between the current experimental and numerical data in the jet region and the equation (27) used by Becker et al. [5] for all different velocity conditions between jet and co-flow. The deviation at the trail of the curve is due to the confinement. Therefore, equation (27) can be used for expressing the normalized velocity distribution in the jet region. From my test results, we can get the new normalized velocity equation (28). Equation (28) is a better estimated fit to the current experimental and numerical results.

$$\overline{U} = \frac{U}{U_c} = \exp\left[-\ln 2.13 \left(r / r_{\frac{U}{2}} \right)^2 \right] \tag{28}$$

Also, usually, in highest co-flow velocity (U_{co}=3.123m/s) and furthest downstream location (X/d=115), there is not a Gaussian distribution of velocity anymore due to high interaction and fluctuation. In low M=0.3 (U_{jet}=96.12m/s) and M=0.5 (U_{jet}=160.19m/s), non-Gaussian distribution of velocity distribution is found at U_{co}=1.856m/s because less momentum of jet is highly sensitive to external disturbance by co-flow at further downstream.

3.1.4. The concentration distribution

The characteristic of the concentration distribution is studied along the axial direction and the radial direction. The axial distribution of the ***NO*** concentration is verified by considering different co-flow velocities at fixed jet velocity. The initial center concentration of ***NO*** (C_o) is normalized by using ***NO*** center concentration (C_c) at the different normalized axial locations (X/d).

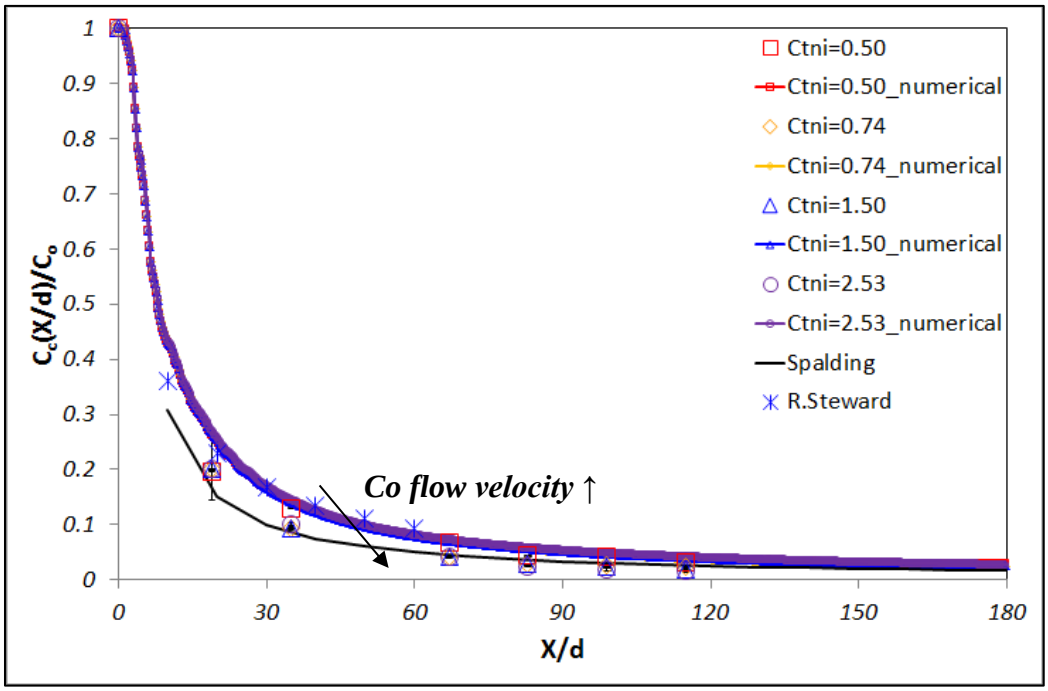

(a)U_{jet}=96.12m/s at each different co-flow

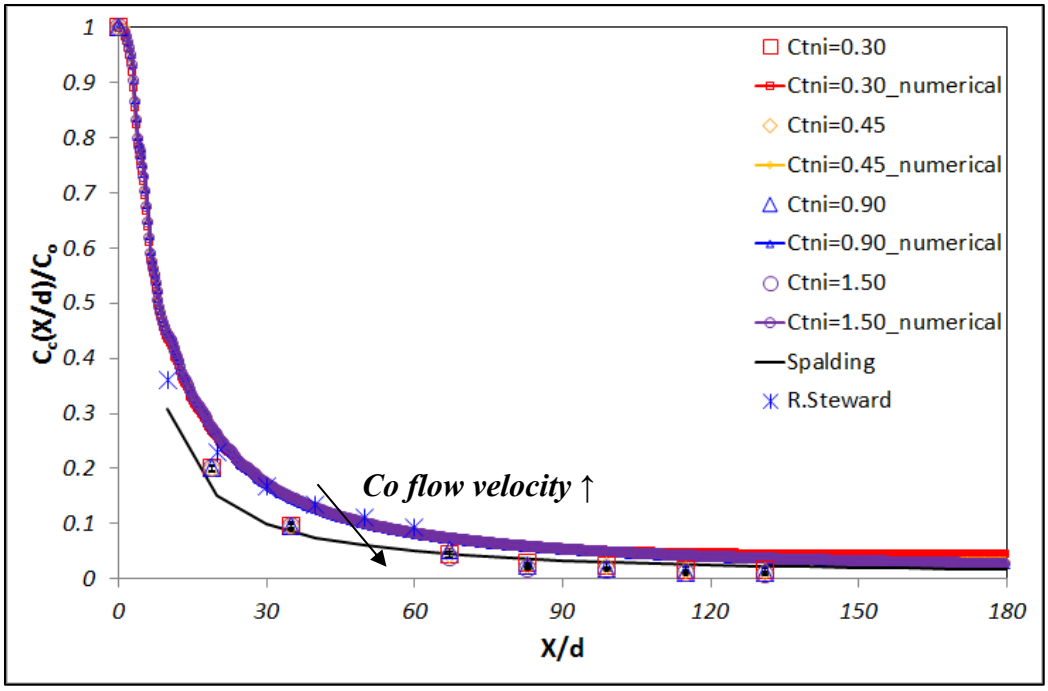

(b) U_{jet}=160.19m/s at each different co-flow

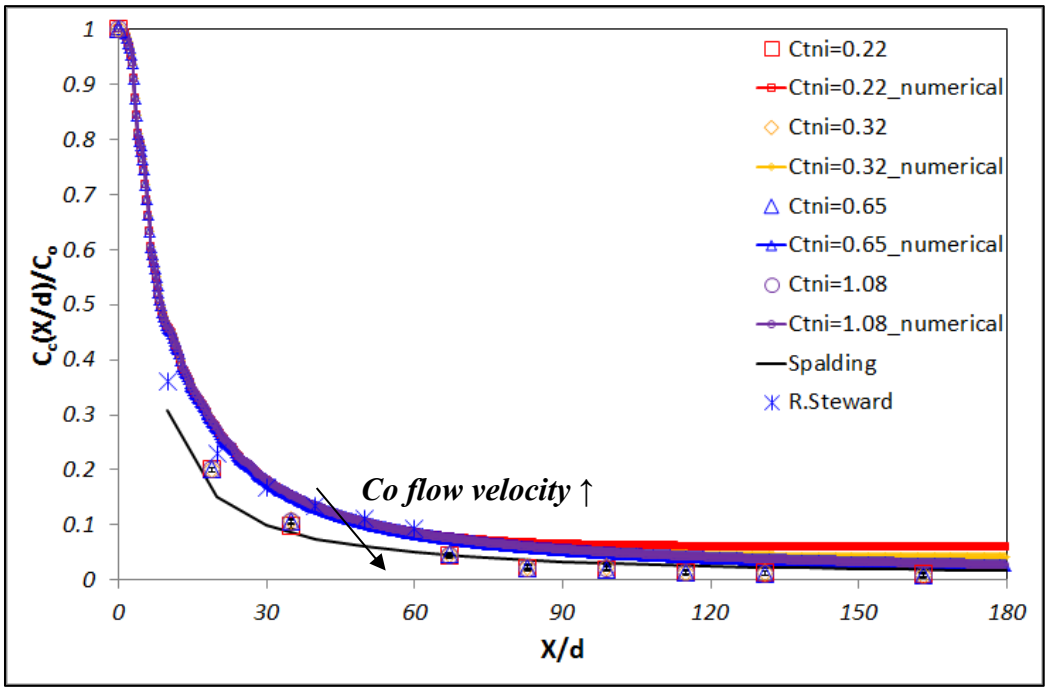

(c)U_{jet}=224.26m/s at each different co-flow

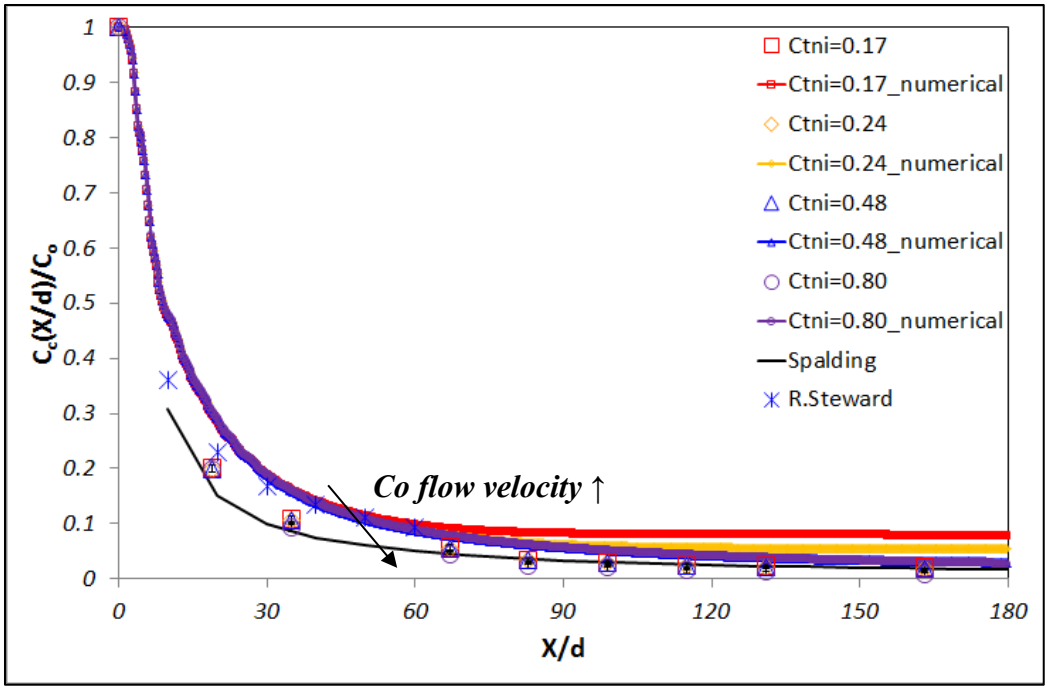

(d) U_{jet}=304.37m/s at each different co-flow

Figure 3.7 The measured concentration along the axial direction

The non-isothermal Craya-Curtet number (C_{tni}) is used to describe the velocity conditions between the jet and the co-flow respectively in figure 3.7. Steward's [15] and Spalding's [55] data from free turbulent jets are plotted in each graph for showing the comparison between my results and previous results. Experiment and numerical results agree well. However, the comparison shows that there is the deviation between my experimental data and numerical results because of the limitation of turbulent model to explain mass diffusion. Also, my data and previous results correspond well along the axial direction. The ***NO*** concentration along the centerline decays and spreads as the jet flow moves along in the axial direction at each velocity condition. Also, the value of concentration is a relatively constant value at low non-isothermal Craya-Curtet number due to the entrainment by the recirculation zone and flow interaction. Usually the recirculation zone enhances the mixing of flow by the flow interaction. Therefore, the concentration distribution is influenced by confinement effects. The results show that the

centerline ***NO*** concentration is diluted more as the non-isothermal Craya-Curtet number increases because of enough entrainment of hot co-flow. The co-flow velocity is increased as the non-isothermal Craya-Curtet number increases. This means that the flow rate from co-flow is increased. Therefore, there is sufficiently hot air for the entrainment into the center jet as high co-flow velocity as well as high non-isothermal Craya-Curtet numbers. Therefore, the value of centerline ***NO*** concentration is smaller as the non-isothermal Craya-Curtet number increases. The results of the normalized concentration have the different slope of the decay around ***X/d*** >60 due to limited entrainment by confined condition.

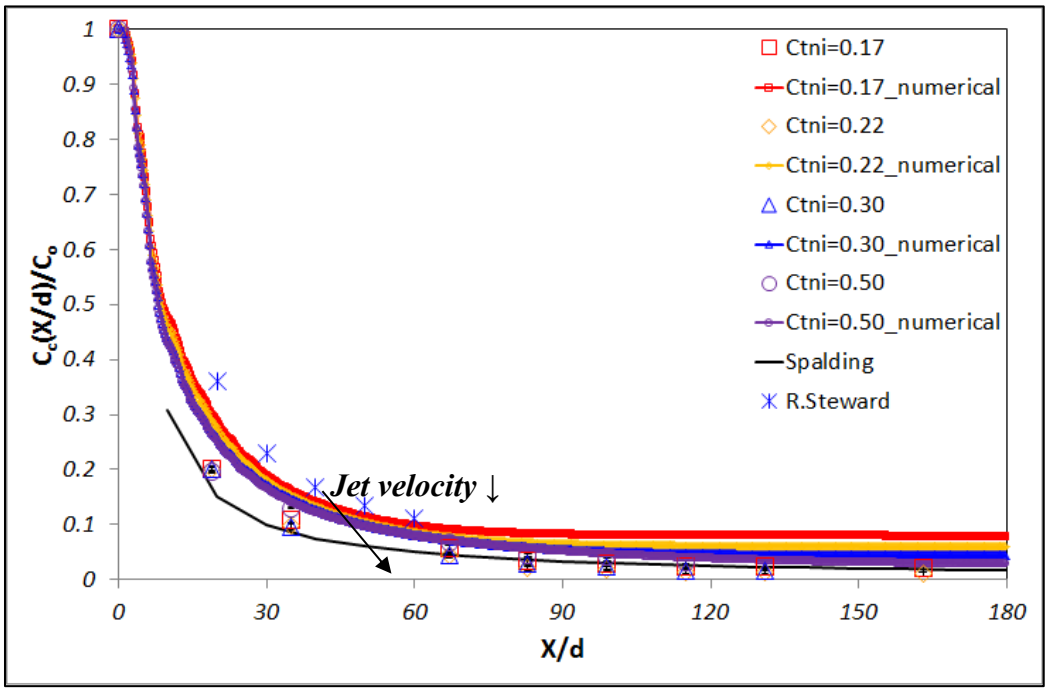

(a) U_{co}=0.612m/s at each jet velocity

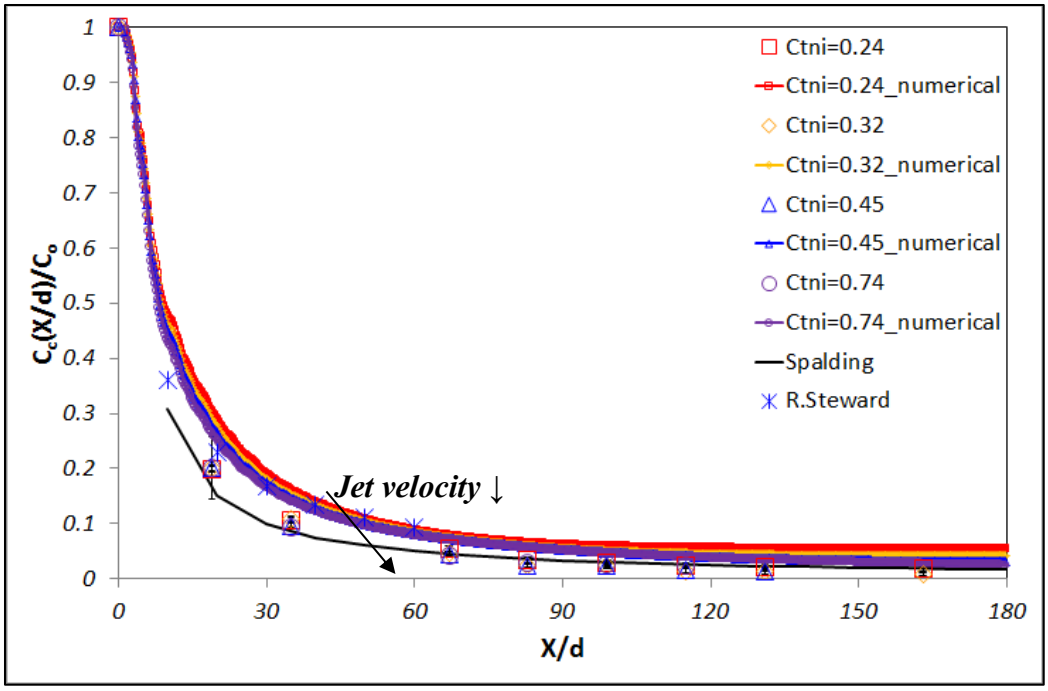

(b) U_{co}=0.913m/s at each jet velocity

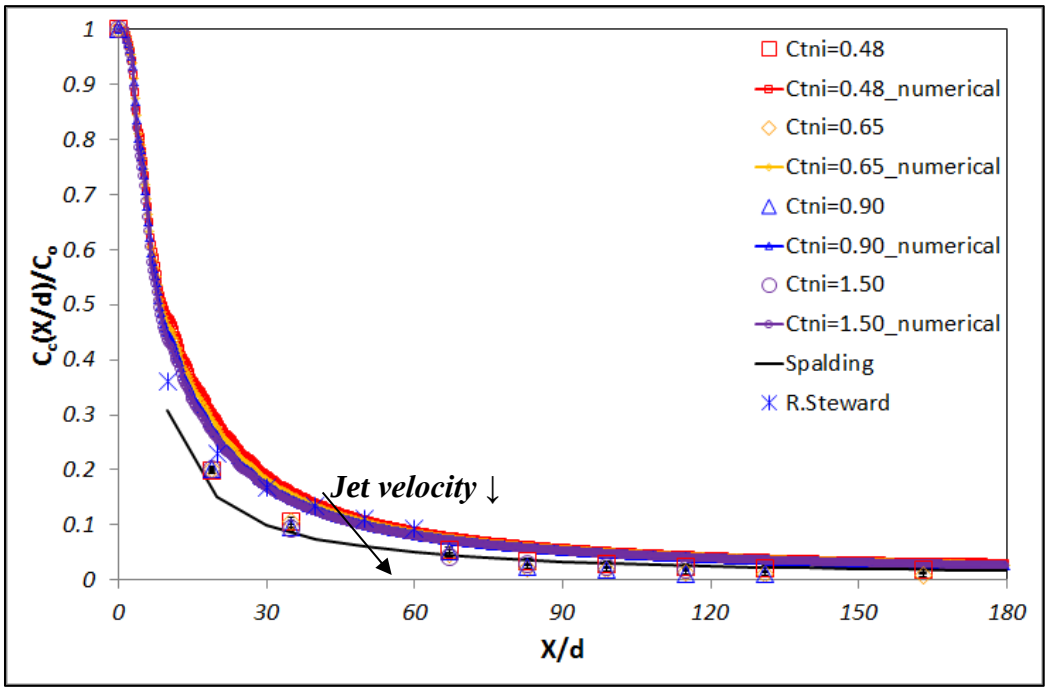

(c) U_{co}=1.856m/s at each jet velocity

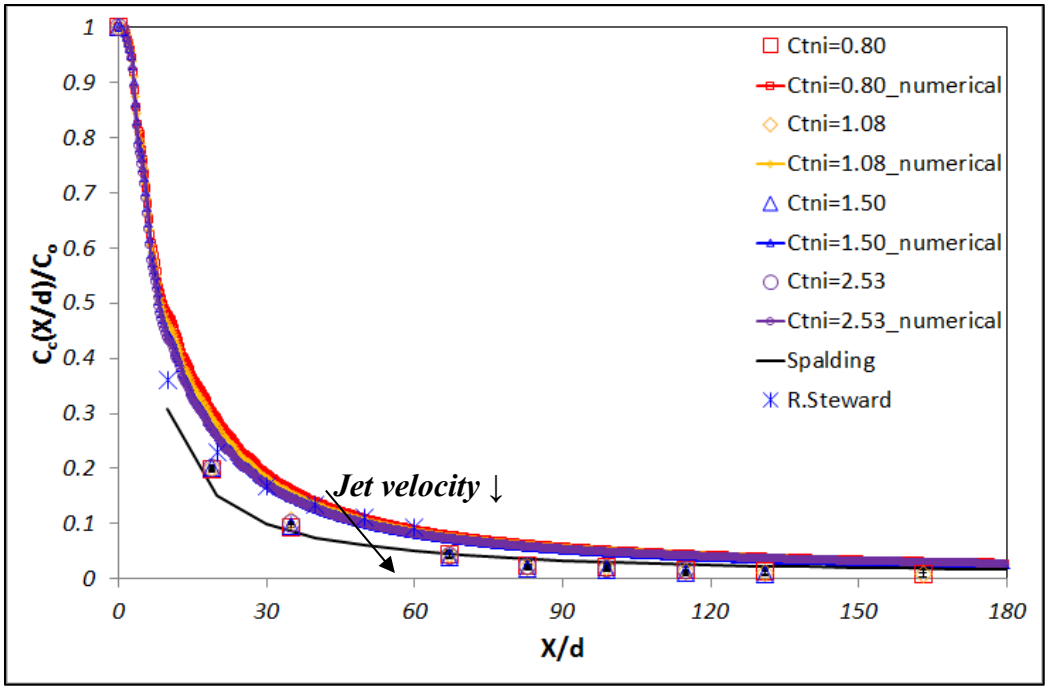

(d) U_{co}=3.123m/s at each jet velocity

Figure 3.8 The measured concentration along the axial direction

Figure 3.8 shows the normalized ***NO*** concentration as the function of ***X/d*** (***X***: axial direction, ***d***: jet nozzle diameter) at fixed co-flow and different jet velocities. Steward's [15] and Spalding's [55] data are used to illustrate the difference. The previous results were resulted from the free turbulent jet condition. The comparison shows that my data and previous data are fairly consistent. The ***NO*** concentration decays along the centerline and spreads as the jet flow moves downstream respectively. In the low non-isothermal Craya-Curtet number, the ***NO*** concentration has the relatively constant value as the jet flow moves along the axial direction because of the entrainment by the recirculation zone and flow interaction. Also, the centerline ***NO*** concentration is diluted more as the non-isothermal Craya-Curtet number increases because the co-flow velocity is increased. Accordingly, there is enough amount of hot air into the center jet.

The radial velocity distribution for different jet velocities and different co-flow conditions are shown in fig 3.9. The experimental and numerical data are expressed as different colored symbols and colored lines of the different locations of ***X/d*** (***X***: axial direction, ***d***: jet nozzle diameter). Becker et al. [5] suggest equation (29) for studying the normalized ***NO*** concentration as the function of the radial direction (***r***). The equation shows as,

$$\overline{C} = \frac{C}{C_c} = \exp\left[-0.693 \left(r / r_{\frac{C}{2}} \right)^{1.82} \right] \tag{29}$$

C is the radial ***NO*** concentration at different locations of ***X/d***, $\boldsymbol{C_c}$ is the ***NO*** concentration along the centerline and $\boldsymbol{r_{c/2}}$ is the width of the half value of ***NO*** concentration. The calculated data from Becker's equation and our measured ***NO*** concentration profiles show the good similarity on a Gaussian function from equation (29). There are differences and scatters in the ***NO*** concentration data at $\boldsymbol{r/r_{c/2}}$>1 but the normalized ***NO*** concentration has self-preservation in the jet region for all of test conditions. The deviation at the trail of the curve is due to the confinement and difficult measurement to low ***NO*** concentration.

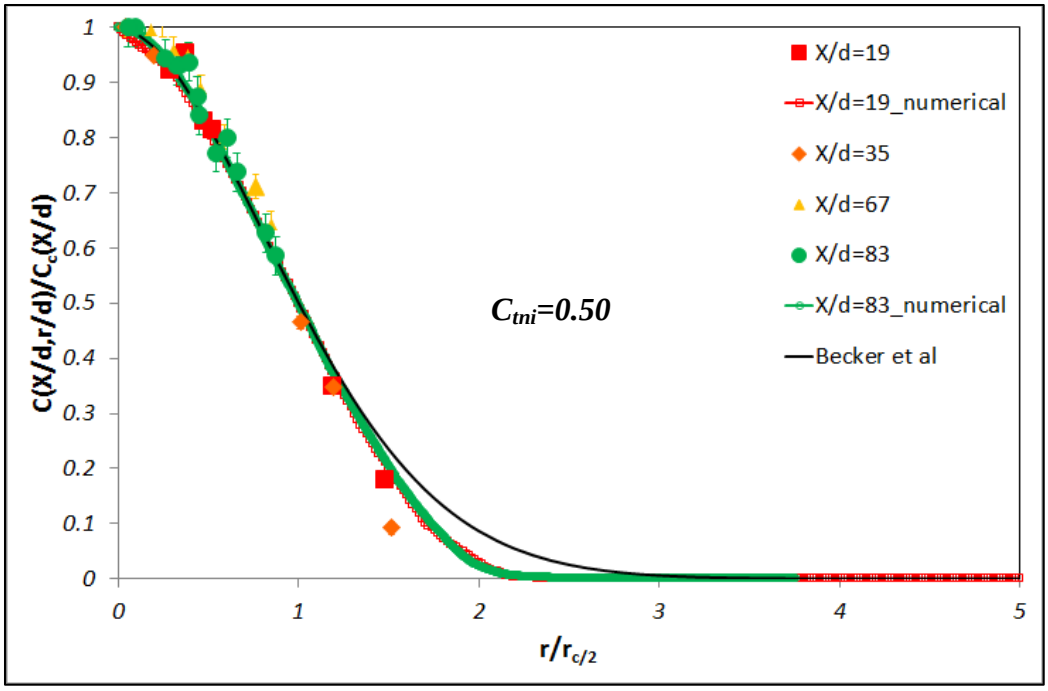

(a) U_{jet}=96.12m/s and U_{co}=0.612m/s

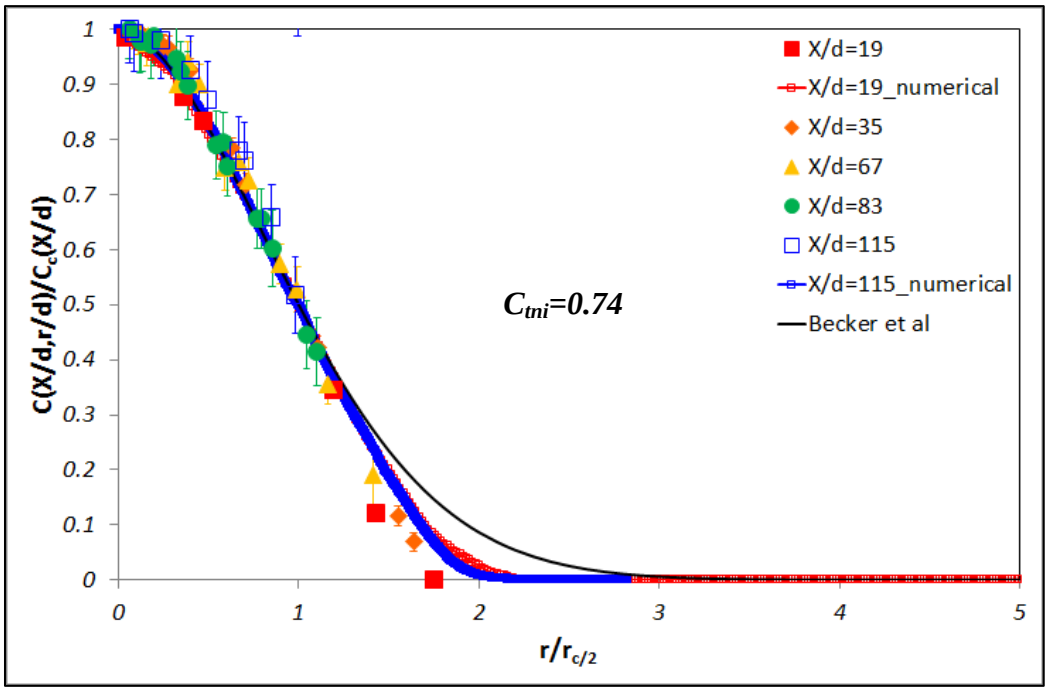

(b) U_{jet}=96.12m/s and U_{co}=0.913m/s

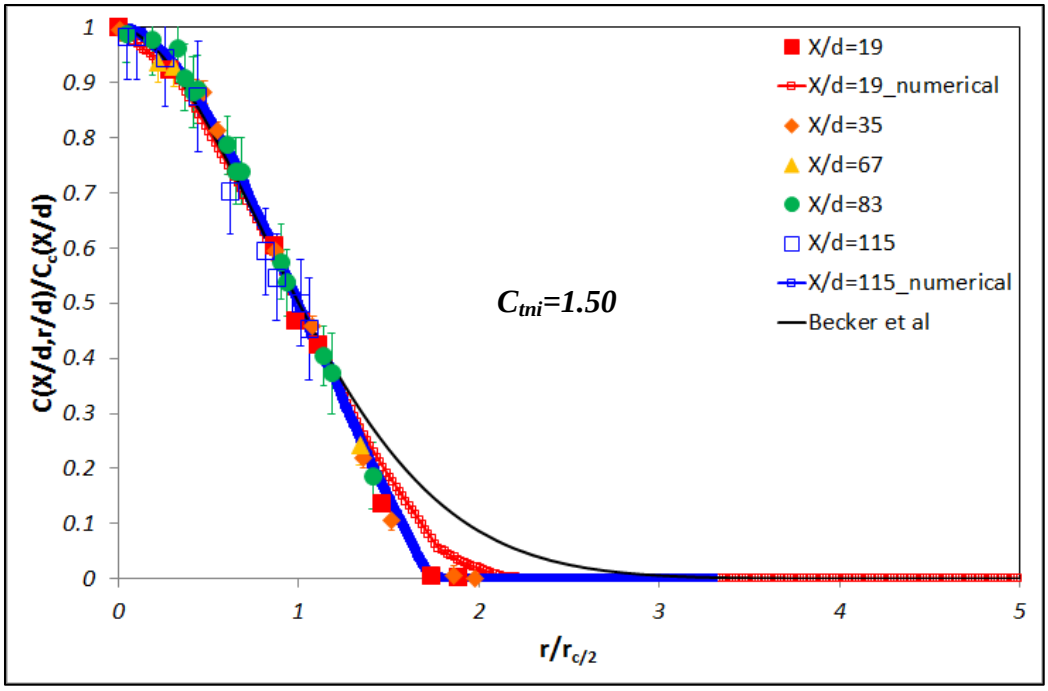

(c) U_{jet}=96.12m/s and U_{co}=1.856m/s

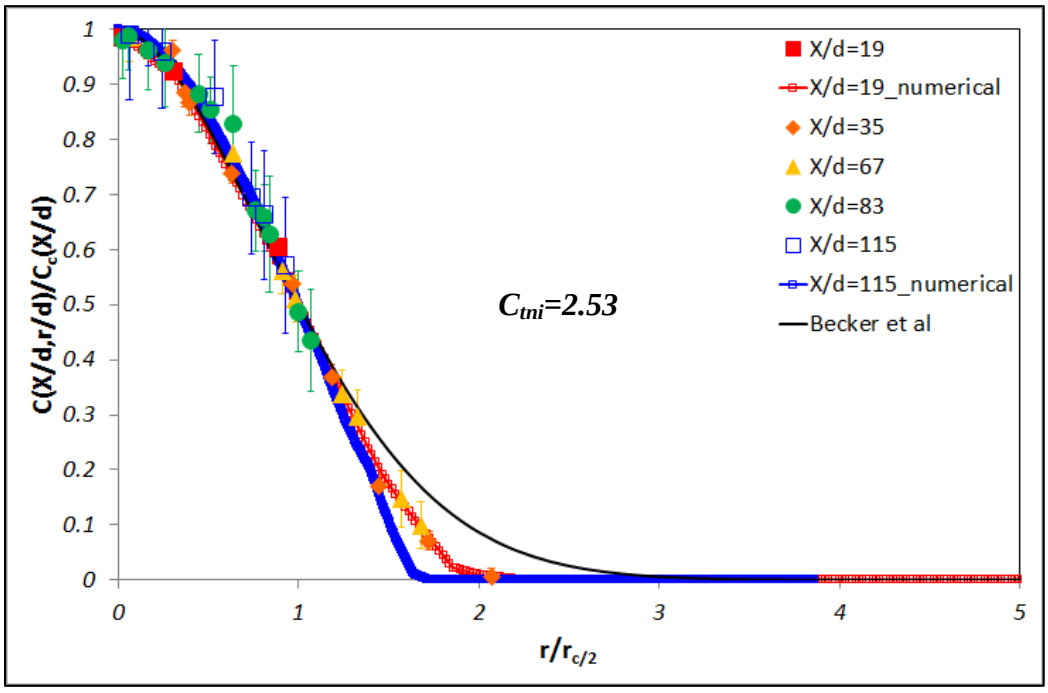

(d) U_{jet}=96.12m/s and U_{co}=3.123m/s

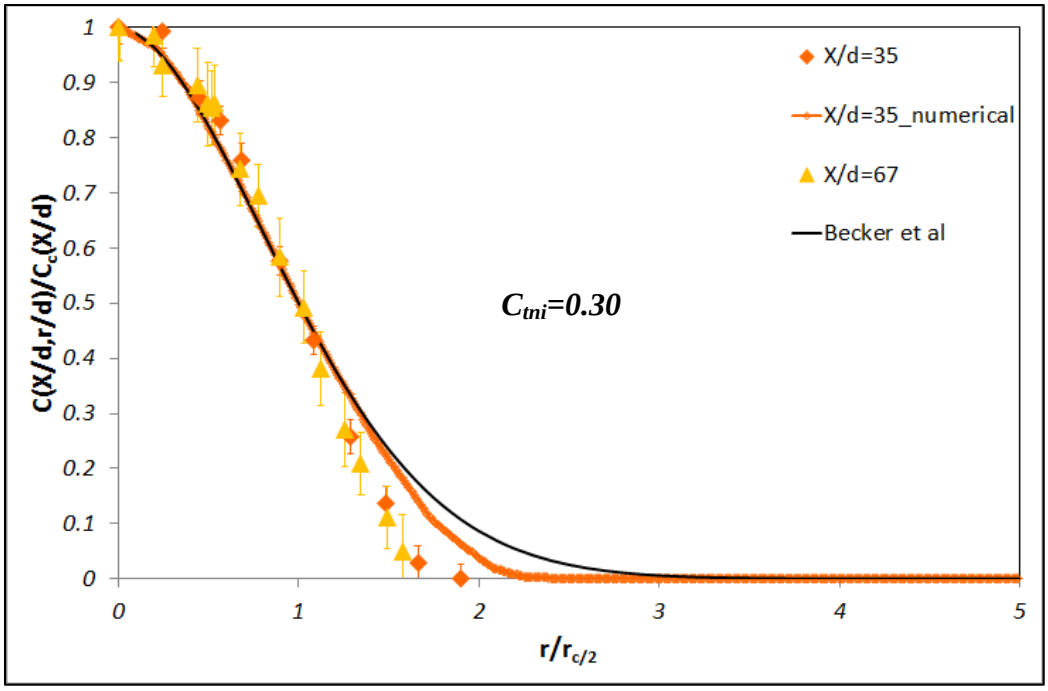

(e) U_{jet}=160.19m/s and U_{co}=0.612m/s

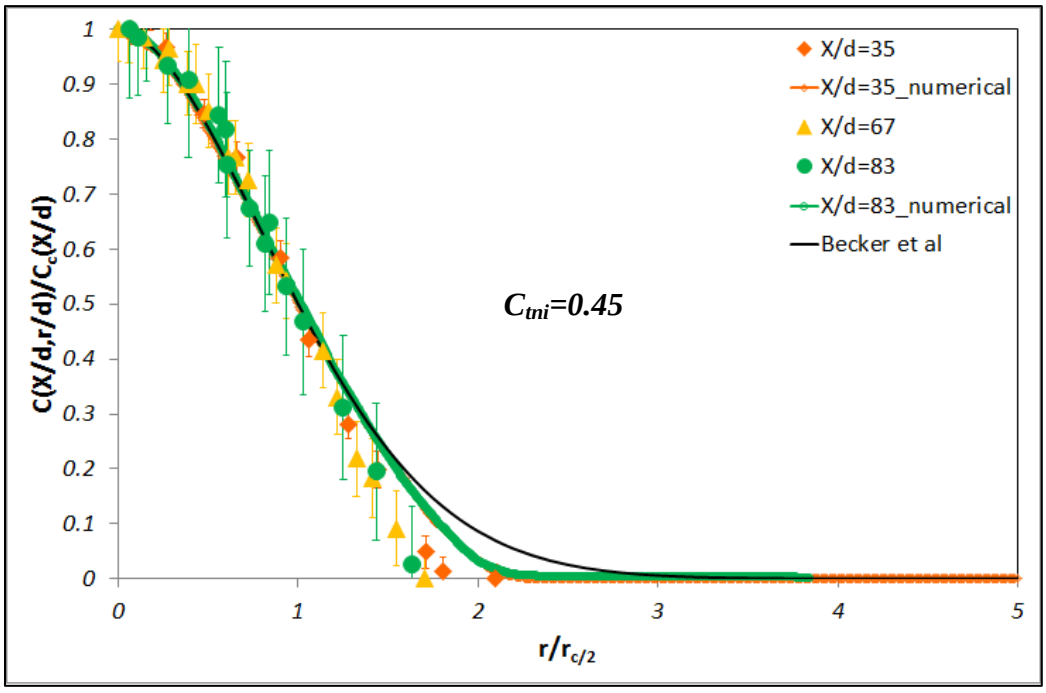

(f) U_{jet}=160.19m/s and U_{co}=0.913m/s

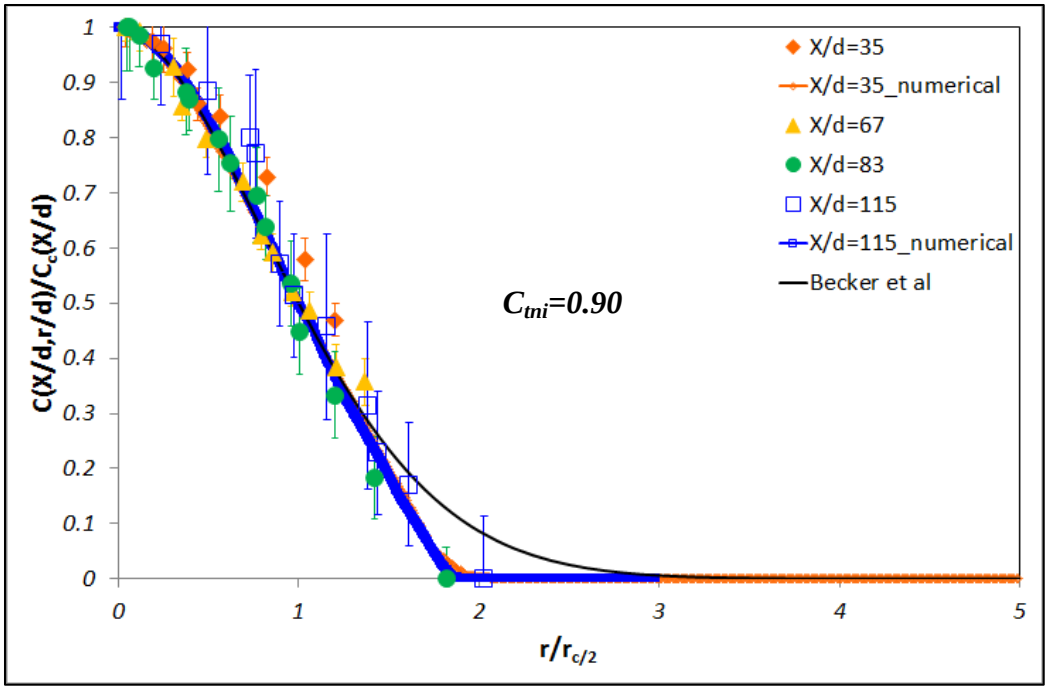

(g) U_{jet}=160.19m/s and U_{co}=1.856m/s

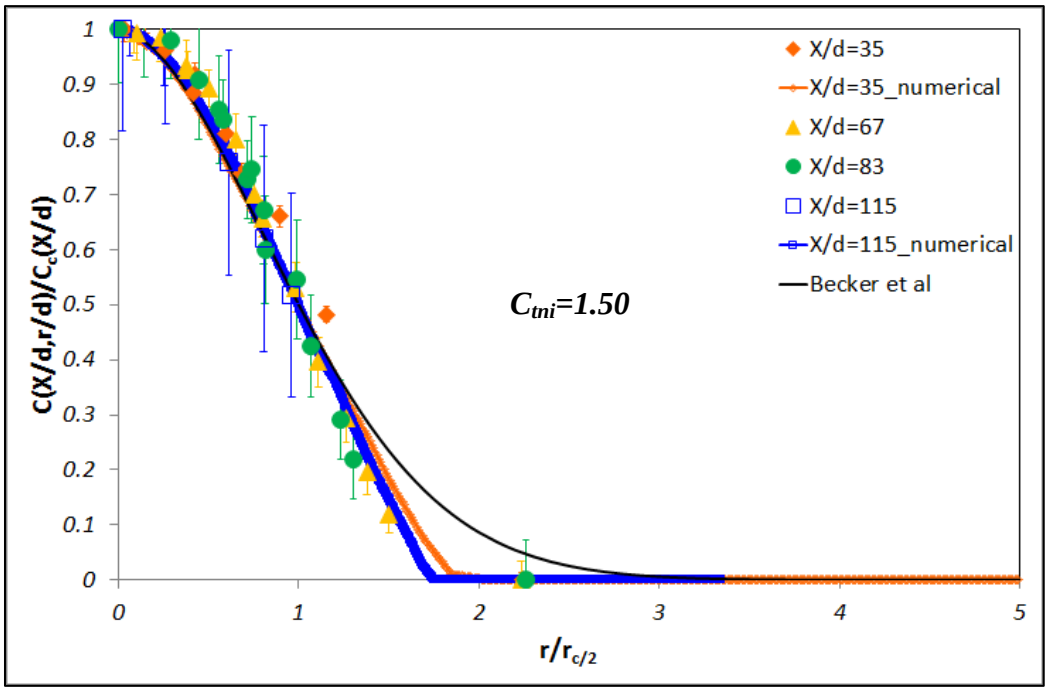

(h) U_{jet}=160.19m/s and U_{co}=3.123m/s

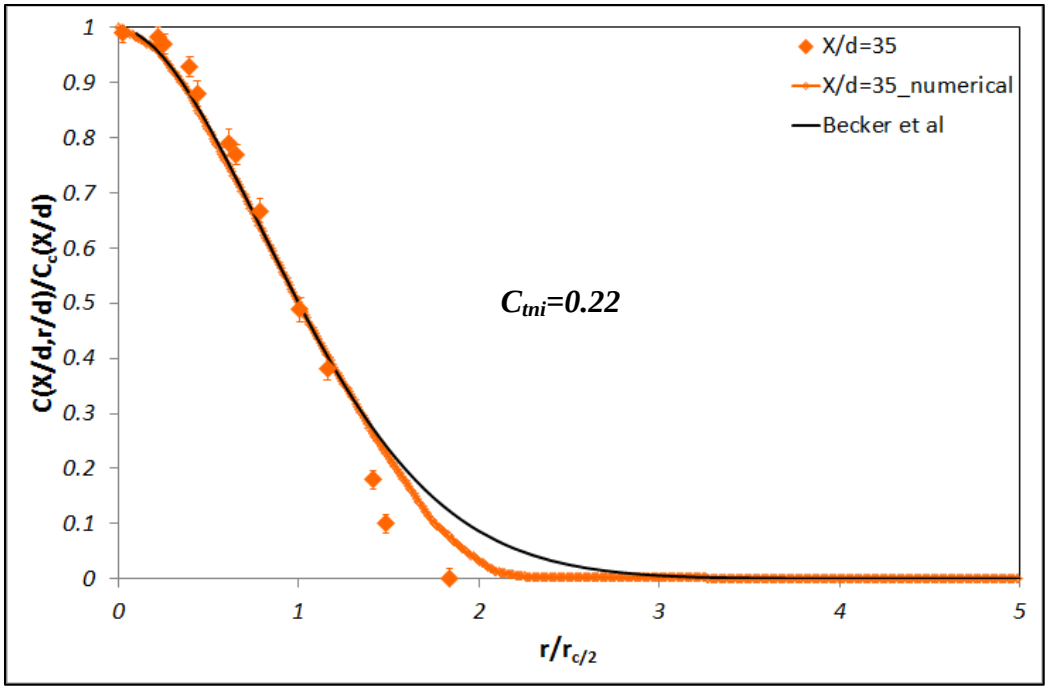

(i) U_{jet}=224.26m/s and U_{co}=0.612m/s

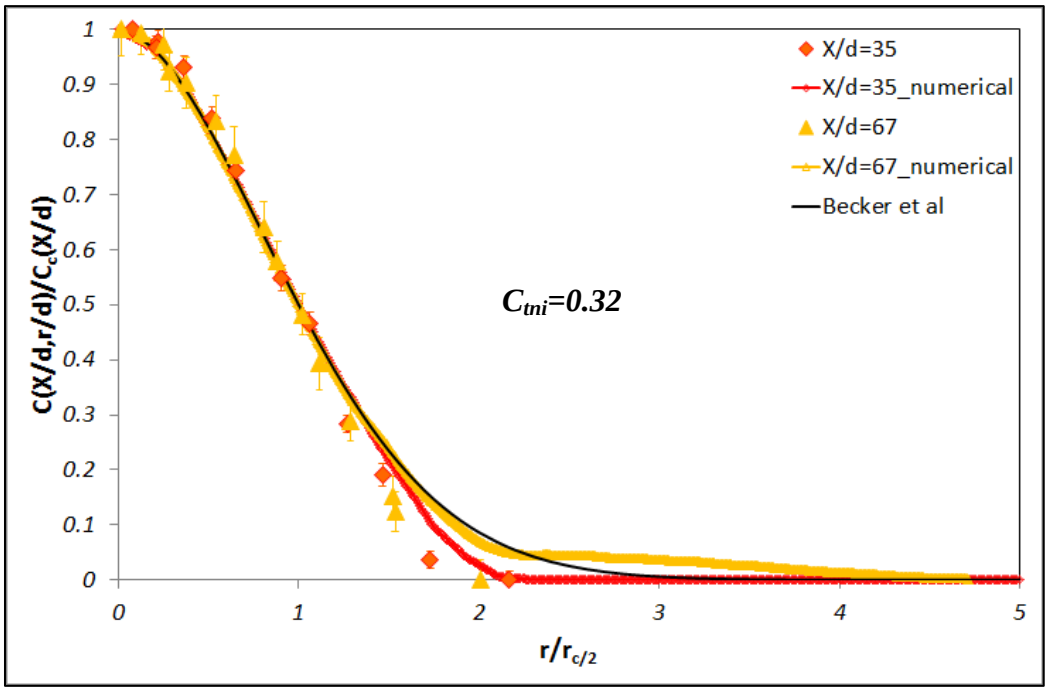

(j) U_{jet}=224.26m/s and U_{co}=0.913m/s

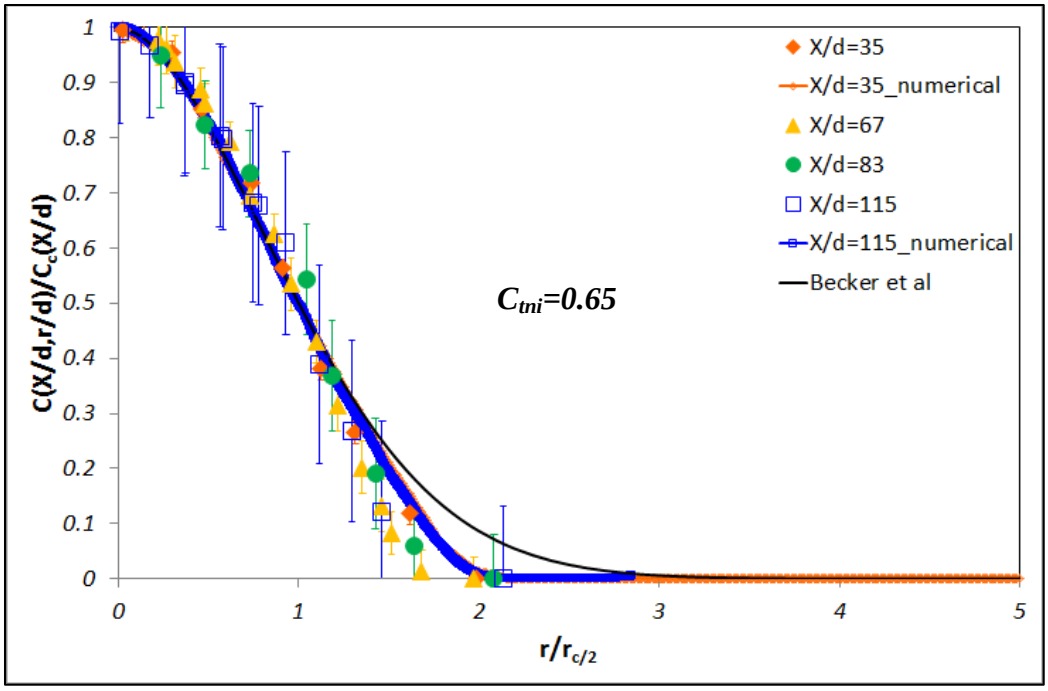

(k) U_{jet}=224.26m/s and U_{co}=1.856m/s

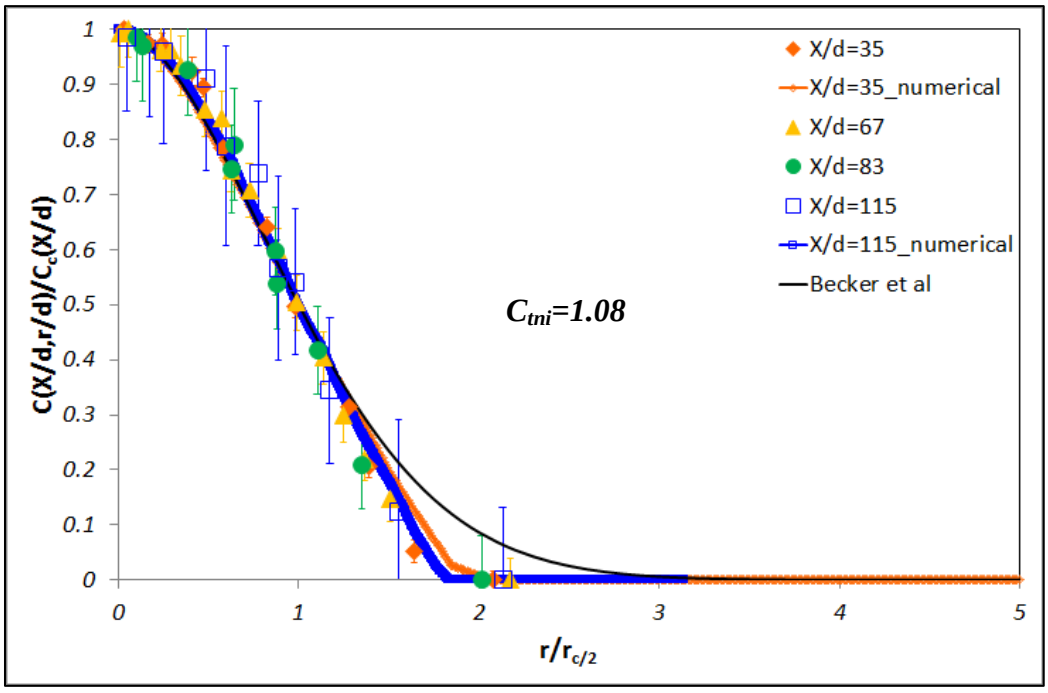

(l) U_{jet}=224.26m/s and U_{co}=3.123m/s

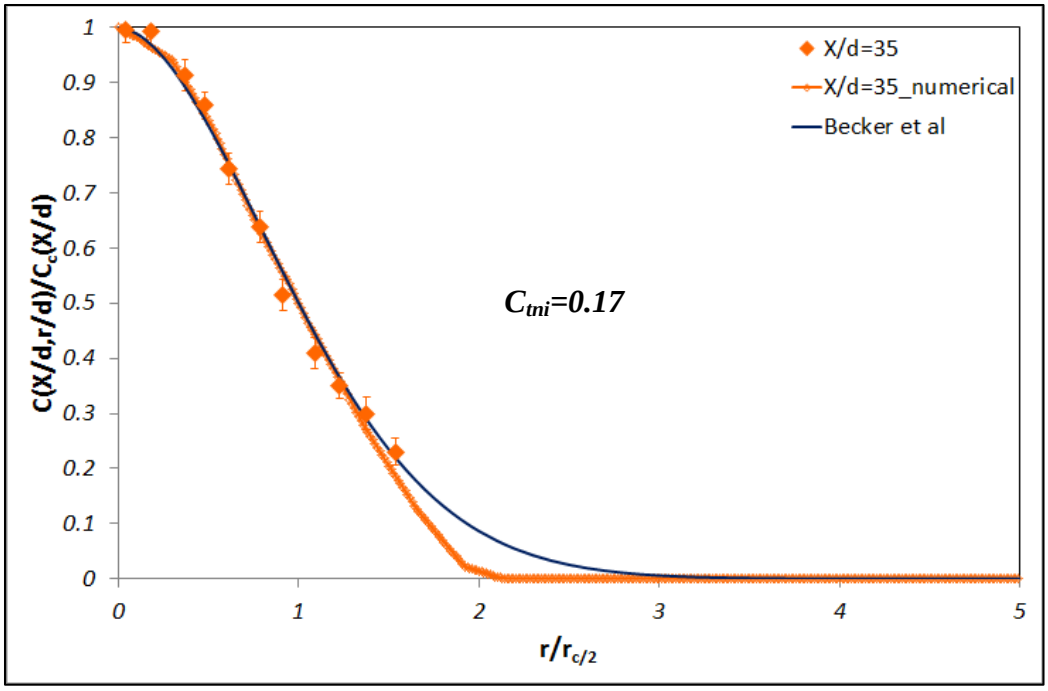

(m) U_{jet}=304.37m/s and U_{co}=0.612m/s

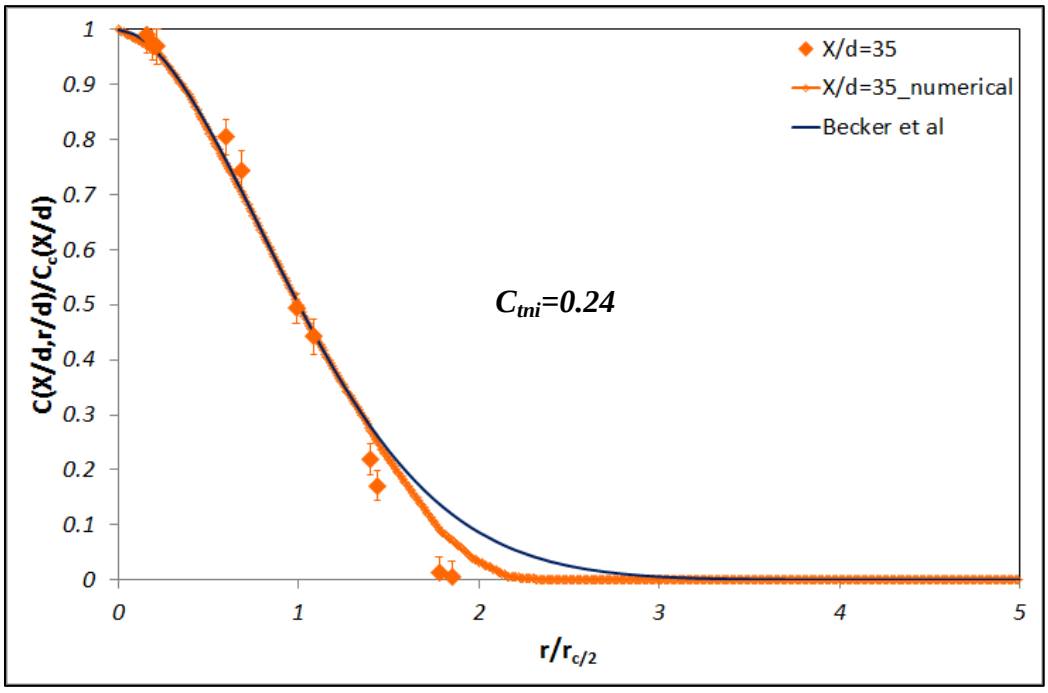

(n) U_{jet}=304.37m/s and U_{co}=0.913m/s

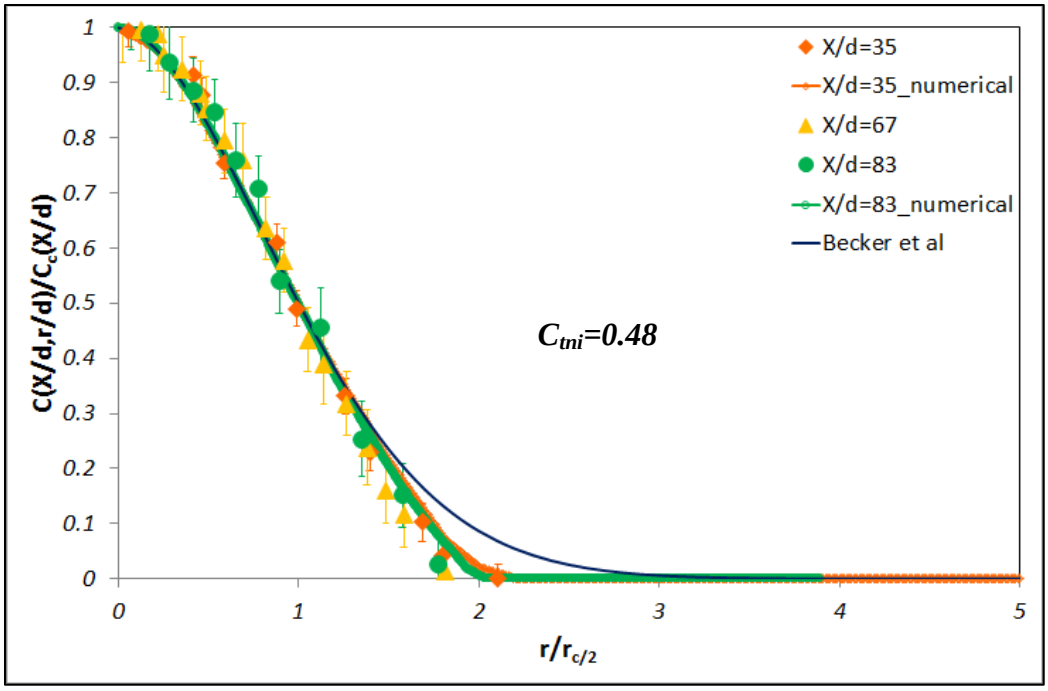

(o) U_{jet}=304.37m/s and U_{co}=1.856m/s

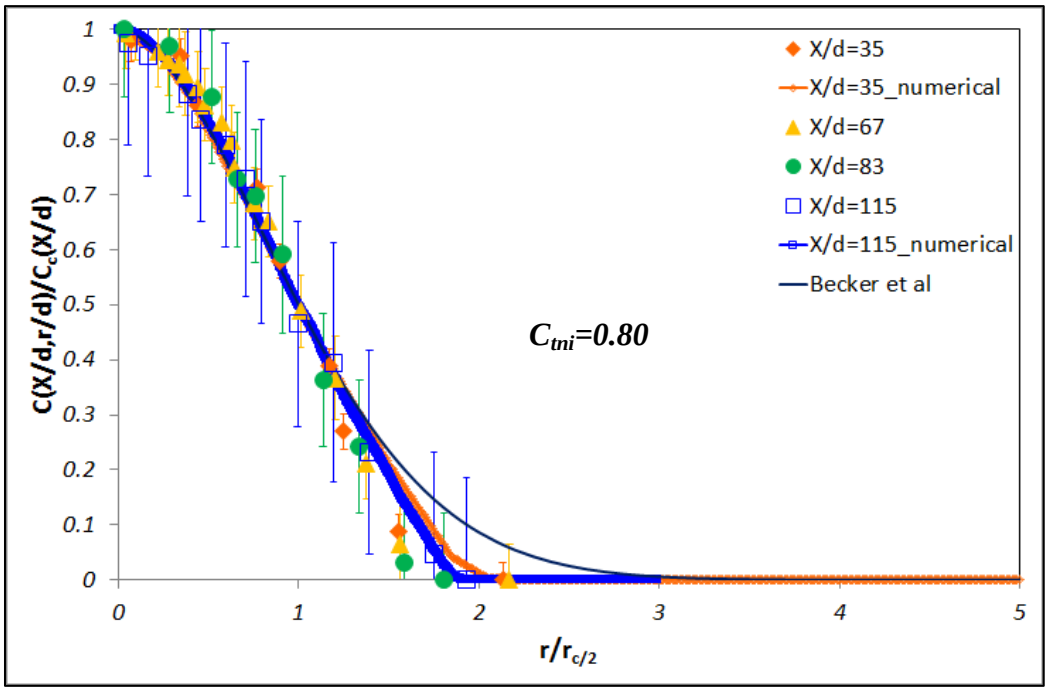

(p) U_{jet}=304.37m/s and U_{co}=3.123m/s

Figure 3.9 The radial concentration distribution

From experimental and numerical results, a new equation of the normalized ***NO*** concentration as a function of the radial direction is found. This equation (30) is much better matched to the expressed results.

$$\overline{C} = \frac{C}{C_c} = \exp\left[-\ln 2.13 \left(r / r_{\frac{C}{2}} \right)^2 \right] \tag{30}$$

Even though velocity distribution has a non-Gaussian distribution at some condition (***M***=0.9/0.7 at $\boldsymbol{U_{co}}$=3.123m/s and ***M***=0.5/0.3 at $\boldsymbol{U_{co}}$=3.123m/s and $\boldsymbol{U_{co}}$=1.856m/s) at the furthest downstream location (***X/d***=115), Concentration distribution is still found to be a Gaussian distribution.

3.1.5. The temperature distribution

The characteristics of the temperature profiles are investigated along the axial direction and the radial direction as the function of ***X/d*** (***X***: axial location, ***d***: jet nozzle diameter). To check the effect of different co-flow velocities at fixed jet velocity as well as the effect of different jet velocities at fixed co-flow velocity, the graphs are plotted by using the non-isothermal Craya-Curtet number (C_{tni}) for comparing easily.

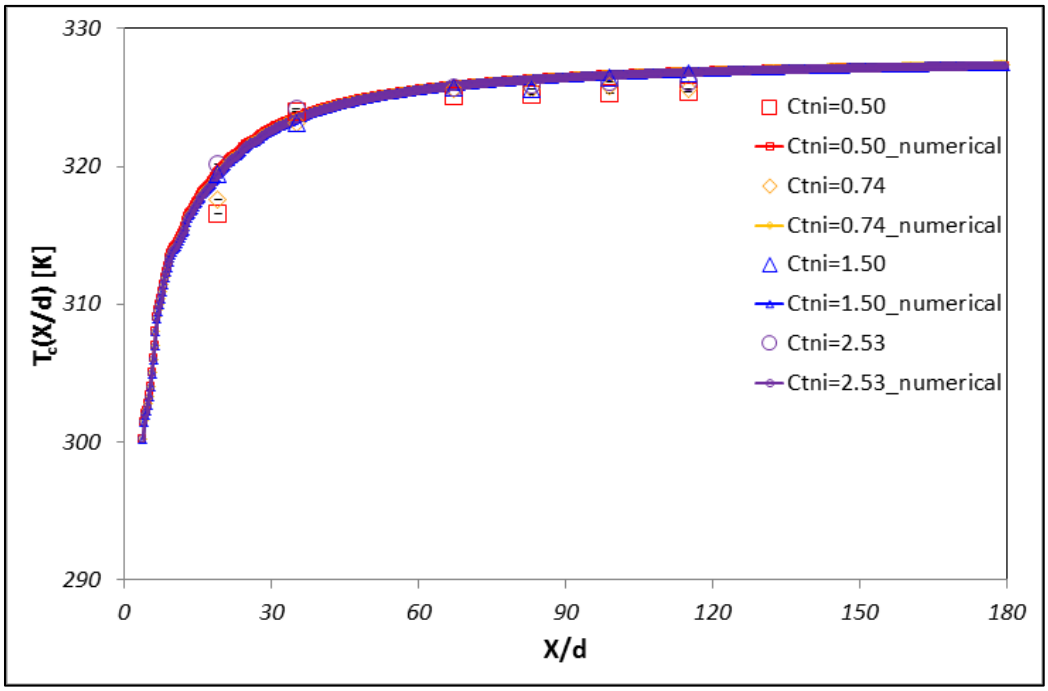

(a) U_{jet}=96.12m/s at each different co-flow

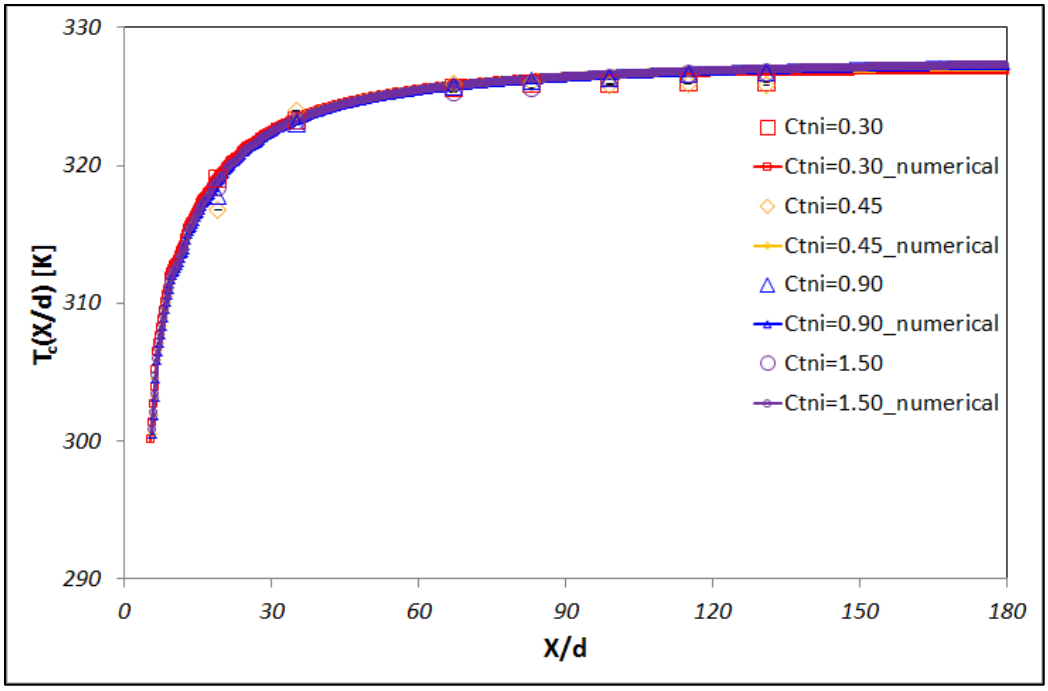

(b) U_{jet}=160.19m/s at each different co-flow

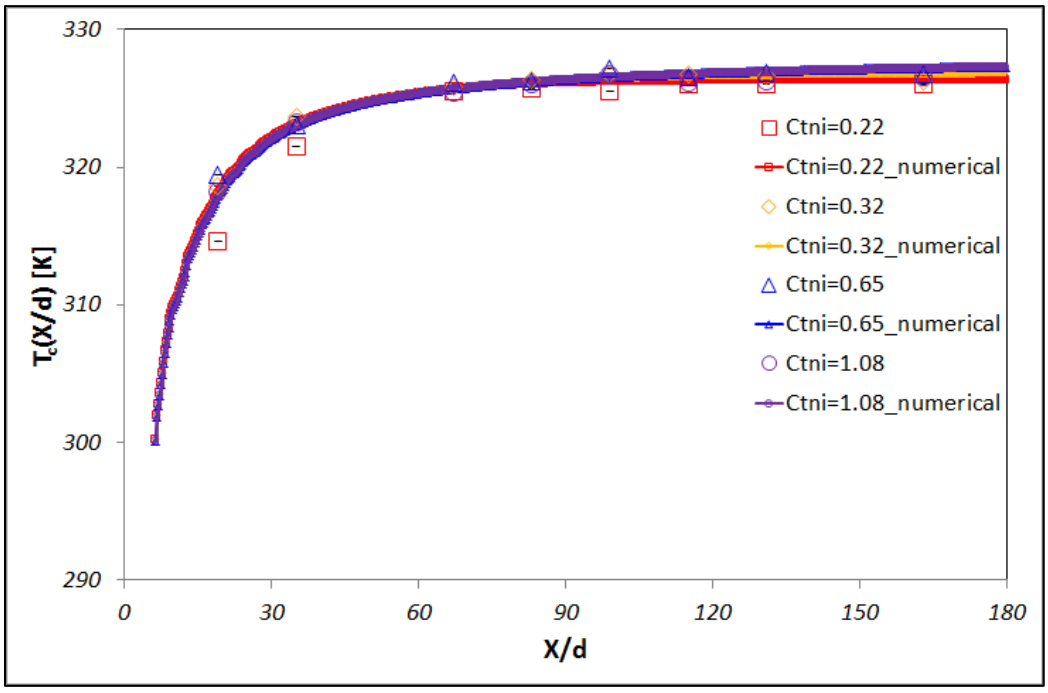

(c) U_{jet}=224.26m/s at each different co-flow

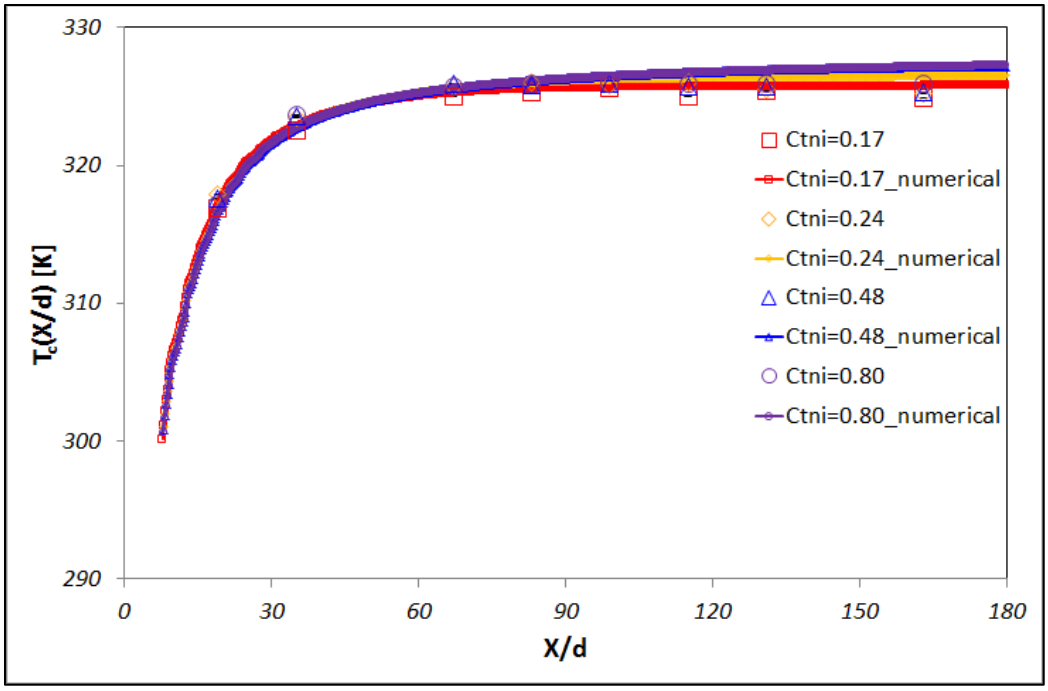

(d) U_{jet}=304.37m/s at each different co-flow

Figure 3.10 The measured temperature along the axial direction

Figure 3.10 shows that temperature profiles are at the fixed jet velocity and different co-flow velocities respectively in non-isothermal condition. The center temperature (***T*****$_c$**) is plotted at the different normalized axial locations (***X/d***). The center temperature increases as the flow moves along the axial direction because of increasing entrainment of hot co-flow into the center jet. After the flow moves along the axial direction, the temperature along the centerline approaches the single value. This means that the profiles of normalized temperature are flat and shows an asymptote. This is shown as a flat temperature profile after ***X/d*** is 60. The high value of centerline temperature profiles is at high the non-isothermal Craya-Curtet number because of the high co-flow velocity. Therefore, the cases of high non-isothermal Craya-Curter number have enough hot air flow. In these cases, the high value of the center temperature is shown.

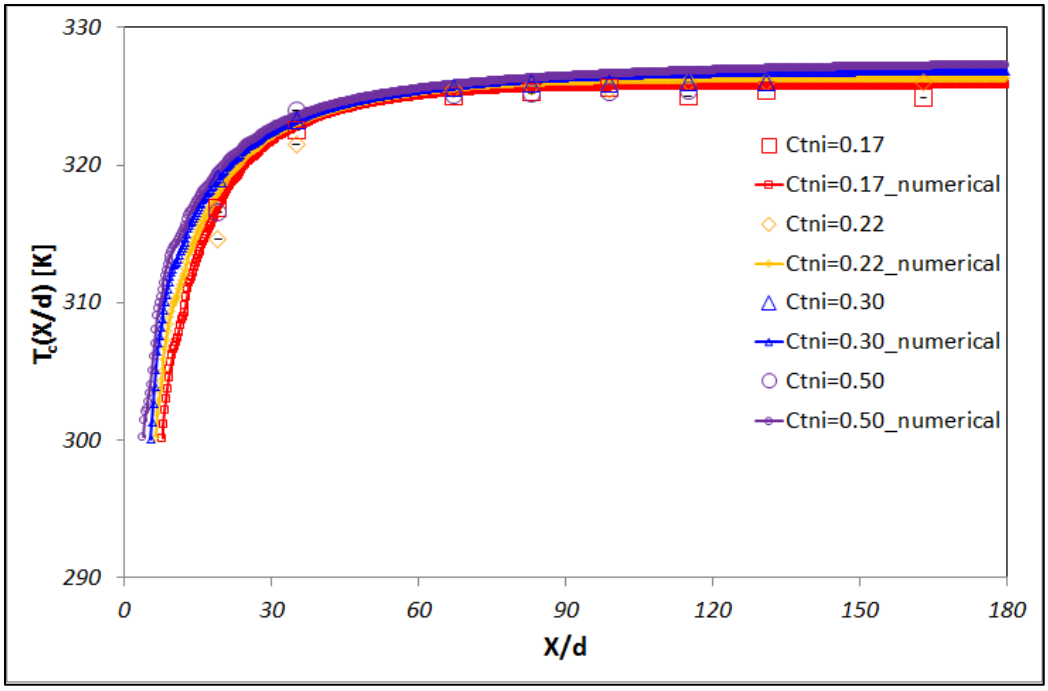

(a) U_{co}=0.612m/s at each different jet velocity

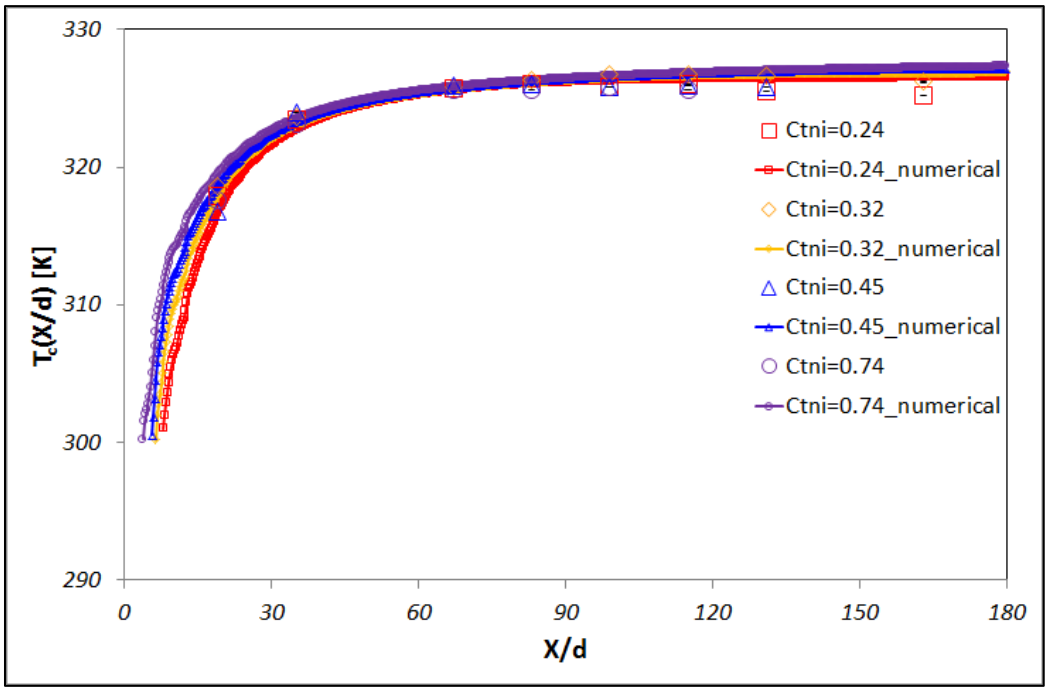

(b) U_{co}=0.913m/s at each different jet velocity

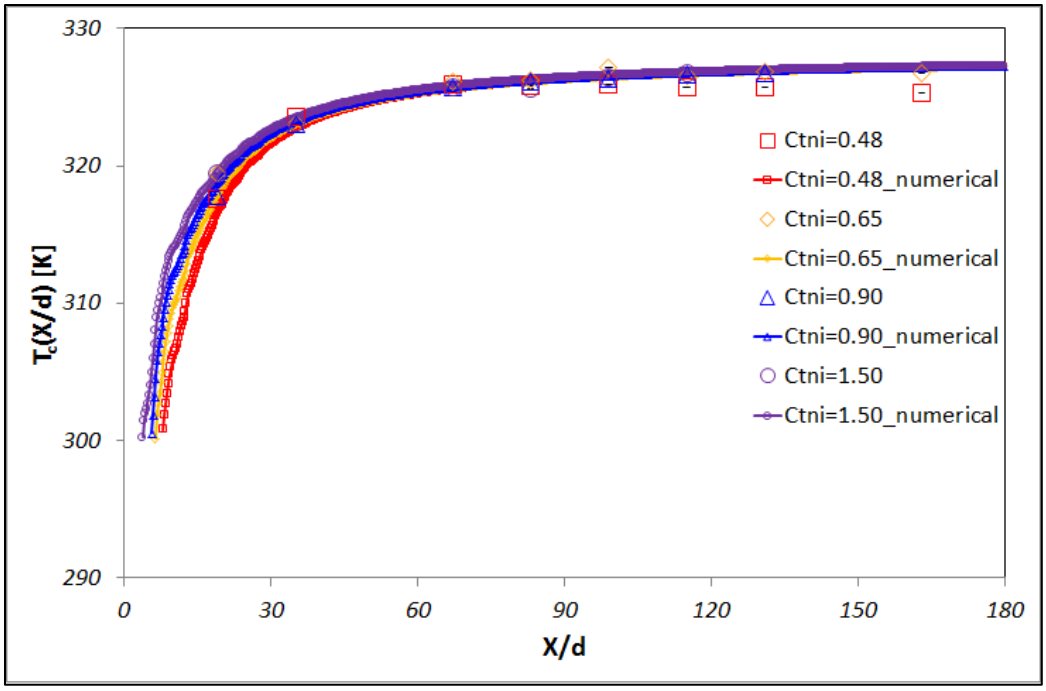

(c) U_{co}=1.856m/s at each different jet velocity

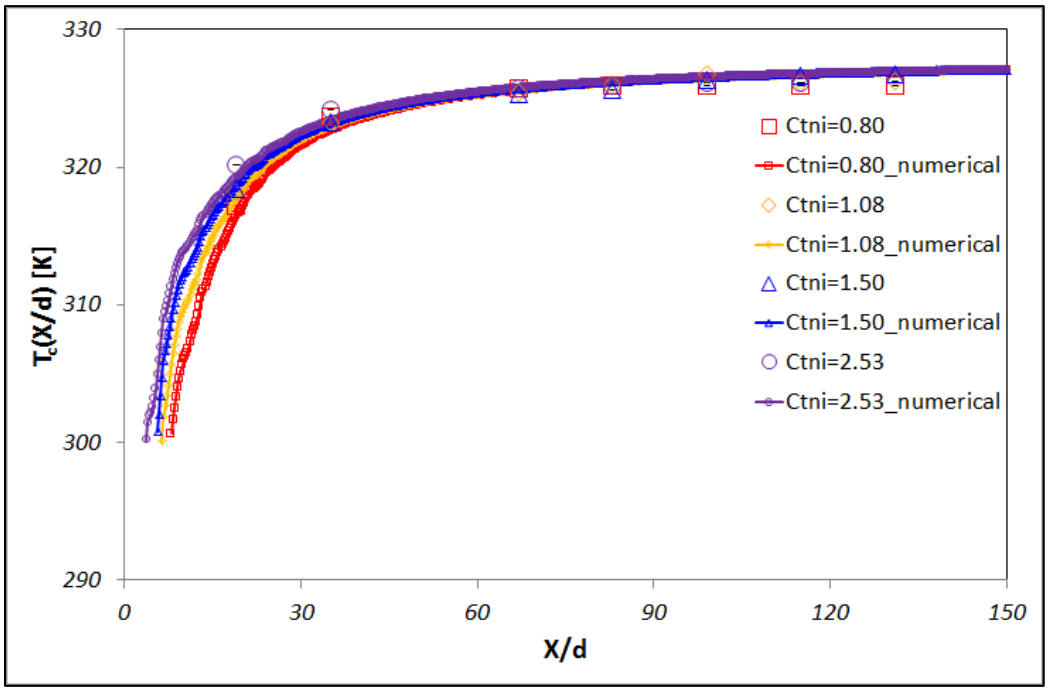

(d) U_{co}=3.123m/s at each different jet velocity

Figure 3.11 The measured temperature along the axial direction

Figure 3.11 finds that temperature profiles along the centerline are at the fixed co-flow velocity and respectively different center jet velocities. The center temperature is changed as the

jet flow moves the axial direction because of an entrainment ratio of hot co-flow into center jet. After the jet flow moves at ***X/d***=60, the temperature along the centerline is converged to the single value. Results also show the high value of the normalized centerline temperature profiles at high non-isothermal Craya-Curtet number due to high volumetric co-flow.

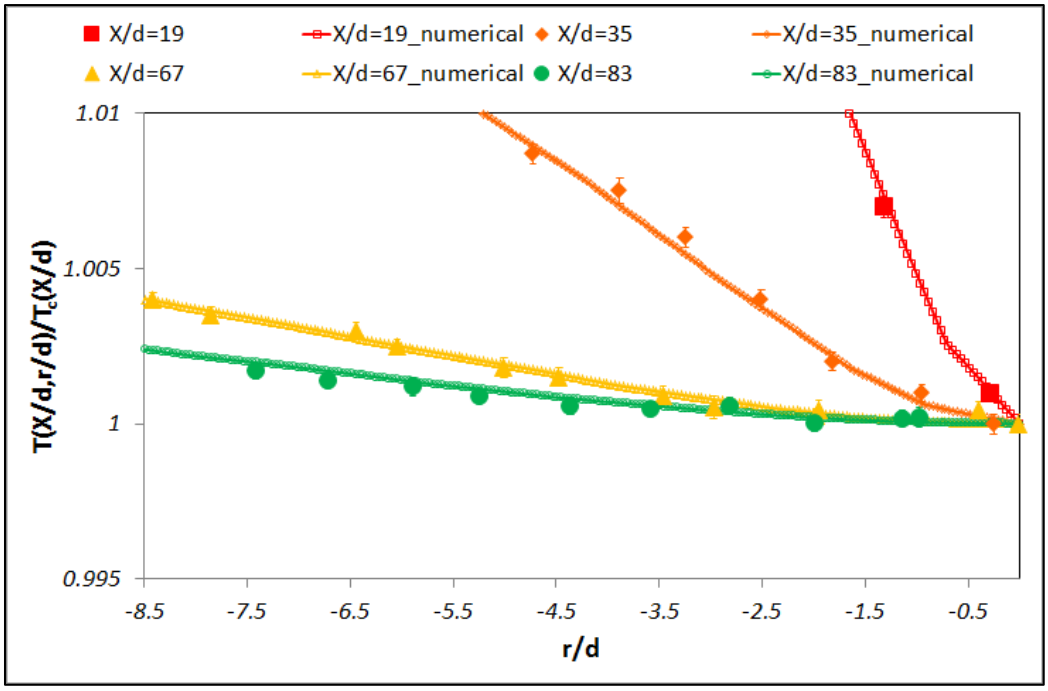

(a) C_{tni}=0.45

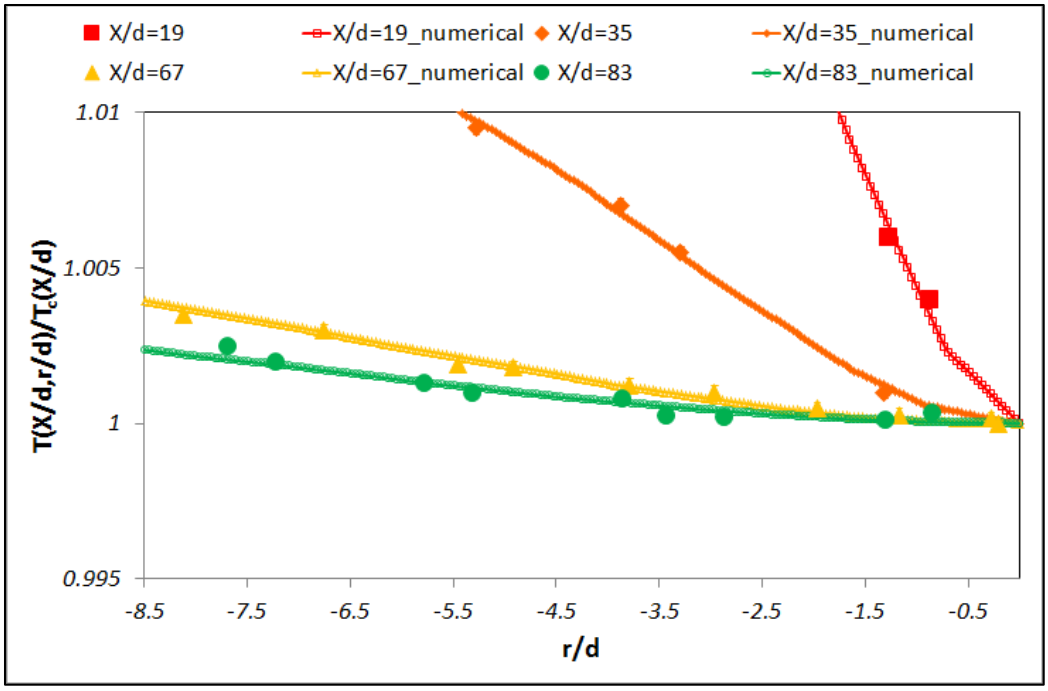

(b) C_{tni}=0.50

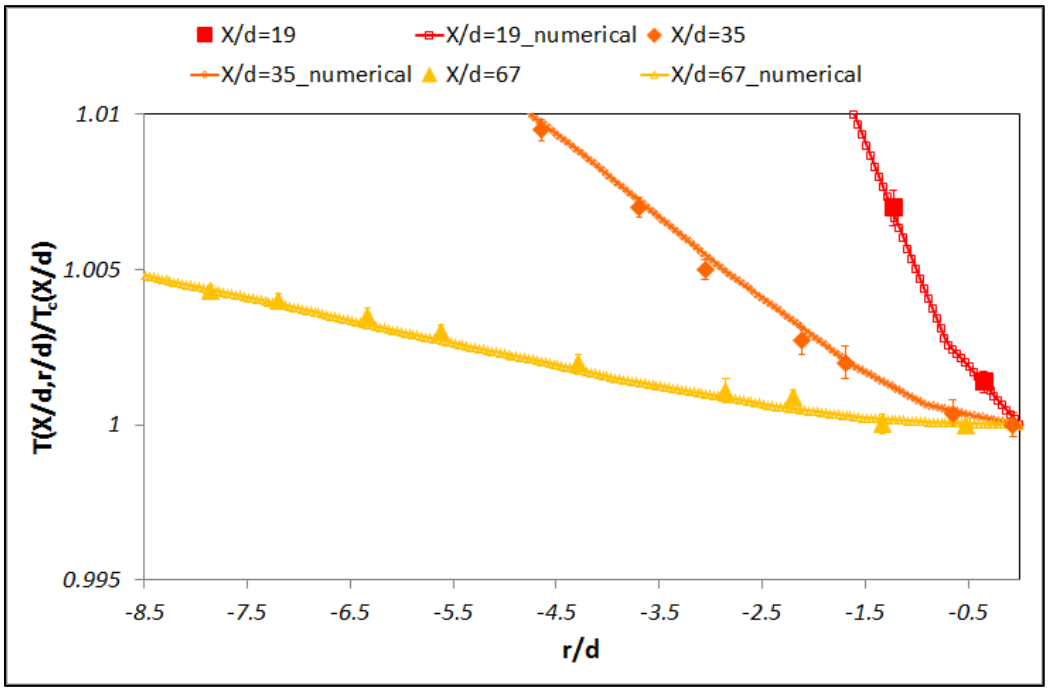

(c) C_{tni}=1.50

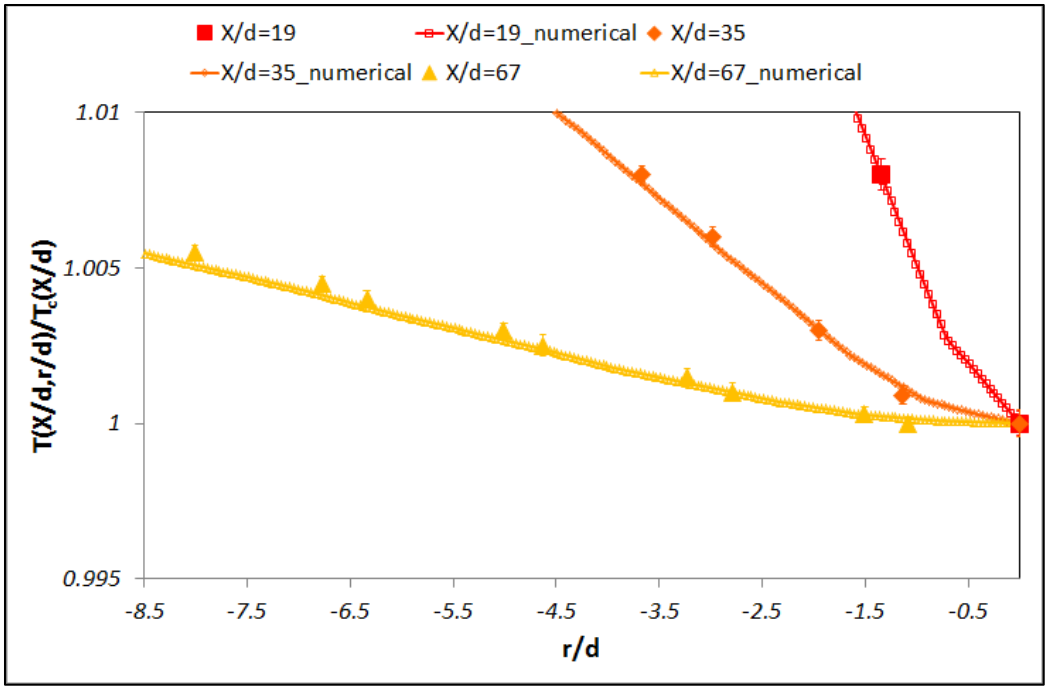

(d) C_{tni}=2.53

Figure 3.12 The measured temperature along the radial direction

The normalized temperature profiles along the normalized radial direction (***r***: radial direction, ***d***: jet nozzle diameter) are plotted in figure 3.12 by defining the center temperature (T_c) at each location. From figure 3.12, as the jet flow moves along the axial direction, the temperature profiles are more uniform due to the heat transfer from hot co-flow to cold turbulent jet. The uniform temperature is getting much faster as the non-isothermal Craya-Curtet number (C_{tni}) is decreased because of recirculation zone at low C_{tni}.

3.1.6. The width

The measured and computed jet widths of the half jet velocity are shown in figure 3.13 and figure 3.14. The widths in figure 3.13 are derived at fixed jet velocity and different co-flow respectively. From the width in figure 3.14, the width of the half jet velocity is calculated at fixed co-flow velocity and different jet velocities. The jet width is increased as the flow moves the normalized axial direction (***X/d***) because of the characteristics of spreading of the jet though interacting surrounding. For comparing my data, the previous results from Hussein et al. [56] in the free turbulent jet condition are plotted in each graph. The comparison shows that the measured widths of the half jet velocity are well agreed by the results from the free boundary condition.

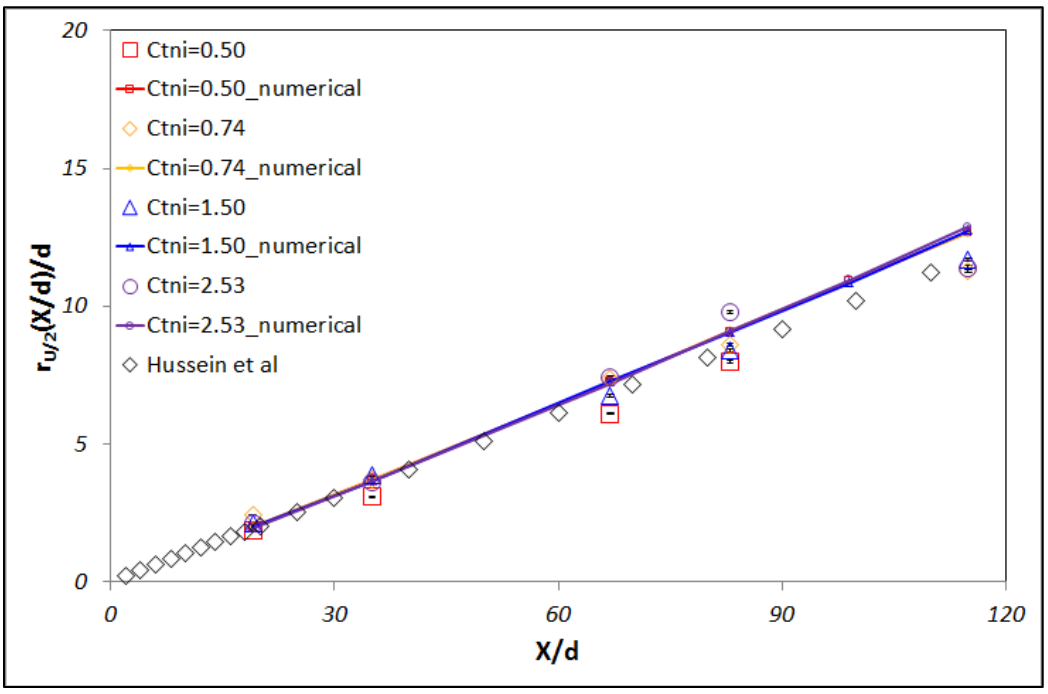

(a) U_{jet}=96.12m/s at each different co-flow

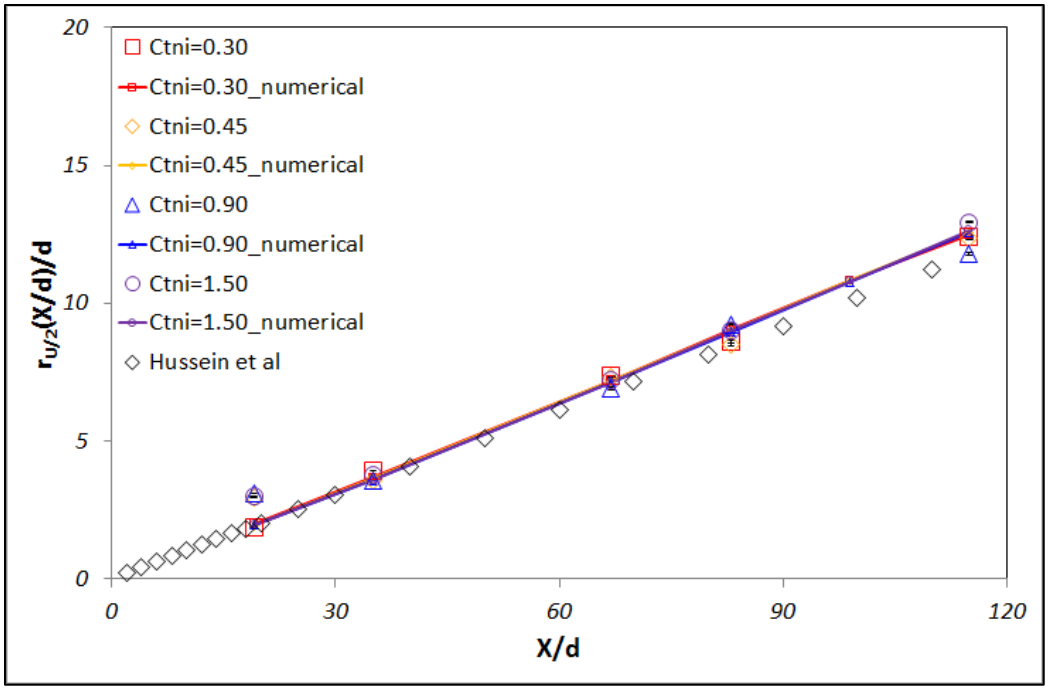

(b) U_{jet}=160.19m/s at each different co-flow

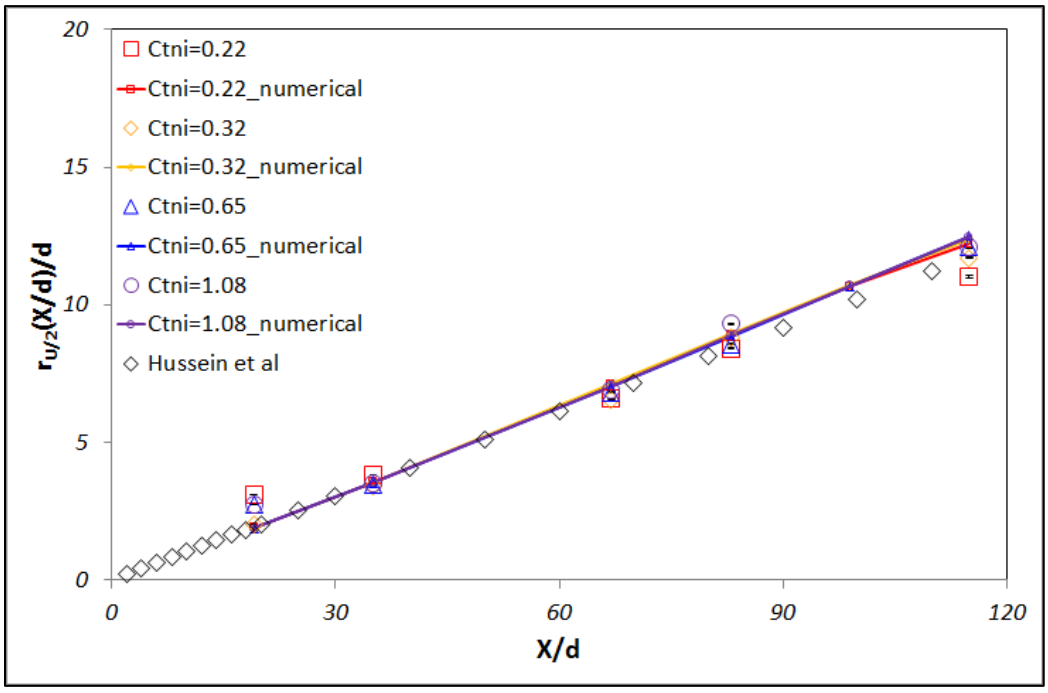

(c) U_{jet}=224.26m/s at each different co-flow

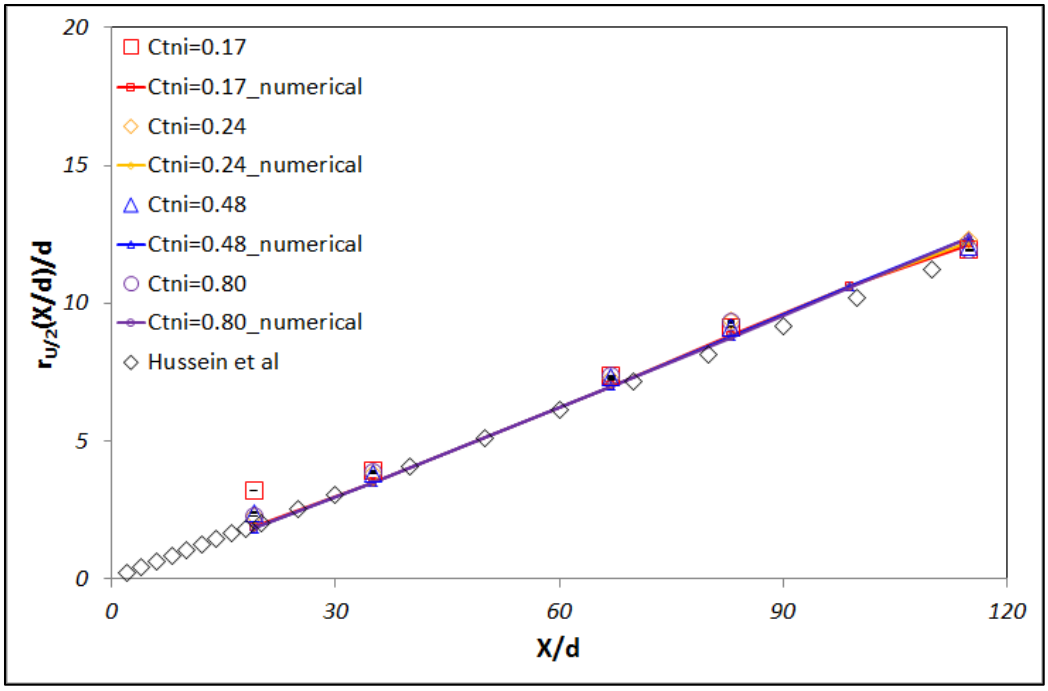

(d) U_{jet}=304.37m/s at each different co-flow

Figure 3.13 The measured jet width at half jet velocity

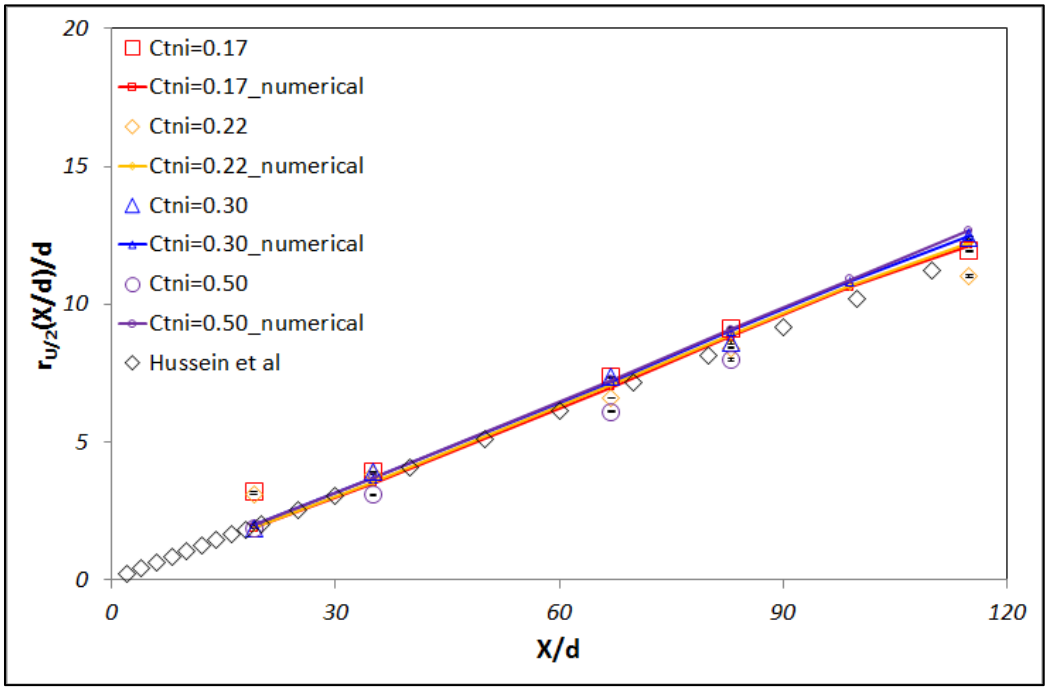

(a) U_{co}=0.612m/s at each jet velocity

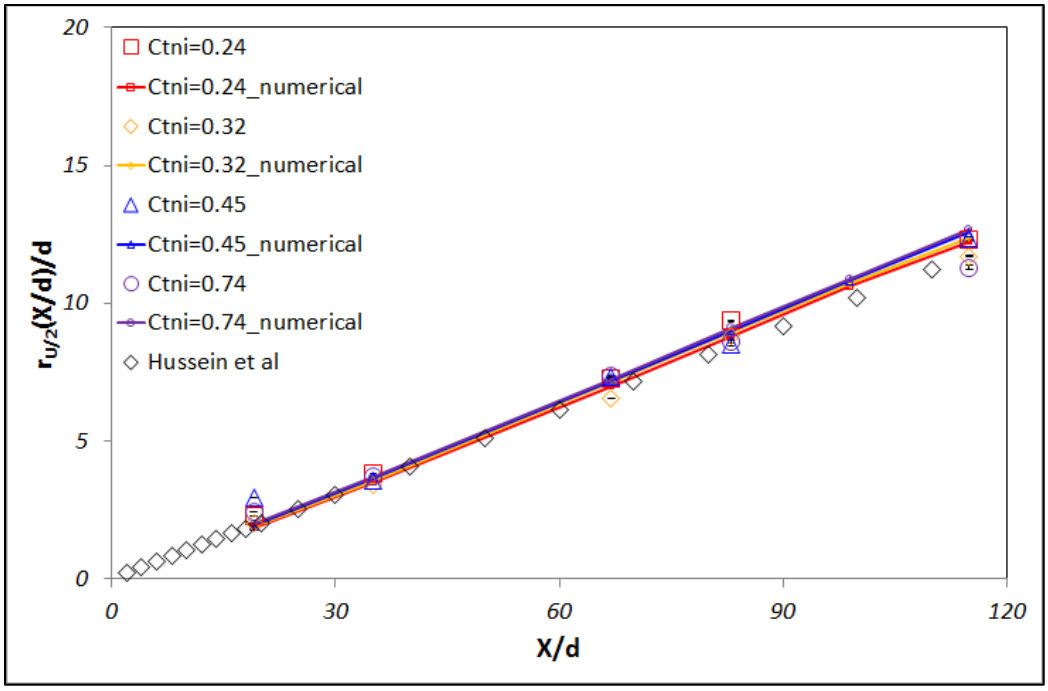

(b) U_{co}=0.913m/s at each jet velocity

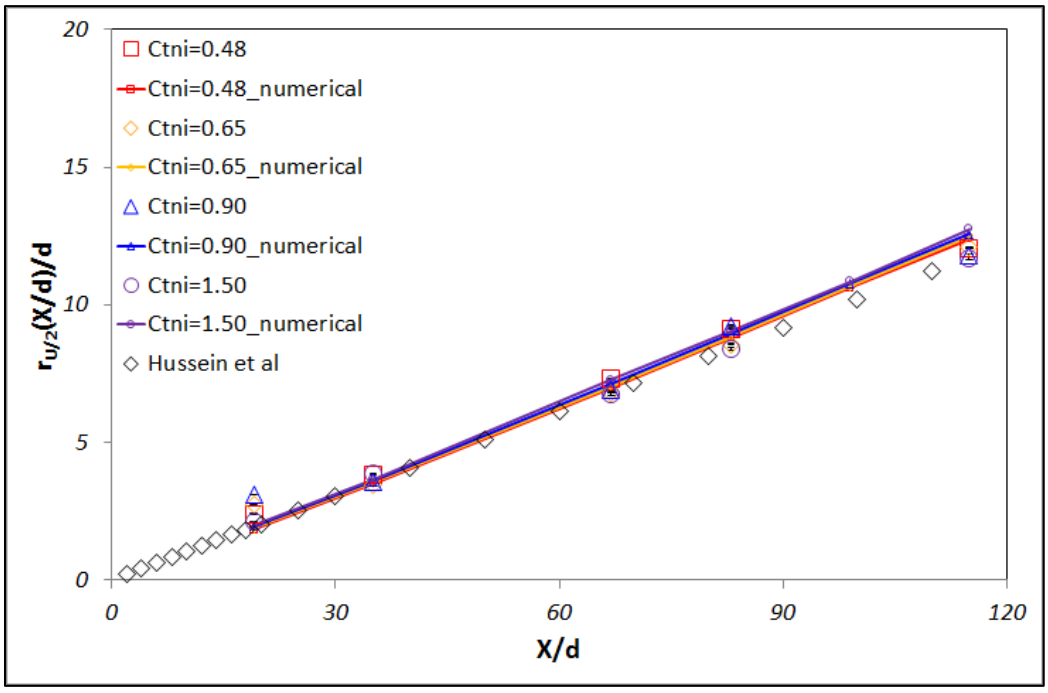

(c) U_{co}=1.856m/s at each jet velocity

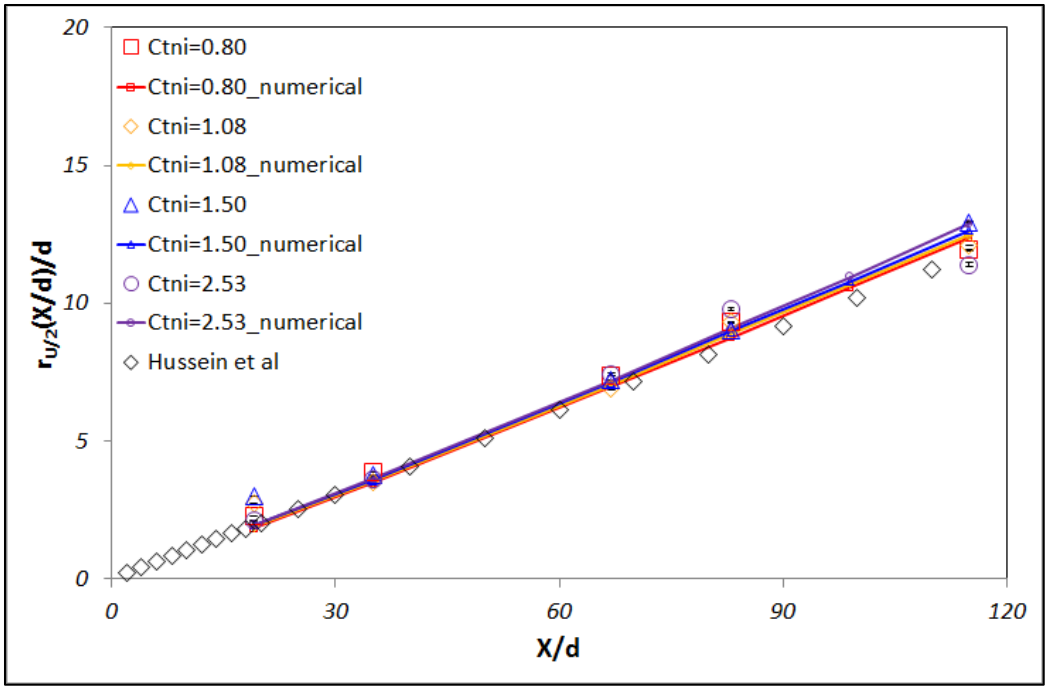

(d) U_{co}=3.123m/s at each jet velocity

Figure 3.14 The measured jet width at half jet velocity

From these finding, the jet width of the half jet velocity is less affected by the confinement. Also, there are very similar values of the jet width at the half jet velocity in spite of different conditions of the non-isothermal Craya-Curtet number.

Figure 3.15 and 3.16 show the concentration widths of the half value of initial ***NO*** concentration experimentally and numerically. The widths in figure 3.15 are derived at fixed jet velocity and different co-flow velocities. The widths of fixed co-flow velocity and different jet velocities are plotted in figure 3.16. The concentration width is increased as the jet flow moves the normalized axial direction (***X/d***) because of the interaction between the jet flow and the co-flow as well as the spreading of the jet. The normalized concentration width is almost similar below ***X/d*** =60 in spite of different Craya-Curtet numbers. However, the values of width are spread out after ***X/d***=60 at each different Craya-Curtet number. The experimental and numerical

results show that the widths at half ***NO*** concentration have usually much smaller value at high non-isothermal Craya-Curtet number. The momentum of the jet is much bigger than that of co-flow at small non-isothermal Craya-Curtet number. The jet is spread out more easily due to the excess momentum flux of the jet against the co-flow momentum. Also, the recirculation zone is getting smaller as non-isothermal Craya-Curtet number increases. Accordingly, the entrainment by recirculation of flow is smaller. The width of half concentration of ***NO*** is much bigger at small non-isothermal Craya-Curtet number (C_{tni}).

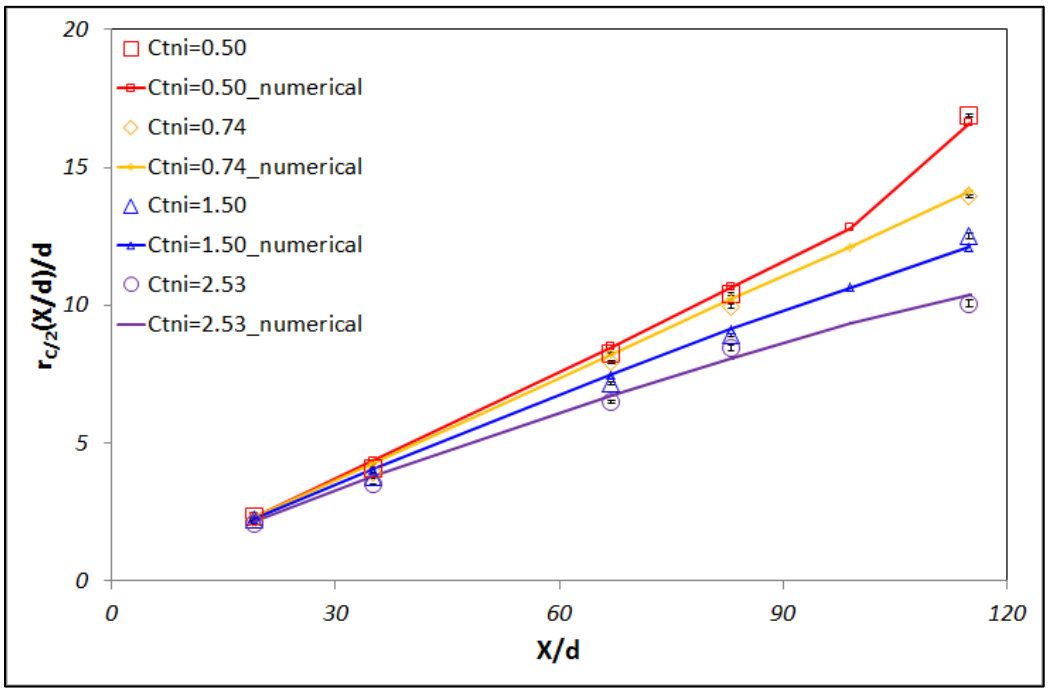

(a) U_{jet}=96.12m/s at each different co-flow

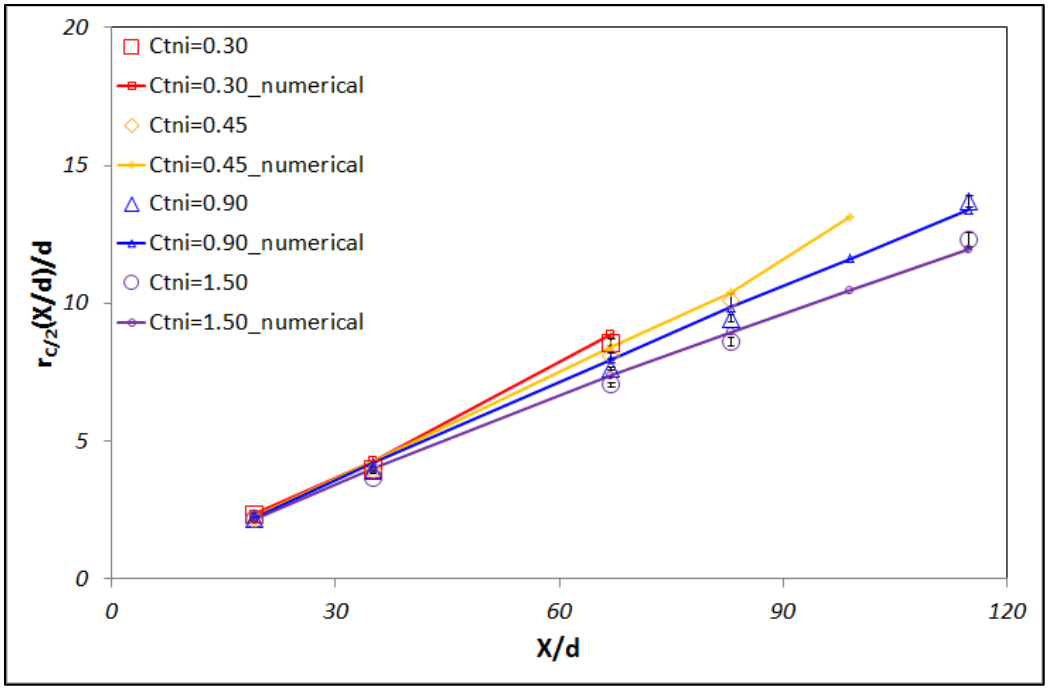

(b) U_{jet}=160.19m/s at each different co-flow

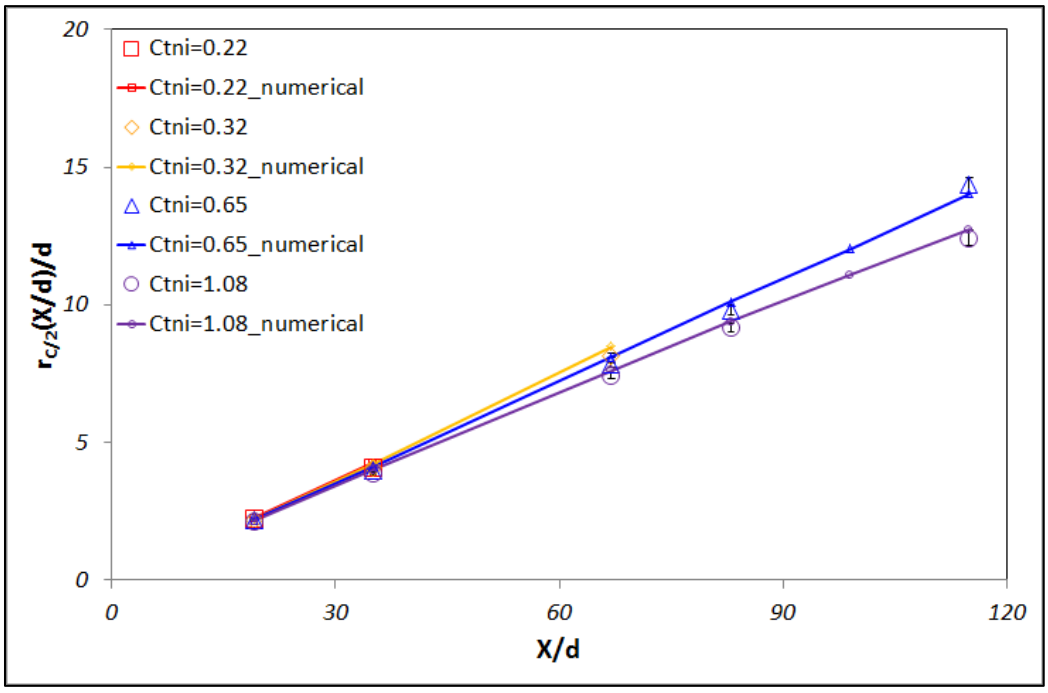

(c) U_{jet}=224.26m/s at each different co-flow

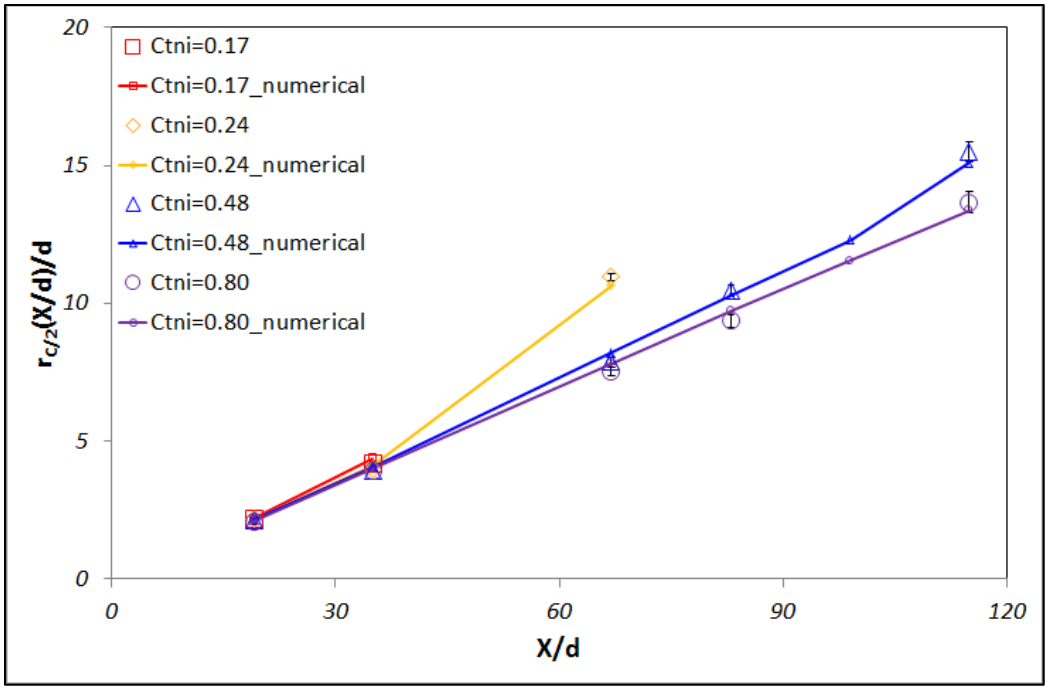

(d) U_{jet}=304.37m/s at each different co-flow

Figure 3.15 The measured concentration width at half concentration

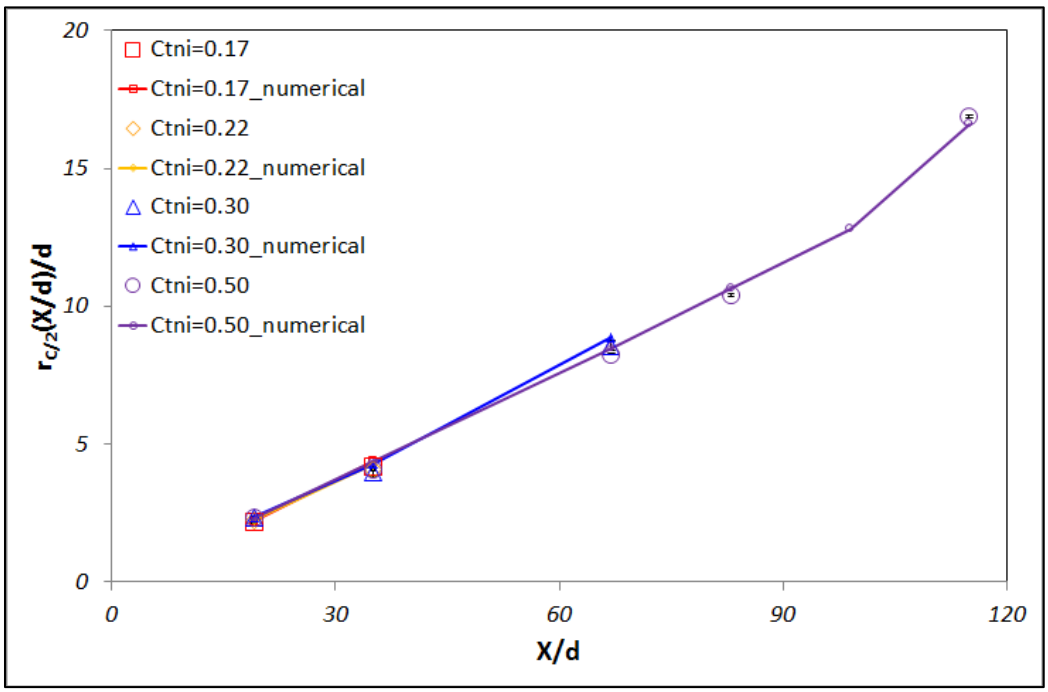

(a) U_{co}=0.612m/s at each different jet velocity

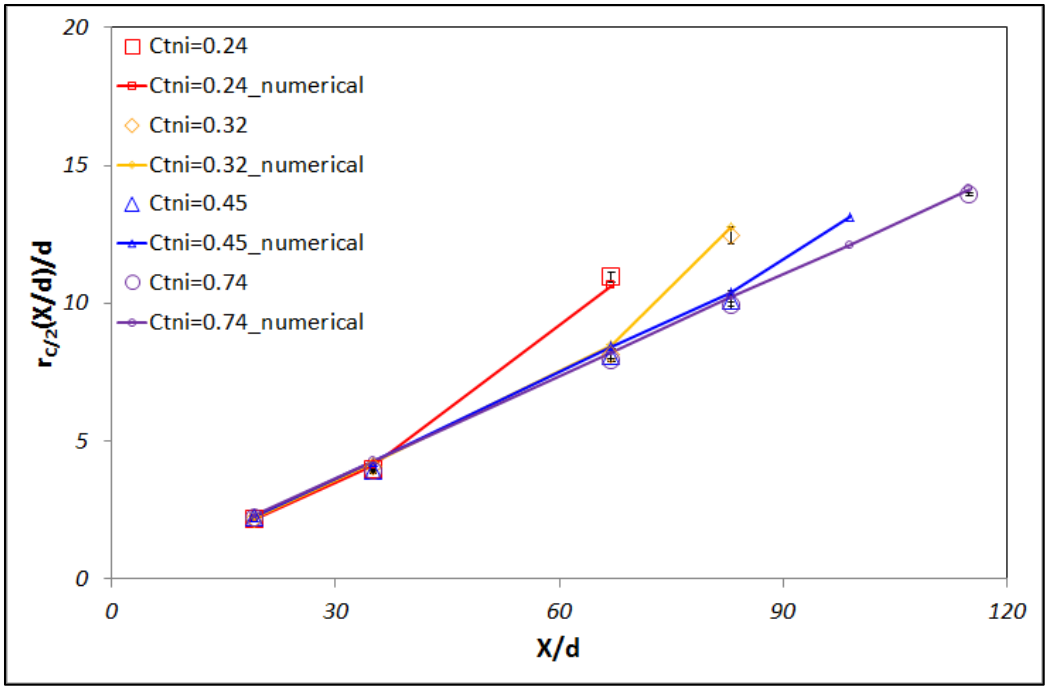

(b) U_{co}=0.913m/s at each different jet velocity

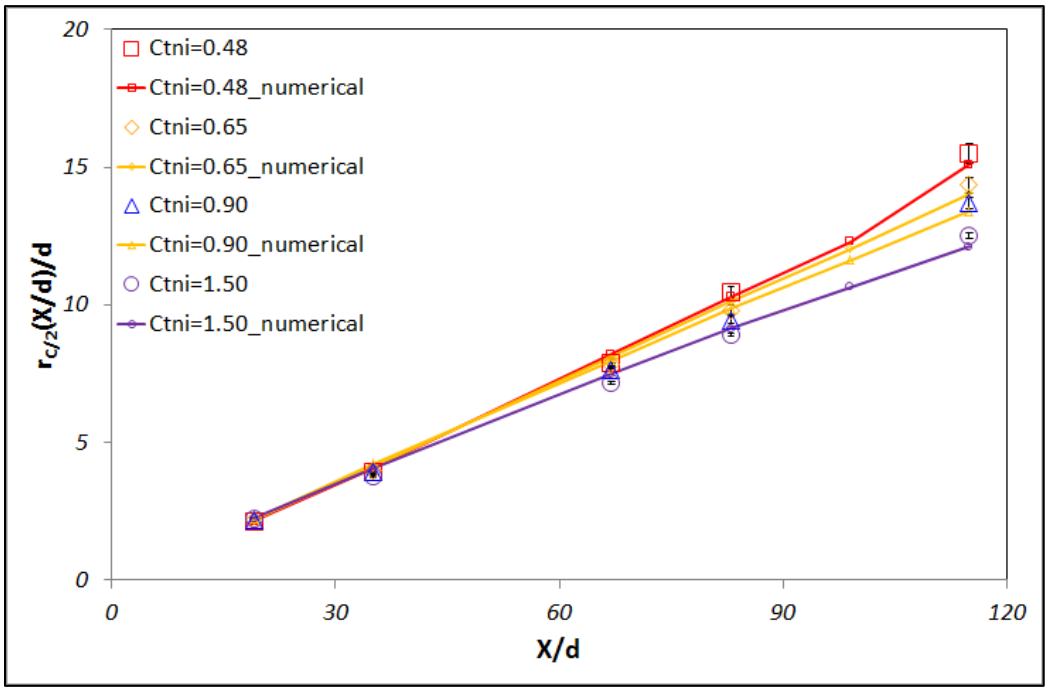

(c) U_{co}=1.856m/s at each different jet velocity

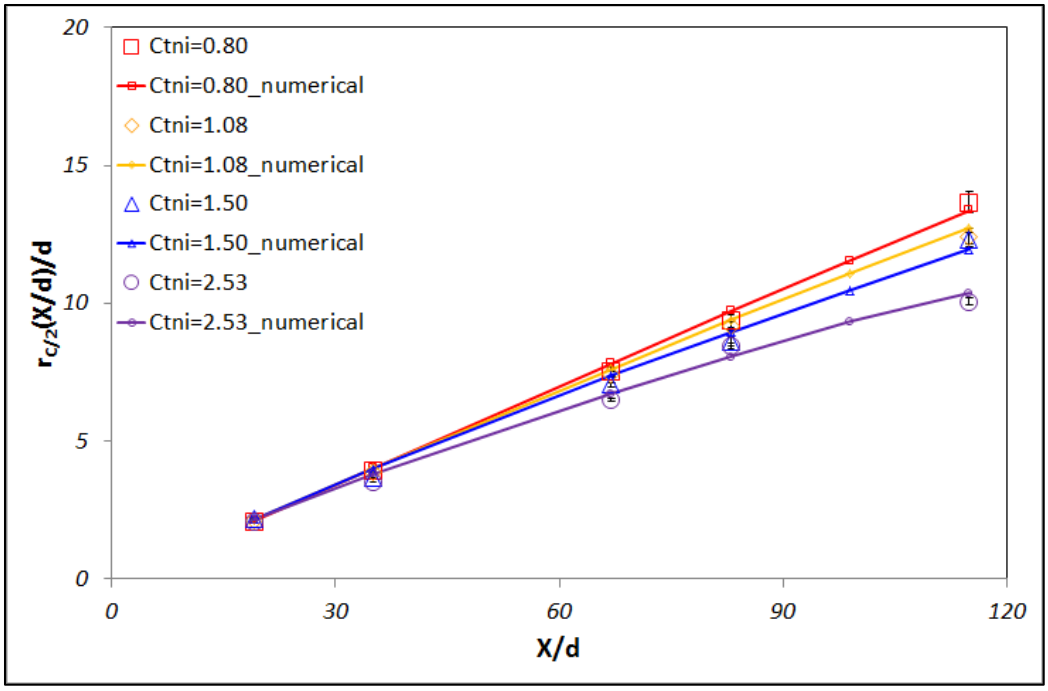

(d) U_{co}=3.123m/s at each different jet velocity

Figure 3.16 The measured concentration width of half concentration

To derive an equation of half concentration as the function of normalized distance ***X/d***, figure 3.17 is plotted at different C_{tni}. ***X/d*** is limited to 67 because the fluctuation and the uncertainty are increased as the flow moves along the axial direction due to the flow interaction by recirculation zone. Therefore, the equation of half concentration is derived as following,

$$r_{\frac{C}{2}} \Big/ d = 0.0858X/d + 0.7343 \tag{31}$$

The equation (31) is just valid below ***X/d***=67. It is hard to evaluate the width of half concentration by using just one empirical equation because of increasing flow fluctuation through the flow interaction as well as the existing recirculation zone by the confinement effect at far down stream location or high axial direction.

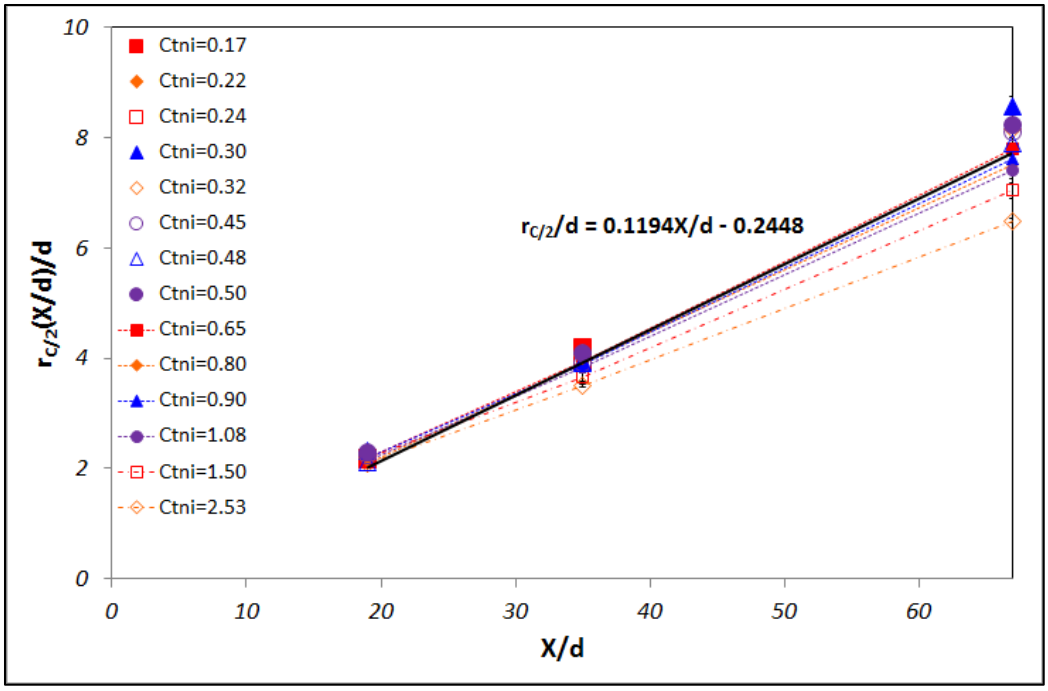

Figure 3.17 The measured concentration width of half concentration at each C_{tni}

3.1.7. The entrainment

The entrainment is studied by using the entrainment ratio as follow.

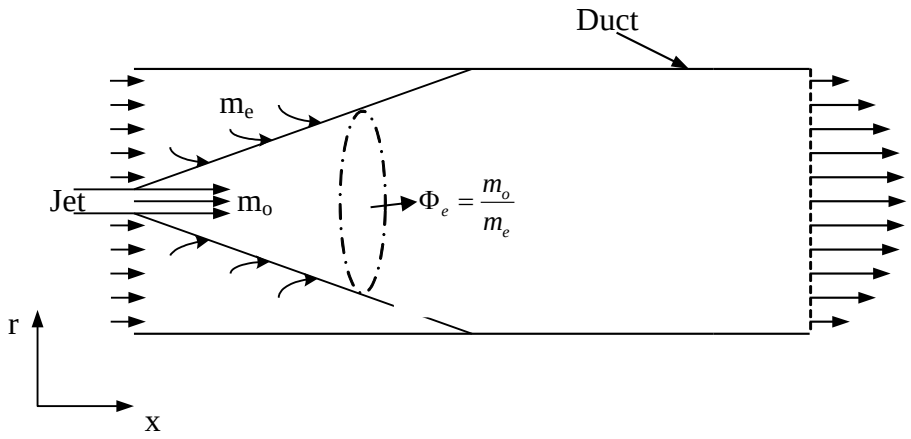

Figure 3.18 Flow configuration for the explanation of entrainment ratio (Φ)

$$\Phi_e = \frac{m_o}{m_e} \tag{32}$$

Where $\boldsymbol{m_o}$ is the initial mass coming from jet and $\boldsymbol{m_e}$ is the entrainment of mass at a certain position into a center area of the jet. The entrainment is studied by considering different co-flow velocities at fixed jet velocity. To calculate entrainment ratio, the initial mass from jet ($\boldsymbol{m_o}$) is normalized by using the entrainment mass ($\boldsymbol{m_e}$) at the different normalized location (***X/d***).

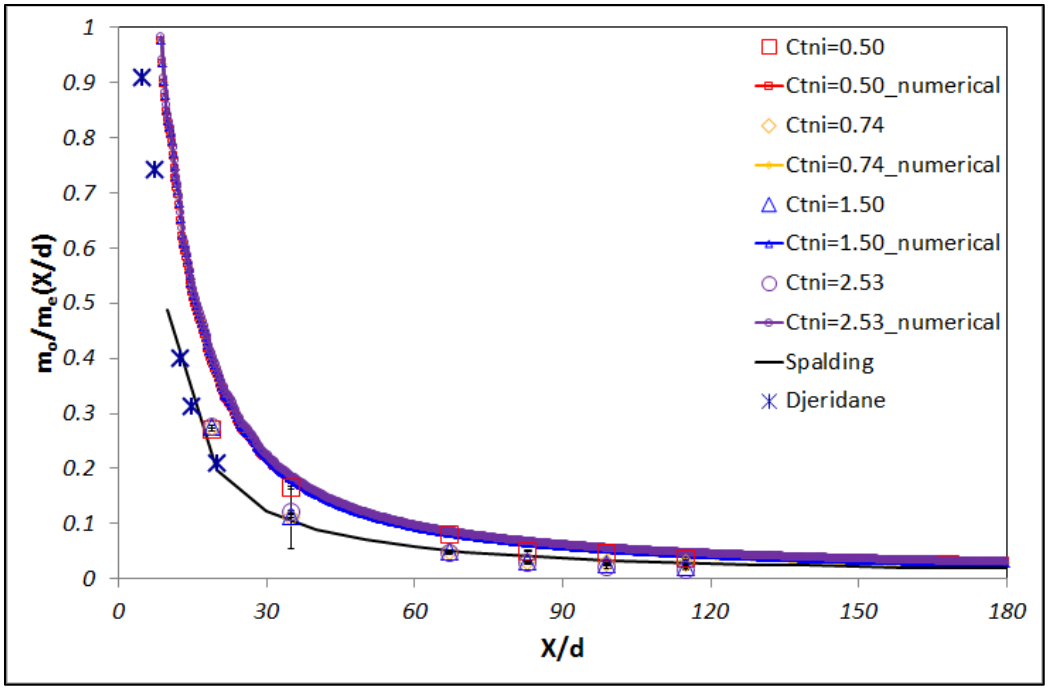

(a) U_{jet}=96.12m/s at each different co-flow

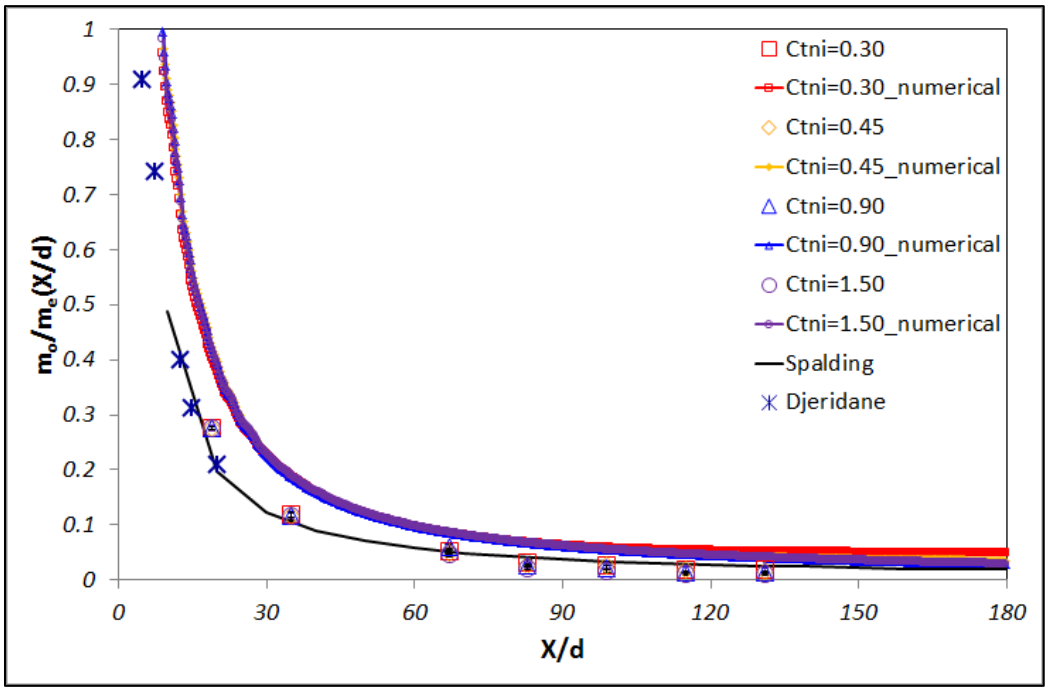

(b) U_{jet}=160.19m/s at each different co-flow

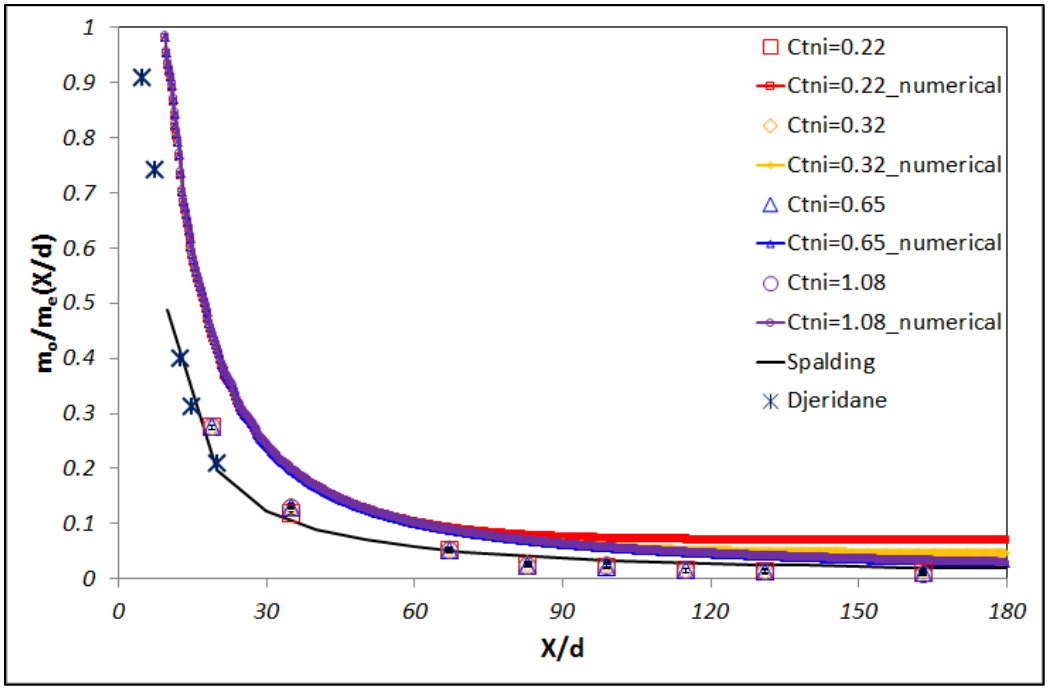

(c) U_{jet}=224.26m/s at each different co-flow

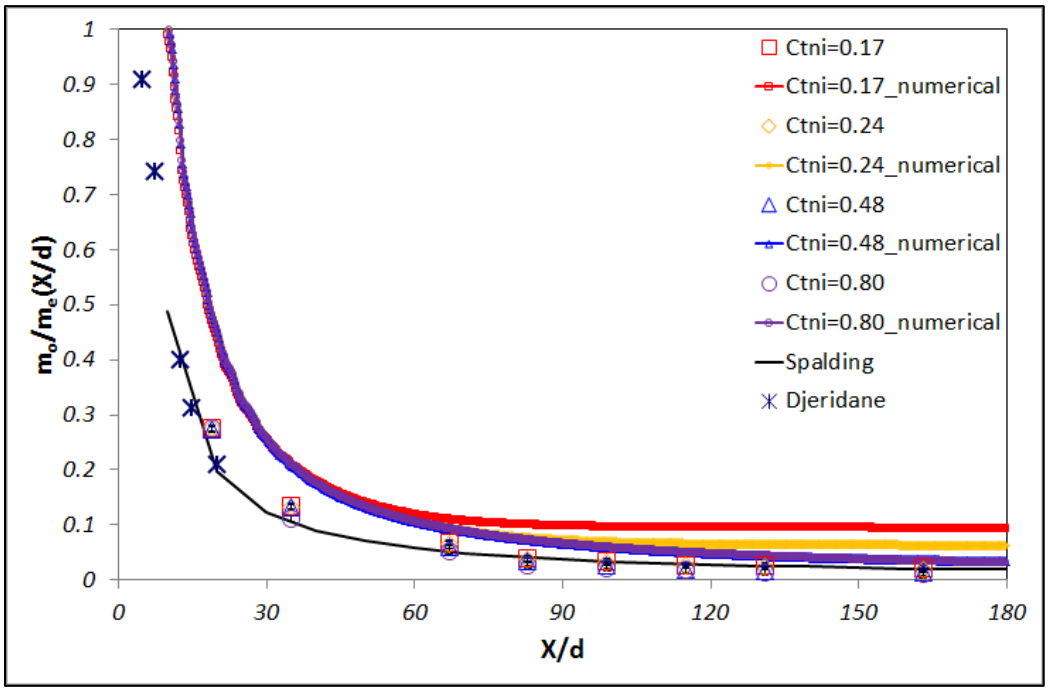

(d) U_{jet}=304.37m/s at each different co-flow

Figure 3.19 The measured entrainment at different co-flows

To show velocity conditions between the jet and the co-flow in figure 3.19 respectively, the non-isothermal Craya-Curtet number is used. Spalding's [55] data from the free turbulent jet and Djeridane' [57] results from the confined turbulent jet are plotted in each graph to describe the comparison between my results and previous results. Experimental results correspond well to Spalding's free stream results. Numerical results are little bit overestimated at all ranges of normalized axial location. The entrainment is generally increased as the jet flow with ***NO*** tracer gas moves along the axial direction due to the increment of entrained mass. The entrainment ratio has smaller values as the non-isothermal Craya-Curtet number increases because of enough entrainment of mass flow from the co-flow. There is enough hot air coming into the jet as the co-flow velocity. However, at low non-isothermal Craya-Curtet number, the value of entrainment ratio is converged to constant value. This means that the mixing is much faster as non-isothermal Craya-Curtet number is decreased due to forming bigger recirculation zone. Usually, the recirculation zone will cause more entrainment of volumetric hot flow going into the jet.

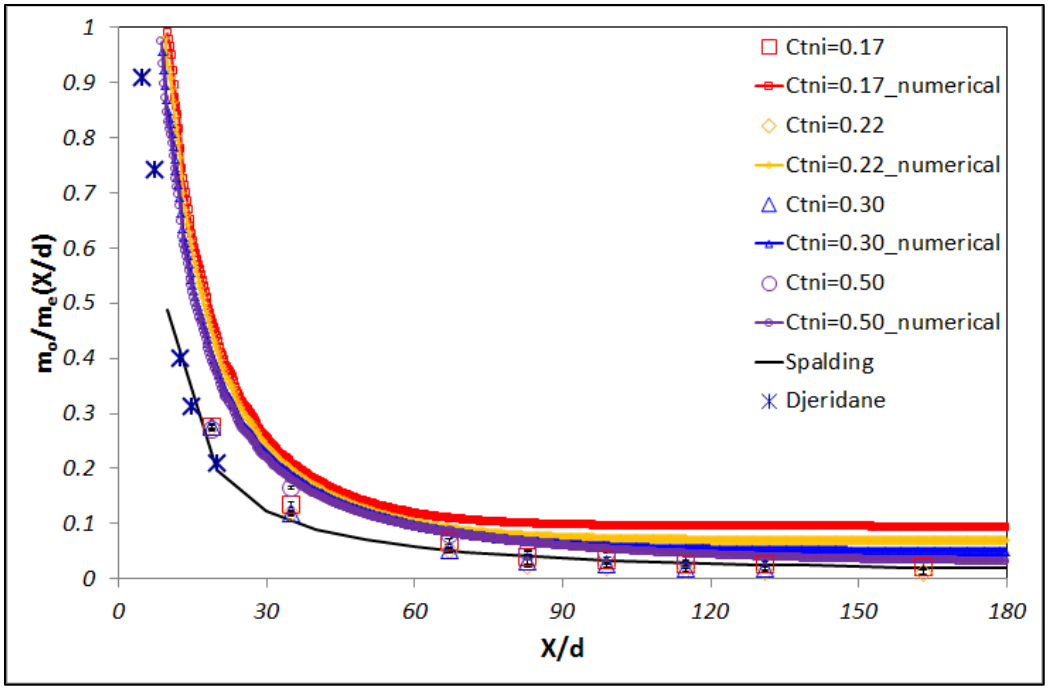

(a) U_{co}=0.612m/s at each different jet velocity

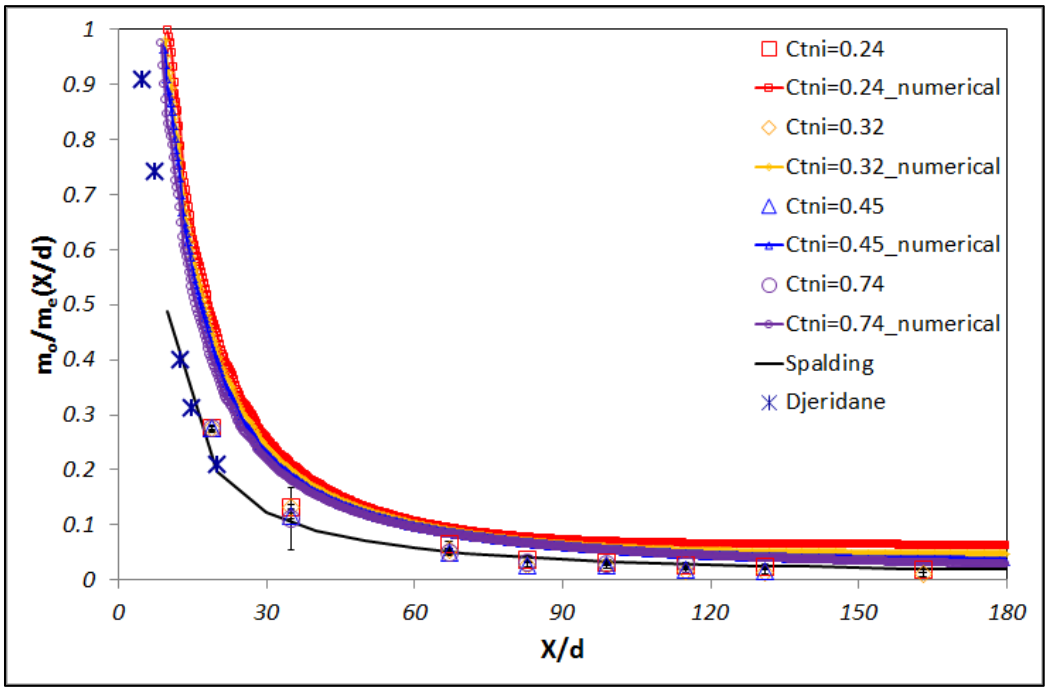

(b) U_{co}=0.913m/s at each different jet velocity

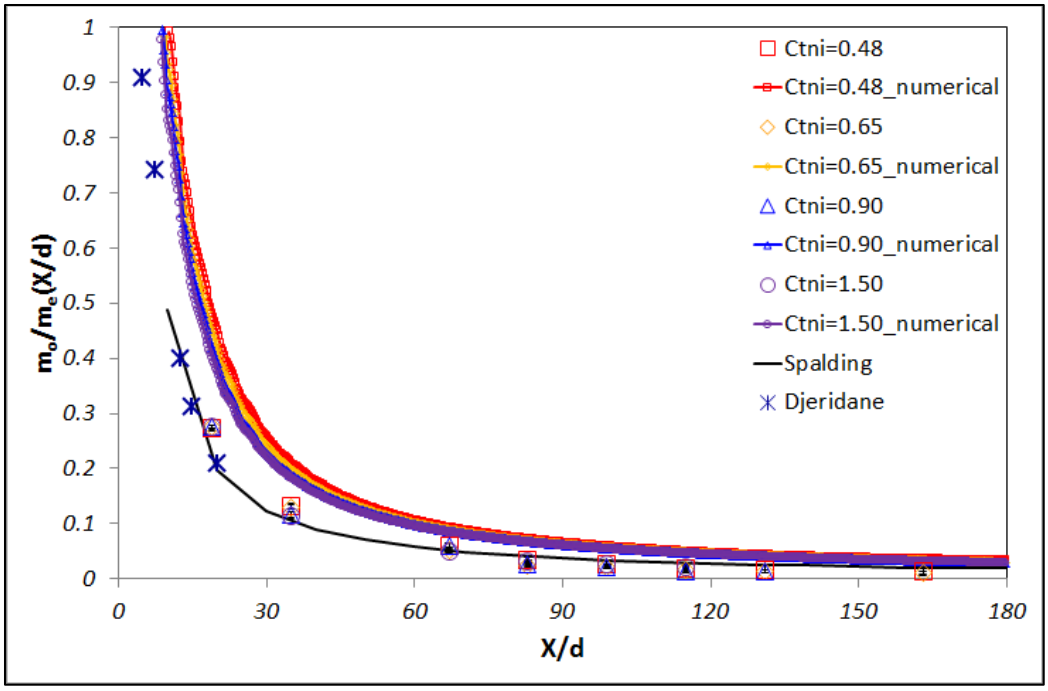

(c) U_{co}=1.856m/s at each different jet velocity

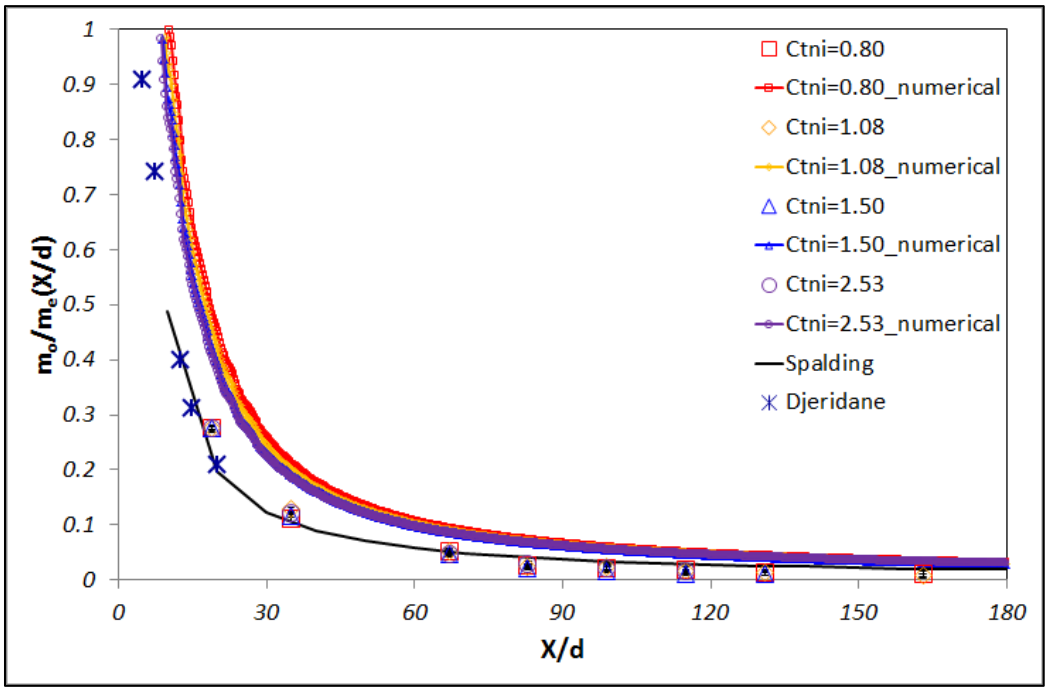

(d) U_{co}=3.123m/s at each different jet velocity

Figure 3.20 The measured entrainment at different jet velocities

The entrainment ratio has the function of ***X/d*** (***d***: the diameter of nozzle) at fixed co-flow and different jet velocities in figure 3.20. Spalding's [55] and Djeridane's [57] data are used to compare the difference. The comparison shows that my data and previous data are well corresponded at normalized axial location. The entrainment ratio is decreased along the normalized axial location as the jet flow moves downstream respectively. The entrainment ratio has the relatively constant value at the low non-isothermal Craya-Curtet number as the jet flow moves along the axial direction because of flow interaction by recirculation zone. The entrainment ratio is going much smaller as the non-isothermal Craya-Curtet number increases because of enough entrained mass by high co-flow velocity.

The analytical solution of entrainment ratio in the confined turbulent jet flow in co-flow is derived as the following in figure 3.21.

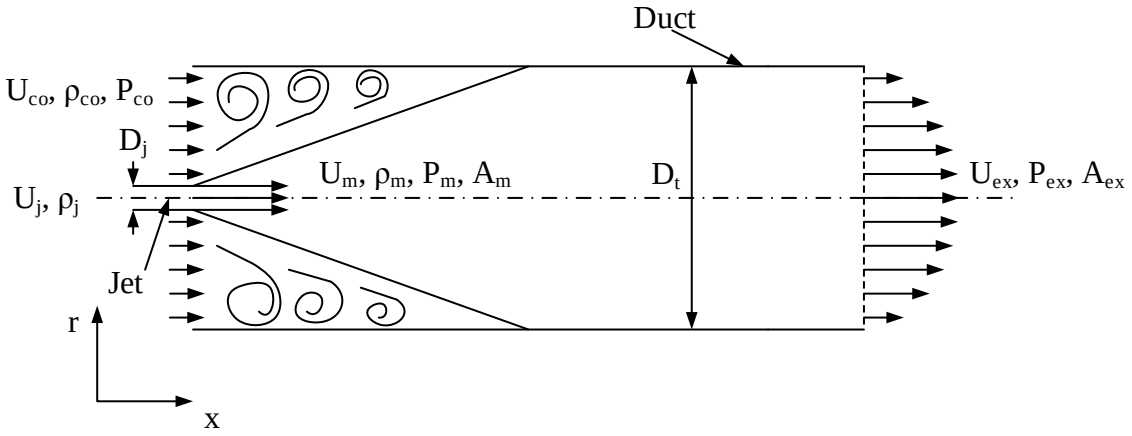

Figure 3.21 The derivation of analytical solution of entrainment ratio

$$\rho_m = \frac{\rho_j \dot{V}_j + \rho_{ex} \dot{V}_{ex}}{\dot{V}_j + \dot{V}_{ex}} = \frac{\rho_j \dot{V}_j + \rho_{co} \dot{V}_{ex}}{\dot{V}_j + \dot{V}_{ex}} = \frac{\dot{m}_j + \dot{m}_{ex}}{\dot{V}_j + \dot{V}_{ex}} \tag{33}$$

$$P_o A_m + \rho_{co} A_{co} U_{co}^2 + \rho_j A_j U_j^2 = P_m A_m + \rho_m A_m U_m^2 \tag{34}$$

From equation (33),

$$\dot{V}_{ex} = \frac{\rho_j \dot{V}_j - \rho_m \dot{V}_j}{\rho_m - \rho_{co}} \tag{35}$$

$$U_m = \frac{\dot{V}}{A_m} = \frac{\dot{V}_j + \dot{V}_{ex}}{A_m} \Rightarrow \frac{\dot{V}_{ex}}{\dot{V}_j} = \frac{U_m A_m}{U_j A_j} - 1 \tag{36}$$

Where $U_m = \frac{1}{A_m}\int_0^{r_m} U(r)dA$. As a result,

$$\frac{\dot{V}_{ex}}{\dot{V}_j} = \frac{1}{U_j A_j}\int_0^{r_m} U(r)dA - 1 \tag{37}$$

From equation (33),

$$\frac{\dot{m}_j}{\dot{m}_{ex}} = \frac{1}{\frac{\rho_m}{\rho_j}(1 + \frac{\dot{V}_{ex}}{\dot{V}_j}) - 1} \tag{38}$$

Also,

$$\frac{\rho_m}{\rho_j} = \frac{\left(1 + \frac{\rho_{co}\dot{V}_{ex}}{\rho_j \dot{V}_j}\right)}{\left(1 + \frac{\dot{V}_{ex}}{\dot{V}_j}\right)} \tag{39}$$

Insert equation (39) into equation (38),

$$\frac{\dot{m}_j}{\dot{m}_{ex}} = \frac{\rho_j \dot{V}_j}{\rho_{co}\dot{V}_{ex}} \tag{40}$$

Add equation (37) to equation (40),

$$\frac{\dot{m}_j}{\dot{m}_{ex}} = \frac{\rho_j A_j U_j}{\rho_{co}\left(\int_0^{r_m} U(r)dA - U_j A_j\right)} \tag{41}$$

The velocity equation is derived in equation (28). Inserting equation (28) into equation (41) and integrating it gives the final analytical solution of entrainment ratio as shown in equation (42).

$$\frac{\dot{m}_j}{\dot{m}_{ex}} = \frac{\rho_j A_j U_j}{\rho_{co}\left(\frac{2\pi r_{U/2}^2 U_c}{\ln 2.13}\left(1 - e^{-\ln 2.13\left(r_m / r_{U/2}\right)}\right) - U_j A_j\right)} \tag{42}$$

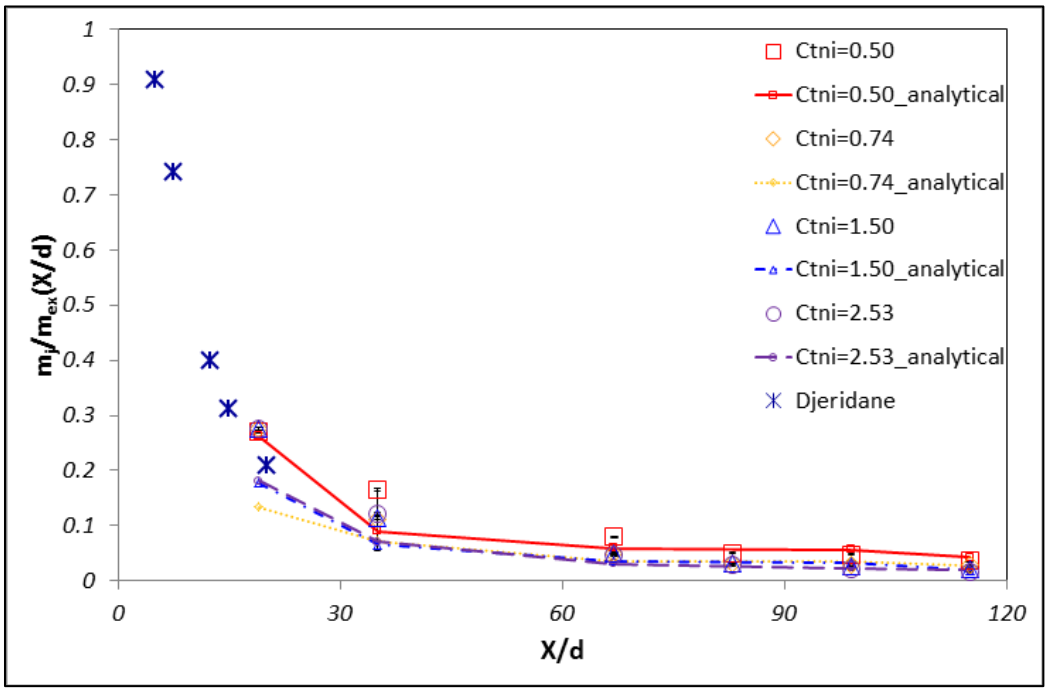

Figure 3.22 The verification of analytical solution of entrainment ratio

Equation 42 is plotted in order to compare experimental results at ***M***=0.3. Figure 3.22 shows that the analytical solution of entrainment ratio corresponds reasonably to measured entrainment ratio including the results of Djeridane [57]. The analytical solution of entrainment ratio is verified.

3.1.8. Streamline

The computed velocity streamline (***FLUENT***) is plotted at different non-isothermal Craya-Curtet number in figure 3.23 As non-isothermal Craya-Curtet number is decreased, the excess jet momentum is also increased. The jet momentum still remains after interacting by the co-flow jet and the walls of the duct. The residue of jet momentum causes the formation of recirculation zone in the duct. The recirculation zone is going smaller as non-isothermal Craya-Curtet number is increased due to the reduction of excess jet momentum. The recirculation zone is extremely bigger at C_{tni}=0.17. Also, the recirculation zone is hard to be identified above C_{tni}=1.08

(a) C_{tni}=0.17

(b) C_{tni}=0.50

(c) C_{tni}=0.74

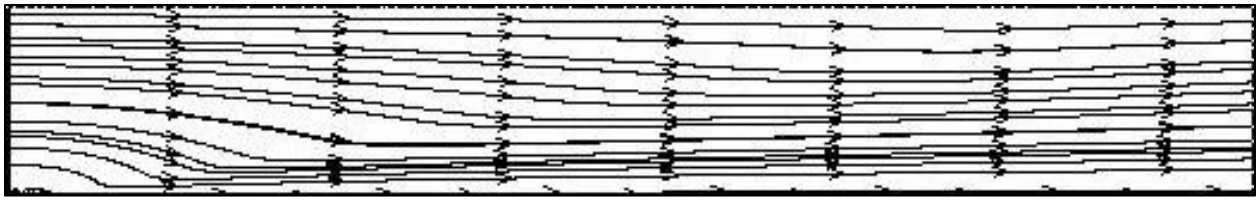

(d) C_{tni}=1.08

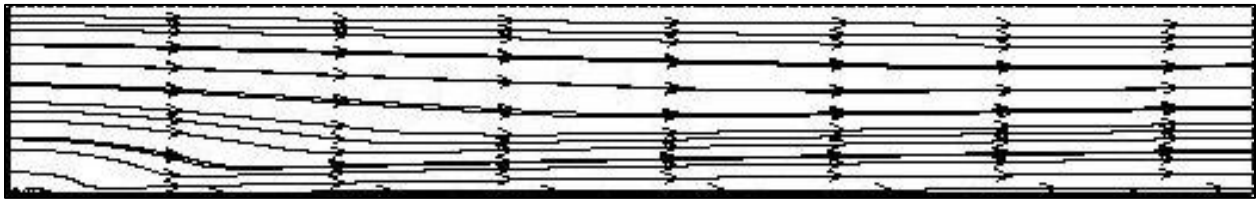

(e) C_{tni}=1.50

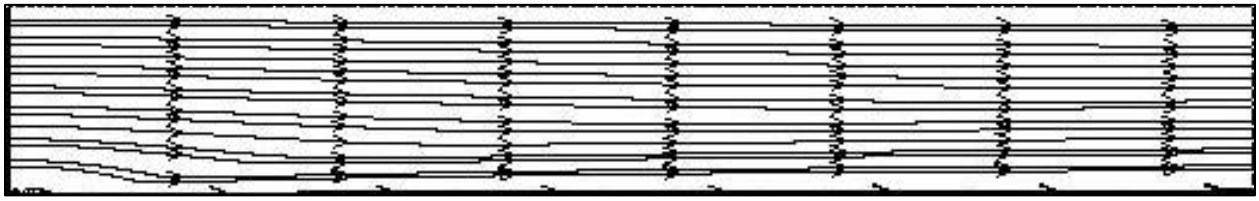

(f) C_{tni}=2.53

Figure 3.23 The computed velocity streamline at different non-isothermal Craya-Curtet number

3.1.9. Correlation between C_{tni} and recirculation zone

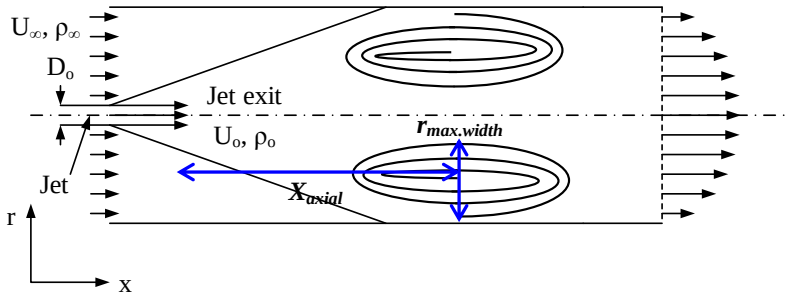

Figure 3.24 The schematic of location and width of recirculation zone

To study the correlation between C_{tni} and the characteristics of recirculation zone in detail, the location and width of recirculation zone are investigated as a function of C_{tni}. The location and width of recirculation zone are defined in figure 3.24.

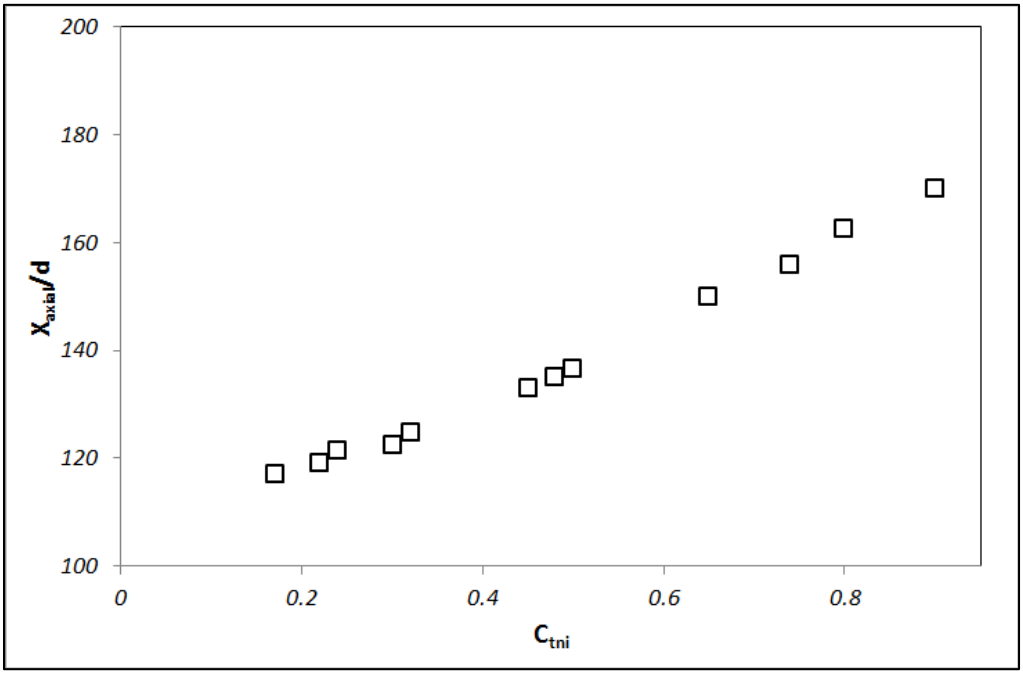

(a) Location of recirculation zone

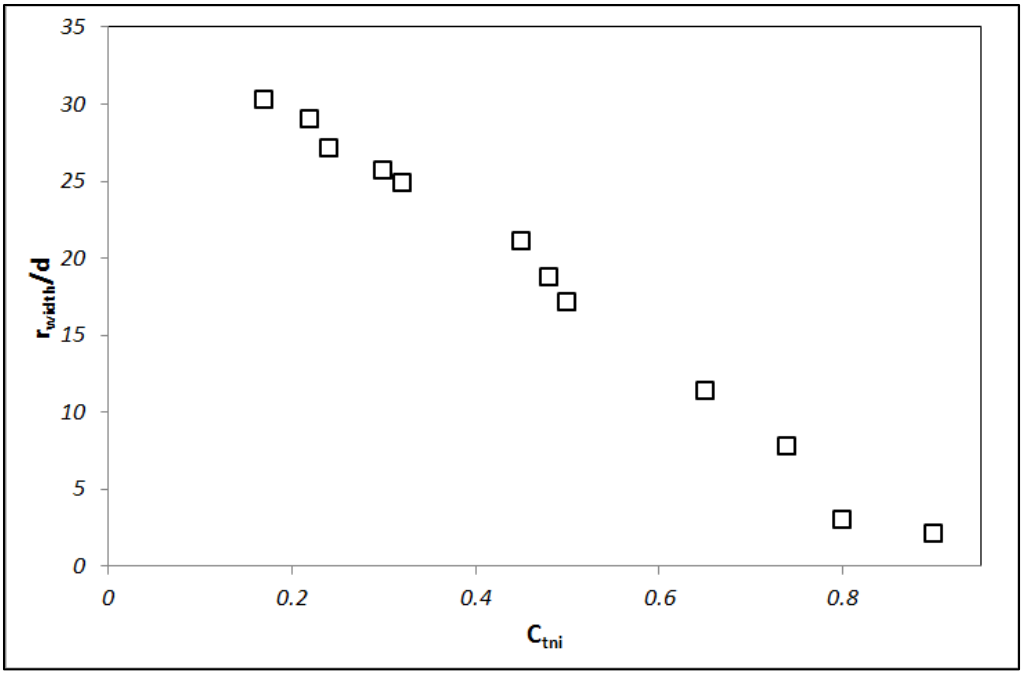

(b) Width of recirculation zone

Figure 3.25 The location and width of recirculation zone as the function of C_{tni}

There is no recirculation zone after C_{tni}=0.90 in figure 3.25. As a result, C_{tni}=0.90 is able to be considered as the critical non-isothermal Craya-Curtet number in these test conditions. The location of recirculation zone moves the downstream and the width of recirculation zone is getting smaller as C_{tni} is increased because the excess jet momentum is decreased by increasing co-flow. The recirculation zone does not exist in the confined duct beyond the critical non-isothermal Craya-Curtet number. This is very important phenomena to explain mixing in confined condition because the recirculation zone has dominant effect on the mixing more so than velocity characteristics in confined turbulent jet flow in the current study.

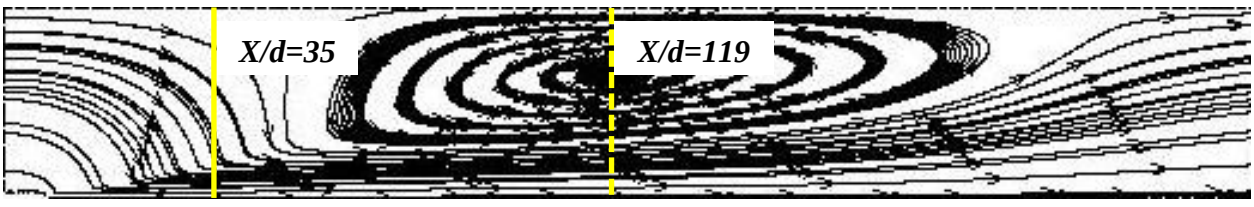

(a) Velocity streamline

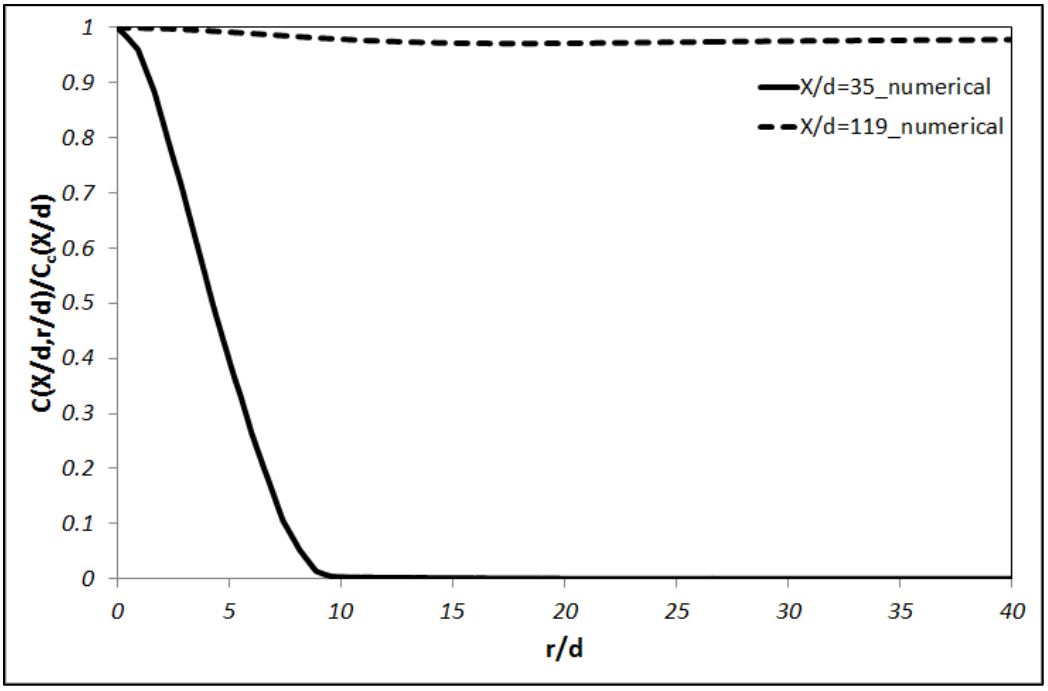

(b) Normalized concentration distribution

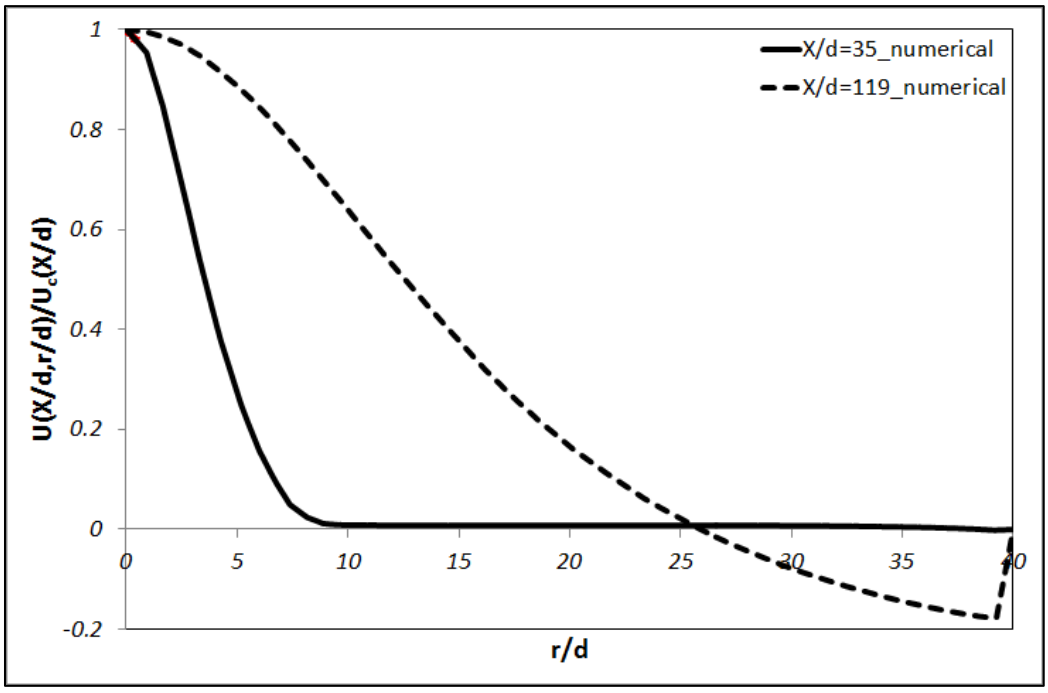

(c) Normalized velocity distribution

Figure 3.26 The role of recirculation zone in confined turbulent jet flow

To validate the role of recirculation zone in confined turbulent jet flow, the numerical calculation is progressed at the velocity condition of C_{tni}=0.22. The characteristics of velocity and concentration has the Gaussian distribution at ***X/d***=35 because of less confinement effect in figure 3.26. Therefore, the flow and mixing characteristics of confined turbulent jet do not differ from free turbulent jet flow at this location. However, as the jet flow moves along the axial direction, the confinement effect such as the recirculation zone has significant effect on flow and mixing characteristics of confined turbulent jet flow. From figure 3.26, after ***X/d***=119, the recirculation zone has dominant effect on the flow and mixing characteristics. The negative velocity near the wall by recirculation zone enhances the mixing. Therefore, after center location of recirculation zone (***X/d***=119), the ***NO*** concentration has very flat and uniform profile along the radial direction. As a result, it considers that the mixing of confined turbulent jet flow into co-flow is fully finished after center location of recirculation zone.

3.1.10. The effect of high co-flow temperature

To find the effect of high temperature of co-flow (1200K) on the characteristics of recirculation zone, two conditions such as constant velocity of co-flow and constant mass of co-flow were selected and calculated numerically. U_{jet}=160.19m/s and U_{co}=1.856m/s is considered as reference values. Therefore, three different non-isothermal Craya-Curtet numbers are found. C_{tni}=0.90 at T_{co}=328.15K (U_{jet}=160.19m/s and U_{co}=1.856m/s), C_{tni}=0.27 at T_{co}=1200K (constant co-flow velocity) and C_{tni}=0.95 at T_{co}=1200K (constant co-flow mass). From figure 36, the location of recirculation zone at high co-flow temperature does correspond well to previous results at T_{co}=328.15K. Therefore, the relation for the location of the recirculation zone and non-isothermal Craya-Curtet numbers is seen as reasonable for the non-isothermal co-flow situation.

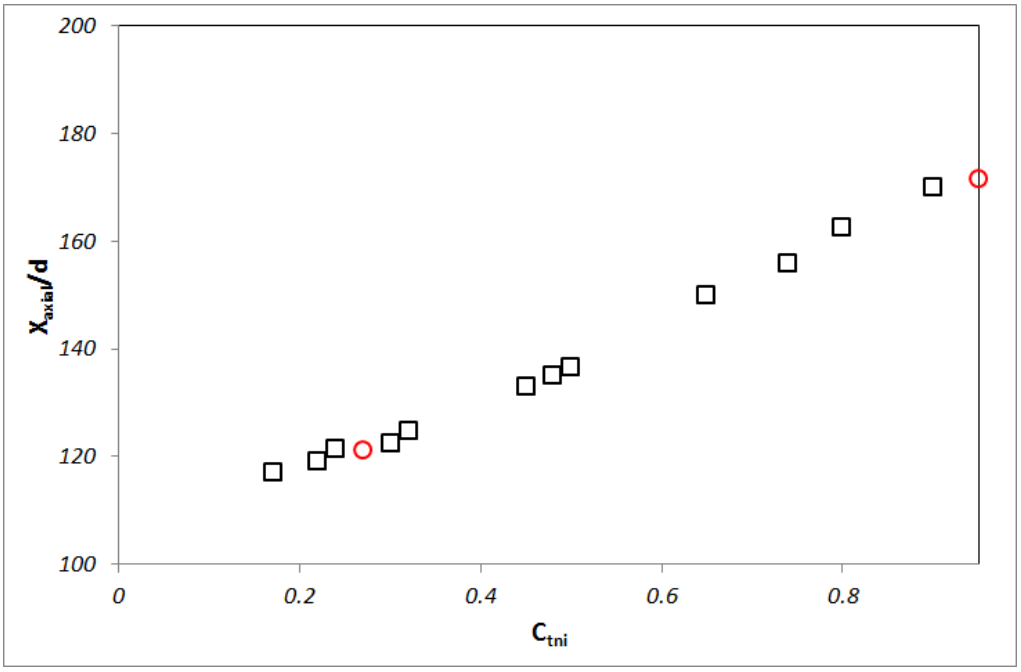

(a) Location of recirculation zone

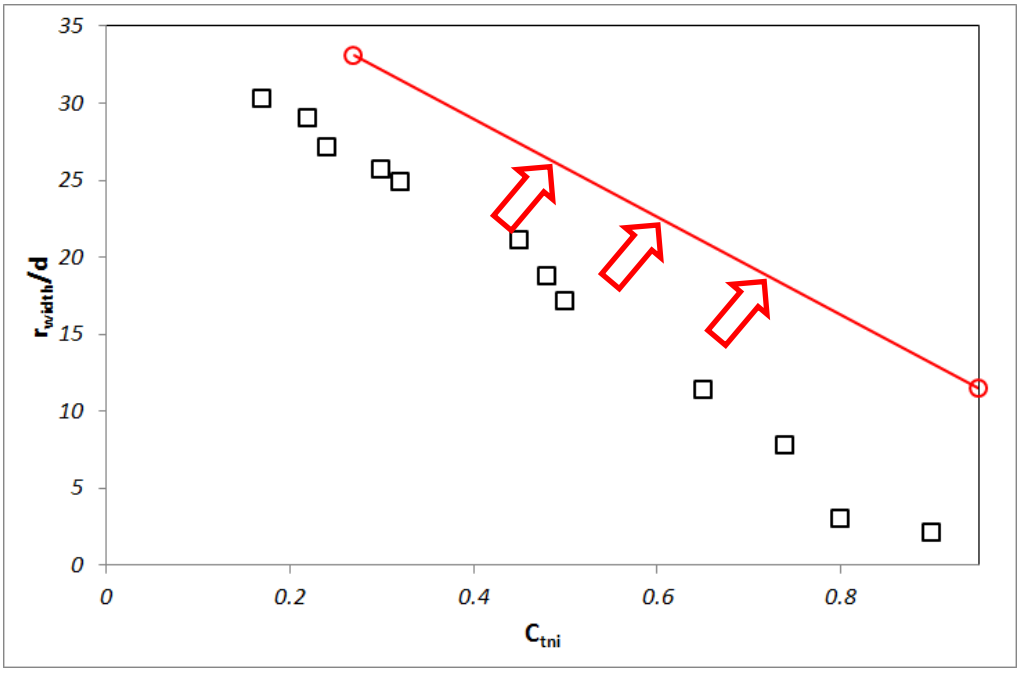

(b) Width of recirculation zone

Figure 3.27 The high temperature effect on location and width of recirculation zone (r_{width})

The critical non-isothermal Craya-Curtet number (T_{co}=328.15K) is found at $C_{cri,tni}$=0.90. However, at high temperature of co-flow (1200K), the recirculation zone still exist above $C_{cri,tni}$=0.90. Therefore, C_{tni}=0.90 is no longer the critical non-isothermal Craya-Curtet number at this condition. As a result, the width of recirculation zone is increased more at high co-flow temperature (1200K) through comparing the result at T_{co}=328.15K due to the buoyancy effect. A nearly constant increment of width of recirculation zone is found. Therefore, the result of width of recirculation zone at T_{co}=328.15K is predicted reasonably well by the high co-flow temperature condition through considering a constant increment of width of the recirculation zone. Finally, the location of recirculation zone is usually determined by momentum ratio. The buoyancy by different temperature has a more dominant effect on width of recirculation zone (r_{width}).

3.1.11. Conclusion

Experimental investigations were performed on the flow and the mixing characteristics through studying the resulting velocity, temperature, ***NO*** concentration fields as well as the entrainment ratio in the confined turbulent jets in terms of the non-isothermal Craya-Curtet number.

The experimental (current work and previous results such as C.J Chen [53] from free turbulent jet and Singh et al. [54] from confined turbulent jet) and numerical results correspond reasonably well to one another in the axial direction. Current data is measured and calculated at further downstream locations ***X/d*** up to 130 whereas previous investigations of confined turbulent jet into co-flow were limited to ***X/d*** up to 60. The numerical results under-predict the velocity decay compared to the experimental results. The centerline velocity decays a little further downstream. The centerline velocity decreases slowly at high non-isothermal Craya-Curtet number because of less confinement effect by recirculation zone. Experimental and numerical results find that the different slope of velocity decay is found after ***X/d*** (***X***: axial direction, ***d***: jet nozzle diameter) = 60 approximately. The normalized centerline velocity has an inversely linear relation to the normalized location (***X/d***). Therefore, the decay of axial velocity along the centerline agrees well with the equations of free turbulent jet. However, when inversely normalized mean excess centerline velocity is considered at low non-isothermal Craya-Curtet number, the recirculation zone has some effects on the flow characteristics such as velocity. Therefore, the estimated equation of velocity from free turbulent jet flow is not acceptable. The computed and the measured radial distributions of velocity at different velocity conditions collapse fairly well on a Gaussian function except near the outer edge ($r/r_{U/2}>1$). However, further downstream the velocity distribution is no longer a Gaussian distribution. The measured

jet widths at half jet velocity are increased as the jet flow moves along the normalized axial direction (***X/d***) because of the characteristics of spreading of the jet by interacting co-flow. The measured widths at half jet velocity correspond well by comparison with the results from free boundary condition.

The study of concentration shows that experiment and numerical results are in agreement. Current data and previous results (Steward's [15] and Spalding's [55] data from free turbulent jets) coincide well along the axial direction. The profile of ***NO*** concentration along the centerline decays and spread as the jet flow moves along the axial direction respectively. The concentration has relatively constant value at low non-isothermal Craya-Curtet number because of the recirculation zone and flow interaction. Therefore, the concentration distribution is influenced significantly by confinement effects. The results show that the value of centerline ***NO*** concentration is decreased as the non-isothermal Craya-Curtet number increases because of enough entrainment of hot co-flow. Also, the measured and calculated normalized concentration has a different slope of the decay of concentration around ***X/d*** >60 due to limited entrainment by confined condition. The calculated and the measured radial concentration profiles at different velocity conditions predict very well a Gaussian function except near the outer edge ($r/r_{c/2}$>1). However, concentration distribution is not Gaussian distribution any longer at further downstream locations. The measured concentration widths at half value of initial ***NO*** concentration are increased as the flow moves along the axial direction because of the interaction between the jet flow and the co-flow as well as the spread of the jet. The measured widths at half ***NO*** concentration have usually much smaller value as the non-isothermal Craya-Curtet number increases.

The center temperature is increased at high normalized axial direction because of sufficient entrained mass of hot co-flow into the center jet. The temperature along the centerline is converged to the single value at large axial location through seeing flat and stable temperature profiles around $\boldsymbol{X/d}$=60. The value of normalized centerline temperature profiles is increased as the non-isothermal Craya-Curtet number increases because of high co-flow velocity in order to make the high non-isothermal Craya-Curtet number. Also, as the jet flow moves along the axial direction, the normalized temperature profiles along the radial direction are more uniform at low non-isothermal Craya-Curtet number. Therefore, we can make the conclusion that the uniform temperature is achieved much sooner at low non-isothermal Craya-Curtet number ($\boldsymbol{C_{tni}}$) because of thermal mixing by the recirculation zone.

The entrainment ratio is studied for verifying the mixing characteristics between the jet and the co-flow. The entrainment of mass into jet is increased as the jet flow moves along the axial direction due to the increment of entrant mass. Experimental results are well matched by Spalding's results from free turbulent jet flow. Numerical results are relatively overestimated at whole normalized axial location. The entrainment ratio is decreasing at higher non-isothermal Craya-Curtet numbers due to sufficient entrained mass flow from the co-flow. However, the value of entrainment ratio converges to a constant value at low non-isothermal Craya-Curtet number by the bigger recirculation zone. The entrainment ratio is decreased faster at the high non-isothermal Craya-Curtet number below each critical non-isothermal Craya-Curtet number ($\boldsymbol{C_{c,tni}}$). Also, the analytical solution of entrainment ratio is verified through comparing measured entrainment ratio.

The study of the role of streamline in confined turbulent jet into co-flow is assessed. As non-isothermal Craya-Curtet number is increased, the size of recirculation zone is reduced due to

the reduction of excess jet momentum. From these analysis, the C_{tni}=0.90 is considered as the critical non-isothermal Craya-Curtet number. The location and width of recirculation zone moves the downstream and is smaller respectively as non-isothermal Craya-Curtet number is increased. Also, after center location of recirculation zone, the concentration has uniform profile along the radial direction. Therefore, the mixing of confined turbulent jet flow into co-flow is fully finished after center location of recirculation zone.

Finally, the study of confined turbulent jet into co-flow at high co-flow temperature is investigated. C_{tni}=0.90 is no longer the critical non-isothermal Craya-Curtet number at high co-flow condition because the recirculation zone still exist for values of C_{tni} greater than 0.90. Therefore, the increased width of recirculation zone is found. From these results, the location of recirculation zone is generally determined by momentum ratio and the width of recirculation zone is influenced significantly by the buoyancy.

3.2. Experimental and numerical results of a confined non-reacting turbulent jet in counter-flow

The experimental results of the distribution of the velocity, the concentration, the temperature and the entrainment in the confined turbulent jet in counter-flow will be shown in this section. Following Dimotakis [52], the high jet Reynolds number above 10^4 is used to create fully developed turbulence condition. The experimental study of the flow and mixing characteristics of the confined turbulent jet in counter-flow is investigated through showing the distribution of the velocity, the concentration, the temperature, the width and the entrainment. The flow sketch of the confined turbulent jet in counter-flow is shown in figure 3.28.

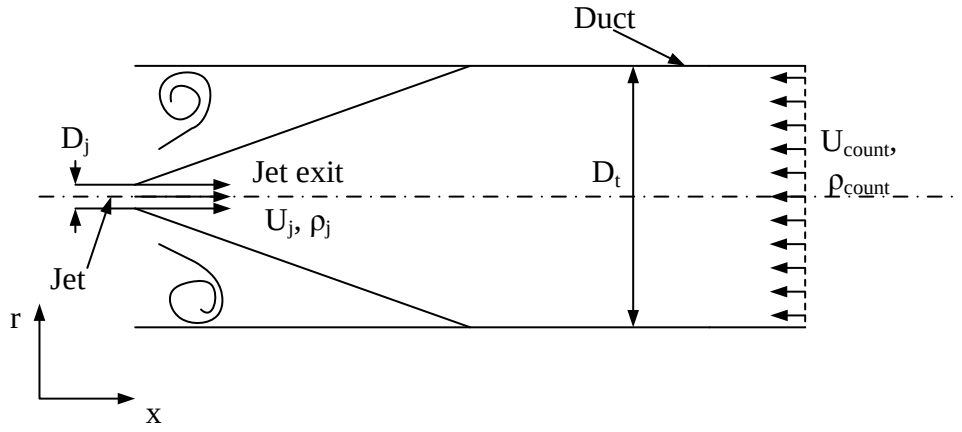

Figure 3.28 Flow sketch of confined turbulent jet in counter-flow

For this study, the modified momentum ratio between the jet velocity and the counter-flow velocity is chosen as follows:

$$M_{sqrt} = \sqrt{\frac{\dot{m}_j U_j}{\dot{m}_{count} U_{count}}} = \sqrt{\frac{\rho_j A_j U_j^2}{\rho_{count} A_{count} U_{count}^2}} \tag{43}$$

The test conditions in this study are listed in table 3.2. For identification of the concentration of the central jet, the ***NO*** tracer gas in the turbulent jet is used to investigate concentration distribution of the jet.

Jet velocity(m/s)	Counterflow velocity(m/s)	M_{sqrt}
96.12	0.612	2.06
	0.913	1.38
	1.856	0.68
	3.123	0.40
160.19	0.612	3.43
	0.913	2.30
	1.856	1.13
	3.123	0.67
224.26	0.913	3.22
	1.856	1.58
	3.123	0.94
304.37	1.856	2.15
	3.123	1.28

Table 3.2. The experiment and numerical conditions of counter-flow

3.2.1. The velocity distribution

In this section, the study of the velocity distribution is shown along the axial and the radial directions. The velocity along the axial direction is studied by changing counter-flow velocities at different ranges of fixed initial jet velocity. The initial jet velocity (U_o) at the nozzle exit is used to normalize each centerline jet velocity (U_c) and the jet nozzle diameter (d) is used to normalize the axial distance.

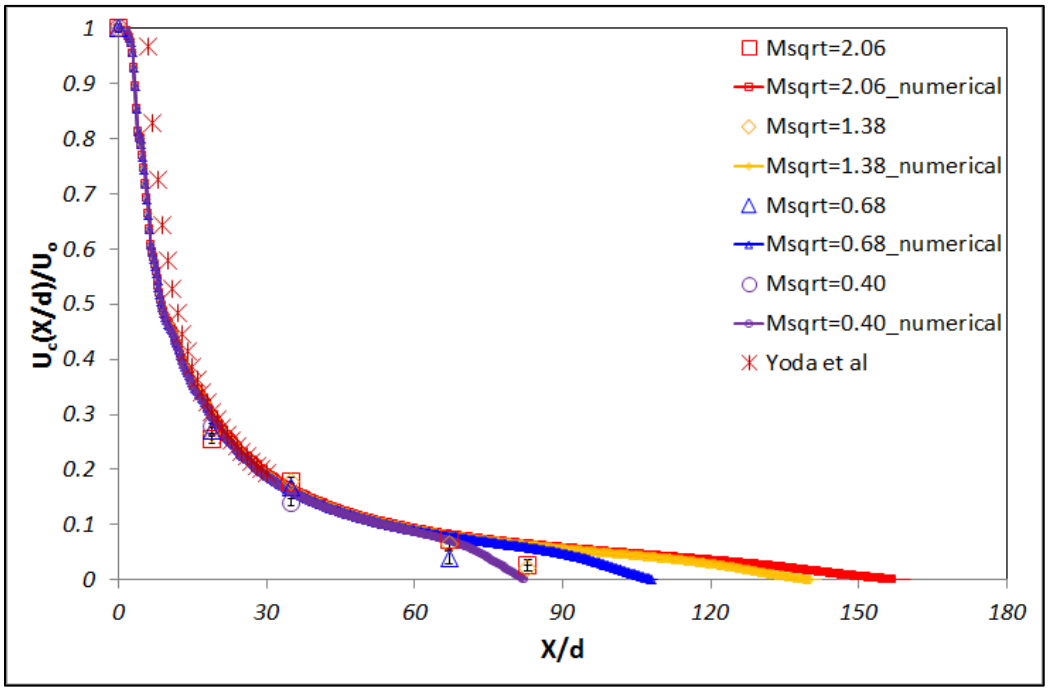

(a) U_{jet}=96.12m/s at each different counter-flow

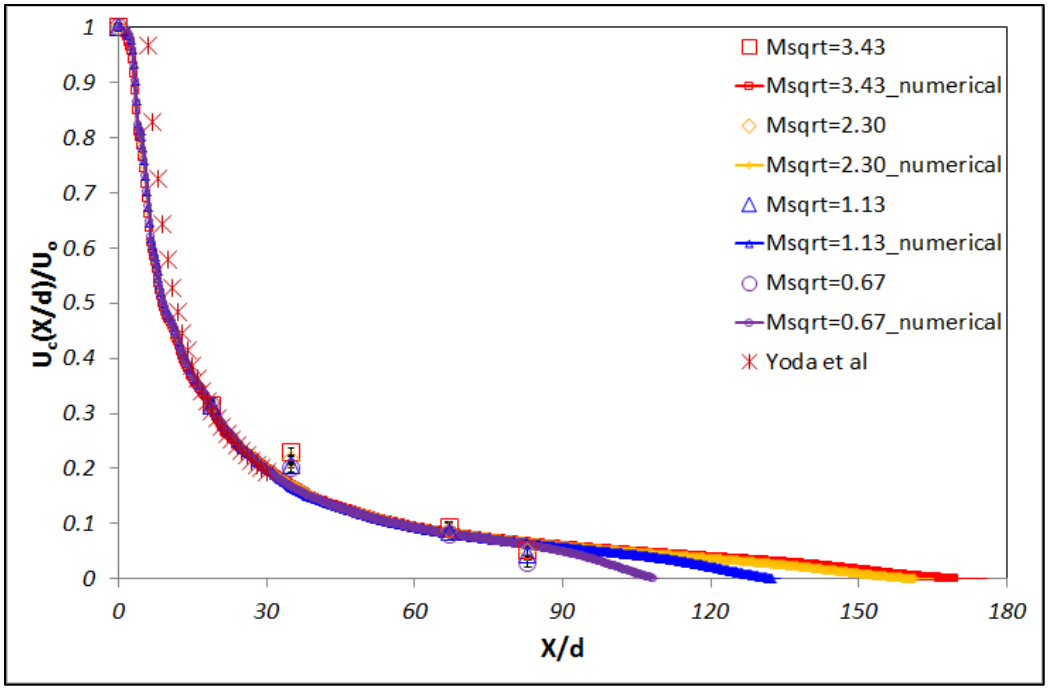

(b) U_{jet}=160.19m/s at each different counter-flow

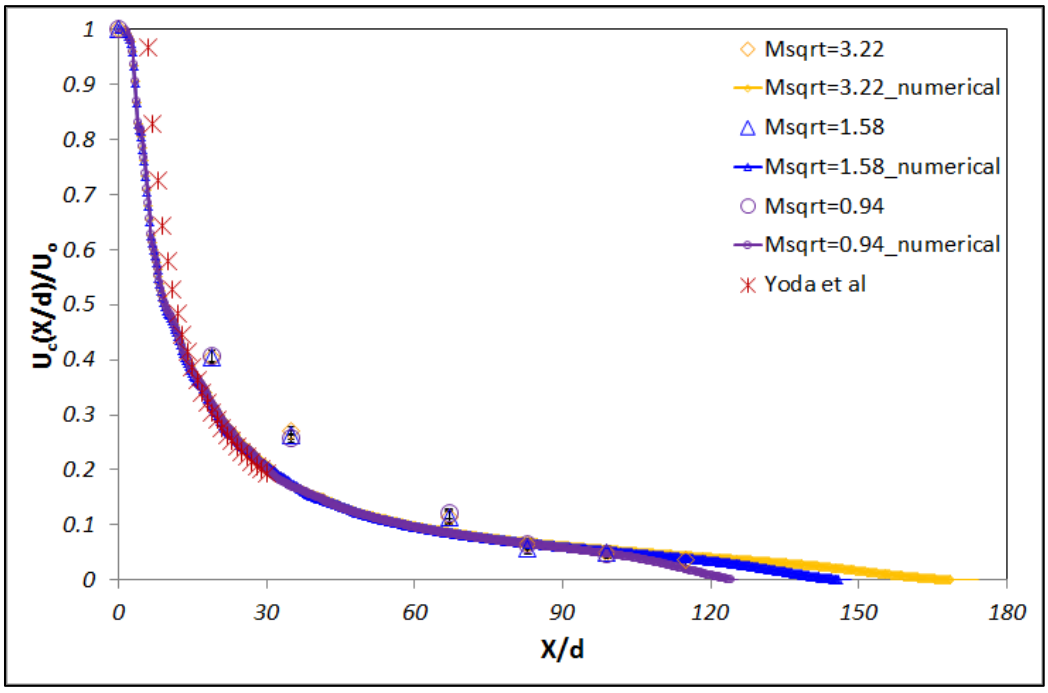

(c) U_{jet}=224.26m/s at each different counter-flow

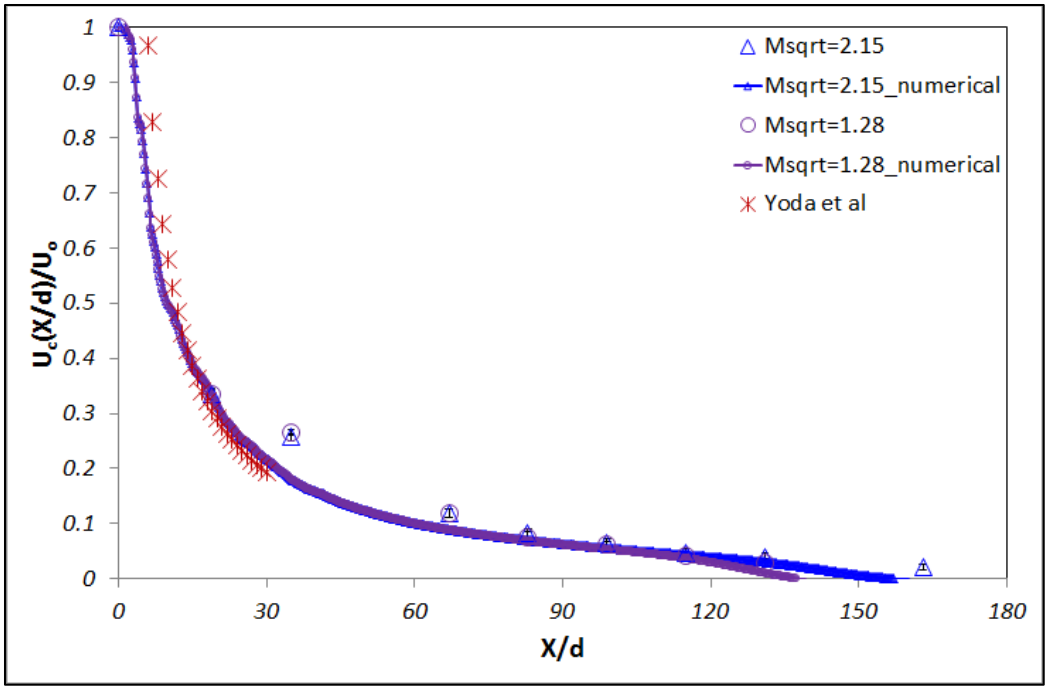

(d) U_{jet}=304.37m/s at each different counter-flow

Figure 3.29 The decay of normalized axial centerline velocity

The decay of the normalized axial centerline velocity is plotted as a function of normalized axial location (***X/d***) by using modified momentum ratios (M_{sqrt}) to define the velocity conditions between jet velocities and counter-flow velocities in figure 3.29. It is difficult to measure velocity in low modified momentum ratios (low jet velocity) at further downstream due to fluctuation yet carried out to more than 100 times the jet diameter, maximum of 170 in Fig.3.29 (d) is reached. One previous result, Yoda et al. [26], was plotted for the comparison with my data and the much shorter range in *X/d* with a maximum of 30 is noticed. The comparison shows that the current results and Yoda's available results are reasonably close at U_j=96.12m/s and U_j=160.19m/s with different counter-flows but there are some deviations between my result of high jet velocity conditions (U_j=224.26m/s and U_j=304.37m/s) and Yoda's data. Also, the decay of the velocity along the centerline has inversely linear relation near the jet exit between my data and Yoda's data. However, the decay of the velocity along the centerline

has different slopes at large ***X/d*** for both experimental and numerical results. This makes sense physically because the jet velocity is decelerated as the jet flow moves along the axial direction because the jet flow finally reaches the formed stagnation plane by the collision of two opposite direction flows. From these findings, the stagnation plane moves downstream as the modified momentum ratio (M_{sqrt}) increases (jet velocity increases or counter-flow velocity decreases at fixed jet velocity) because the momentum balance between high jet velocity and counter-flow occurs at large axial distance.

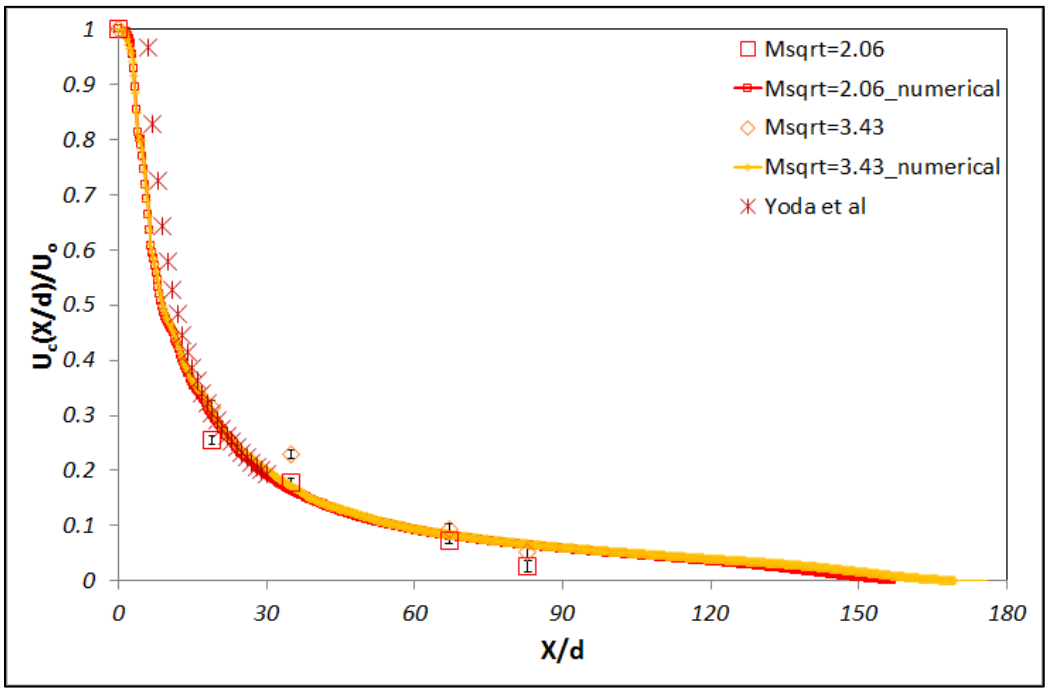

(a) U_{count}=0.612m/s at each jet velocity

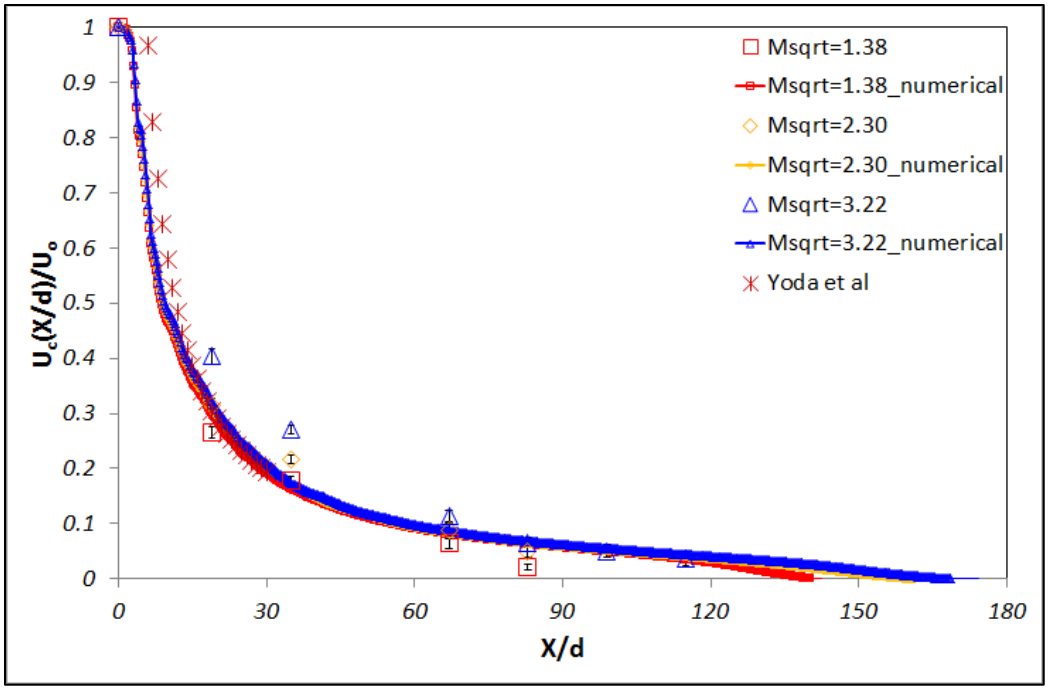

(b) U_{count}=0.913m/s at each jet velocity

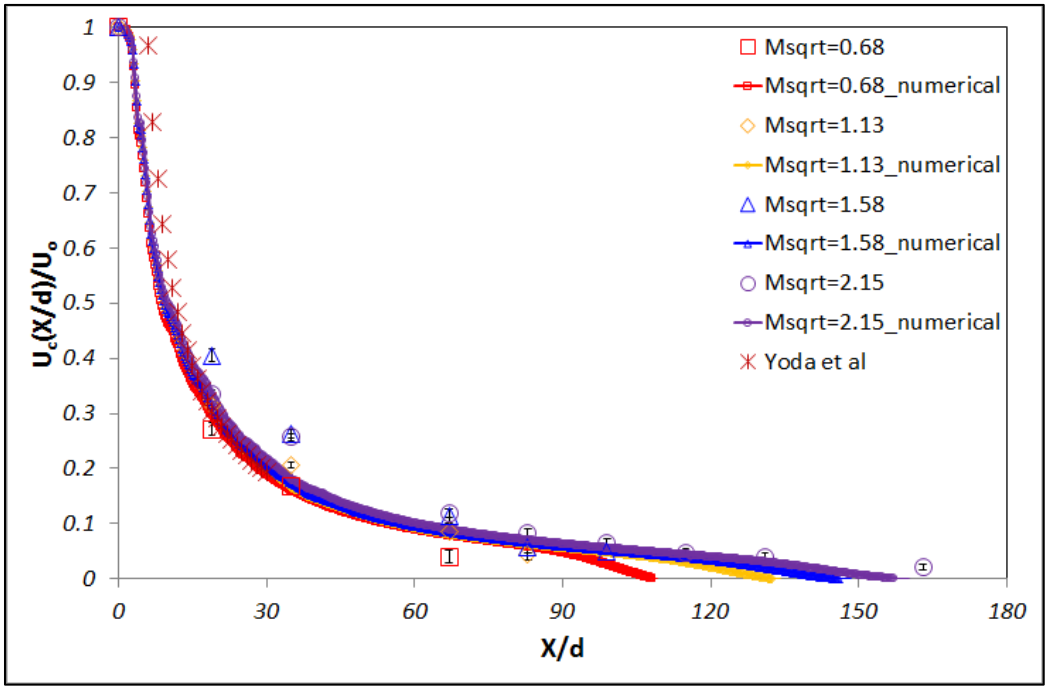

(c) U_{count}=1.856m/s at each jet velocity

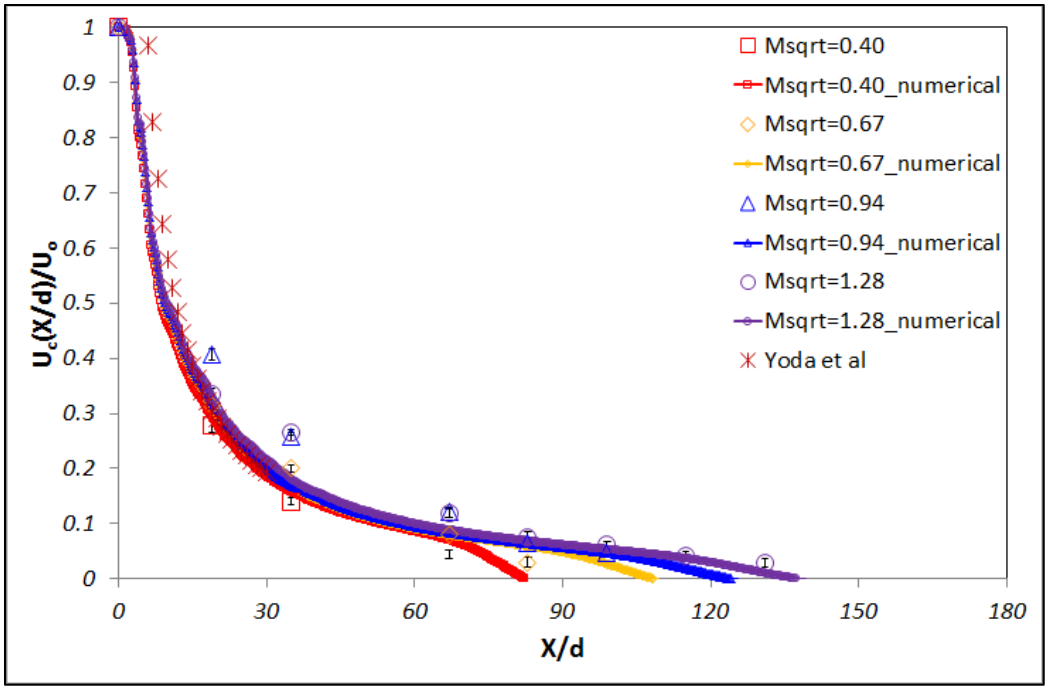

(d) U_{count}=3.123m/s at each jet velocity

Figure 3.30 The decay of normalized axial centerline velocity

Figure 3.30 shows the decay of the normalized centerline velocity at different jet velocities with fixed counter-flow velocities through using $\boldsymbol{M_{sqrt}}$ (Where $\boldsymbol{U_o}$ is the initial jet velocity and $\boldsymbol{U_c}$ is the centerline jet velocity). Also, to compare between my results and previous results, Yoda's [26] results are plotted in each graph. My results and Yoda's available results agrees well at low jet velocity at fixed counter-flow condition in each graph but there are some differences as the jet velocity at fixed counter-flow increases or the modified momentum ratio increases. The slope of decay of the centerline velocity changes respectively as the jet flow moves along the axial direction due to the collision of two opposite direction flows at some axial distance. From the definition of modified momentum ratio, equation (33), for increasing modified momentum ratio, the numerator has to be increased because the denominator is fixed by fixed counter-flow. This means high jet velocity. Therefore, the center jet is able to move further downstream due to relatively high jet momentum against fixed momentum of counter-

flow. Accordingly, the stagnation plane moves further downstream as the modified momentum ratio increases.

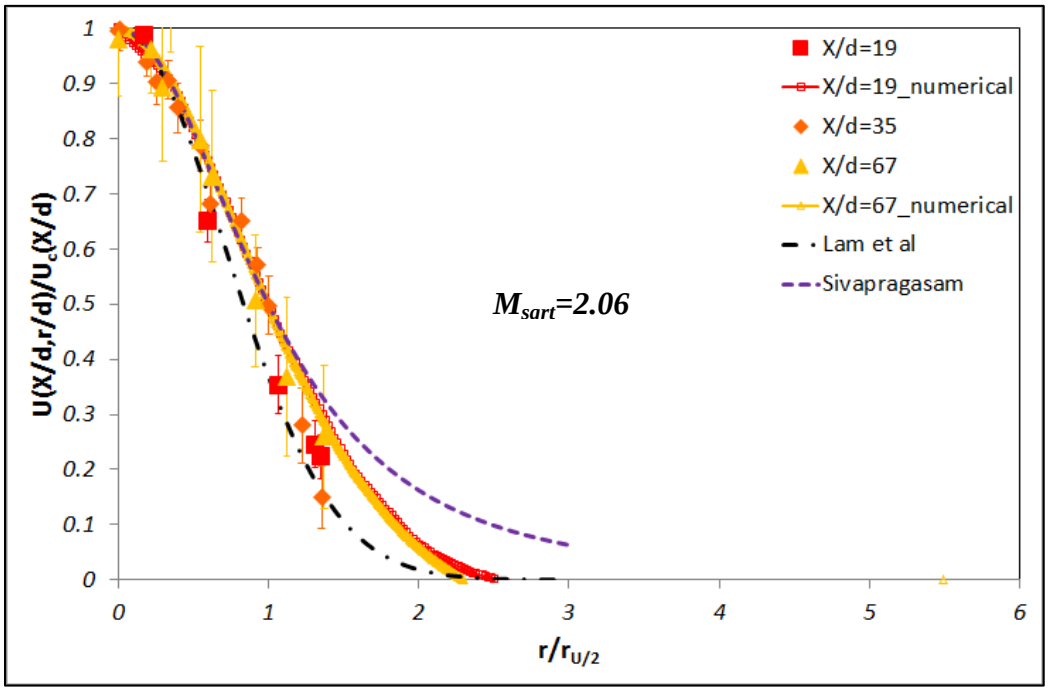

(a) U_{jet}=96.12m/s and U_{count}=0.672m/s

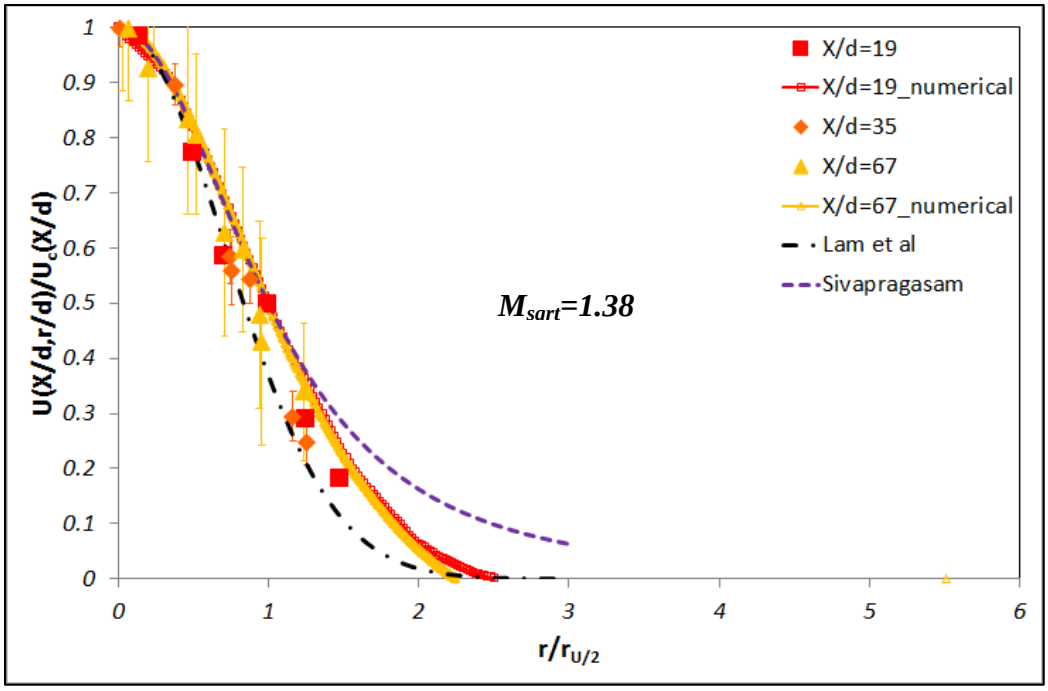

(b) U_{jet}=96.12m/s and U_{count}=0.913m/s

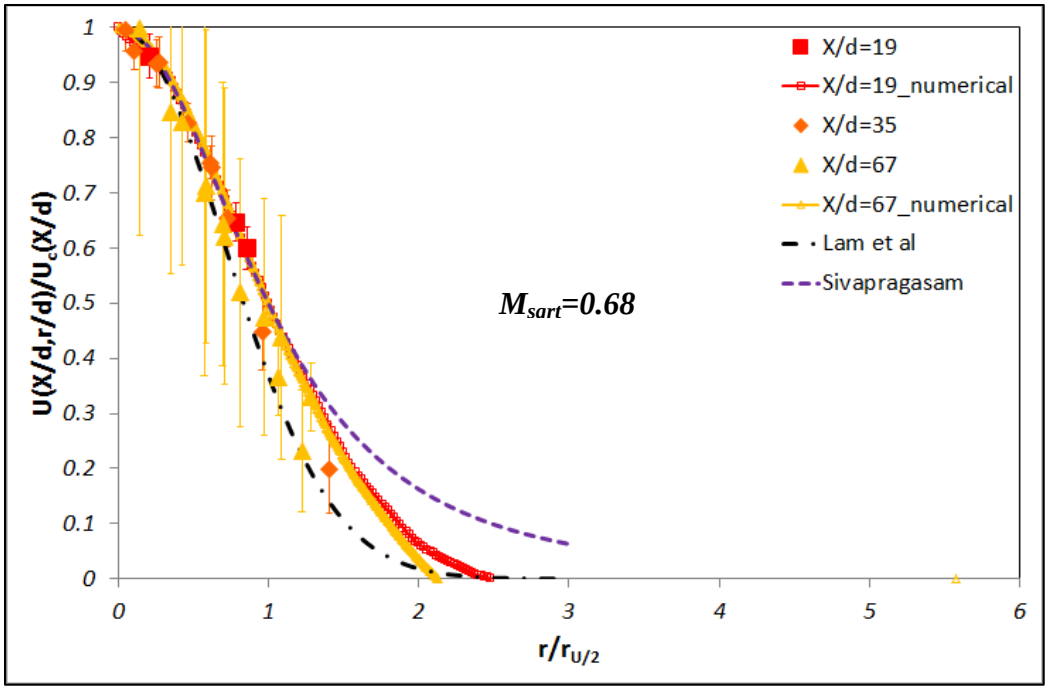

(c) U_{jet}=96.12m/s and U_{count}=1.856m/s

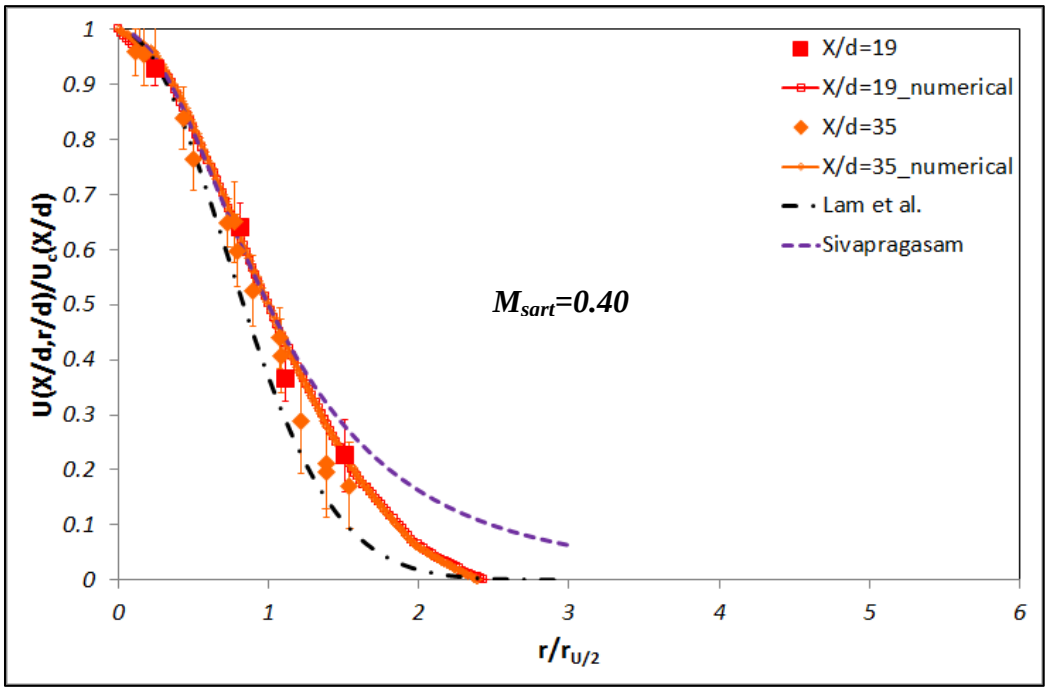

(d) U_{jet}=96.12m/s and U_{count}=3.123m/s

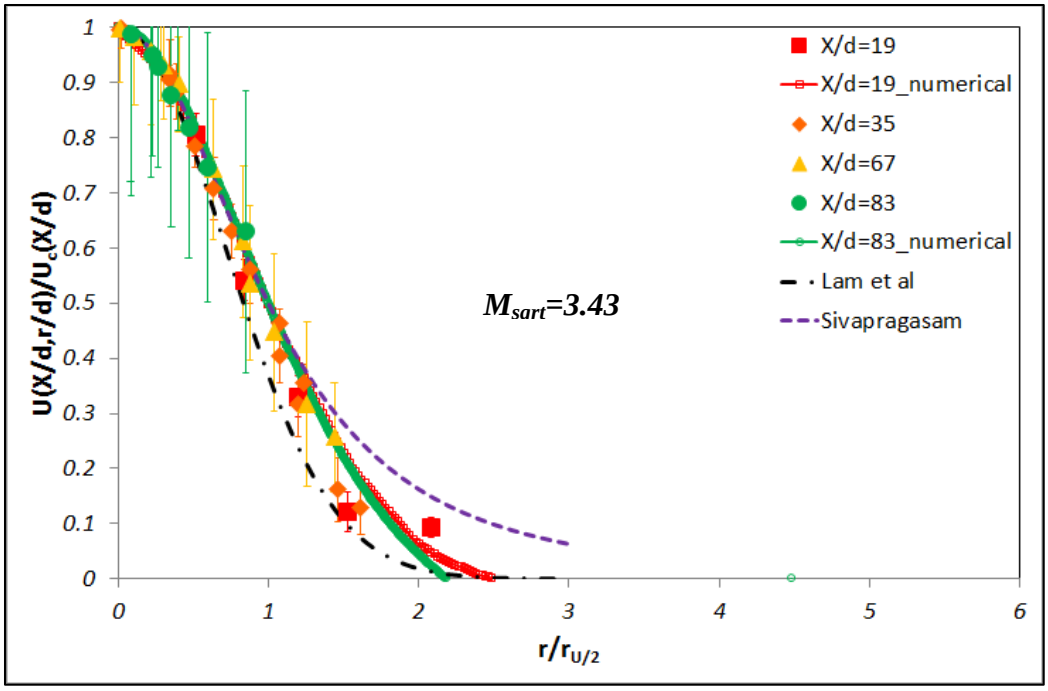

(e) U_{jet}=160.19m/s and U_{count}=0.612m/s

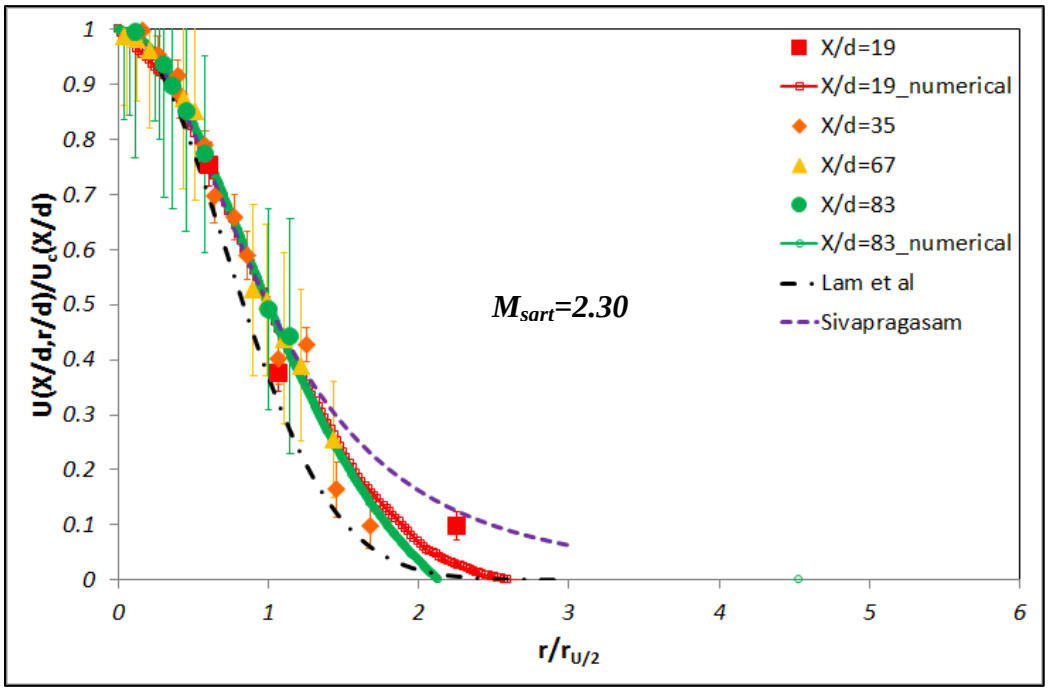

(f) U_{jet}=160.19m/s and U_{count}=0.913m/s

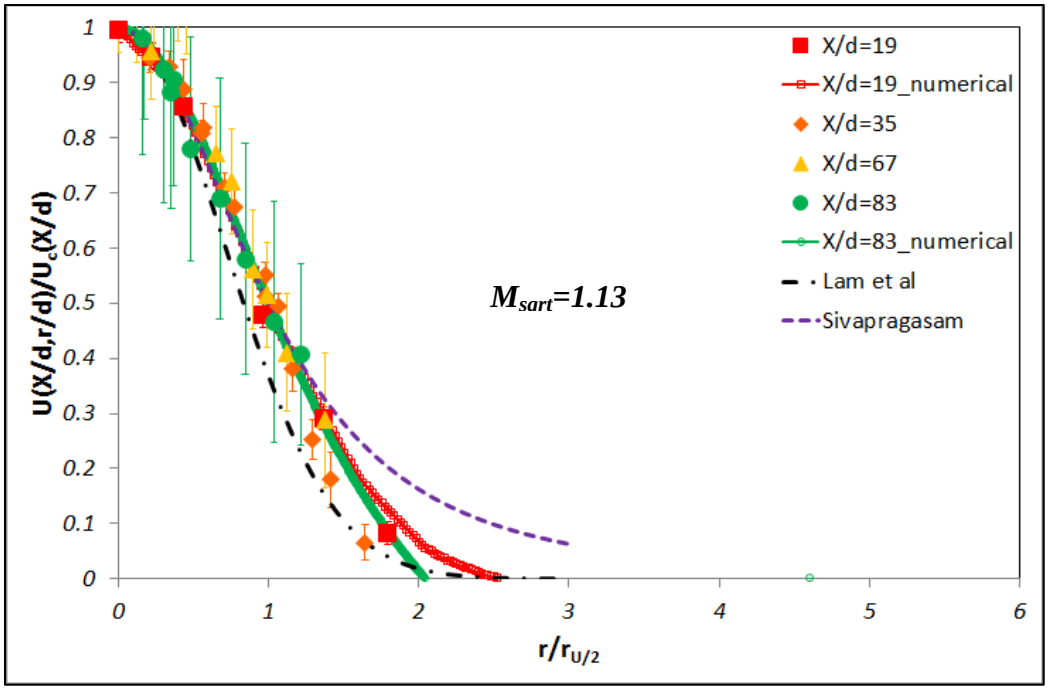

(g) U_{jet}=160.19m/s and U_{count}=1.856m/s

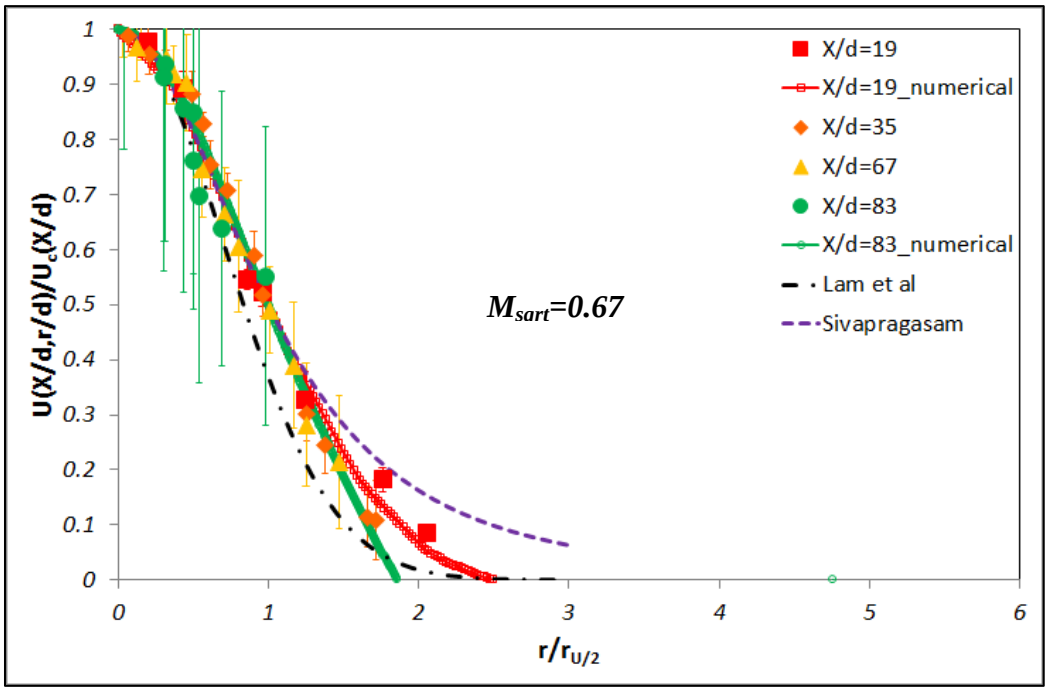

(h) U_{jet}=160.19m/s and U_{count}=3.123m/s

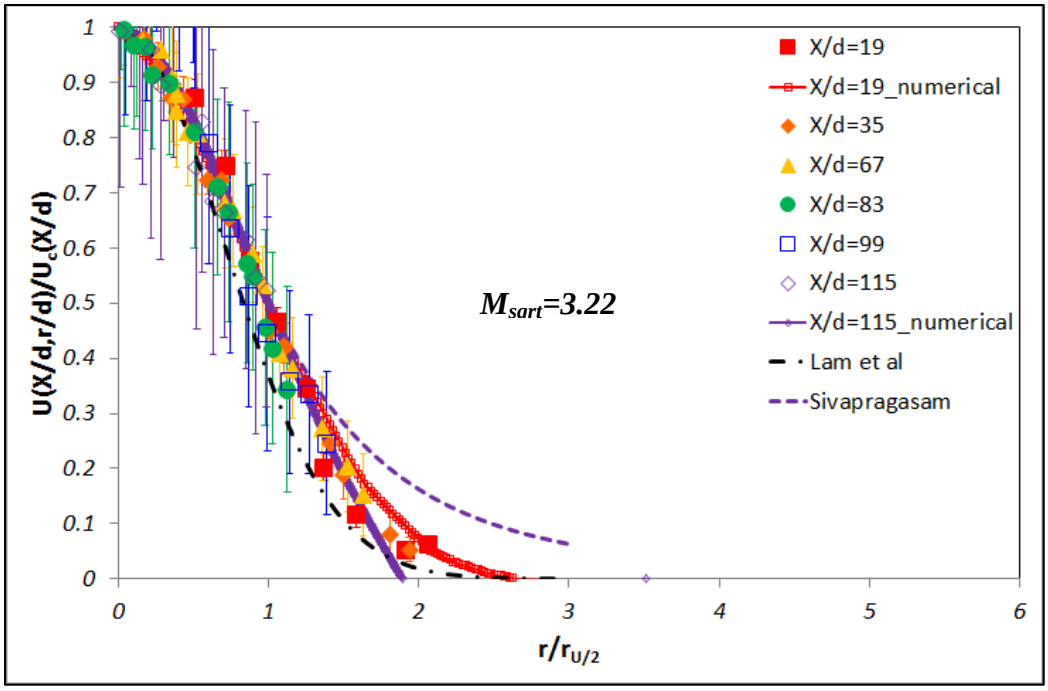

(i) U_{jet}=224.26m/s and U_{count}=0.913m/s

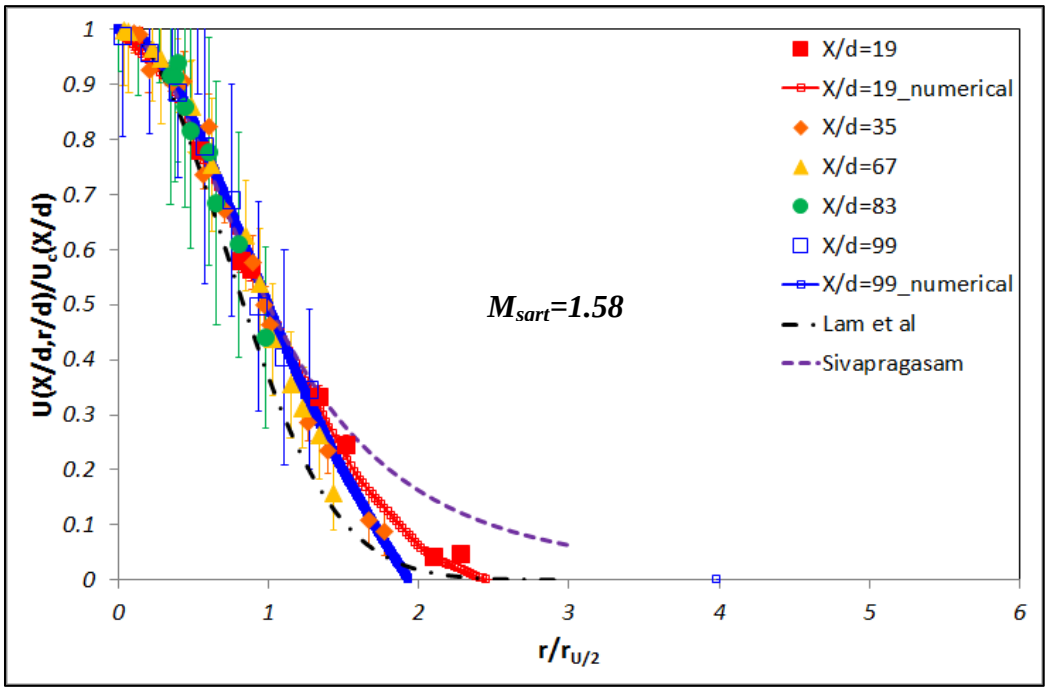

(j) U_{jet}=224.26m/s and U_{count}=1.856m/s

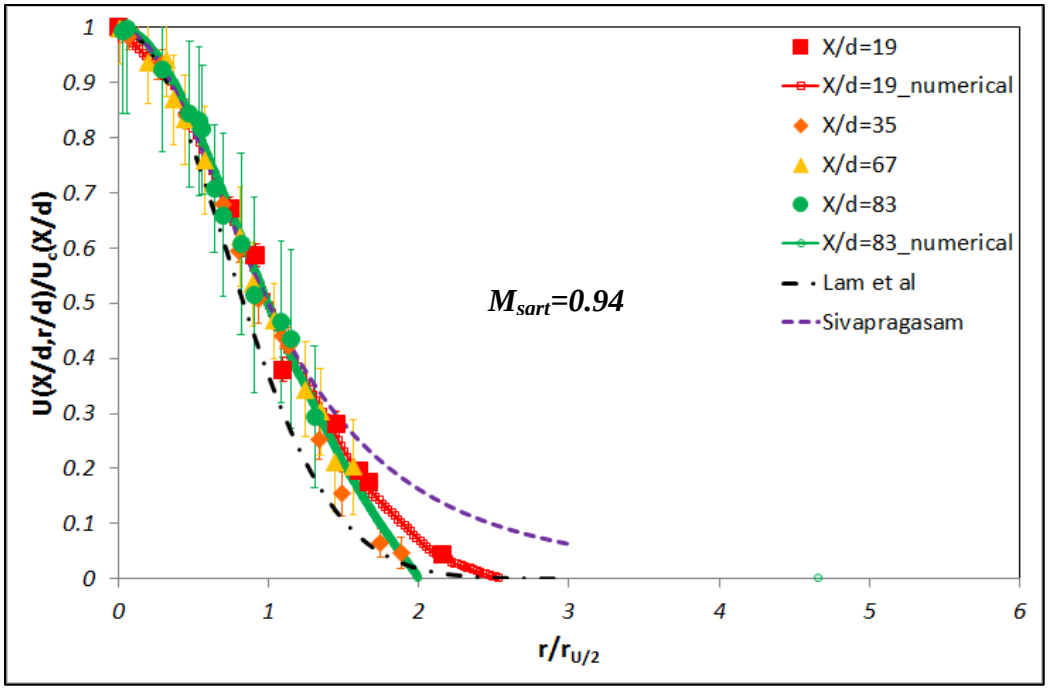

(k) U_{jet}=224.26m/s and U_{count}=3.123m/s

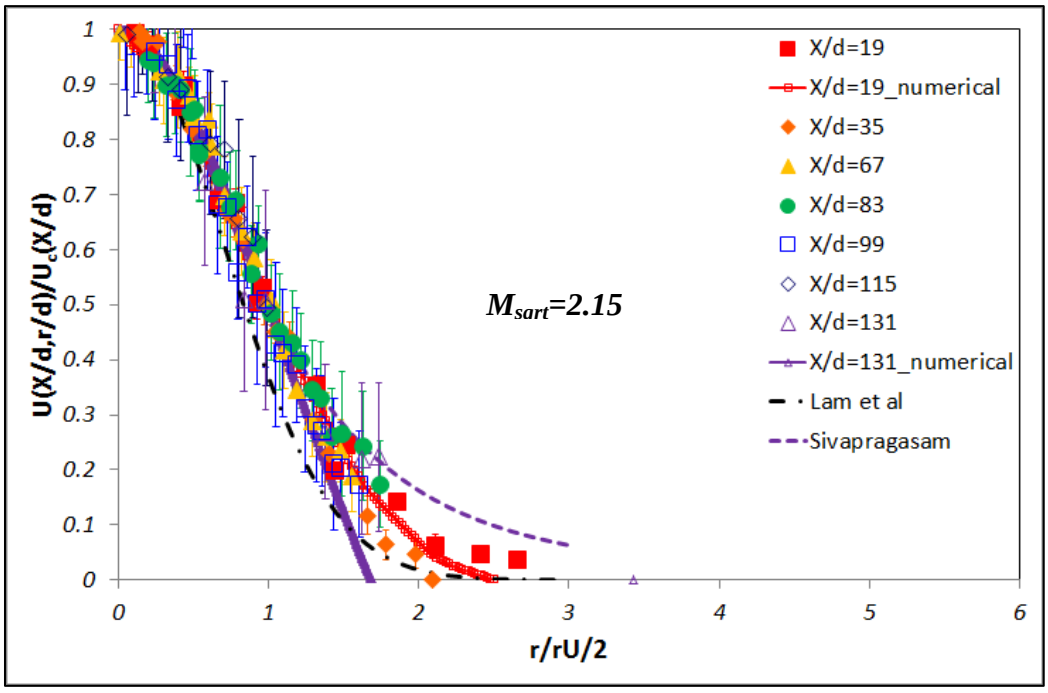

(l) U_{jet}=304.37m/s and U_{count}=1.856m/s

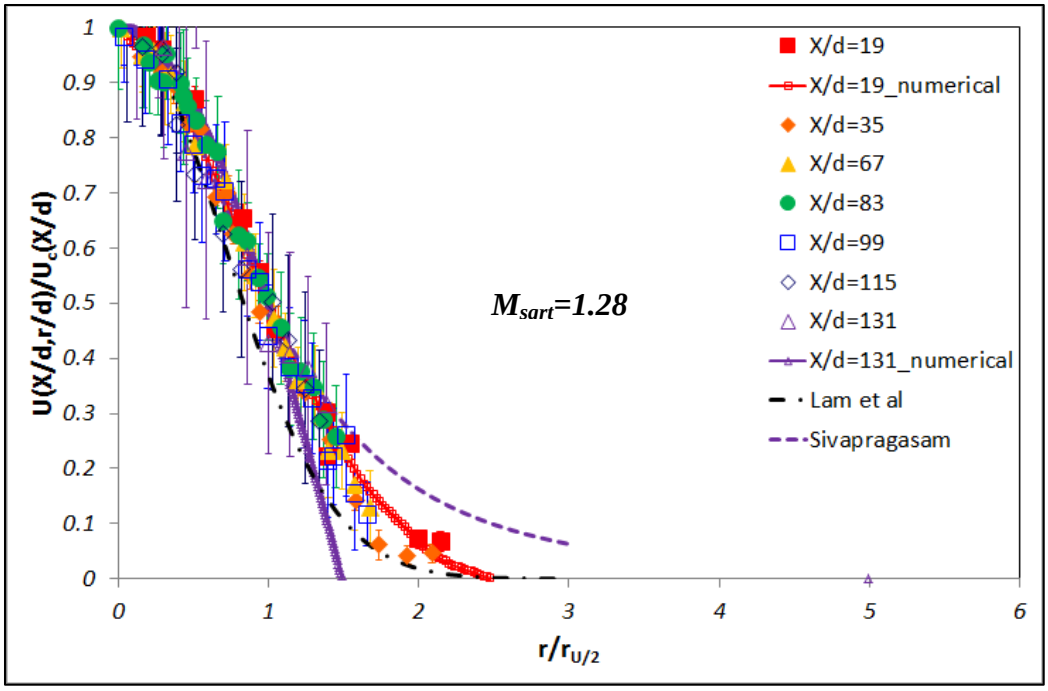

(m) U_{jet}=304.37.44m/s and U_{count}=3.123m/s

Figure 3.31 The radial velocity distribution

The radial velocity distributions at different jet velocities and different counter-flow conditions (or different modified momentum ratios) are shown in figure 3.31. From experimental and numerical results, different colored rhombuses (experimental results) and colored solid lines (numerical results) are used at different locations of ***X/d*** (***X***: axial direction, ***d***: jet nozzle diameter). Previous results are expressed as two colored dash lines. The equations (44) and (45) for two colored dash lines are found in Lam et al [24] and Sivapragasam [36]. These are shown as:

$$\frac{U}{U_c} = \exp\left[-\left(r \Big/ r_{\frac{U}{2}}\right)^2\right] \tag{44}$$

$$\frac{U - U_{count}}{U_c - U_{count}} = \left[1 + 0.59\left(r / r_{\frac{U}{2}}\right)^2\right]^{-\frac{3}{2}} \quad (45)$$

Where $\boldsymbol{U}$ is the radial velocity at different normalized location of $\boldsymbol{X/d}$, $\boldsymbol{U_c}$ is the centerline jet velocity, $\boldsymbol{U_{count}}$ is the counter-flow velocity and $\boldsymbol{r_{U/2}}$ is the width of half jet velocity. From the equation (44), (45) and my results, the jet flow retains the self-similar region in spite of the counter-flow condition. Therefore, the velocity distribution can be expressed as Gaussian function. However, the characteristics of self-similar region of counter-flow conditions are destroyed by the stagnation plane a much lower axial location as compared to free turbulent jet flow or co-flow conditions. In self-similar regions, normalized radial velocity distributions collapse fairly well between results of Lam et al [24] and Sivapragasam [36]. This means that there is a good agreement between current results and previous results for all velocity conditions between the jet and the counter-flow. The velocity fluctuation increases as the jet flow moves along the axial direction by a turbulent intensity. The increment of turbulent intensity is identified by observing high standard deviations at large axial location.

3.2.2. The concentration distribution

To verify the characteristics of concentration, the axial and radial normalized concentration distribution are shown in this part. The normalized axial distribution of ***NO*** concentration is shown through changing counter-flow velocities at each fixed jet velocity. The value of C_o (initial center concentration of ***NO***) is normalized by using C_c (***NO*** center concentration) at the different ***X/d*** (***X***: axial direction, ***d***: jet nozzle diameter).

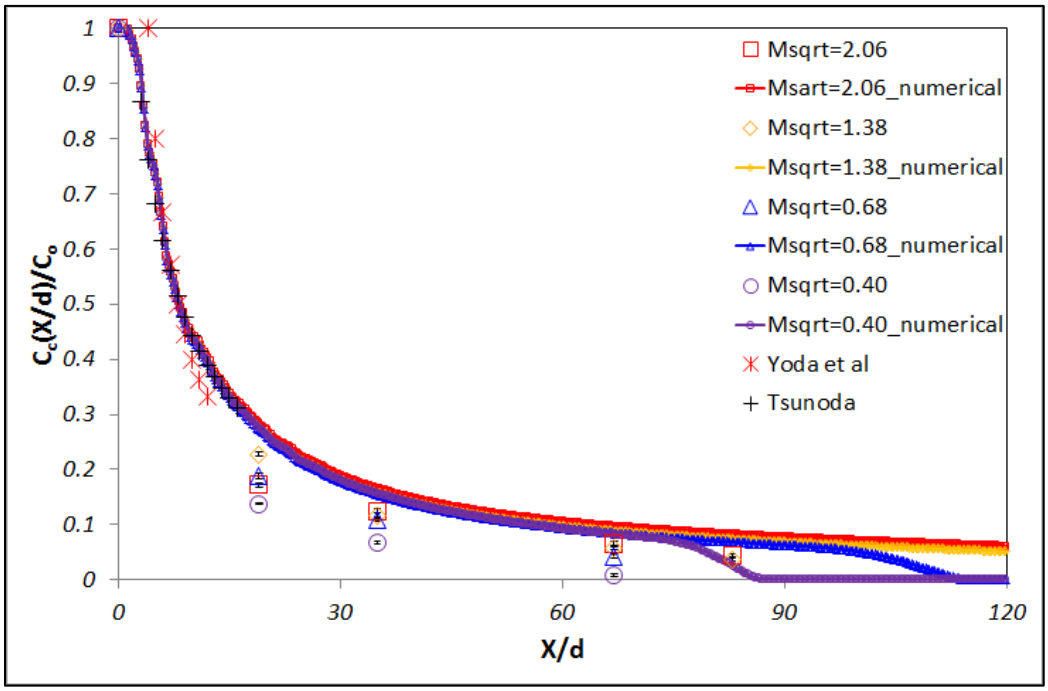

(a) U_{jet}=96.12m/s at different counter-flows

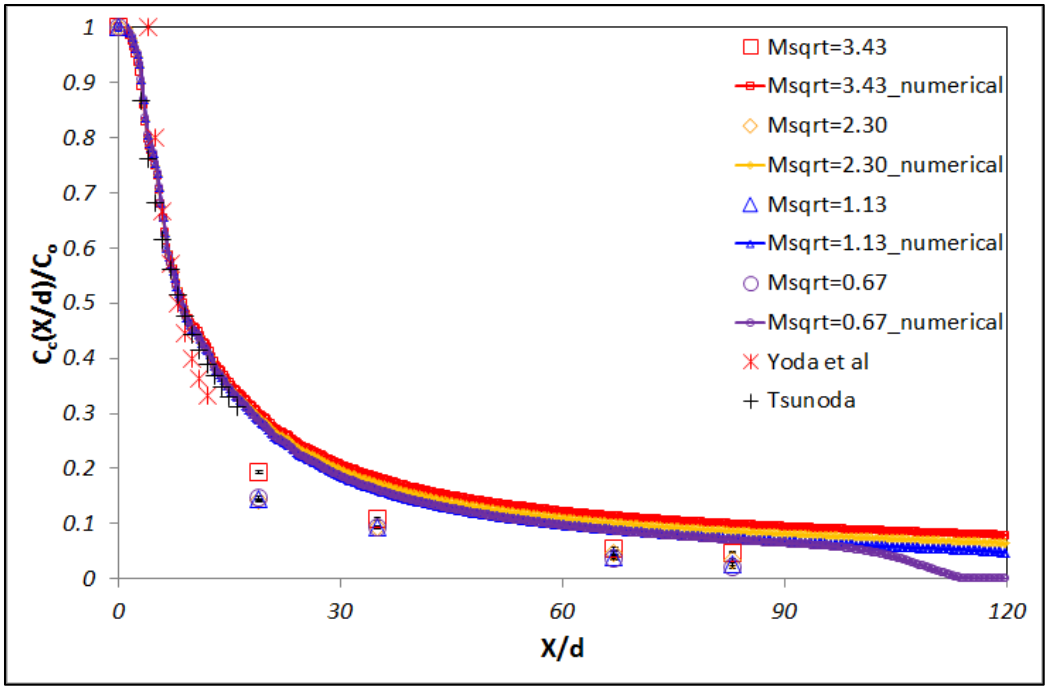

(b) U_{jet}=160.19m/s at different counter-flows

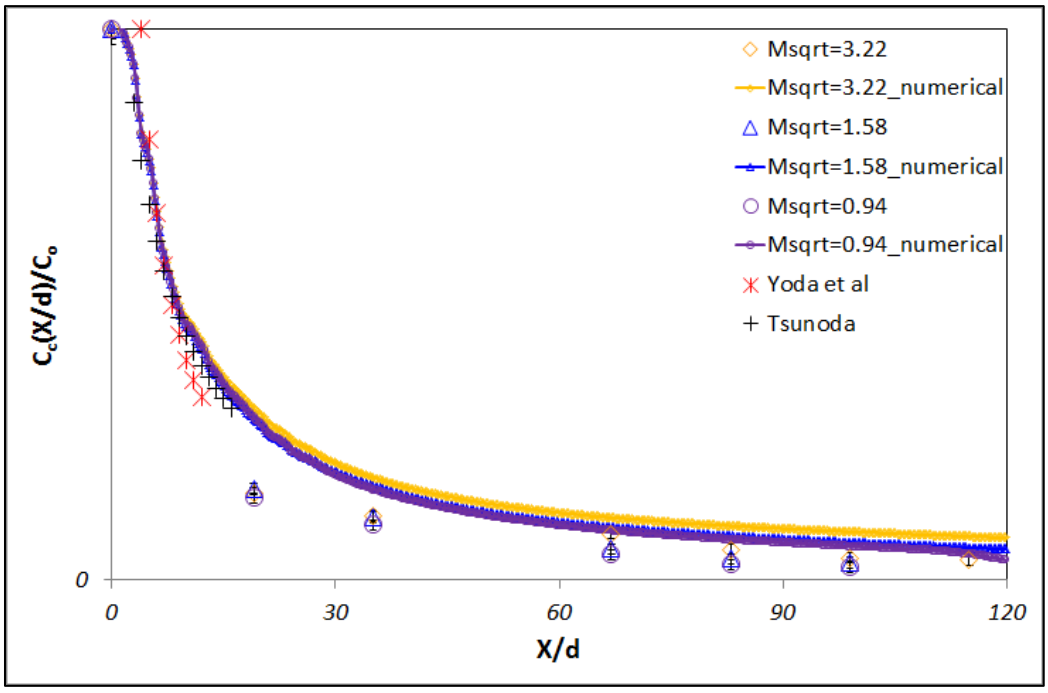

(c) U_{jet}=224.26m/s at different counter-flows

Figure 3.32 The measured concentration along the axial direction

From figure 3.32, the decay of normalized concentration along the axial direction is shown by using different modified momentum ratios (different counter-flow velocity with fixed jet velocity). Yoda's [26] and Tsunoda's [34] results are plotted in the graph for comparison to previous results. Current results and previous results are reasonably close near the jet exit (below ***X/d*** =20). The decay of the center concentration shows two trends at fixed jet and different counter-flow velocity conditions. First of all, the normalized concentration has two different slopes around ***X/d***=30 as the jet flow moves along the axial direction. This trend changes from linear function to exponential function due to the location of the stagnation plane. From these results, the decay of concentration is mainly influenced by counter-flow because of the stagnation plane by colliding two flows (the effect of counter-flow).

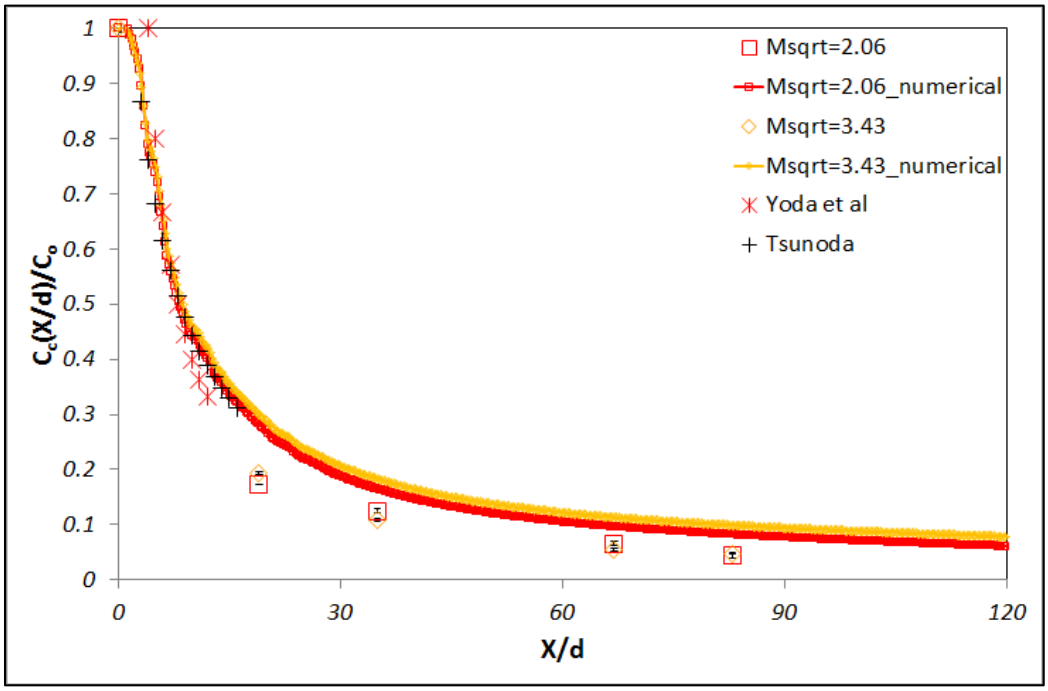

(a) U_{count}=0.612m/s at each jet velocity

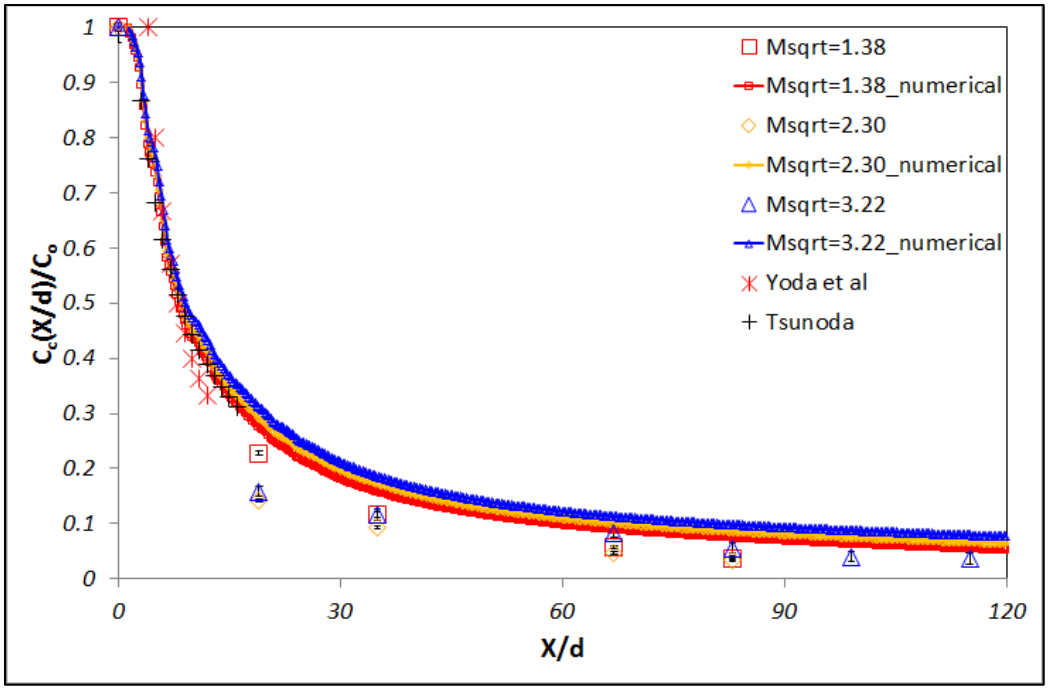

(b) U_{count}=0.913m/s at each jet velocity

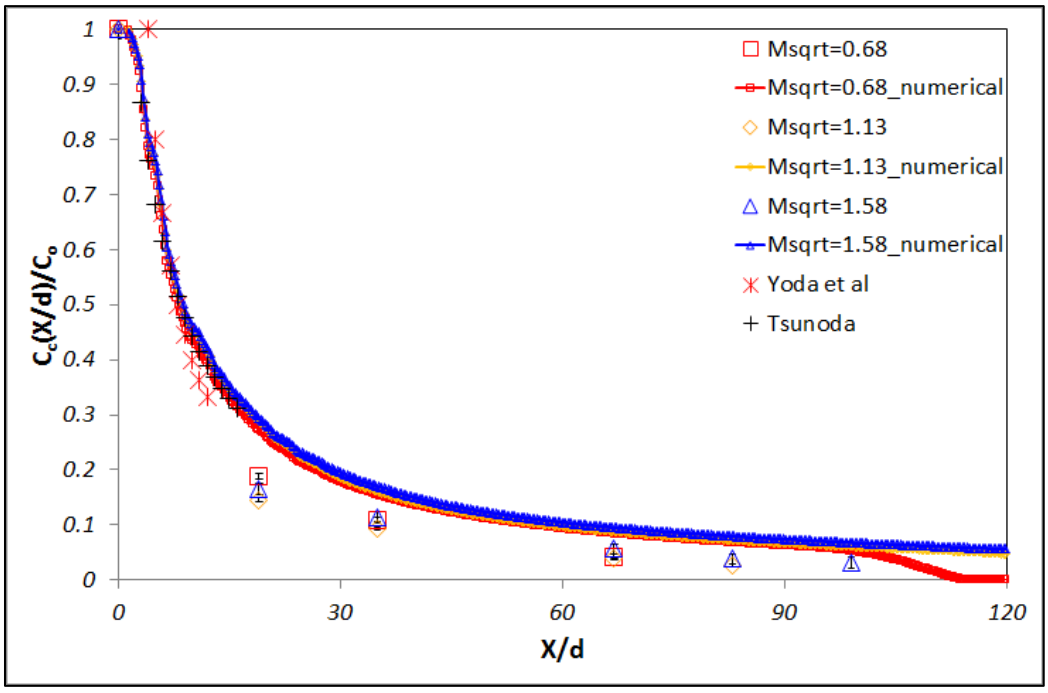

(c) U_{count}=1.856m/s at each jet velocity

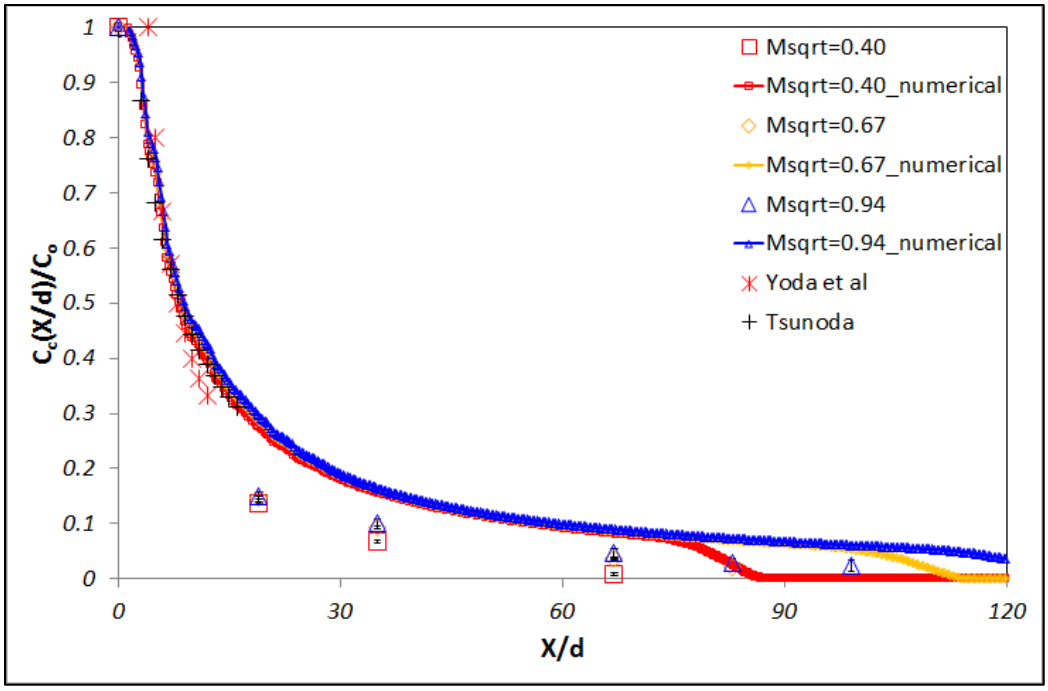

(d) U_{count}=3.123m/s at each jet velocity

Figure 3.33 The measured concentration along the axial direction

The axial decay of the normalized concentration is expressed by using different momentum ratios (different jet velocities with fixed counter-flow velocity) in figure 3.33. To show the comparison between previous results such as Yoda's [26] and Tsunoda's [34] results and current concentration results, the previous results are also plotted in figure 3.33. At small value of ***X/d***=20(near the exit of jet), similar trends are found between our test results and previous results. In the case of different jet velocities at respectively fixed counter-flow velocity, two trends of the decay of the center concentration are found. First, usually, the decay of the normalized concentration has inversely linear function of ***X/d***. Therefore, the trend of the decay of the concentration is changed by the stagnation plane (by colliding between jet flow and counter-flow). The concentration is spread more quickly along the radial direction because of blocking the axial direction by the stagnation plane. This phenomena causes to make the dilution

of ***NO***. Second, the concentration is moving further downstream and decayed slowly at low fixed counter-flow condition and high jet velocity or high modified momentum ratio.

Figure 3.34 represents the radial velocity distribution at modified momentum ratio or different jet velocities and different counter-flow conditions. To show experimental and numerical results, different colored rhombuses and colored solid lines are used at different locations of ***X/d*** (***X***: axial direction, ***d***: jet nozzle diameter) in figure 3.34. The radial ***NO*** concentration at different location of ***X/d*** is ***C***, the ***NO*** concentration along the centerline is C_c and the width of half value of ***NO*** concentration is $r_{c/2}$.

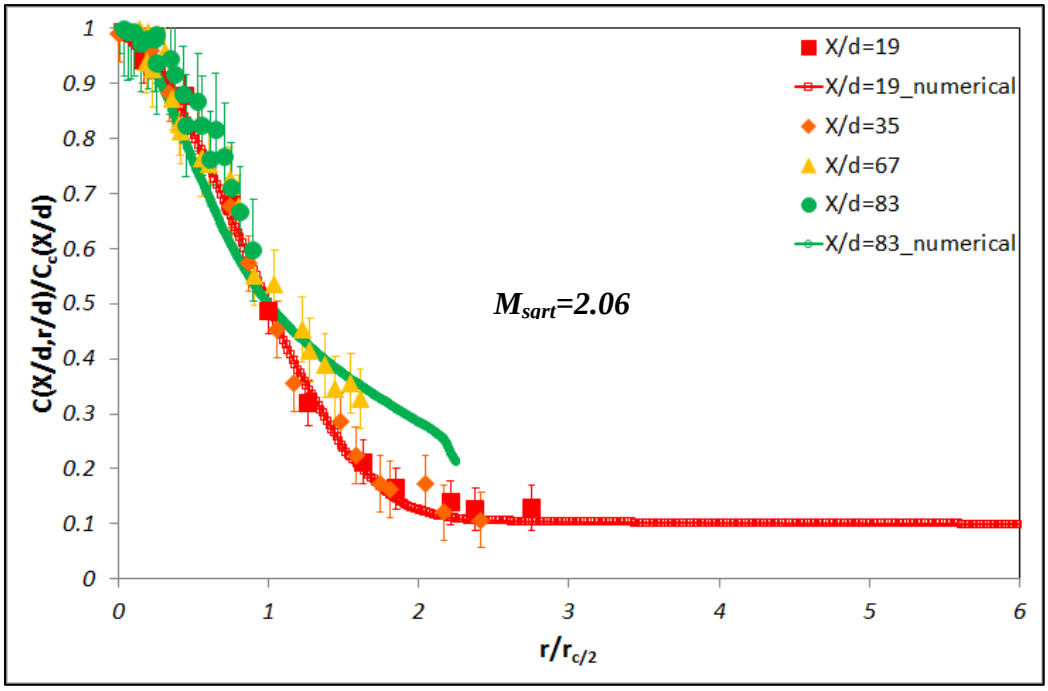

(a) U_{jet}=96.12m/s and U_{count}=0.613m/s

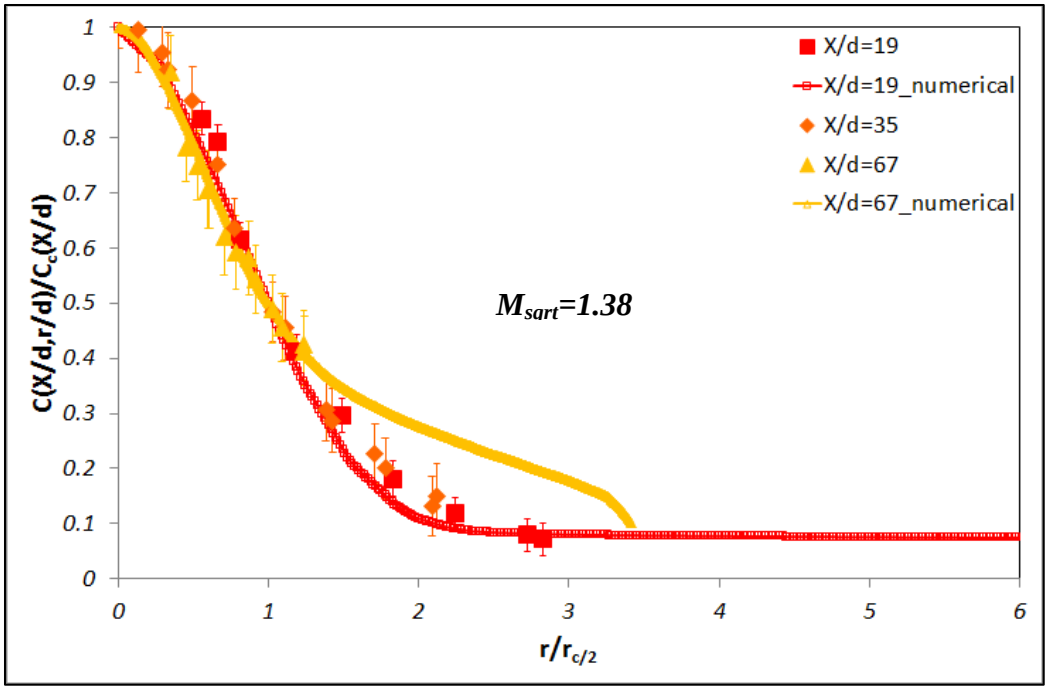

(b) U_{jet}=96.12m/s and U_{count}=0.913m/s

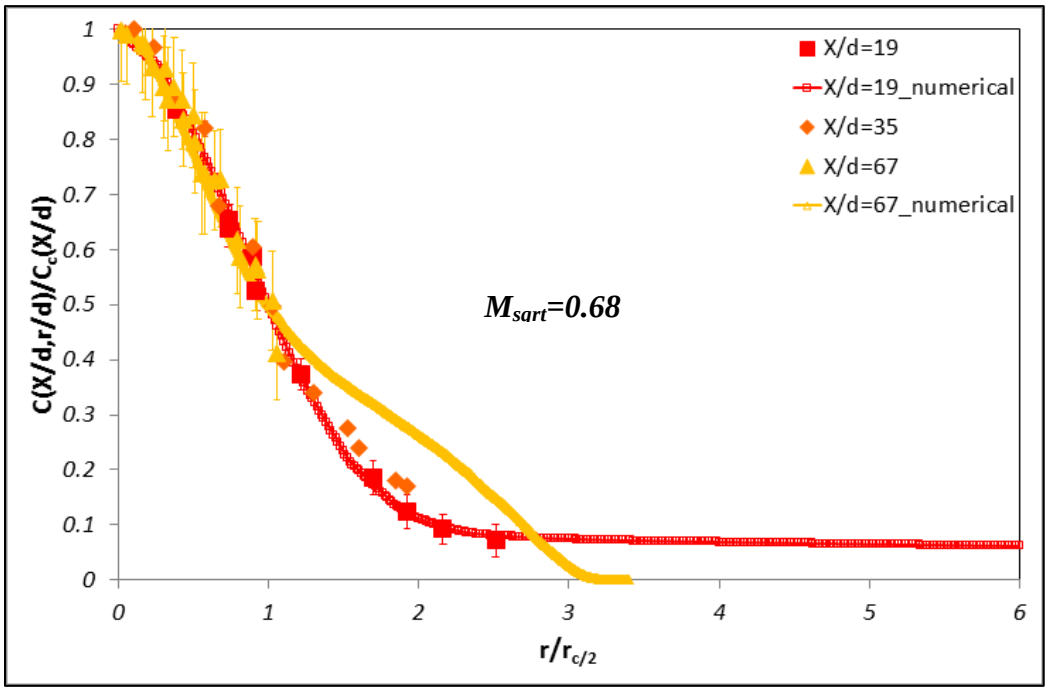

(c) U_{jet}=96.12m/s and U_{count}=1.856m/s

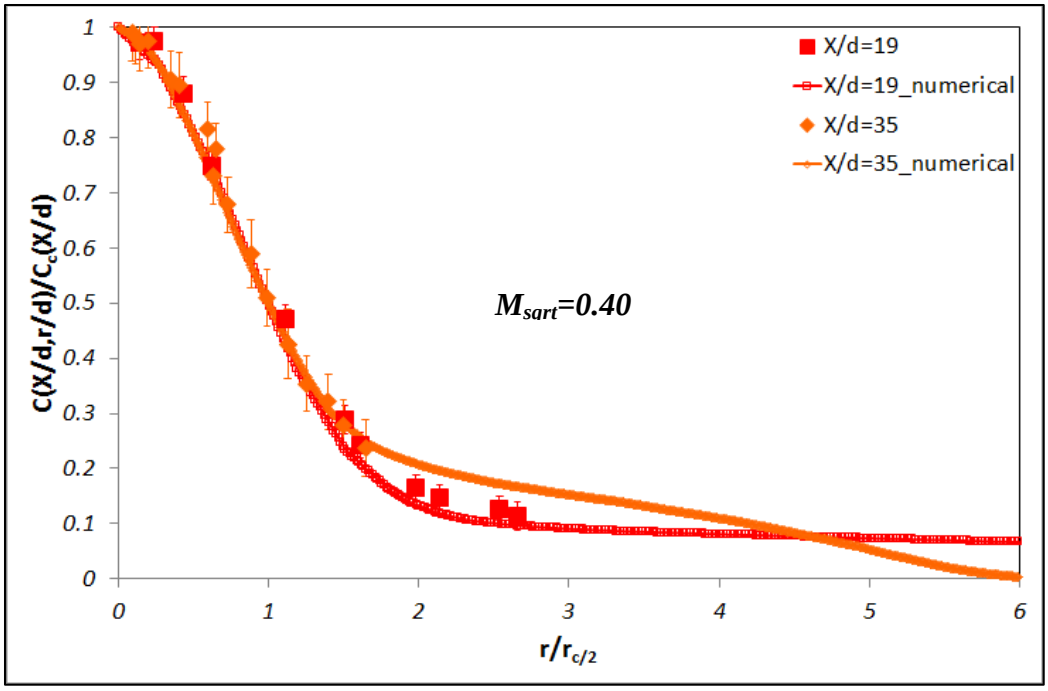

(d) U_{jet}=96.12m/s and U_{count}=3.123m/s

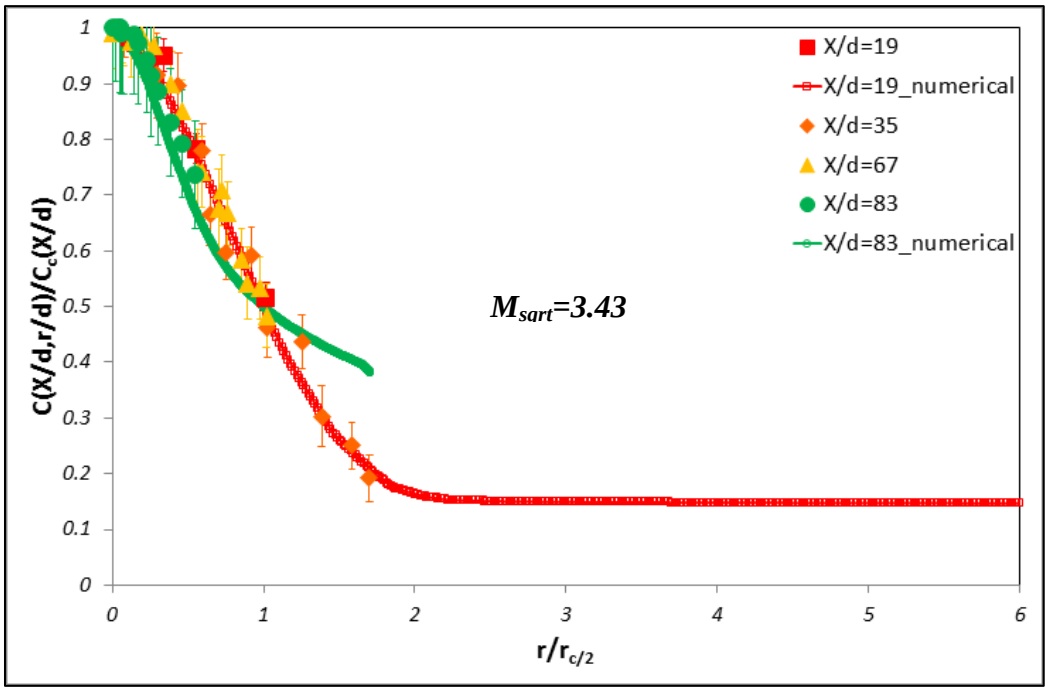

(e) U_{jet}=160.19m/s and U_{count}=0.612m/s

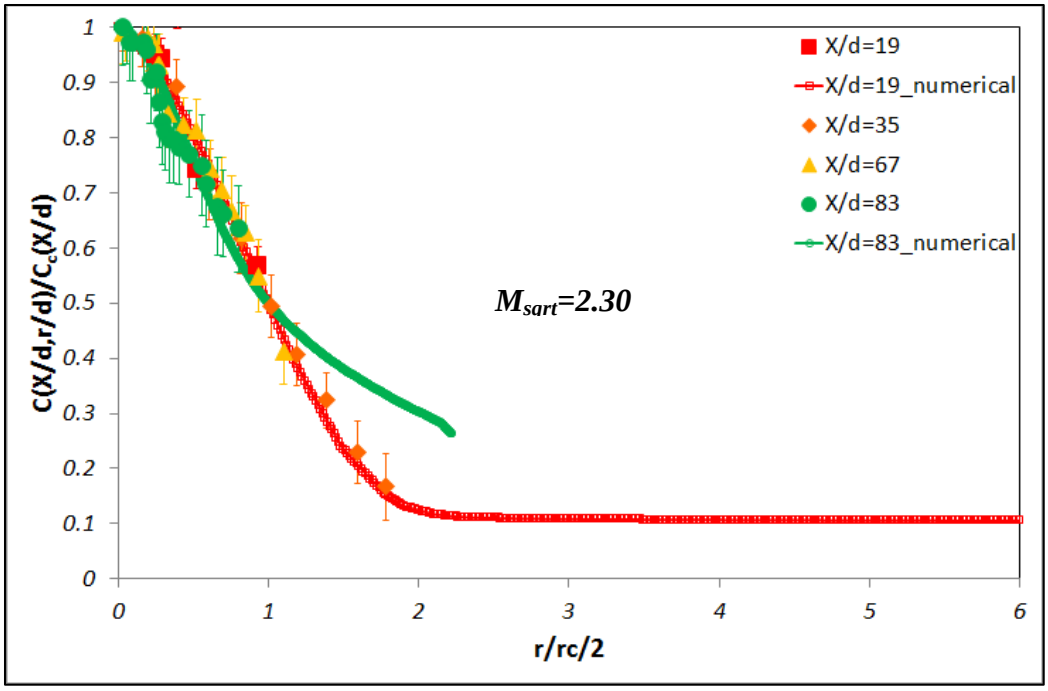

(f) U_{jet}=160.19m/s and U_{count}=0.913m/s

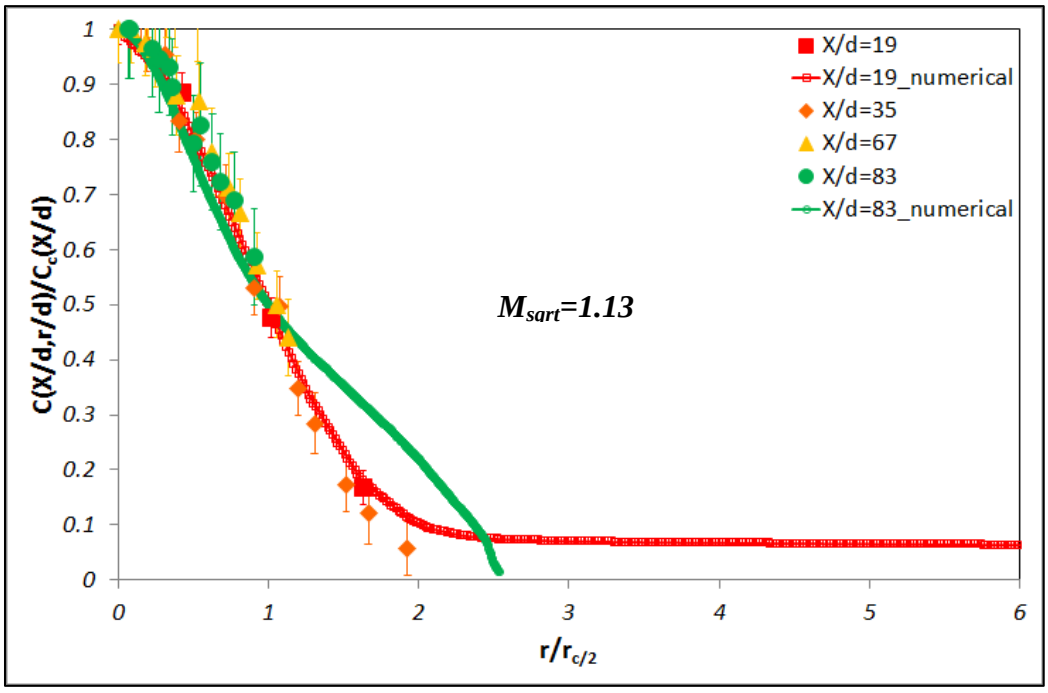

(g) U_{jet}=160.19m/s and U_{count}=1.856m/s

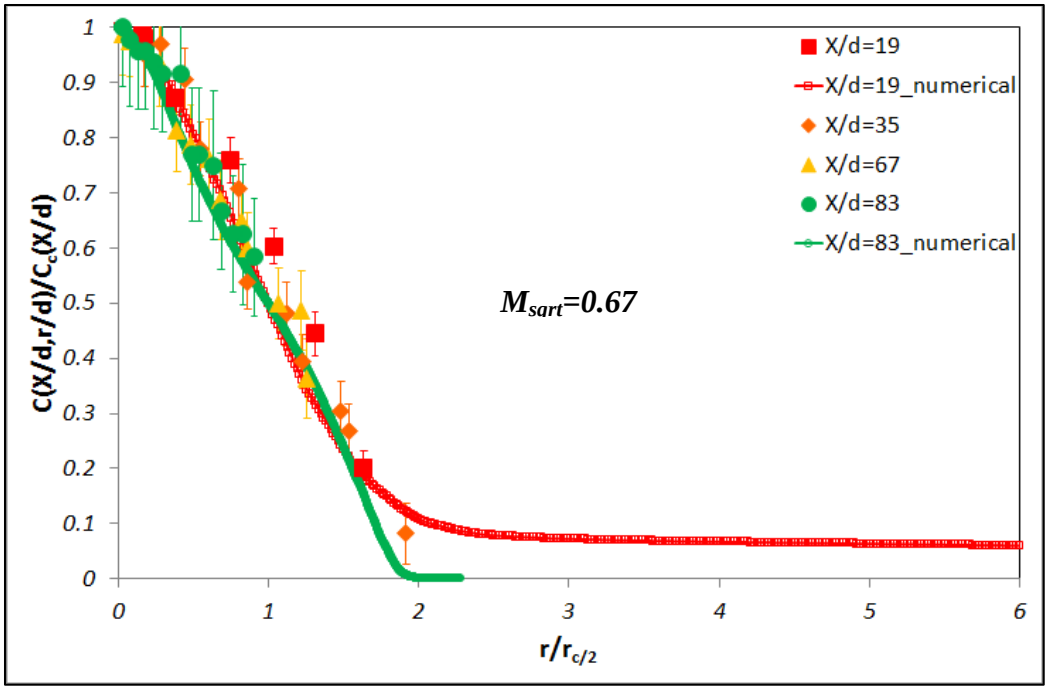

(h) U_{jet}=160.19m/s and U_{count}=3.123m/s

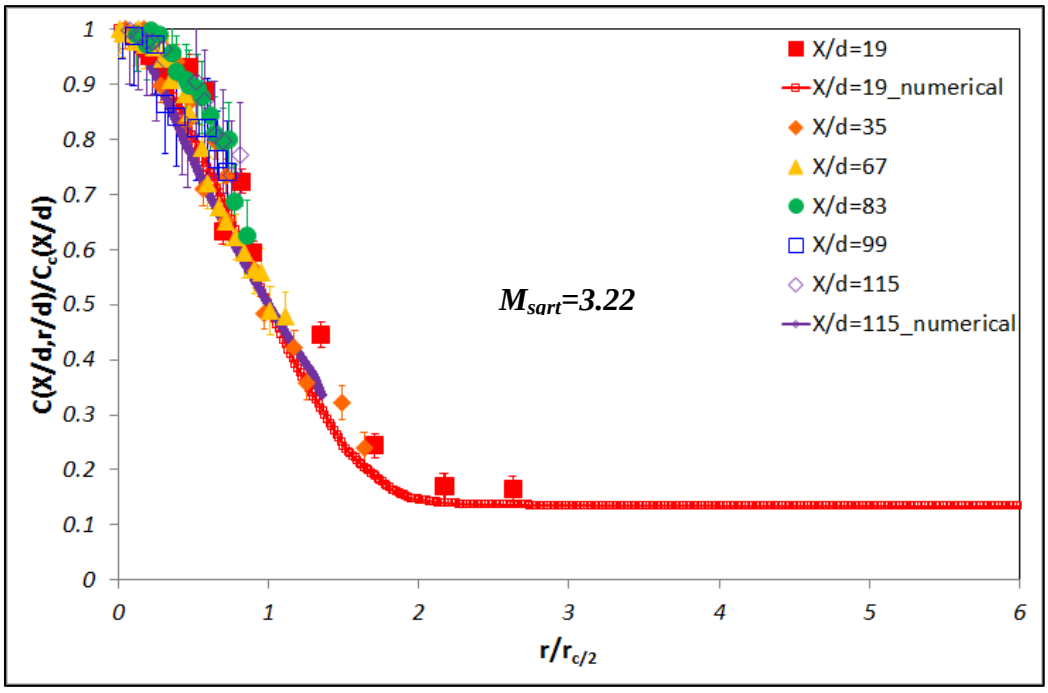

(i) U_{jet}=224.26m/s and U_{count}=0.913m/s

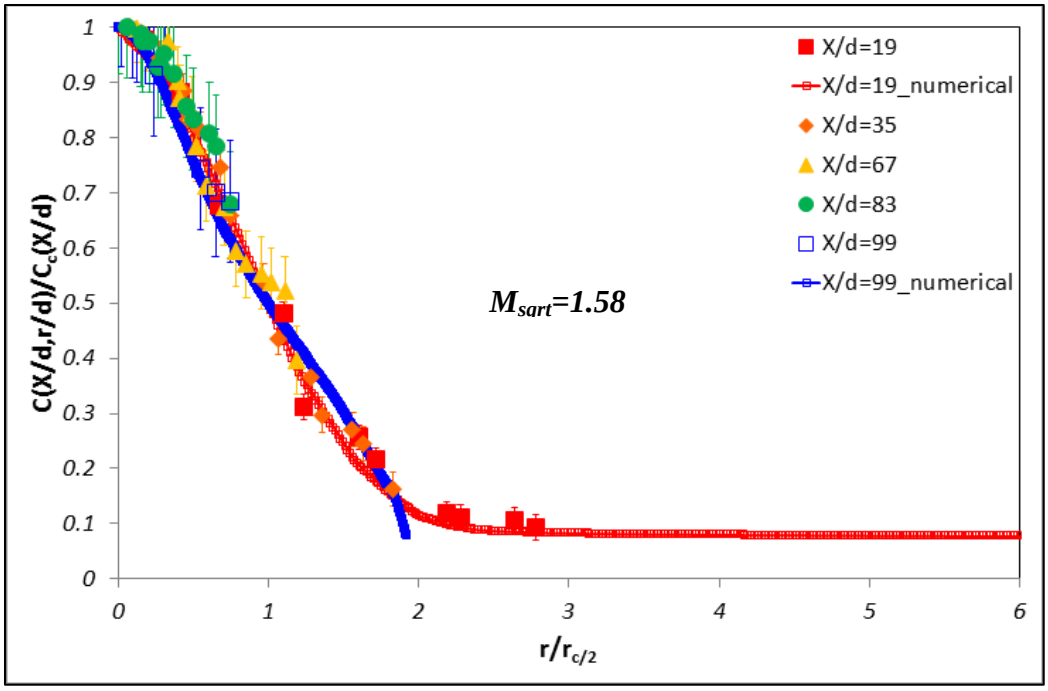

(j) U_{jet}=224.26m/s and U_{count}=1.856m/s

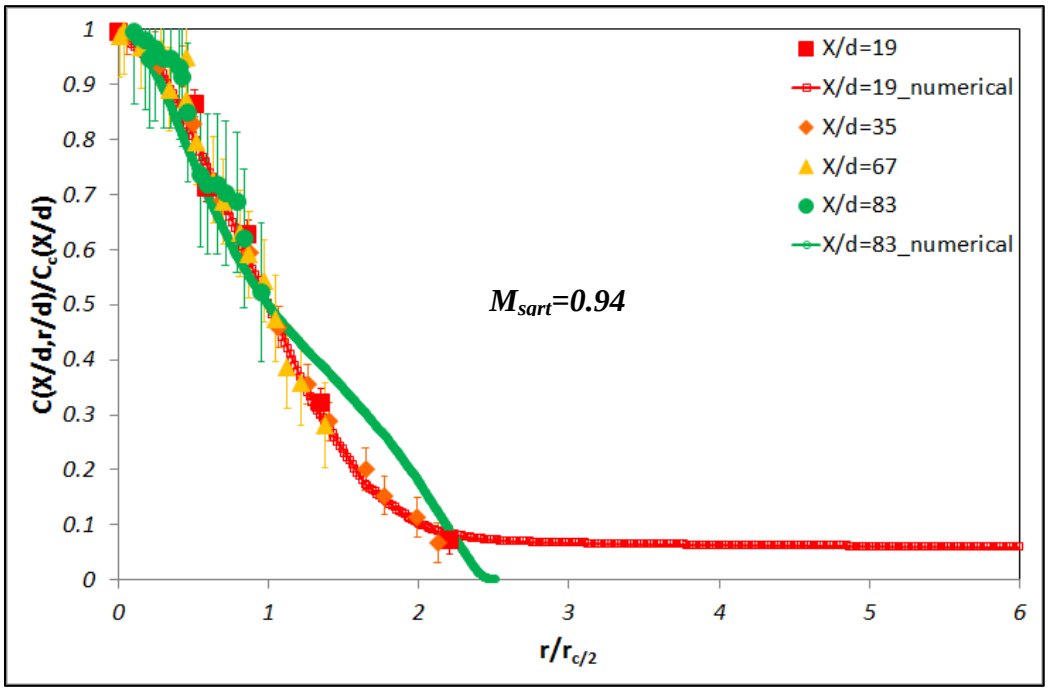

(k) U_{jet}=220.64m/s and U_{count}=3.123m/s

Figure 3.34 The radial concentration distribution

Our normalized radial concentration distributions are shown coherently (not spread out) in certain normalized axial direction which is depended on $\boldsymbol{M_{sqrt}}$. Therefore, a single curve equation [47] to be represented by a Gaussian function is derived through collapsing fairly well on the basis of experimental and numerical results. This equation is,

$$\overline{C} = \frac{C}{C_c} = \exp\left[-0.58 \left(r / r_{\frac{C}{2}} \right)^{1.5} \right] \tag{46}$$

The results find that the concentration fluctuation is increased as the jet flow moves along the axial direction due to the turbulent intensity. However, the concentration fluctuation is very small compared to the velocity fluctuation. This means that the concentration fluctuation has less affected by the turbulent intensity. From our equation of normalized ***NO*** concentration (46), it verifies that the self-similar region of the radial distribution of concentration also exists in counter-flow condition. Therefore, the profiles of the normalized concentration are able to express as a Gaussian function at only near some location from the jet exit.

3.2.3. The temperature distribution

To investigate the characteristics of temperature in the confined turbulent jet in counter-flow, the axial and the radial temperature distribution are studied as the function of ***X/d*** (***X***: axial location, ***d***: jet nozzle diameter) in this section. The graphs are plotted by using modified momentum ratios for verifying the effect of different counter-flow velocities at fixed jet velocity as well as the effect of different jet velocities at fixed counter-flow velocity.

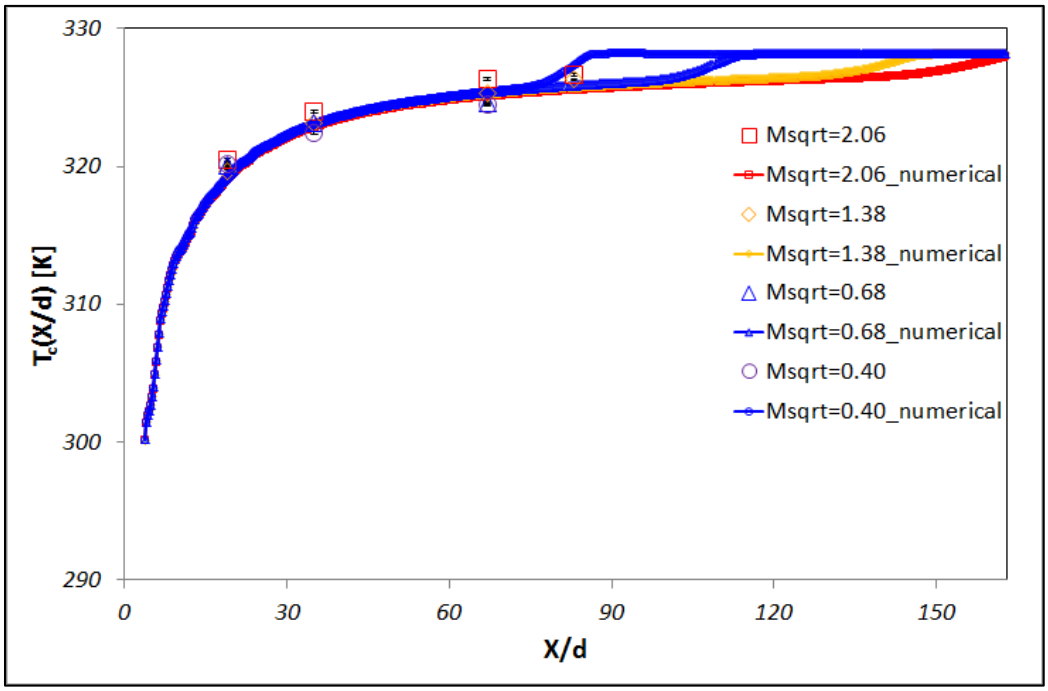

(a) U_{jet}=96.12m/s at different counter-flow velocities

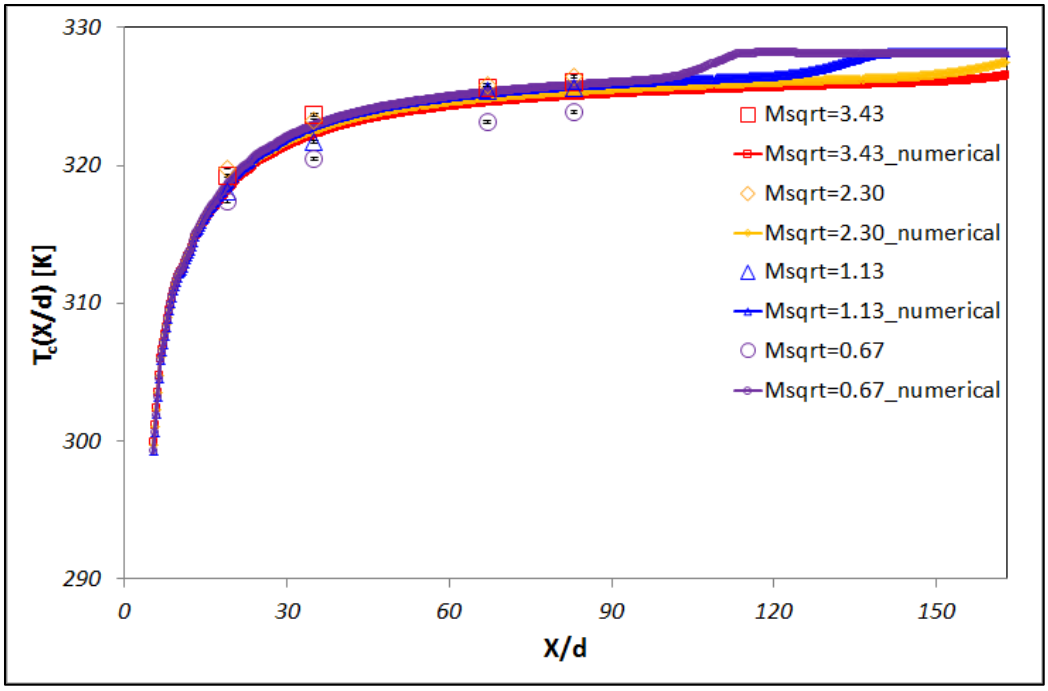

(b) U_{jet}=160.19m/s at different counter-flow velocities

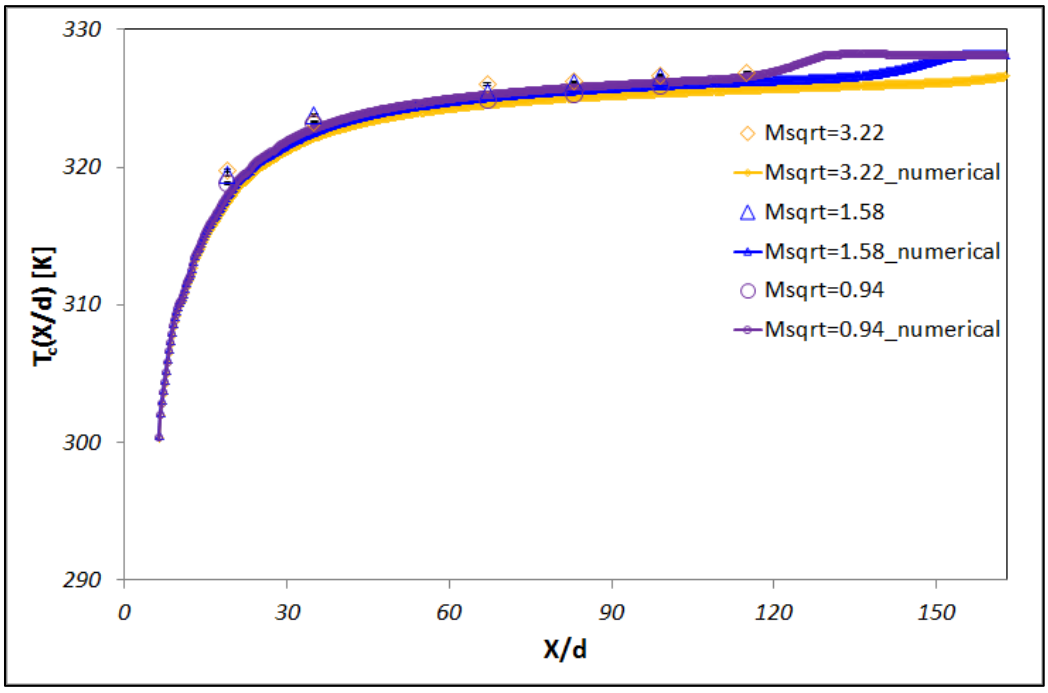

(c) U_{jet}=224.26m/s at different counter-flow velocities

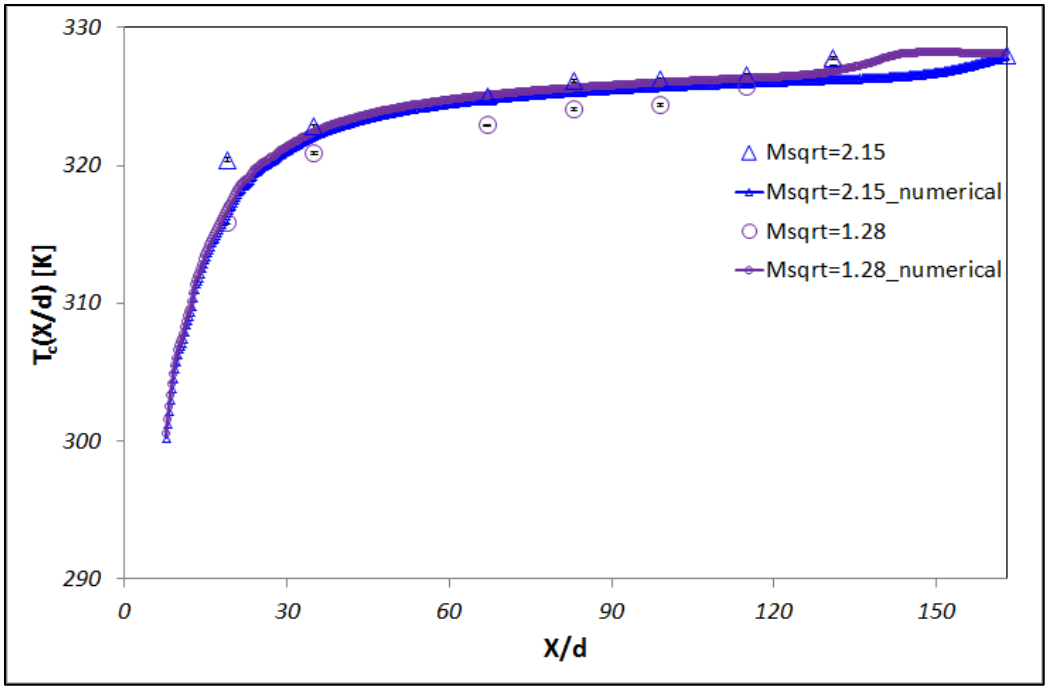

(d) U_{jet}=304.37m/s at different counter-flow velocities

Figure 3.35 The measured temperature along the axial direction at different counter-flows

The temperature profiles are shown in figure 3.35 at the fixed jet velocity and respectively different counter-flow velocities by using modified momentum ratios. $\boldsymbol{T_c}$ (centerline jet temperature) is plotted at the different normalized locations-$\boldsymbol{X/d}$ (where $\boldsymbol{X}$ is axial direction and $\boldsymbol{d}$ is jet nozzle diameter). The $\boldsymbol{T_c}$ is increased at high axial location due to moving to the stagnation plane or moving more closer to counter-flow region. The centerline temperature, $\boldsymbol{T_c}$, is converged to the single value as the jet flow moves along the axial direction. Therefore, the normalized temperature profiles are flat and stable at large axial distance because of the heat transfer from the stagnation plane. The stagnation plane usually divides two flows between a cold jet flow and a hot counter-flow. Therefore, it is difficult for the hot counter-flow to move the jet stream. Accordingly, the jet temperature is increased slowly in the first part of the jet due to insufficient heat transfer. The location of uniform centerline temperature moves downstream as modified momentum ratio increases because of the movement of stagnation plane.

Figure 3.36 shows the temperature profiles along the centerline at the fixed counter-flow and different center jet velocities by using $\boldsymbol{M_{sqrt}}$. The center temperature approaches an asymtote as the jet flow moves along the axial direction because of heat transfer and mixing. The same trends and levels are seen for different modified momentum ratios (different velocity conditions between the jet velocity and the counter-flow velocity). Also, at low modified momentum ratio in each figure, the centerline temperature has a near uniform temperature at smaller ***X/d*** due to location of stagnation plane. From these results, the stagnation location has significant role of making uniform temperature of confined turbulent jet flow into counter-flow.

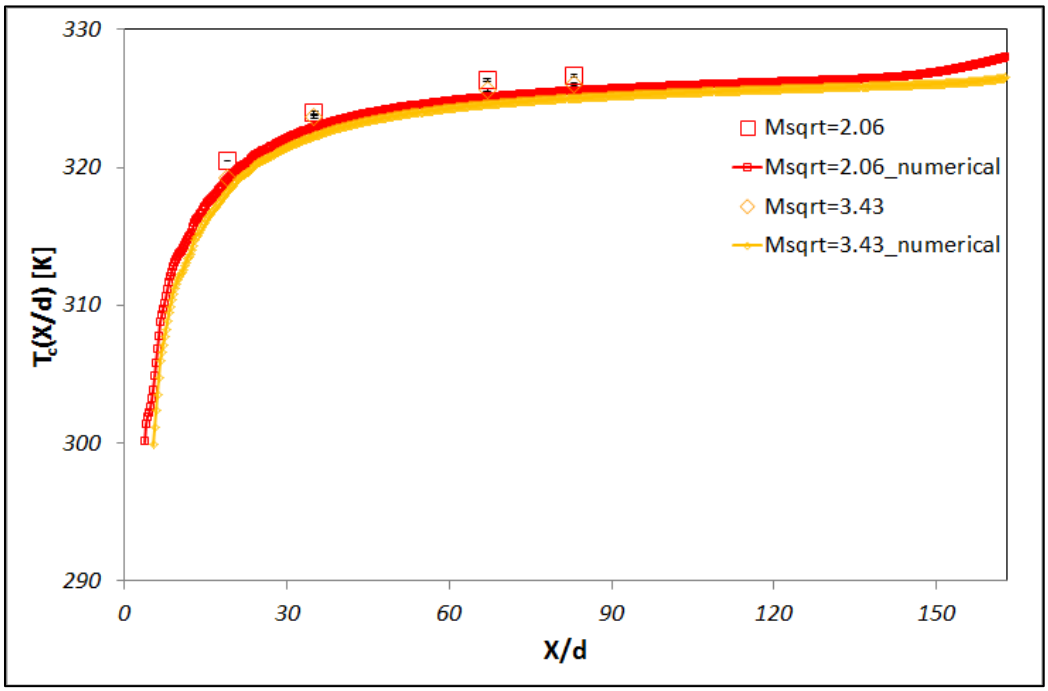

(a) U_{count}=0.612m/s at different jet velocities

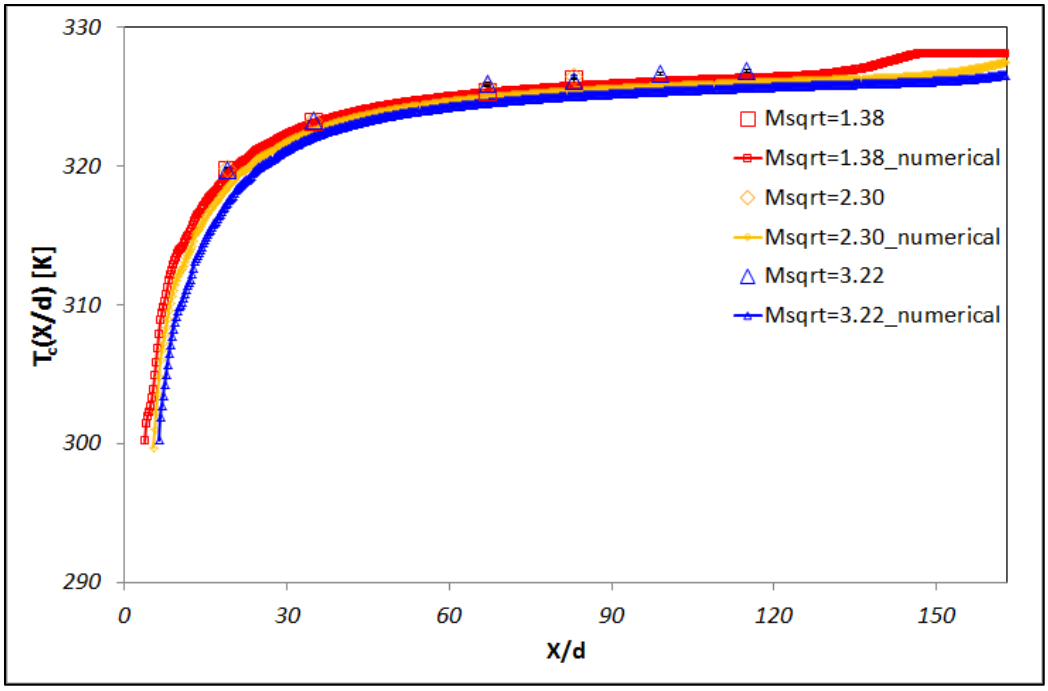

(b) U_{count}=0.913m/s at different jet velocities

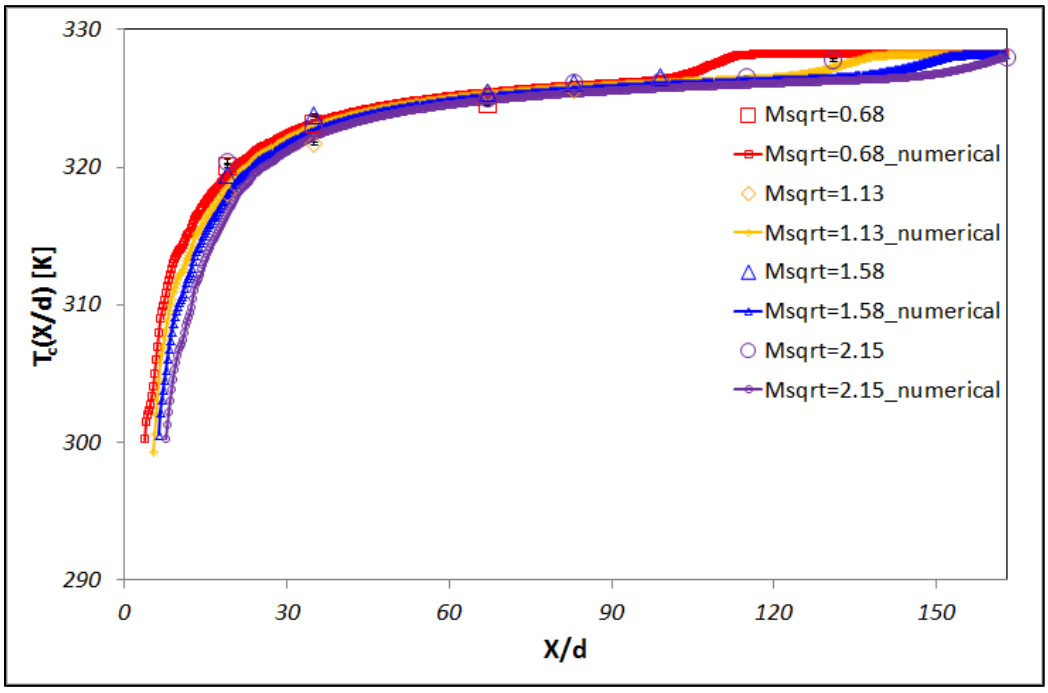

(c) U_{count}=1.856m/s at different jet velocities

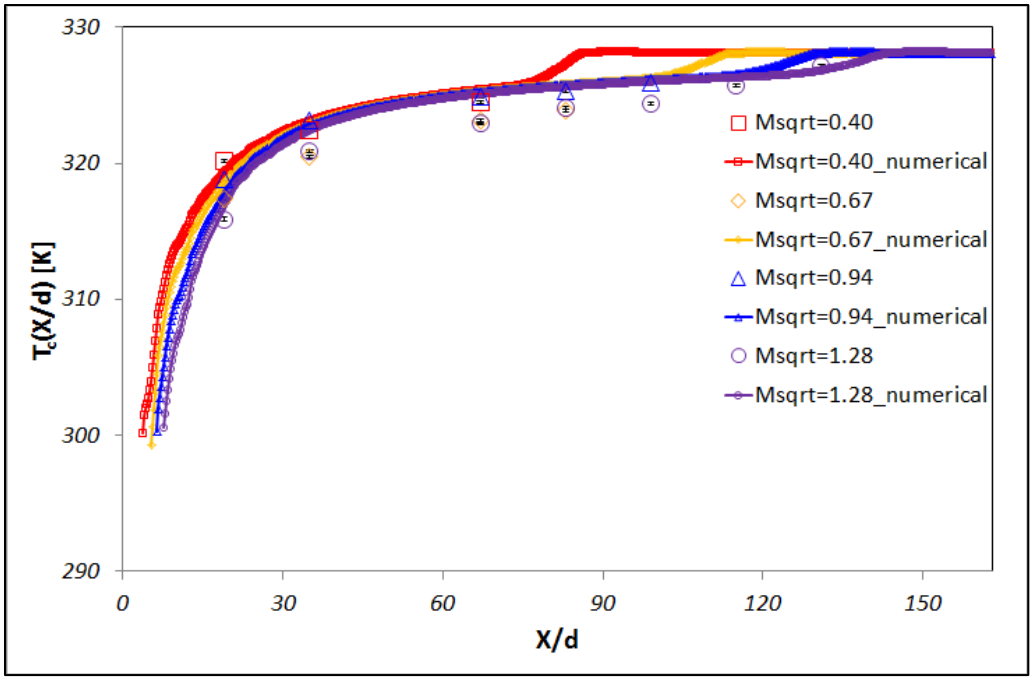

(d) U_{count}=3.123m/s at different jet velocities

Figure 3.36 The measured temperature along the axial direction at different jet velocities

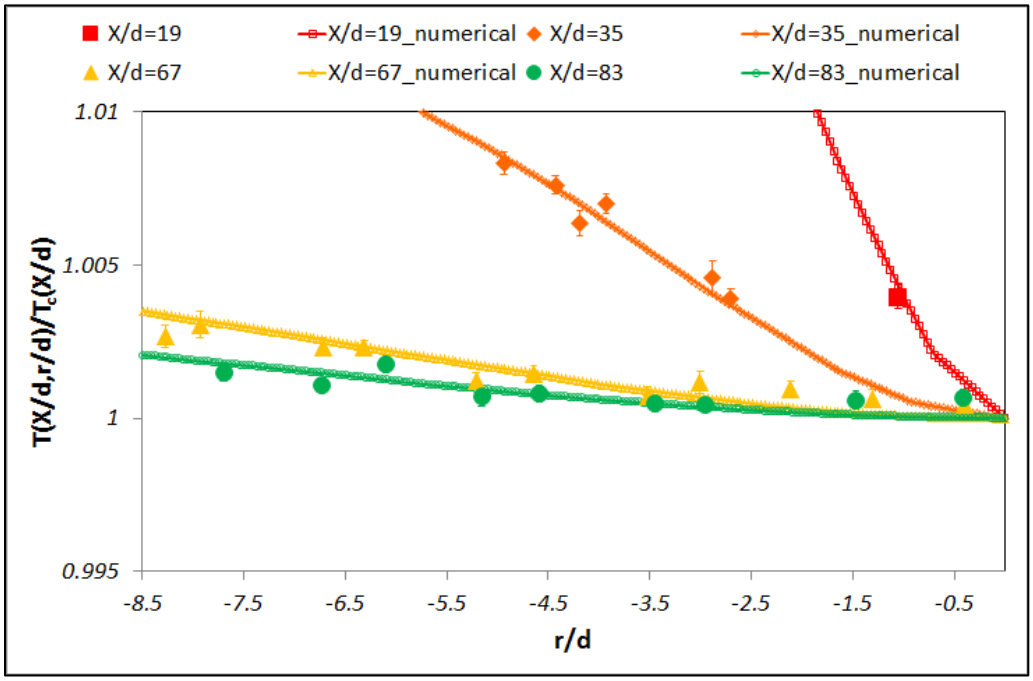

(a) M_{sqrt}=3.43

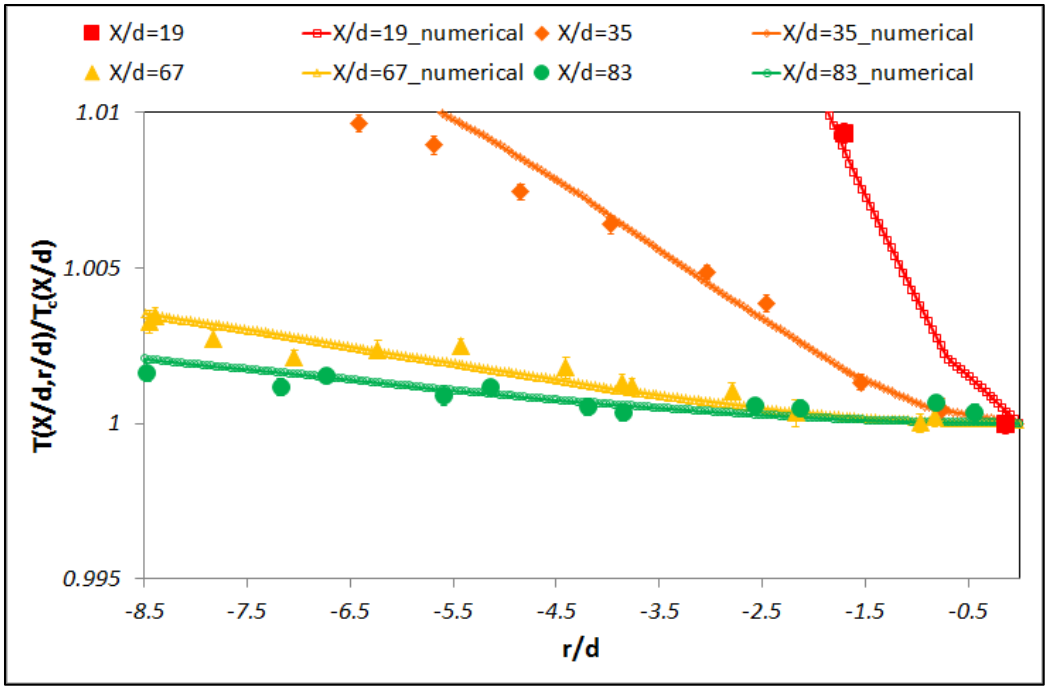

(b) M_{sqrt}=2.30

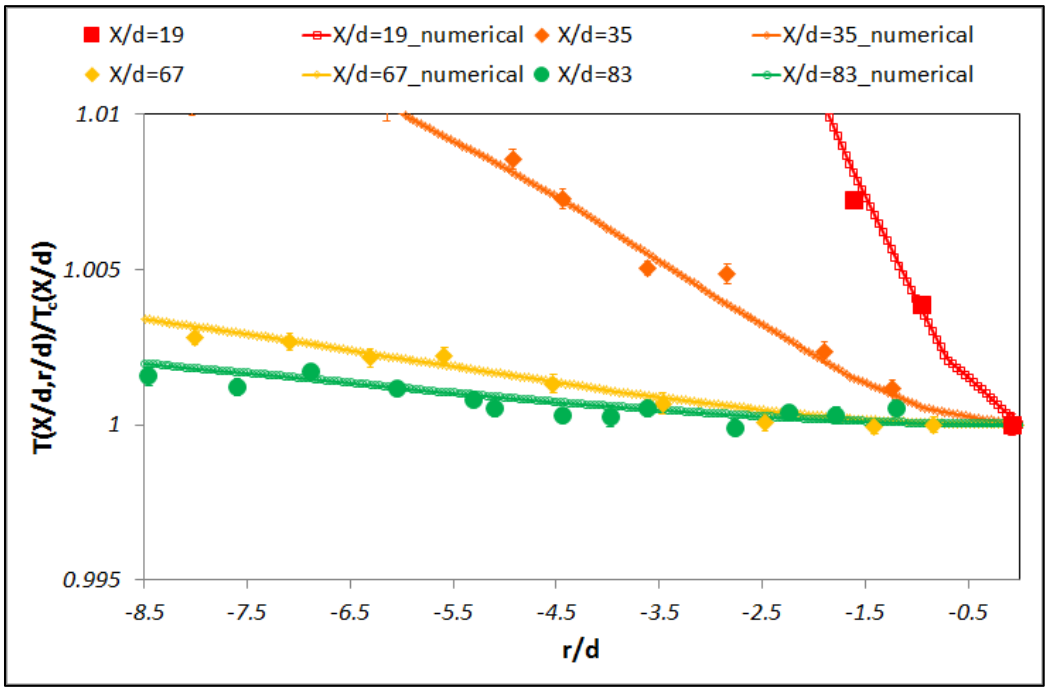

(c) M_{sqrt}=1.38

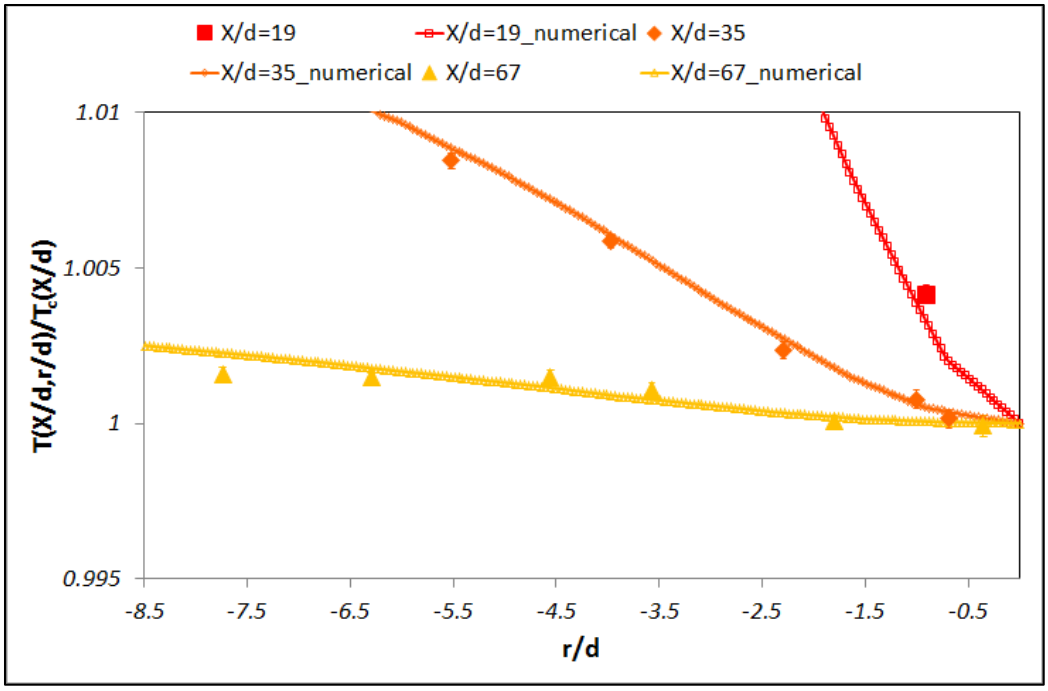

(d) M_{sqrt}=0.40

Figure 3.37 The measured temperature along the radial direction

The normalized radial temperature distributions (***r***: radial direction, ***d***: jet nozzle diameter, T_c: temperature at the centerline) are plotted in figure 3.37. From figure 3.37, as the jet flow moves along the axial direction, the temperature profiles are more uniform usually at ***X/d***=67 due to the turbulent mixing and heat transfer between the cold turbulent jet and the hot counter-flow. The radial temperature distribution becomes uniform slightly faster as the modified momentum ratio decreases because the hot counter-flow must be increased for making small value of modified momentum ratio (M_{sqrt}) as well as movement of stagnation plane. Therefore, the case of low value of M_{sqrt} has enough thermal energy for making uniform profiles of temperature.

3.2.4. The width

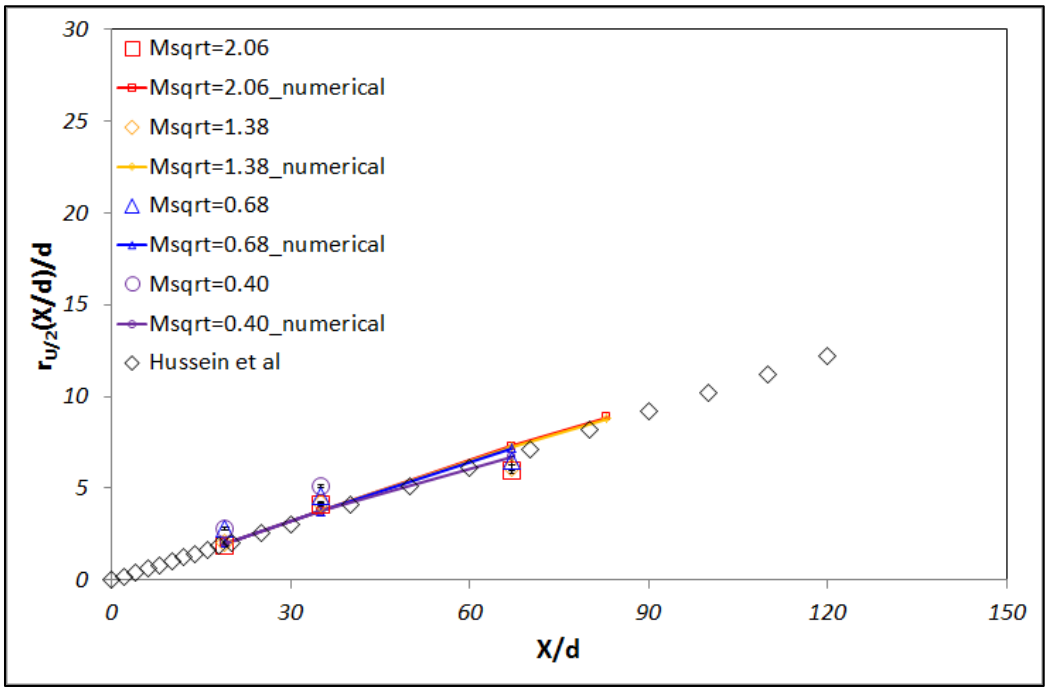

(a) U_{jet}=96.12m/s at different counter-flow velocities

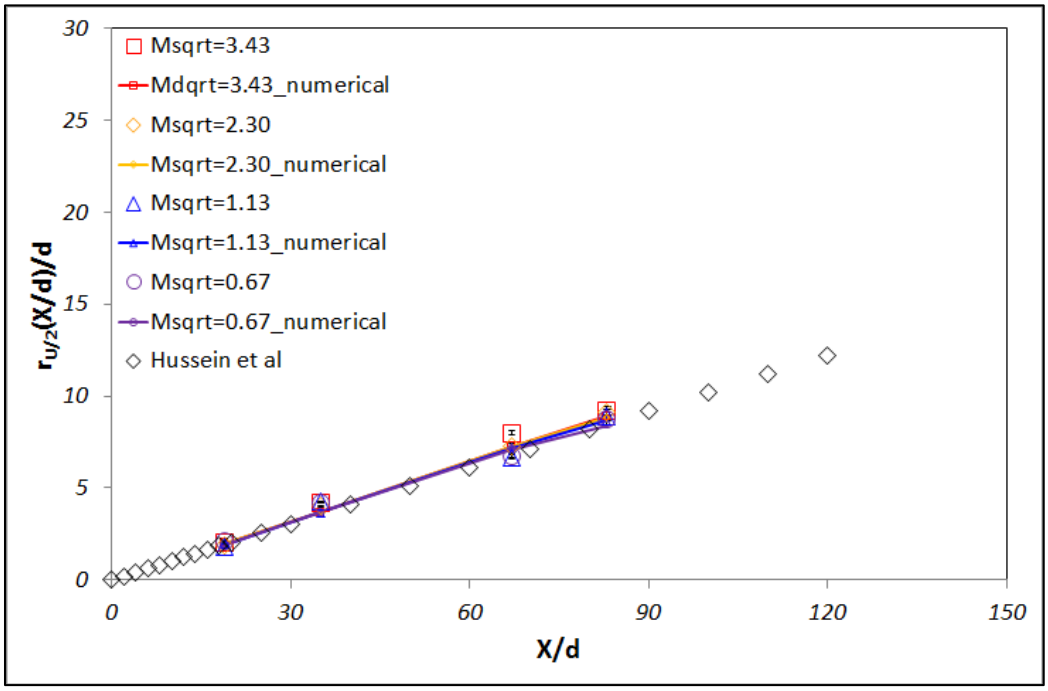

(b) U_{jet}=160.19m/s at different counter-flow velocities

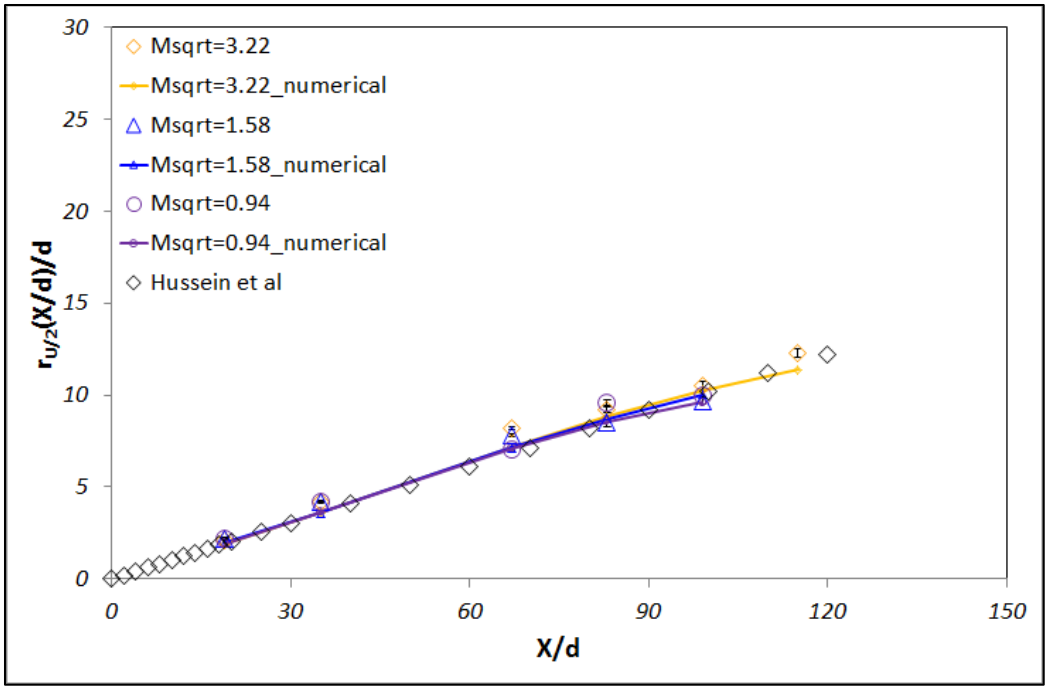

(c) U_{jet}=224.26m/s at different counter-flow velocities

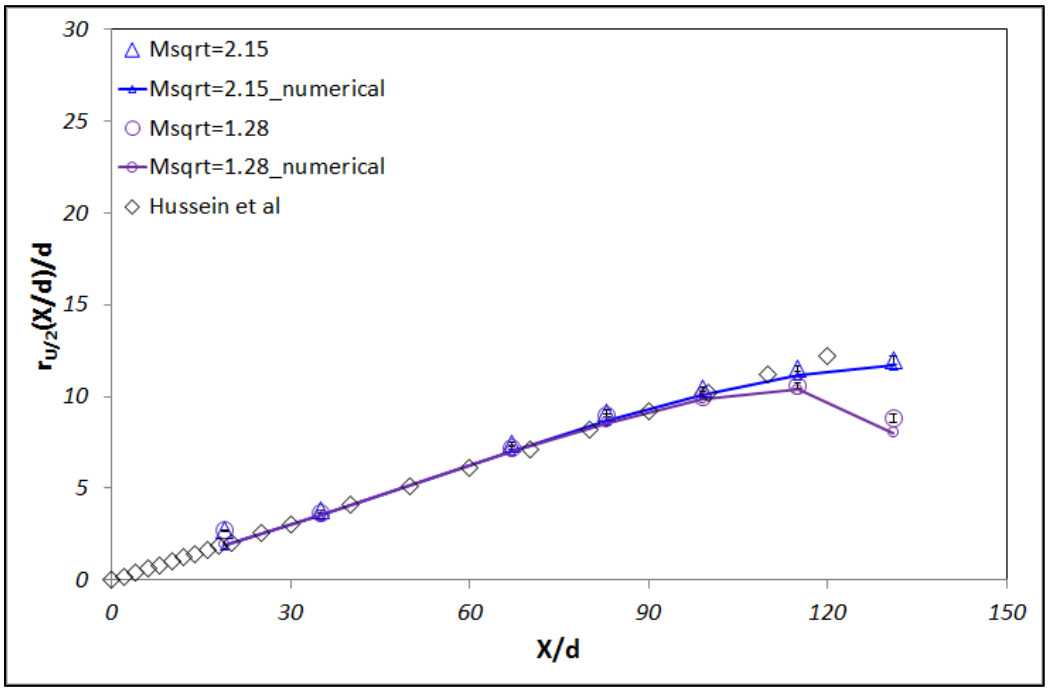

(d) U_{jet}=304.37m/s different counter-flow velocities

Figure 3.38 The measured jet width at half jet velocity

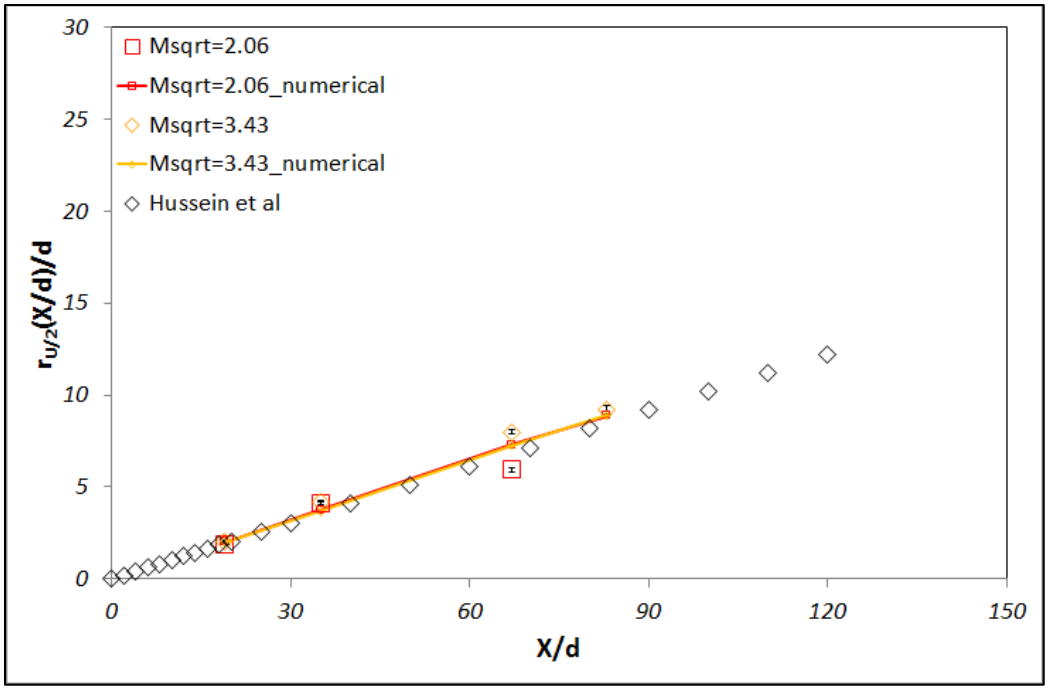

(a) U_{count}=0.612m/s at each different jet velocities

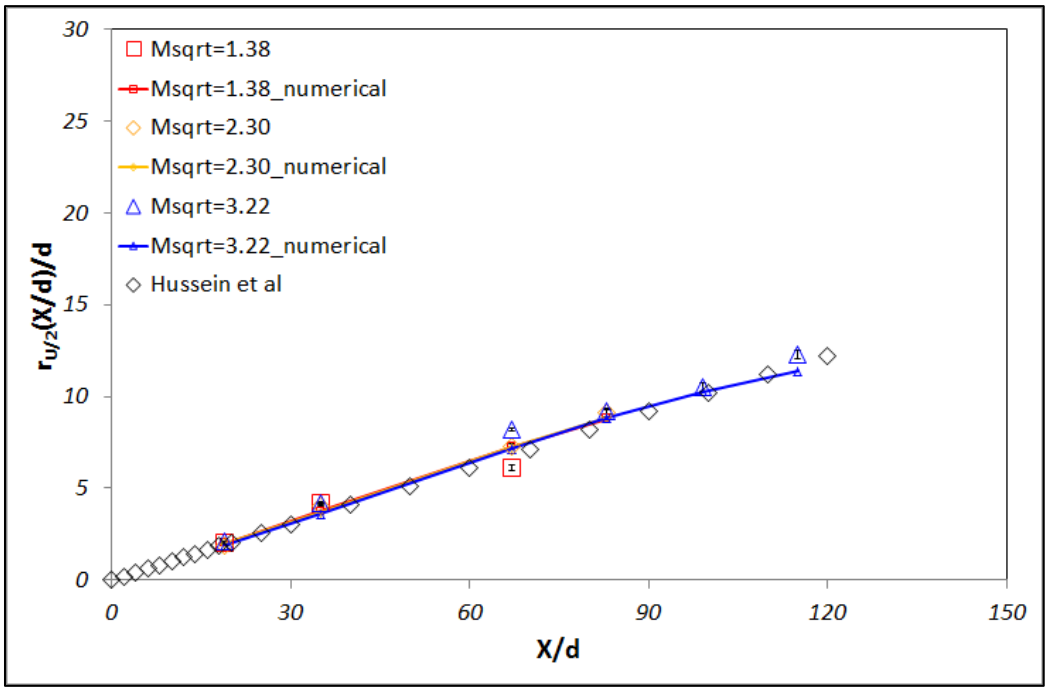

(b) U_{count}=0.913m/s at each different jet velocities

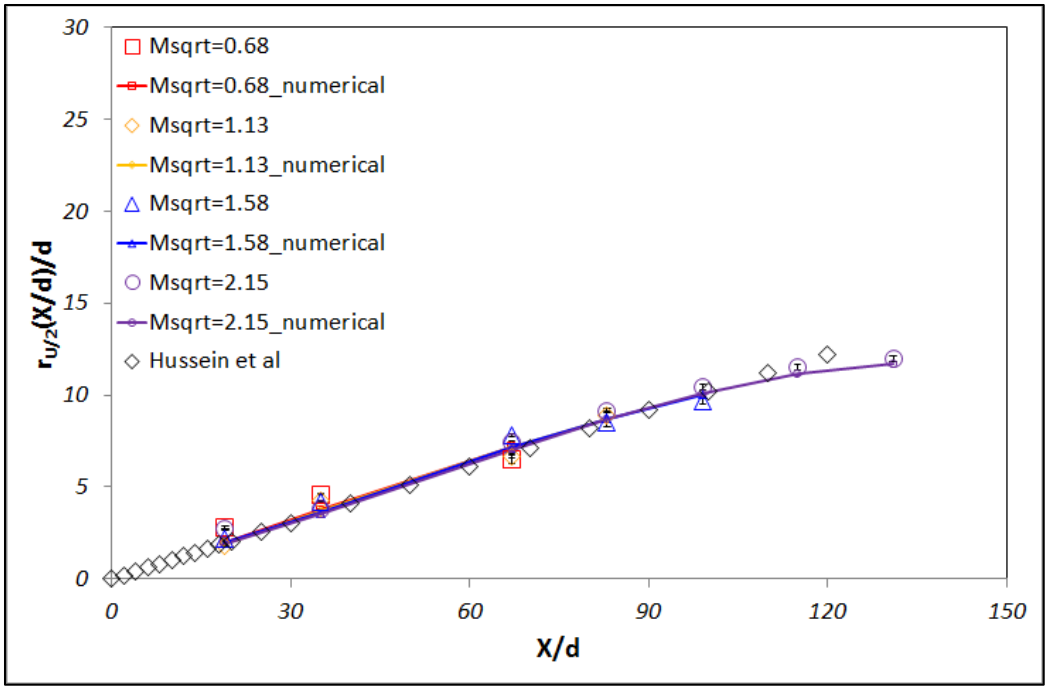

(c) U_{count}=1.856m/s at each different jet velocities

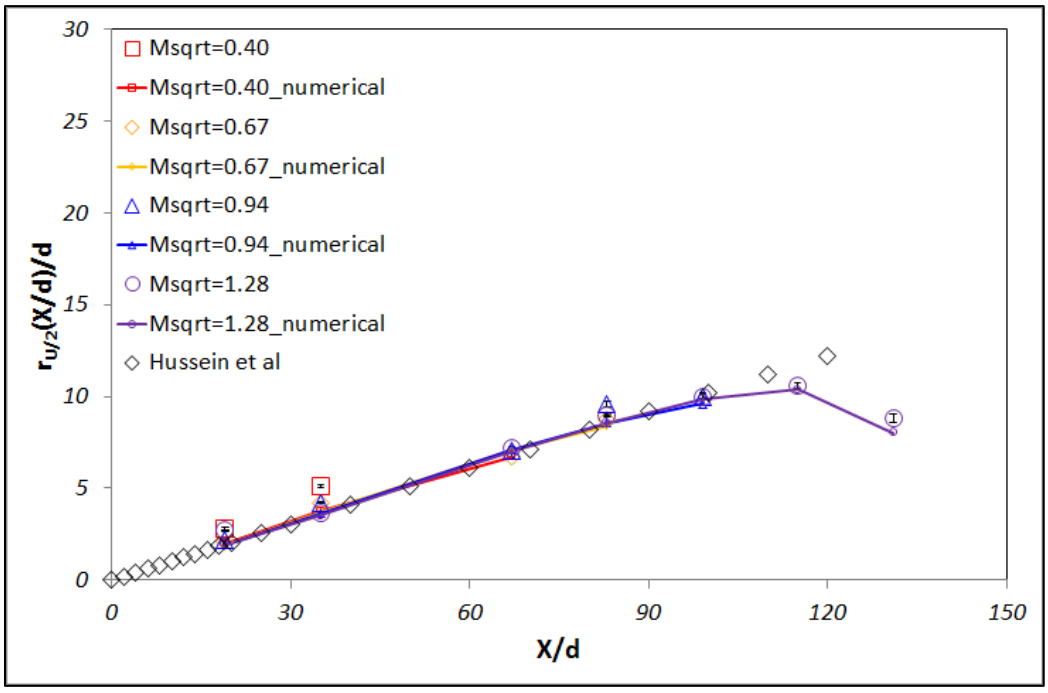

(d) U_{count}=3.123m/s at each different jet velocities

Figure 3.39 The measured jet width at half jet velocity

Figure 3.38 and 3.39 show the measured jet widths of half jet velocity. The widths in figure 3.38 are defined at fixed jet velocity and different counter-flows. Figure 3.39 shows that the widths are plotted at fixed counter-flow velocity and different jet velocities. The jet width of half jet velocity increases as the jet flow moves along the axial direction due to the entrainment and mixing between the jet and counter flow. One previous result, Hussein et al. [56], in the free turbulent jet condition is plotted in each graph for comparing our test result. The measured width of half jet velocity matches well with the results from the free boundary condition. As the momentum ratio and the axial location increase, there are some deviations between current result and the result of the free turbulent jet [56] due to counter-flow effects. From figure 3.38 and 3.39, the widths are increased linearly as the jet flow moves downstream. There is no significant difference in spite of different modified momentum ratios. However, physically, the case of the low counter-flow (high modified momentum ratio) causes small width of the jet flow because the width is usually produced not by colliding but by the spreading characteristics of jets. Therefore, there are some other factors to influence on the jet width of half jet velocity at the confined turbulent jet in the counter-flow. Accordingly, we conclude that the half width of jet velocity is mainly caused by the mixing similar to the conclusions from considering concentration and temperature profiles. In the case of $\boldsymbol{M_{sqrt}}$=1.28 ($\boldsymbol{U_j}$=304.37m/s and $\boldsymbol{U_{count}}$= 3.123m/s), the width of half jet velocity is increased linearly up to $\boldsymbol{X/d}$=120 but decreased at $\boldsymbol{X/d}$=131 because of the location of stagnation plane. That means that the high jet flow condition results in a high fluctuation and an intermittency of a jet region near the stagnation plane and this flow region also becomes unstable in figure 3.43 and 3.49.

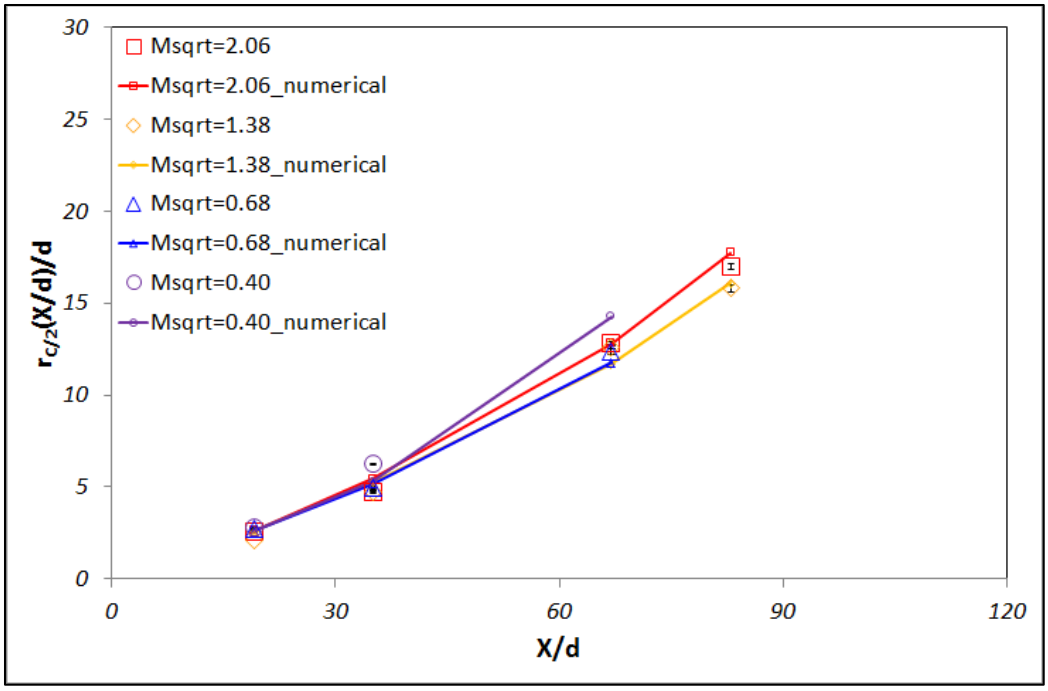

(a) U_{jet}=96.12m/s at different counter-flow velocities

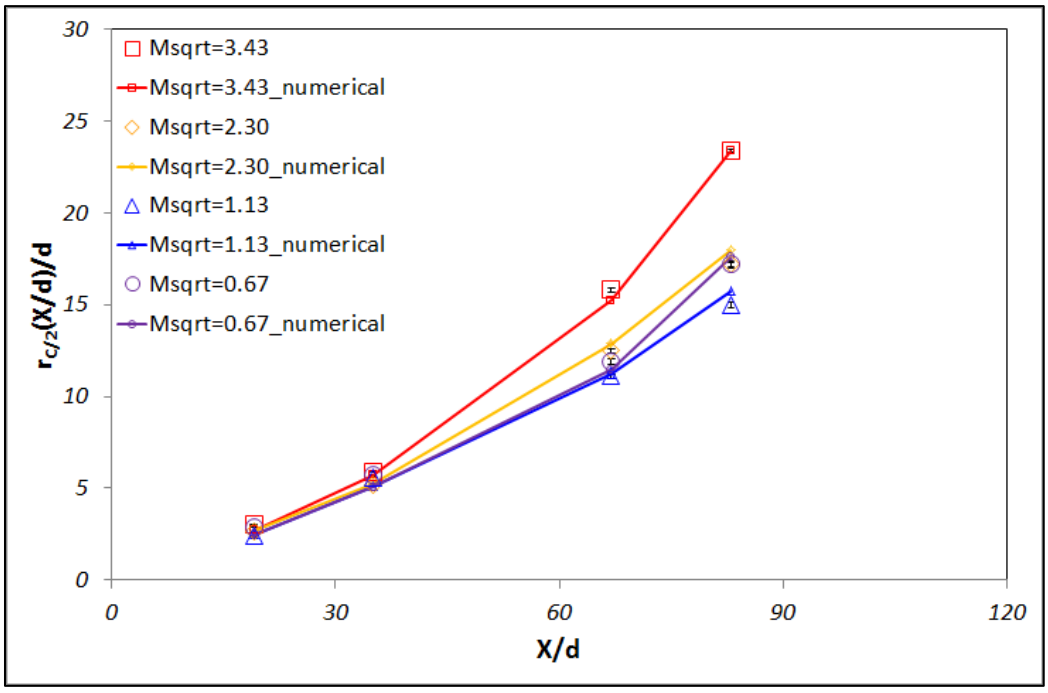

(b) U_{jet}=160.19m/s at different counter-flow velocities

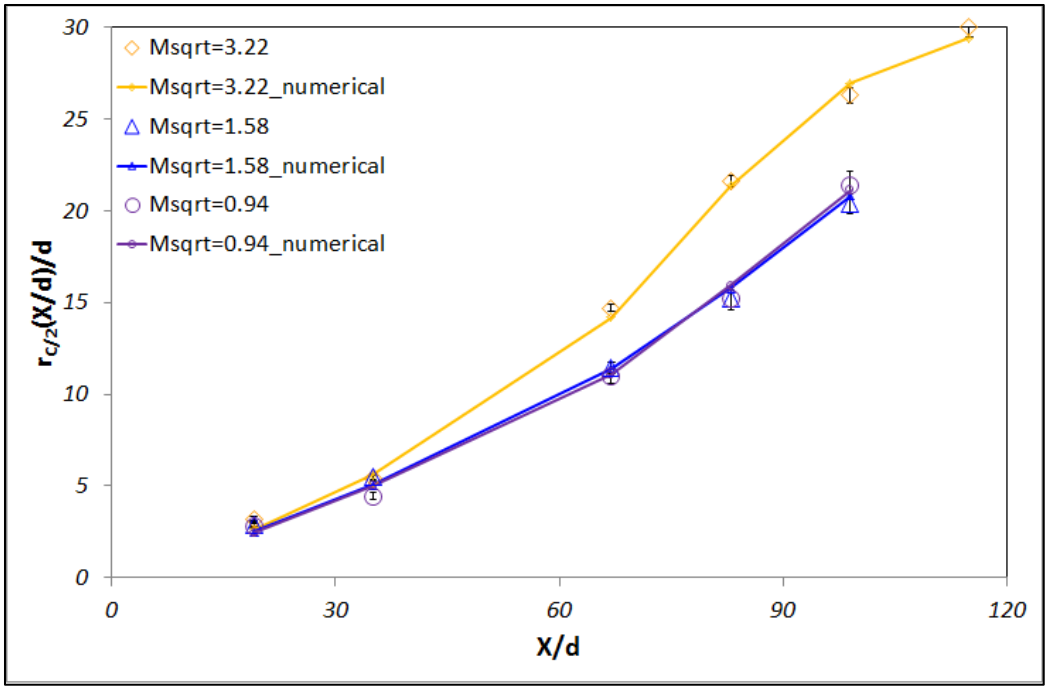

(c) U_{jet}=224.26m/s at different counter-flow velocities

Figure 3.40. The measured concentration width at half concentration

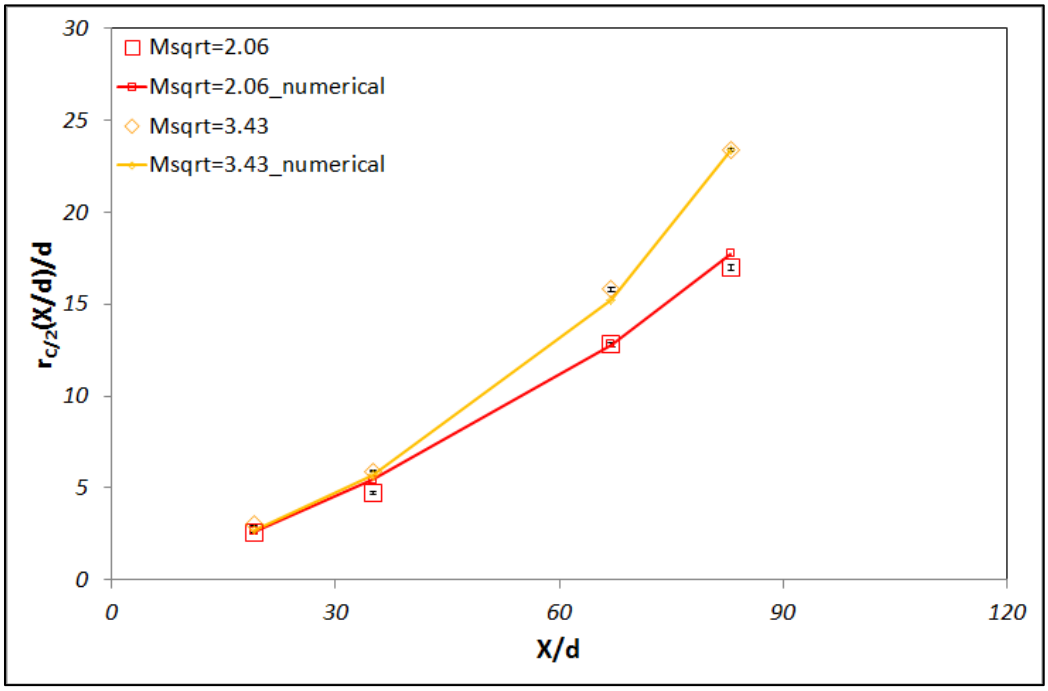

(a) U_{count}=0.612m/s at each different jet velocities

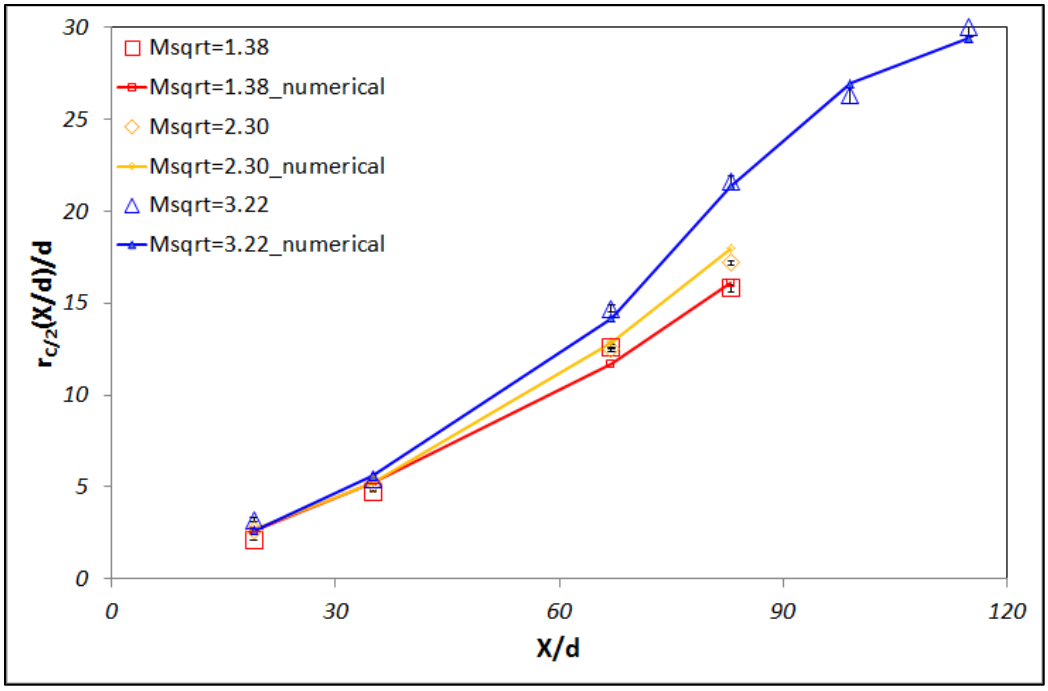

(b) U_{count}=0.913m/s at each different jet velocities

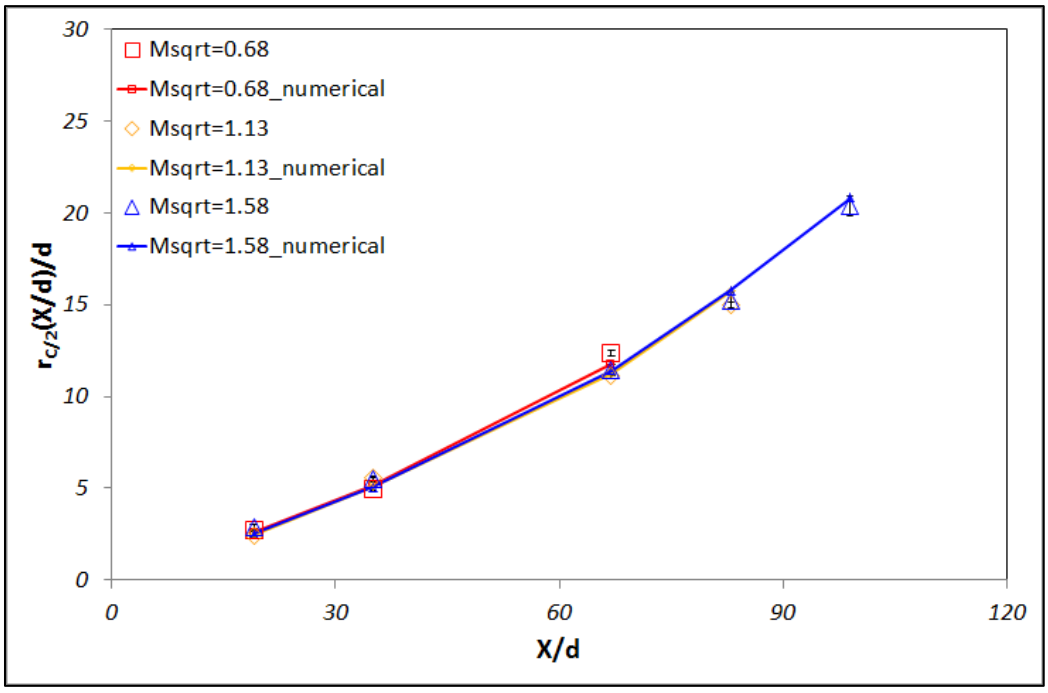

(c) U_{count}=1.856m/s at each different jet velocities

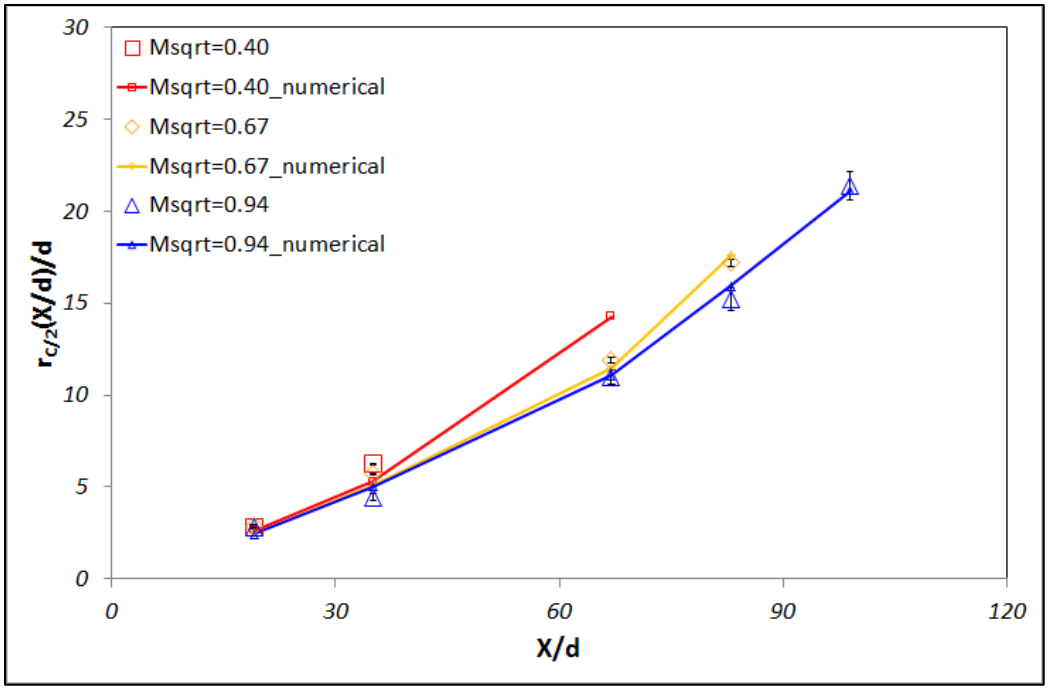

(d) U_{count}=3.123m/s at each different jet velocities

Figure 3.41. The measured concentration width at half concentration

From figure 3.40 and 3.41, the experimental and numerical concentration width of half value of initial ***NO*** concentration is shown. The width of half ***NO*** concentration in figure 3.40 and 3.41 is plotted respectively at fixed jet velocity with different counter-flows and at fixed counter-flow velocity with different jet velocities. The half ***NO*** concentration width is increased as the jet flow moves along the normalized axial direction (***X/d***) because of the stagnation plane by the interaction between jet flow and counter-flow as well as the characteristics of jet spreading. From figure 3.41, the normalized half ***NO*** concentration width is almost similar value below ***X/d***=60 in spite of different modified momentum ratios or different velocity conditions between jet and counter-flow velocities. However, after ***X/d*** is 60 (where ***X*** is axial location and ***d*** is jet nozzle diameter), the value of the width of half ***NO*** concentration spreads out at each different modified momentum ratio. Current results show that the widths of half ***NO*** concentration have usually much larger values as modified momentum ratio increases at fixed jet

velocity with different counter-flows. This means that the width of half ***NO*** concentration is increased at low counter-flow with fixed jet velocity. This is also same conclusion from the width of half jet velocity. Therefore, also, the mixing movement has the effect on the width of half ***NO*** concentration at the confined turbulent jet in counter-flow. There is the same trend (not highly spread-out) at fixed counter-flow with different jet velocities. Also, the value of the widths of half ***NO*** concentration increase at higher modified momentum ratio. However, at fixed $\boldsymbol{U_{count}}$=3.123m/s, the width of ***NO*** concentration is decreased at higher modified momentum ratio. Therefore, also, the jet velocity has significant role at higher counter-flow velocity. Generally, the width of half ***NO*** concentration is more influenced by the mixing movement of counter-flow.

3.2.5. The stagnation plane as well as penetration length

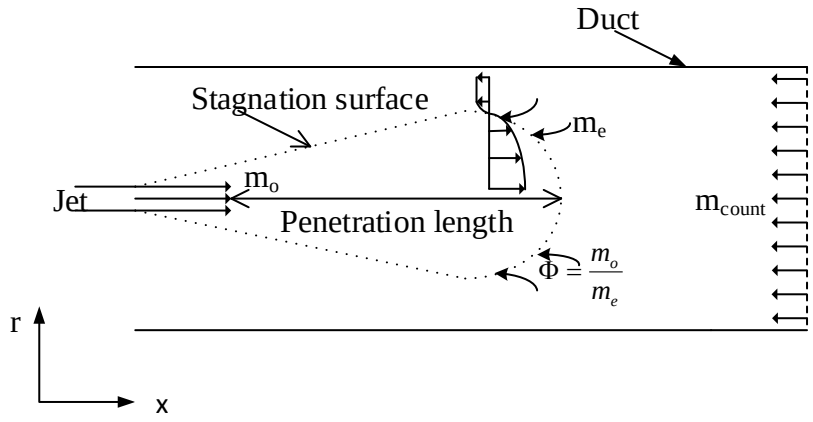

Figure 3.42 Flow configuration for the explanation of stagnation surface

To study the role of the stagnation plane in confined turbulent jet flow into counter-flow, two terminologies are defined as stagnation surface or plane and penetration length in figure 3.42. From figure 3.43, as modified momentum ratio increase, the stagnation surface is enlarged and moved into the region of counter-flow further due to higher $\boldsymbol{U_{jet}}$ or smaller $\boldsymbol{U_{count}}$.

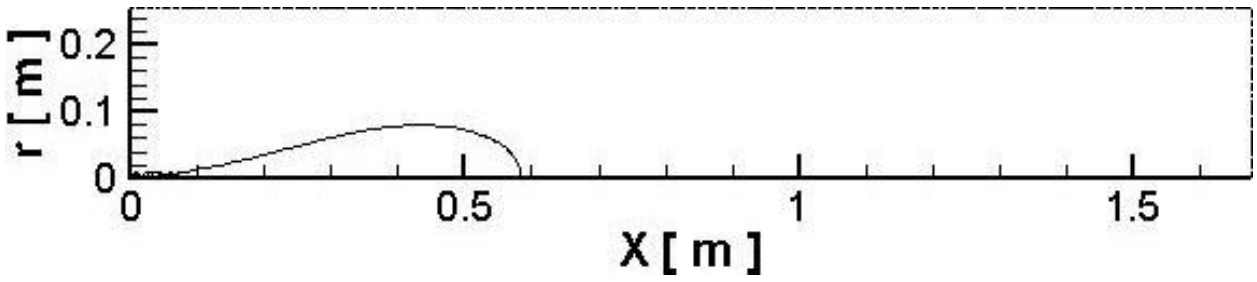

(a) $\boldsymbol{M_{sqrt}}$=0.40

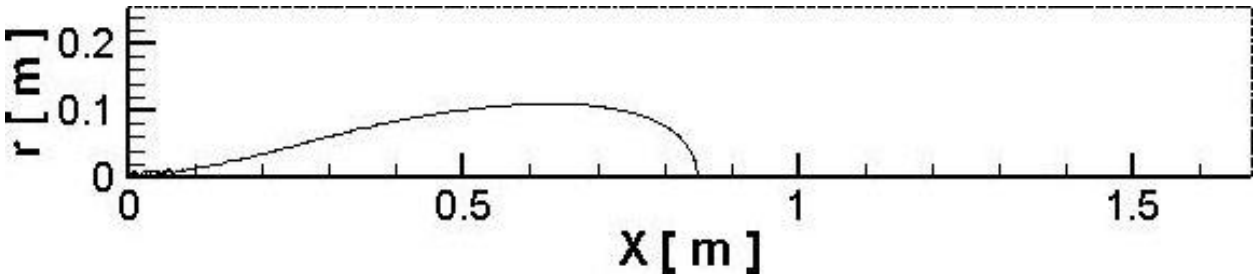

(b) $\boldsymbol{M_{sqrt}}$=0.94

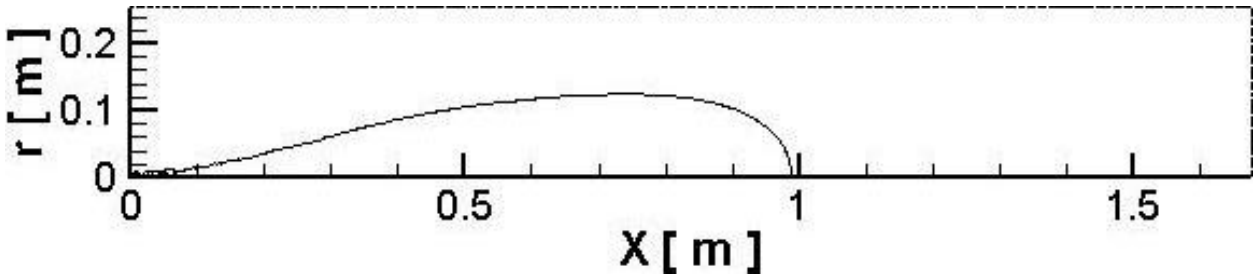

(c) M_{sqrt}=1.58

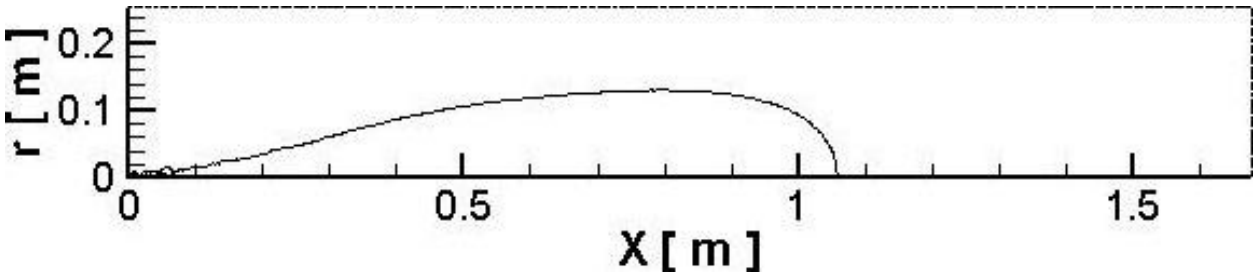

(d) M_{sqrt}=2.15

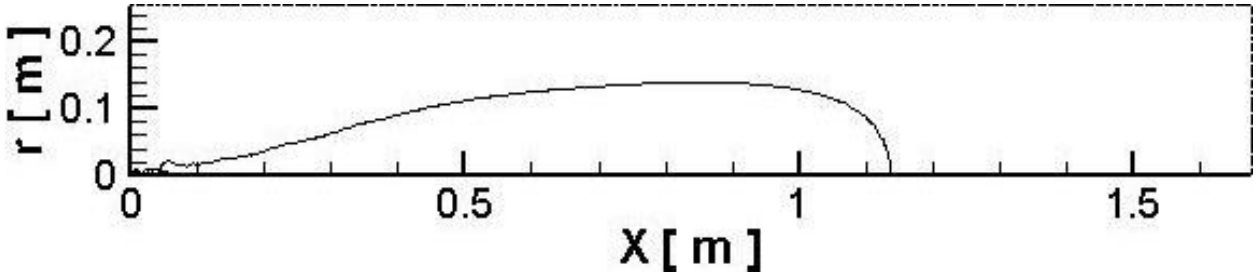

(e) M_{sqrt}=3.43

Figure 3.43 Stagnation surface at different modified momentum ratios

To check the penetration length, computed penetration length (X_p) is defined at different velocity ratios and $U_{jet}d_j/U_{count}D_o$ in figure 3.44. The penetration length is normalized by using jet nozzle diameter (d_j) or duct diameter (D_o). The recent numerical study of penetration length done by Sivapragasam et. al [58](in isothermal and incompressible condition) is plotted for comparison in figure 3.44. Penetration length is increased as modified momentum ratio is increased due to high jet velocity or low counter-flow velocity. Finally, the penetration length approaches a constant value as modified momentum ratio increases. This is the same conclusion in stagnation surface in spite of the isothermal and incompressible conditions.

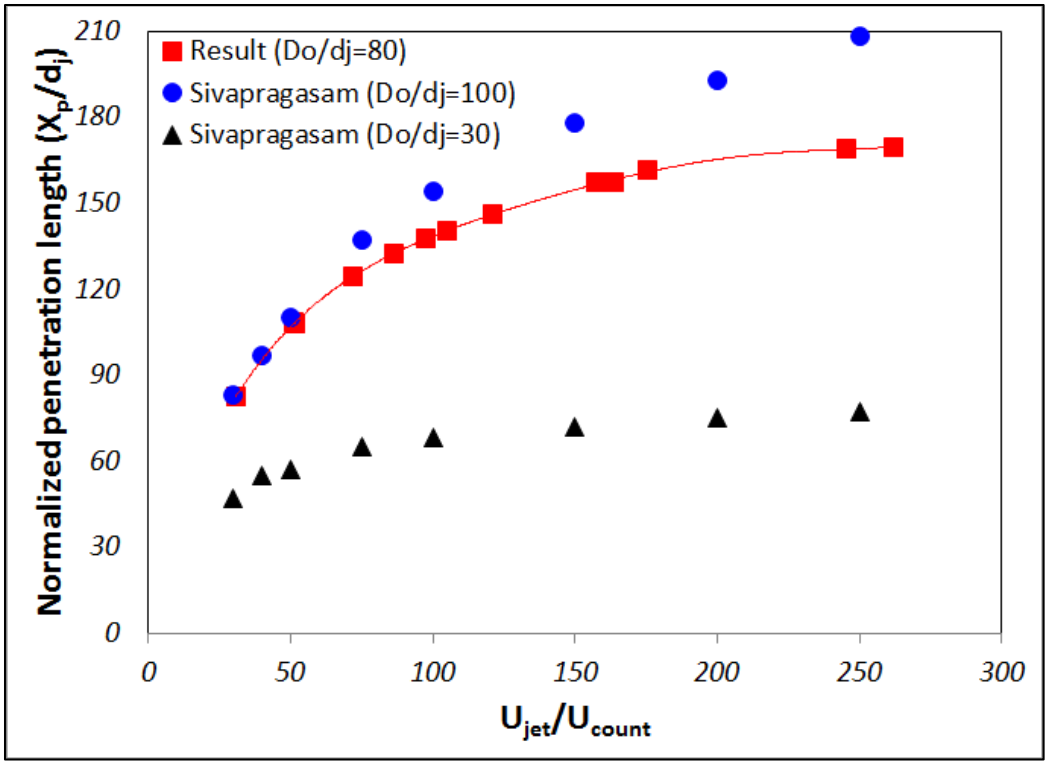

(a) X_p/d_j as function of velocity ratio (U_{jet}/U_{count})

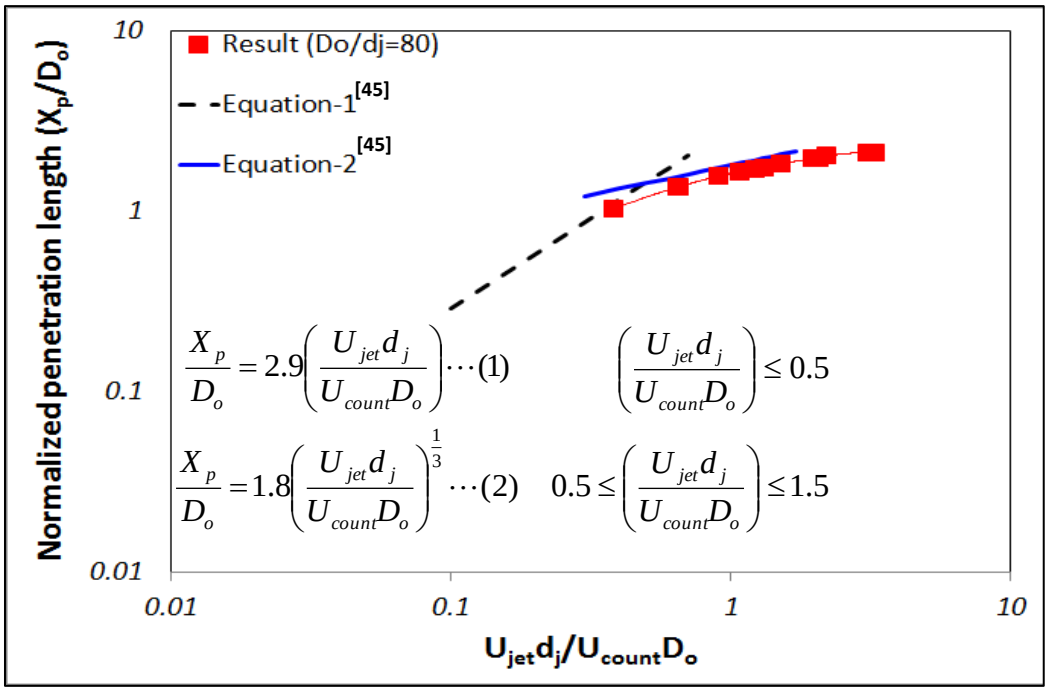

(b) X_p/D_o as function of $U_{jet}d_j/U_{count}D_o$

Figure 3.44. Computed penetration length at different velocity ratios and $U_{jet}d_j/U_{count}D_o$

3.2.6. The effect of high counter-flow temperature

The high temperature of counter-flow (1200K) effects on the characteristics of stagnation plane and penetration length (red circle) is considered in this section numerically. Also, two conditions such as constant counter-flow velocity and constant counter-flow mass were selected. $\boldsymbol{U_{jet}}$=160.19m/s and $\boldsymbol{U_{co}}$=1.856m/s is used as reference value. Three different modified momentum ratios are found such as $\boldsymbol{M_{sqrt}}$=1.13 at $\boldsymbol{T_{counter}}$=328.15K as reference, $\boldsymbol{M_{sqrt}}$=6.57 at $\boldsymbol{T_{counter}}$=1200K (constant counter-flow velocity) and $\boldsymbol{M_{sqrt}}$=1.80 at $\boldsymbol{T_{counter}}$=1200K (constant counter-flow mass). In figure 3.45, the penetration length is showed. There is not any difference among the estimation at different counter-flow temperature. As a result, the buoyancy does not have any significant effect on the penetration length.

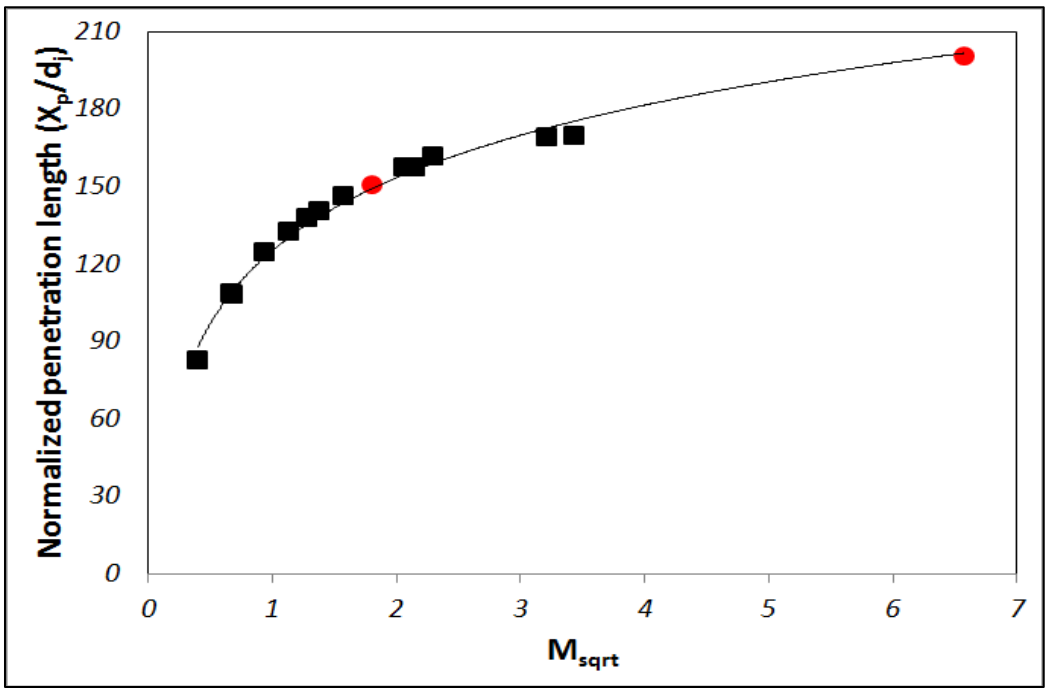

Figure 3.45 Penetration length at high counter-flow temperature

3.2.7. The entrainment

For studying the entrainment, the entrainment ratio is used as follow in figure 3.46.

$$\Phi_e = \frac{m_o}{m_e} \tag{47}$$

Where $\boldsymbol{m_o}$ is the initial mass coming from the jet at the center location, $\boldsymbol{m_e}$ is the entrained mass at certain position into center area of the jet and $\boldsymbol{m_{count}}$ is the mass coming from counter-flow. The entrainment at the confined turbulent jet in counter-flow is studied through considering different counter-flow velocities at fixed jet velocity and different jet velocities at fixed counter-flow velocity. For calculating the entrainment ratio, the initial mass from jet ($\boldsymbol{m_o}$) is normalized by using the entrainment mass ($\boldsymbol{m_e}$) and expressed as the different normalized locations ($\boldsymbol{X/d}$).

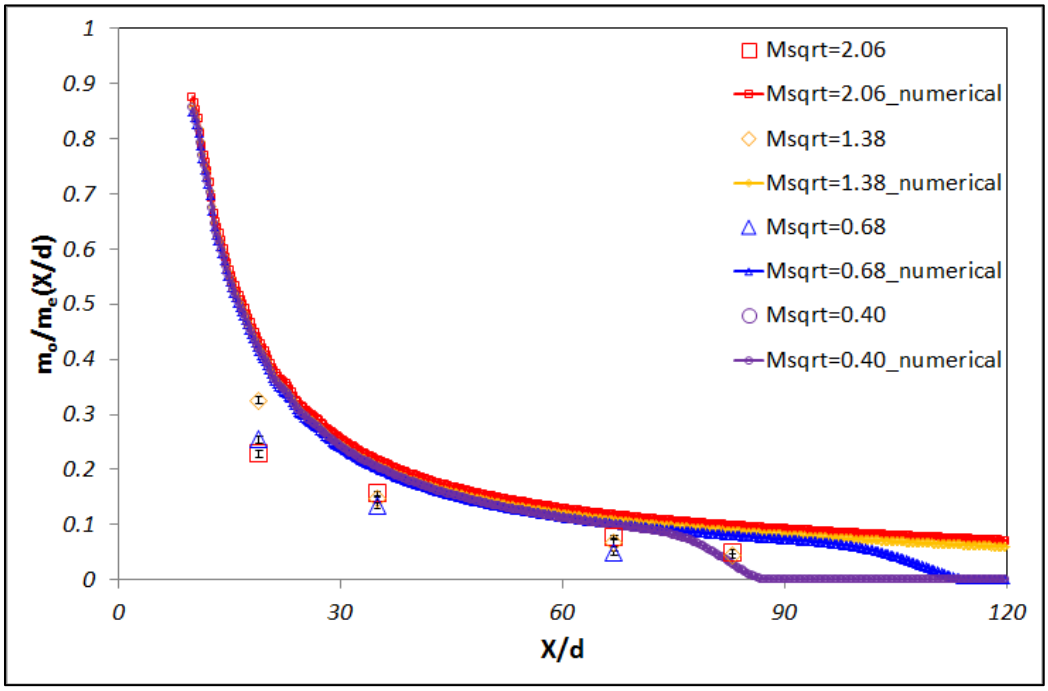

(a) U_{jet}=96.12m/s at different counter-flow velocities

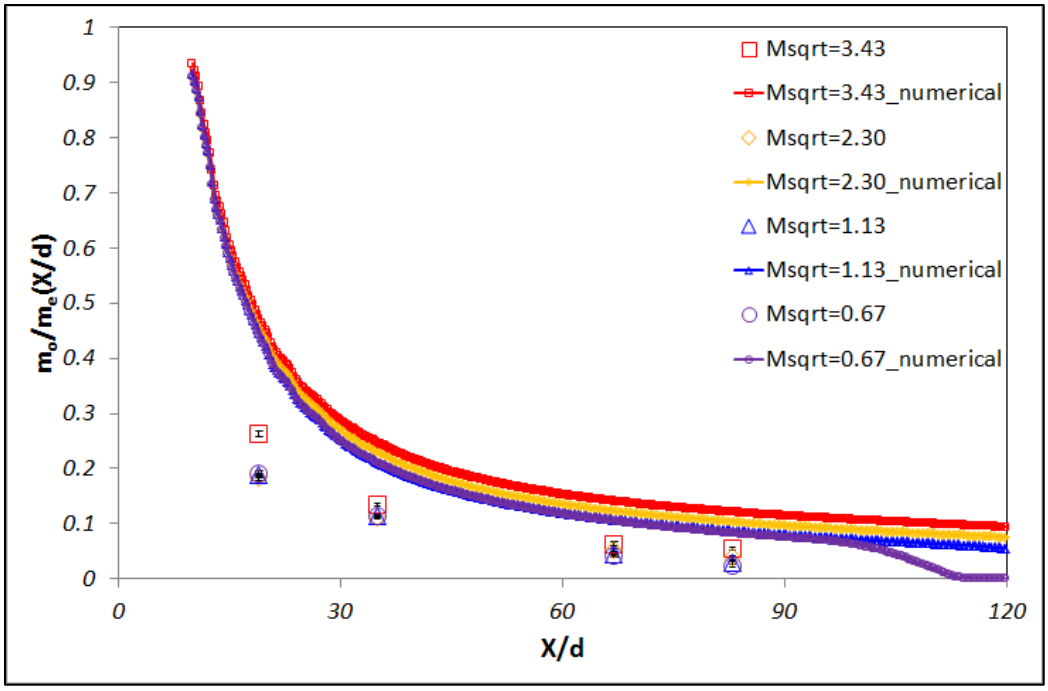

(b) U_{jet}=160.19m/s at different counter-flow velocities

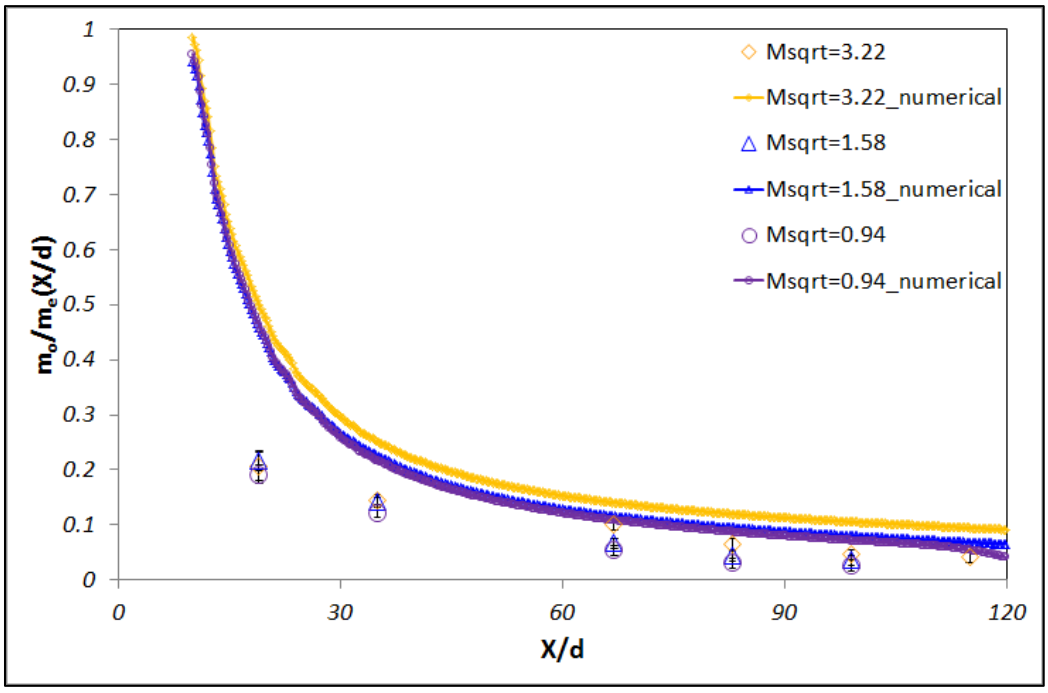

(c) U_{jet}=224.26m/s at different counter-flow velocities

Figure 3.46 The measured entrainment

Modified momentum ratios are used for representing the velocity conditions between jet and counter-flow at each plot in figure 3.46. The comparison shows that there are almost similar values between measured results and numerical results. Usually, the entrainment is increased at high axial location by the flow interactions between the jet and the counter-flow. The entrainment ratio is decreased relatively faster at low modified momentum ratios ($\boldsymbol{M_{sqrt}}$) in each graph because of the effect of high counter-flow such as better mixing by stronger interaction between the jet and the counter-flow. Also, the entrainment ratio is influenced by the effect of the counter-flow. Also, this difference between measured results and results from numerical calculation is increased as high jet velocity and is decreased at higher axial location respectively. The measured entrainment ratio is decreased as the counter-flow velocity increases at fixed jet velocity. This phenomenon is already explained by concentration profiles (due to the mixing movement by counter-flow effect). As a result, the entrainment ratio is usually highly changed.

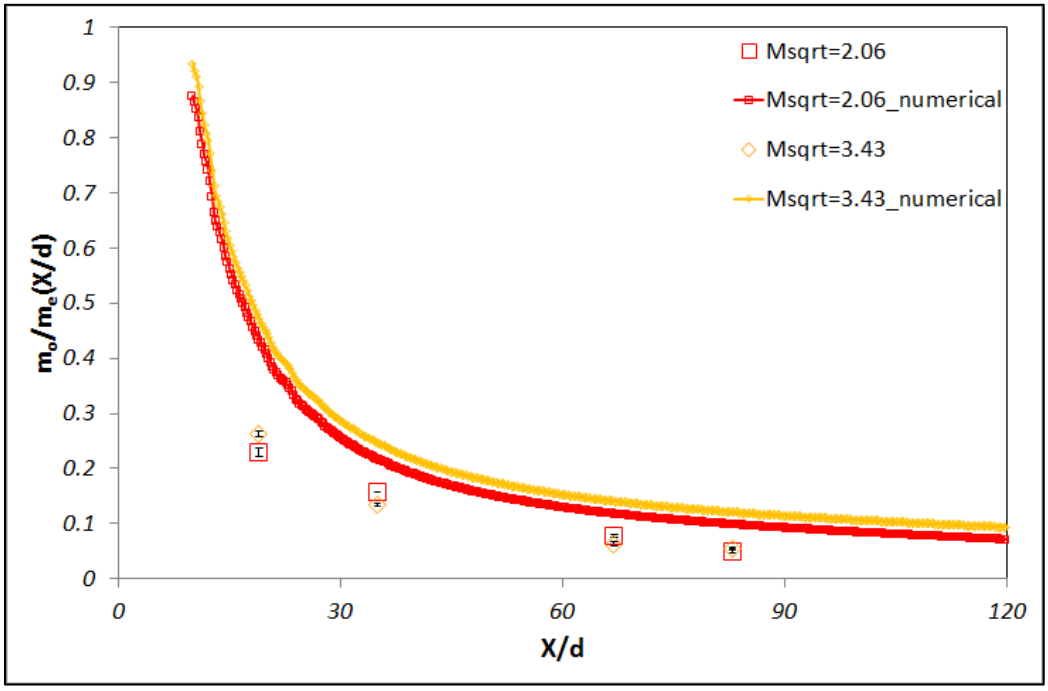

(a) U_{count}=0.612m/s at different jet velocities

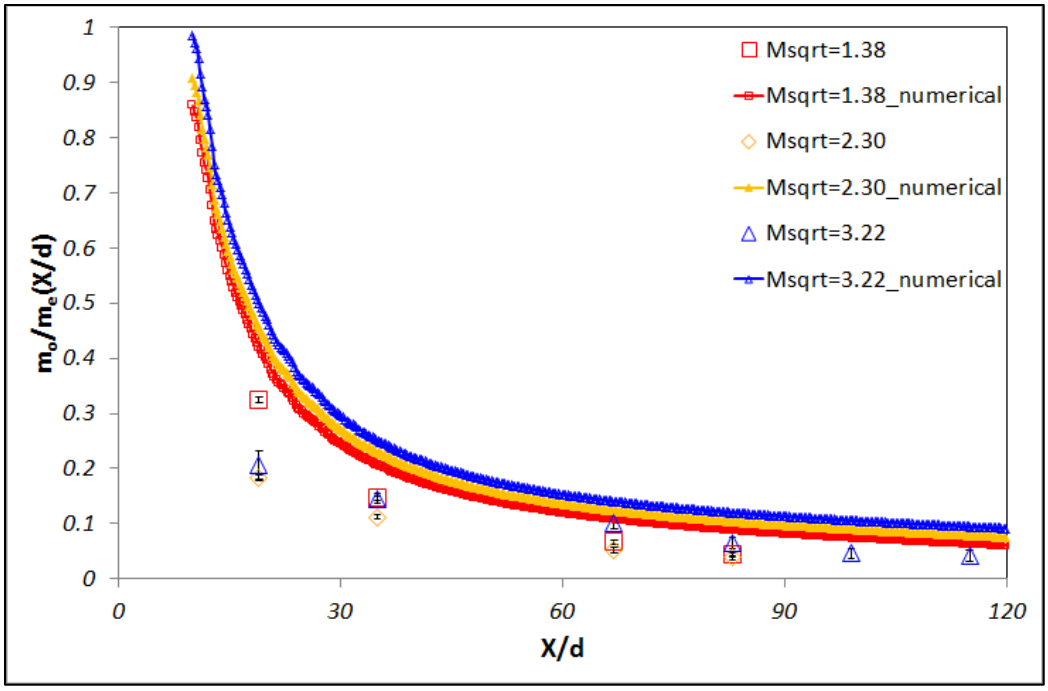

(b) U_{count}=0.913m/s at different jet velocities

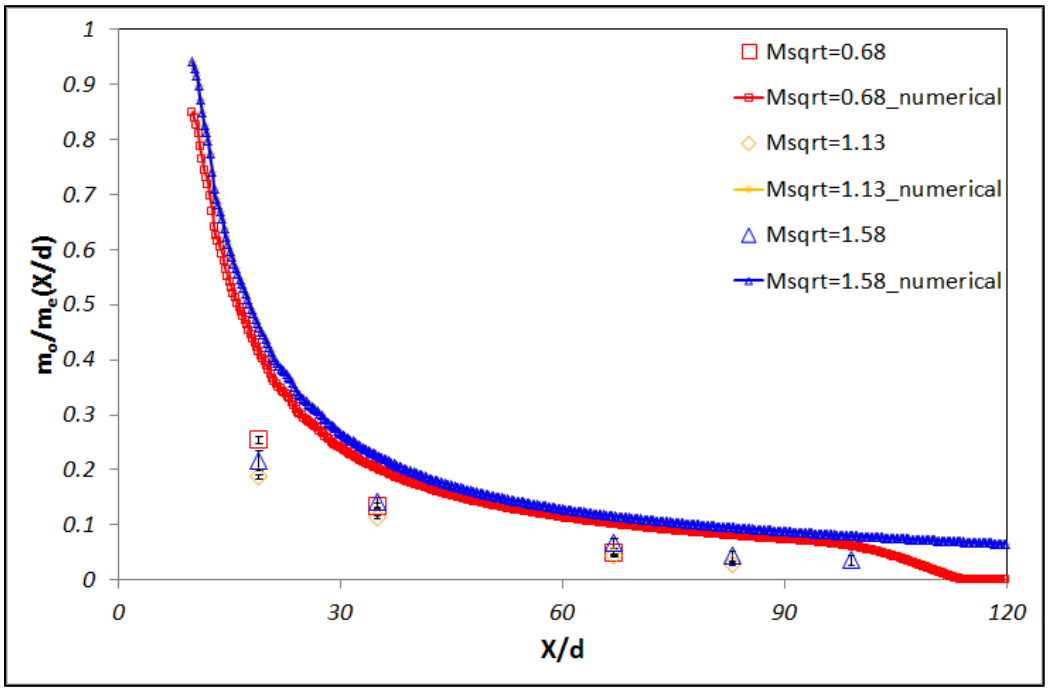

(c) U_{count}=1.856m/s at different jet velocities

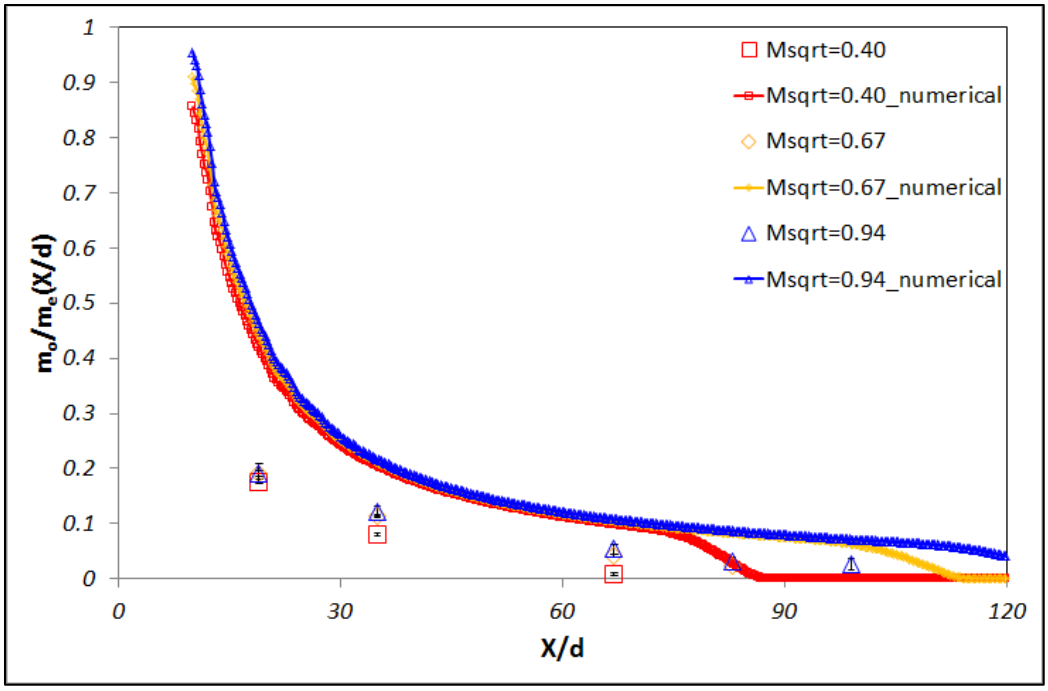

(d) U_{count}=3.123m/s at different jet velocities

Figure 3.47 The measured entrainment

Figure 3.47 shows that the entrainment ratio has the function of ***X/d*** (***d***: jet nozzle diameter) at fixed counter-flow and different jet velocities. The numerical results are relatively underestimated through comparing experimental results at all of ranges of normalized axial location. Generally, entrainment ratio is linear decayed as function of normalized axial location. Usually, the value of entrainment ratio has the smaller values at low modified momentum ratio due to closer stagnation plane. At fixed counter-flow velocity, the low modified momentum ratio mean low jet velocity. Therefore, the stagnation plane is able to move near jet region. Also, usually, the value of entrainment ratio is smaller at fixed higher counter-flow because the high counter-flow condition causes a recirculation zone (by the stagnation plane) near jet region. Therefore, more entrained mass is able to go into jet region at large axial distance.

To check the change of the entrainment ratio at the location of the stagnation plane, one special test case is studied. Figure 3.48 shows the comparison between one special case and

Spalding's [55] results from the free turbulent jet. One special case (U_j=96.12m/s and U_{count}=3.123m/s) is measured up to the region of the stagnation plane (X/d=83, the location of stagnation at centerline is X/d=82.4 numerically) successively through several trials. The entrainment ratio is not seriously increased through comparing the entrainment ratio of the free turbulent jet condition except large axial location or near the location of the stagnation plane. The blocking by the stagnation plane causes insufficient entrained mass. However, the entrainment ratio is increased exponentially near the location of the stagnation plane due to sufficient entrained mass by mixing of colliding two flows. Finally, the Spalding's equation of the entrainment cannot evaluate the entrainment of the confined turbulent jet flow in counter-flow at large axial location due to the existence of the stagnation plane but be useful near jet exit

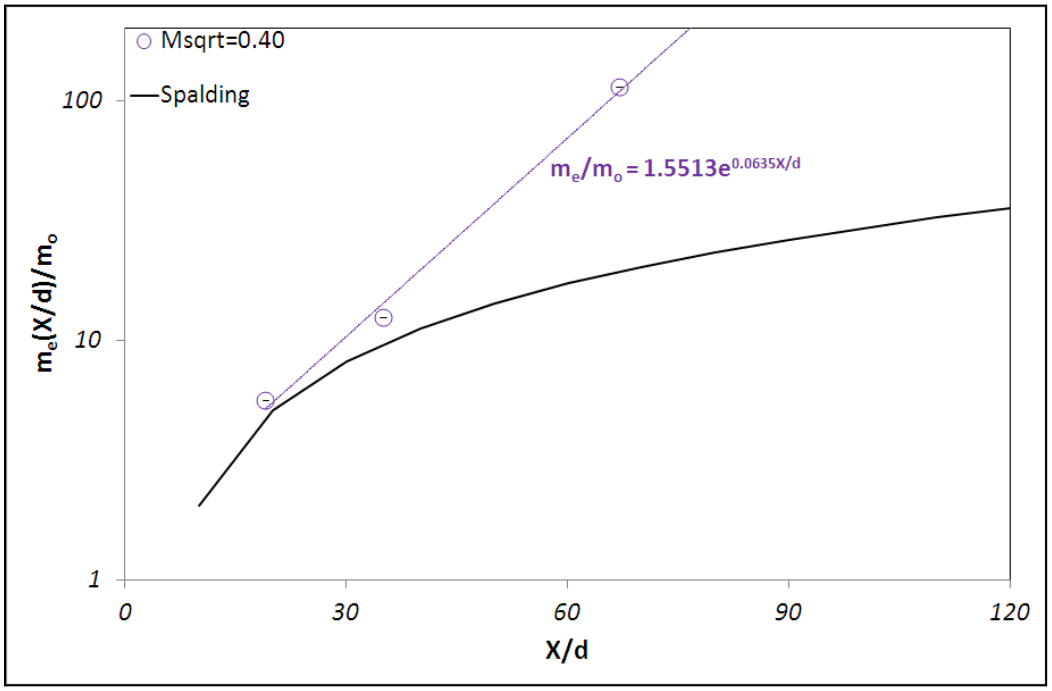

Figure 3.48 The comparison between entrainment from counter-flow and from free flow

To explain this phenomenon graphically, the stagnation plane is shown in figure 3.49 at this velocity conditions. The stagnation plane results in dividing between the jet and the counter-

flow. The two flows collide at the location of stagnation surface. Therefore, the side of the jet has insufficient entrained mass before the stagnation surface. Entrainment is increased exponentially at location of stagnation surface.

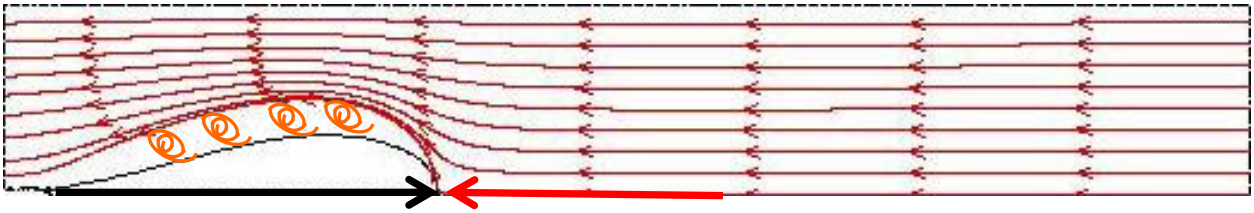

Figure 3.49 The schematic of flow near the stagnation plane

3.2.8. Conclusion

Experimental studies were performed on the flow and the mixing characteristics such as the resulting velocity, the temperature, the ***NO*** concentration fields as well as the entrainment ratio of the confined turbulent jets in the counter-flow by using the modified momentum ratio (velocity conditions between the jet velocity and the counter-flow).

The decay of axial velocity along the centerline agree reasonably well at relatively low jet velocity ($\boldsymbol{U_j}$=96.12m/s and $\boldsymbol{U_j}$=160.19m/s) with different counter-flow velocity but some deviations at relatively high jet velocity conditions exist ($\boldsymbol{U_j}$=224.26m/s and $\boldsymbol{U_j}$=304.37m/s) with different counter-flows when compared to previous results (which was limited to measure up to $\boldsymbol{X/d}$=30 in Yoda's result [26]). The decay of the centerline velocity has an inversely linear form near the jet exit but has an exponential form for the function of normalized locations ($\boldsymbol{X/d}$, where $\boldsymbol{d}$ is jet nozzle diameter) at some normalized axial locations (to be decided by different velocity conditions between jet and counter-flow velocity) due to the formed stagnation plane by the colliding two flows. As the modified momentum ratio ($\boldsymbol{M_{sqrt}}$) increases, the centerline velocity decays slowly because of high jet velocity. Therefore, the jet is able to move further downstream because of relatively high jet momentum against the counter-flow momentum. The radial distributions of the velocity at different velocity conditions collapse fairly well on a Gaussian function by comparing previous results because of self-similar characteristics of the jet in spite of the condition of the confined turbulent jet in counter-flow. Also, the fluctuation of the velocity increases at the high axial direction because of the turbulent intensity. As the jet flow moves along the axial direction, the measured jet widths of half jet velocity are increased because of the characteristics of jet spreading as well as the blocking by the stagnation plane (counter-flow

effect). The measured widths of half jet velocity correspond well (where ***X*** is axial location and ***d*** is jet nozzle diameter) to the results of the free turbulent jet.

The results of this study show the decay of ***NO*** concentration along the centerline. Our measured results and previous results of the concentration are in reasonable agreement below ***X/d*** =20 where previous results are available. There are two kinds of trends to explain the decay of ***NO*** concentration of the confined turbulent jet in counter-flow. 1) The normalized ***NO*** concentration decreases linearly at the high modified momentum ratio as the jet flow moves along the axial direction. 2) As the counter-flow velocity (the modified momentum ratio decreases) increases at each velocity condition, the normalized ***NO*** concentration decays faster at high ***X/d***. The changed trend of the decay of concentration is caused by high counter-flow because the stagnation plane (by the collision between jet and counter-flow) moves towards the side of the jet exit as the counter-flow becomes higher. Accordingly, the concentration is spread relatively fast along the radial direction because of blocking the jet movement against the axial direction. Current normalized radial concentration distributions are shown coherently at even high normalized axial direction. These radial concentration distributions are able to be shown by using a Gaussian function. Therefore, the confined turbulent jet in counter-flow has the self-similar region up to some axial distances. The measured width of half ***NO*** concentration is increased at the high normalized axial direction (***X/d***) because of the blocking by the stagnation plane (to be interacted between jet flow and counter-flow) as well as the jet spreading. The normalized half ***NO*** concentration width is almost similar value below ***X/d***=60 in spite of different modified momentum ratios but spreads out at ***X/d***>60 at each different modified momentum ratio. The measured widths of half ***NO*** concentration have usually much larger

values at higher modified momentum ratio at fixed jet velocity with different counter-flows by the effect of the mixing movement of counter-flow in the confined turbulent jet.

The T_c is increased at high axial location due to enough heat transfer coming from the stagnation plane or the counter-flow region. The centerline temperature, T_c, is converged to the single value as the jet flow moves along the axial direction. The normalized temperature profiles are flat and stable at large axial distance because of stagnation plane. Hot counter-flow is difficult to move the jet stream because the stagnation plane usually makes roles as obstacles between a cold jet flow and a hot counter-flow. Accordingly, the jet temperature is heated slowly because of amount of insufficient heat transfer. As the jet flow moves along the normalized axial direction, the temperature radial distributions are usually more uniform at X/d=67 due to the heat transfer by interacting between the cold turbulent jet and the hot counter-flow. The uniform temperature is getting slightly faster at low modified momentum ratio due to the sufficient amount of hot counter-flow for making low value of M_{sqrt}.

To check the stagnation surface and penetration length, Stagnation surface and penetration length are defined. Stagnation surface and penetration length are increased as modified momentum ratio is enlarged because of high jet velocity or low counter-flow velocity. The penetration length has constant values at higher modified momentum ratio. Also, to check the buoyancy effect on the penetration length, the temperature of counter flow is changed from 328.15K to 1200K. It shows that there is not any difference among the numerical estimation of penetration length at different counter-flow temperature.

Finally, our measured results of the entrainment ratio are similar and slightly smaller than numerical results. Usually, as the jet flow moves along the axial direction, the entrainment is

increased by the interaction of two flows. However, in the confined turbulent jet in counter-flow, the entrainment ratio is increased at the location of stagnation surface. The difference between measured entrainment ratio and results of numerical results is increased as the counter-flow velocity (or low modified momentum ratio) increases and the axial location decrease. Usually, the entrainment ratio of the confined turbulent jet into the counter-flow generally is smaller than that of the free turbulent jet condition except the large axial location or the stagnation plane. However, in the case of the confined turbulent jet in counter-flow, the entrainment ratio at the region of the stagnation plane increases exponentially by sufficient entrained mass of mixing of colliding two flows. Therefore, the Spalding's equation of entrainment does not evaluate the entrainment of the confined turbulent jet flow in the counter-flow but is useful near the jet exit.

CHAPTER 4

Numerical study of a confined non-reacting and reacting turbulent jet in a current furnace for homogeneous combustion

4.1 Numerical setup of a confined non-reacting and reacting turbulent jet in a current furnace for homogeneous combustion

Although several investigations of homogeneous combustion were studied, most research has focused not on flow characteristics but on chemical characteristics of homogeneous combustion. The investigation of flow and reacting characteristics of homogeneous combustion is needed in order to better understand some of the fundamental conditions that can lead to homogeneous combustion. Flow as well as reacting characteristics of homogenous combustion will be investigated numerically through changing the independent controllable variables, air nozzle diameter (d_{air}), fuel nozzle diameter (d_f), equivalence ratio (Φ), oxygen concentration, gravity, different bottom temperature, separation distance and soot radiation. ***FLUENT*** among several commercial CFD programs is used for this numerical approach. In this study, the same geometry as an existing experimental furnace in the lab is used as shown in figure 4.1. The existing furnace has one fuel jet at the center, four air jets surrounding the top center, and six exhaust vents at the bottom. The separation distance between the fuel and the air jet is 280mm; this distance is fixed. The temperature of the bottom of the combustor is 150°C due to a water-cooled bottom plate. To study the flow and reacting characteristics of homogeneous combustion numerically, the current combustor is modeled. The entire domain of this combustor has 8.4

million grid points which leads to typical cell dimensions of (x: 4mm y: 4mm z: 4.4mm) which is a resolution that is sufficient to describe the large scale flow and mixing features by considering the accuracy under the constraint of a reasonable computation time in figure 4.1-(c). This resolution is not enough to resolve a typical unsteady laminar flamelet of thickness 0.5-1 mm. This is in contrast to direct numerical simulation (DNS) which resolves all the small scale structures in the unsteady flow, but then does not cover a physical domain larger than 1-2 mm [62]. The current numerical method will thus be able to solve for all the large scale flow and geometry including turbulence, but must be modeling the small scale effects. Just the opposite is the case for the DNS and from the current state of the art the two methods barely meet i.e. the current single cell size is larger than the total domain for the DNS by a factor of 64.

(a) Interior **(b) Exterior** **(c) Numerical domain**

Figure 4.1 Schematic of furnace

First, for the study of modelling a reacting turbulent gas, the Realizable ***K-ε*** model [44] with enhanced wall function is utilized. The realizable ***K-ε*** model was proposed to resolve the limitation of the traditional ***K-ε*** model. The transport equations for the realizable ***K-ε*** model are

$$\frac{\partial}{\partial t}(\rho k)+\frac{\partial}{\partial x_i}(\rho k u_i)=\frac{\partial}{\partial x_i}\left(\left(\mu+\frac{\mu_t}{\sigma_k}\right)\frac{\partial k}{\partial x_j}\right)+G_k+G_b-\rho\varepsilon-Y_M+S_k \tag{48}$$

$$\frac{\partial}{\partial t}(\rho\varepsilon)+\frac{\partial}{\partial x_j}(\rho\varepsilon u_j)=\frac{\partial}{\partial x_j}\left(\left(\mu+\frac{\mu_t}{\sigma_\varepsilon}\right)\frac{\partial \varepsilon}{\partial x_j}\right)+\rho C_1 S\varepsilon-\rho C_2\frac{\varepsilon^2}{k+\sqrt{\nu\varepsilon}}+C_{1\varepsilon}\frac{\varepsilon}{k}C_{3\varepsilon}G_b+S_\varepsilon \tag{49}$$

$$C_1=\max\left[0.43,\frac{\eta}{\eta+5}\right],\eta=S\frac{k}{\varepsilon} \tag{50}$$

$$G_k=-\rho\overline{u_i'u_j'}\frac{\partial u_j}{\partial x_i},\ G_b=-\frac{g_i}{\rho}\frac{\mu_t}{\mathrm{Pr}_t}\left(\frac{\partial\rho}{\partial T}\right)_p\frac{\partial T}{\partial x_i},\ Y_M=2\rho\varepsilon\left(\frac{k}{\gamma RT}\right) \tag{51}$$

Where $\boldsymbol{G_k}$ means the generation of mean turbulent kinetic energy by the mean velocity gradient, $\boldsymbol{G_b}$ represents the production of turbulent kinetic energy due to the buoyancy, and $\boldsymbol{Y_M}$ is the contribution of the fluctuating dilatation. To manipulate this turbulence model, $\boldsymbol{Pr_t}$ (Turbulent Prandtl number)=0.85, $\boldsymbol{C_2}$=1.9, $\boldsymbol{C_{1\varepsilon}}$=1.44, $\boldsymbol{\sigma_k}$=1.1, $\boldsymbol{\sigma_\varepsilon}$=1.2, $\boldsymbol{C_\mu}$=0.09, $\boldsymbol{S_k}$ and $\boldsymbol{S_\varepsilon}$ (user defined source terms) are used as default values. An enhanced wall function is considered to estimate the effect by the wall. An enhanced wall function is called near wall modeling when it uses a two-layer model [43]. The whole domain for numerical calculation is subdivided into a near wall region (viscosity-dominant region, $\boldsymbol{Re_y<Re_y^*}$) and a fully turbulent region ($\boldsymbol{Re_y>Re_y^*}$, $\boldsymbol{Re_y^*}$=200).

$$\mathrm{Re}_y=\frac{\rho y\sqrt{k}}{\mu} \tag{52}$$

where $\boldsymbol{y}$ is the normal distance of wall at the cell centers. The $\boldsymbol{y}$ is calculated as:

$$y\equiv\min_{\vec{r}_w\in\Gamma_w}\left\|\vec{r}-\vec{r}_w\right\|,\ \vec{r}\text{ and }\vec{r}_w\text{:position vector of the field and wall} \tag{53}$$

In this study of the combustion phenomena in the furnace, a reduced chemistry model is used for the combustion process, it is a two-step reaction model of methane and air accompanied by addition of the carbon monoxide reaction [59].

$$CH_4 + 1.5O_2 \rightarrow CO + 2H_2O \text{ , } \frac{d[CH_4]}{dt} = -A_1[CH_4]^{a_1}[O_2]^{b_1} \exp\left(-\frac{E_1}{RT}\right) \tag{54}$$

$$CO + 0.5O_2 \rightarrow CO_2 \text{ , } \frac{d[CO]}{dt} = -A_2[CO]^{a_2}[O_2]^{b_2} \exp\left(-\frac{E_2}{RT}\right) \tag{55}$$

Here ***E*** is the activation energy, ***A*** is the steric factor or kinetic pre-exponential factor and ***a***&***b*** are the exponent values. To predict the slow chemical reaction of homogeneous combustion (low Damköhler number) [60], the Eddy Dissipation Concept (***EDC***) model [61] is selected in ***FLUENT*** [43]. The ***EDC*** model is an extension of the eddy dissipation model to consider the detailed chemical reaction mechanism in turbulent reacting flow. The *EDC* model assumes that all reactions will occur at the smallest turbulent length scale such as the Kolmogorov scale and that this domain occupies a volume fraction less than 1 based on considerations of the cascading process [49]. This length scale is validated as an equation (56). Also, the time scale of this small length scale is modeled in equation (57) where ***** connotes small scale quantities.

$$\xi^* = C_\xi \left(\frac{\gamma\varepsilon}{k^2}\right)^{\frac{1}{4}} \text{ , } C_\xi = 2.1377 \tag{56}$$

$$\tau^* = C_\tau \left(\frac{\gamma}{\varepsilon}\right)^{\frac{1}{2}} \text{ , } C_\tau = 0.4082 \tag{57}$$

The source term (***R*$_i$**) in the conservation equation of the mean species is defined in the following equation where Y_i^* is the mass fraction of species ***i*** on a small scale:

$$R_i = \frac{\rho(\xi^*)^2}{\tau^*\left[1-(\xi^*)^3\right]}\left(Y_i^* - Y_i\right) \tag{58}$$

The EDC model covers the fast to slow chemistry where it is completely determined by the mixing rate on the small scale. This model does not employ the local well stirred reactor, but makes the reaction rate equal to the dissipation on the small scales which equal the transport rate of kinetic energy down to the small scales [61].

It is a reasonable approximation to consider methane a gray medium and non-scattering gas because of its radiation properties with wavelength/frequency. With this in mind the Discrete Ordinates (***DO***) radiation model is selected to simplify the treatment of radiation and still provide some reasonable results. The ***DO*** radiation model [43] consists of the radiative transfer equation (***RTE***) by formulating the field direction, $\vec{s}$ in ***FLUENT***. The ***RTE*** is expressed as an equation of gray radiation (59):

$$\nabla\cdot\left(I(\vec{r},\vec{s})\vec{s}\right) + (a+\sigma_s)I(\vec{r},\vec{s}) = an^2\frac{\sigma T^4}{\pi} + \frac{\sigma_s}{4\pi}\int_0^{4\pi} I(\vec{r},\vec{s}')\Phi(\vec{s}\cdot\vec{s}')d\Omega' \tag{59}$$

The ***DO*** radiation model is combined with the weighted sum of gray gas model (***WSGGM***) in which spatial variation in the total emissivity is calculated as a function of gas composition and temperature. The ***WSGGM*** is an approximate estimate as a compromise between a completely detailed model and the oversimplified model of defining a specific absorption band.

To estimate the $\boldsymbol{NO_x}$ emission in homogeneous combustion, thermal and prompt $\boldsymbol{NO_x}$ formations are considered with the ***EDC*** model and the two step reaction model. The thermal $\boldsymbol{NO_x}$ formation is calculated by an extended Zeldovich mechanism. The extended Zeldovich reaction mechanisms are as follows,

$$O + N_2 \leftrightarrow N + NO \tag{60}$$

$$N + O_2 \leftrightarrow O + NO \tag{61}$$

$$N + OH \leftrightarrow H + NO \tag{62}$$

The rate of ***NO*** formation through the extended Zeldovich mechanism in equation 60−62 is defined by,

$$\frac{d[NO]}{dt} = k_{f,1}[O][N_2] + k_{f,2}[N][O_2] + k_{f,3}[N][OH] - k_{r,1}[NO][N] - k_{r,2}[NO][O] - k_{r,3}[NO][H] \tag{63}$$

OH concentration is assumed to be negligible due to the rate constants $k_2[O_2]_{eq} >> k_3[OH]_{eq}$. To determine the ***O*** radical concentration, a partial equilibrium approach is used by considering third-body reactions in the $\boldsymbol{O_2}$ dissociation-recombination process,

$$O_2 + M \leftrightarrow O + O + M \tag{64}$$

Prompt $\boldsymbol{NO_x}$ mechanism is more important in rich flames during combustion of hydrocarbon fuels. Actual Prompt $\boldsymbol{NO_x}$ mechanism consists of a complicated series of reactions with many possible intermediate radicals.

$$CH + N_2 \leftrightarrow HCN + N \tag{65}$$

$$N + O_2 \leftrightarrow O + NO \tag{66}$$

$$HCN + OH \leftrightarrow CN + H_2O \tag{67}$$

$$CN + O_2 \leftrightarrow NO + CO \tag{68}$$

Major contribution from equation 65 controls the prompt NO_x formation rate,

$$\frac{d[NO]}{dt} = k_o[CH][N_2] \tag{69}$$

The thermal and prompt NO_x formations are used to estimate the net rate of NO formation in this dissertation.

RUN	X_{O2}	d_{air} [m]	Φ	d_f [m]	etc
1	0.21	0.00795	0.6	0.0152	
2			0.7		
3			0.8		
4			1.1		
5		0.011925	0.7		
6			0.8		
7			1.1		
8		0.0159	0.8		
9			1		
10			1.1		
11		0.02385	0.8		
12			0.9		
13			1.1		
14		0.0318	0.9		
15			1		
16			1.1		
17	0.30	0.0159	1		
18	0.40	0.0159	1		
19	0.40	0.0159	1		T_{cold}=50°C
20	0.21	0.0159	1		No gravity
21	0.21	0.0159	0.9		S=140
22	0.21	0.0159	1		
23	0.21	0.0159	1.1		
24	0.21	0.0159	0.9		S=350
25	0.21	0.0159	1		
26	0.21	0.0159	1.1		
27	0.3	0.0159	1		m_{soot}=0.01m_f
28	0.3	0.0159	1		m_{soot}=0.05m_f
29	0.4	0.0159	1		S=140
30	0.4	0.0159	1		S=350
31	0.21	0.0159	1	0.0304	
32	0.21	0.0159	1	0.0076	

Table 4.1 The numerical calculation matrix for the study of homogeneous combustion

To find and investigate flow and reacting characteristics of homogeneous combustion as well as looking into operating maps of homogeneous combustion, the numerical conditions are selected as shown in table 4.1. The flow rate of fuel is fixed to 1900 cm^3/s with three circular fuel diameters ($\boldsymbol{d_f}$) used 7.6, 15.2 and 30.4mm. Five circular air ($\boldsymbol{d_{air}}$) diameters are selected as 7.95, 11.925, 15.9, 23.85 and 31.8mm in order to obtain a suitable range of equivalence ratios. To check the effect of oxygen concentration ($\boldsymbol{X_{O2}}$) to homogeneous combustion, three oxygen concentrations are chosen to 21%, 30% and 40%. Three separation distances ($\boldsymbol{S}$) uses 140, 280 and 350mm to show the influence of separation distance. Finally, the buoyancy (run20), different bottom temperature (run19) and soot radiation (run 27 and 28) are checked.

4.2 Numerical investigation of non-reacting turbulent jet in a current furnace for the study of homogeneous combustion

4.2.1 General overview of non-reacting turbulent jet flow inside combustor

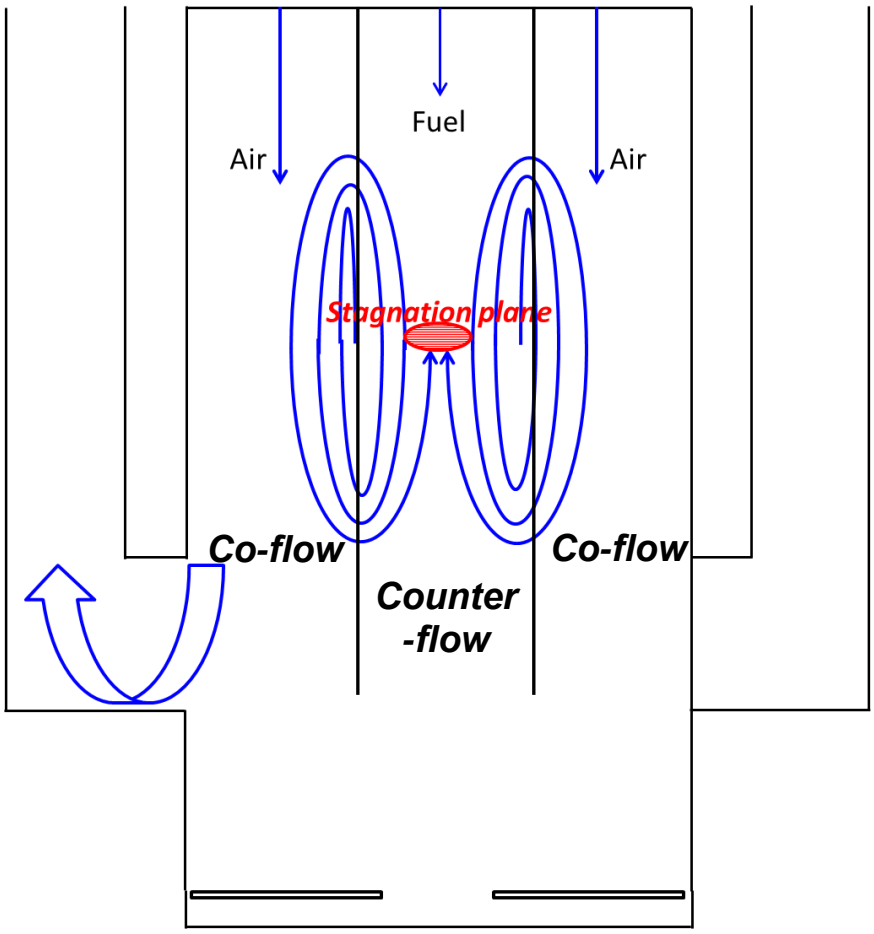

Figure 4.2 Schematic of non-reacting flow motion inside combustor for the study of homogenous combustion

Non-reacting turbulent jets in the current furnace are studied in order to verify the flow characteristics inside the furnace. From figure 4.2, the flow zone is divided into two simple flow zones such as counter-flow and co-flow assuming the flow is mainly near symmetric. The counter-flow is found along the fuel axis and the co-flow is found along the air axis respectively.

This description is shown as the result from a numerical simulation for the non-reacting flow in figure 4.3 to better understand the features and the non-symmetric real flow. The streamlines for the non-reacting condition (run9) is shown in figure 4.3. The fuel jet and the recirculating air collide resulting in a stagnation location along the fuel axis. The fuel and air moves along in a co-flow beyond the stagnation location creating a smaller recirculating zone for the fuel. Notice this flow structure is 3-dimensional so in the XZ plane you do not see the large air recirculation except it is noticeable in the bottom right corner. This air flow moves back up to the top in between the air jets and gets drawn into the fuel jet stream near the top. This is one of the explanations for the large mixing possible between the air and fuel. Therefore, the location of the stagnation and the flow structures are key features of the mixing mechanism.

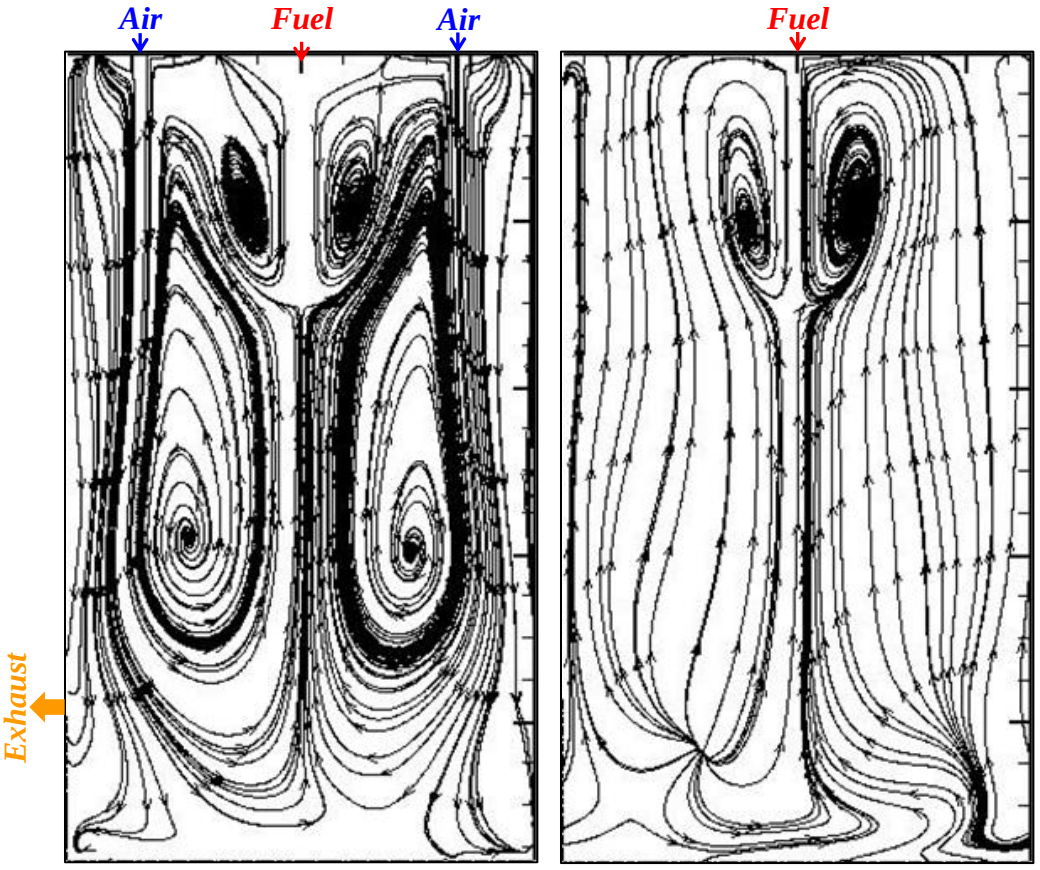

(a) *YZ* plane (b) ***XZ* plane**

Figure 4.3 Streamline at run9 (non-reacting)

Previous studies showed that fast mixing is one of the most essential parameters in order to make homogeneous combustion possible. Therefore, it is most important to define the flow characteristics inside the combustor in order to understand the mixing mechanism. To verify, estimate and correlate the non-reacting co- and counter-flow characteristics inside combustor, in this chapter, the previous results of co-flow and counter-flow experiments are used.

4.2.2 The characteristics of non-reacting turbulent jet flow inside combustor

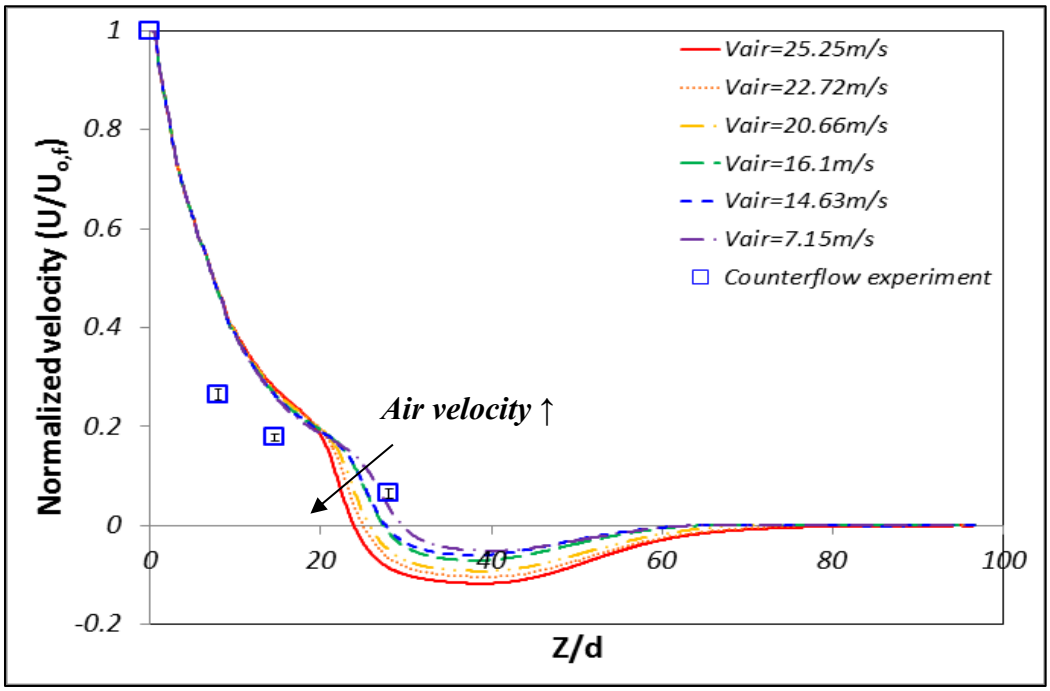

Figure 4.4 Normalized velocity along the fuel-axis ($U_{o,f}$: original fuel velocity)

Centerline fuel velocity (U_c) is normalized by the fuel jet inlet velocity (U_o=10.47m/s) in figure 4.4. The experimental result (which is expressed as blue square symbol) from the previous counter-flow experiments is plotted for the comparison. First of all, experimental and numerical results are well matched along the axial direction in spite of different geometry and conditions. In figure 4.4, '+' sign is +Z direction (down) and '–' sign is –Z direction. Therefore, flow direction is changed after the stagnation location or point. The fuel is going down until the stagnation location at which point the fuel flow and air flow collide. Therefore, as the air flow is increased the stagnation location moves upwards and the air recirculation zones have higher momentum. The stagnation location and the recirculation zones are important to make mixing faster and more uniform, which is confirmed between the experimental and numerical results of confined turbulent jet flow into counter-flow.

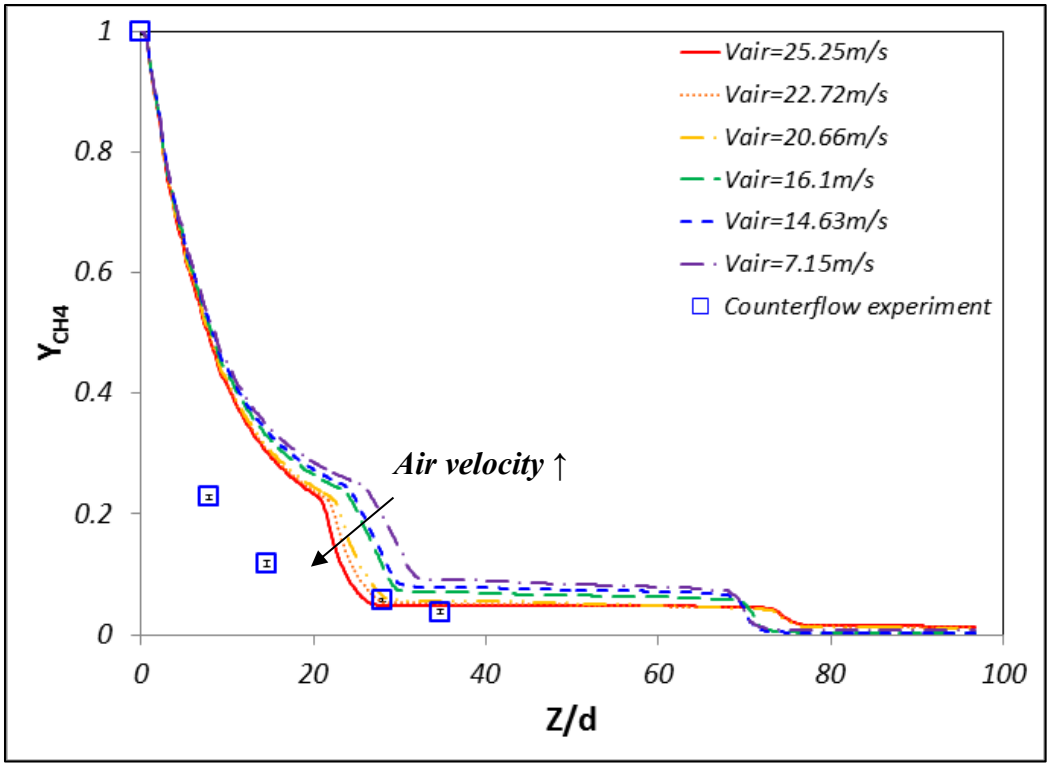

Figure 4.5 Mass fraction of methane (CH_4) along the fuel-axis

Figure 4.5 shows the mass fraction of methane (***CH_4***) along the fuel-axis. A previous counter-flow experiment result (which is plotted as blue square symbols) and numerical results are well matched along the axial direction in spite of different geometry and conditions. The features of the previous counter-flow experimental results look similar when compared to the normalized fuel velocity and mass fraction of methane along fuel axis. The mass fraction of ***CH_4*** drops very rapidly near the stagnation location due to the collision with the recirculation air zone and this happens earlier (smaller Z/d) as air velocity is increased. The low nearly constant level of the fuel concentration in Figure 4.5 is a result of the recirculated air that mixed a little with the fuel near the top of the furnace and came back in the 3-dimensional motion. Only near the very bottom of the furnace does the fuel concentration drop to zero. The results of the velocity and concentration variations along the fuel line do show the effect of the fuel/air mixing and the

complex 3-dimensional flow and it is only fully understood when also the complex streamline pattern in Figure 4.3 is considered.

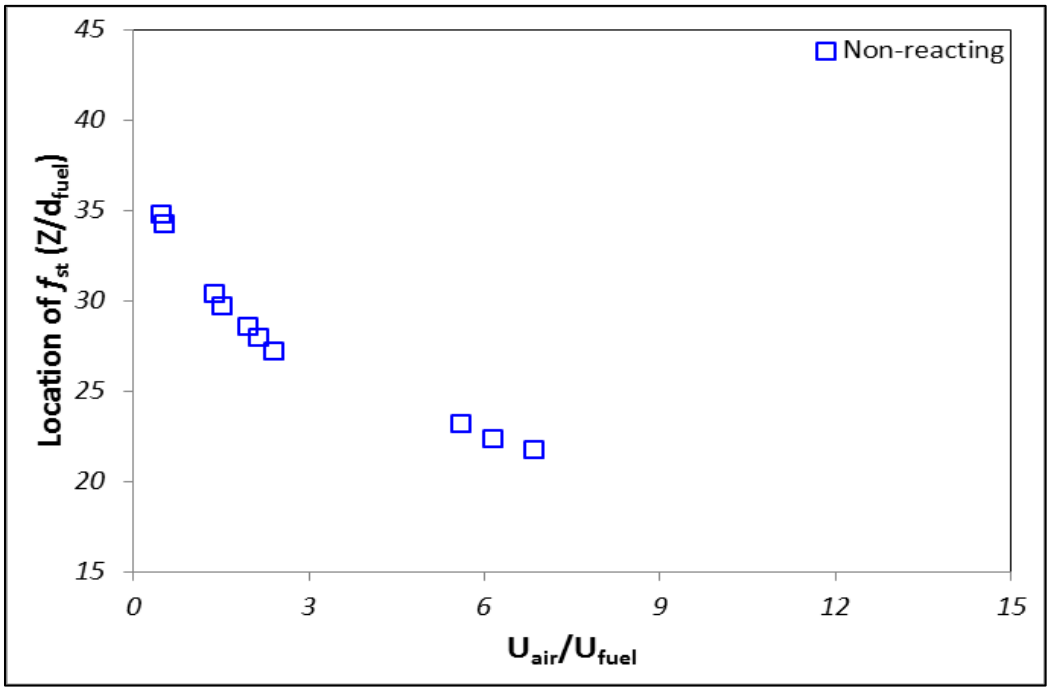

Figure 4.6 Location of stoichiometric mixture fraction (f_{st}) as function of air and fuel velocity ratio along the fuel axis

The location of the stoichiometric mixture fraction is plotted as a function of air and fuel velocity ratio in figure 4.6. This value is important as it will be close to the initial reaction zone obtained after heated to reach ignition. The mixture fraction is found from equation (70) and (71) and the location for the stoichiometric value along the fuel axis is determined.

$$\nu_F F + \nu_O O \leftrightarrow \nu_P P \tag{70}$$

$$Z = \frac{sY_F - Y_O + Y_O^o}{sY_F^O + Y_O^o}, \text{ where } s = \frac{\nu_O W_O}{\nu_F W_F} \tag{71}$$

$\boldsymbol{F}$, $\boldsymbol{O}$ and $\boldsymbol{P}$ are fuel, oxidant and product, respectively. $\boldsymbol{v_O}$ and $\boldsymbol{v_F}$ are stoichiometric coefficients of each oxidant and fuel. $\boldsymbol{W_O}$ and $\boldsymbol{W_F}$ are molecular weight of oxidant and fuel. $\boldsymbol{Y_F}$ and $\boldsymbol{Y_O}$ are mass fraction of fuel and oxidant at specific locations. Y_O^o and Y_F^o are mass fraction of oxidant and fuel at each inlet location. From figure 4.6, location of the stoichiometric mixture fraction moves up as air velocity increases because the mixing occurs earlier due to stagnation location as the air velocity increases. This reaction location creates hot products that are able to preheat and dilute air and fuel due to the close proximity. The combinations of enhanced mixing, spreading of the fuel jet, lower velocities and yet high levels of turbulence all contribute to an increased possibility of converting the standard diffusion flame to a homogeneous combustion reaction. These characteristics such as dilution and preheating will be explained in the next section.

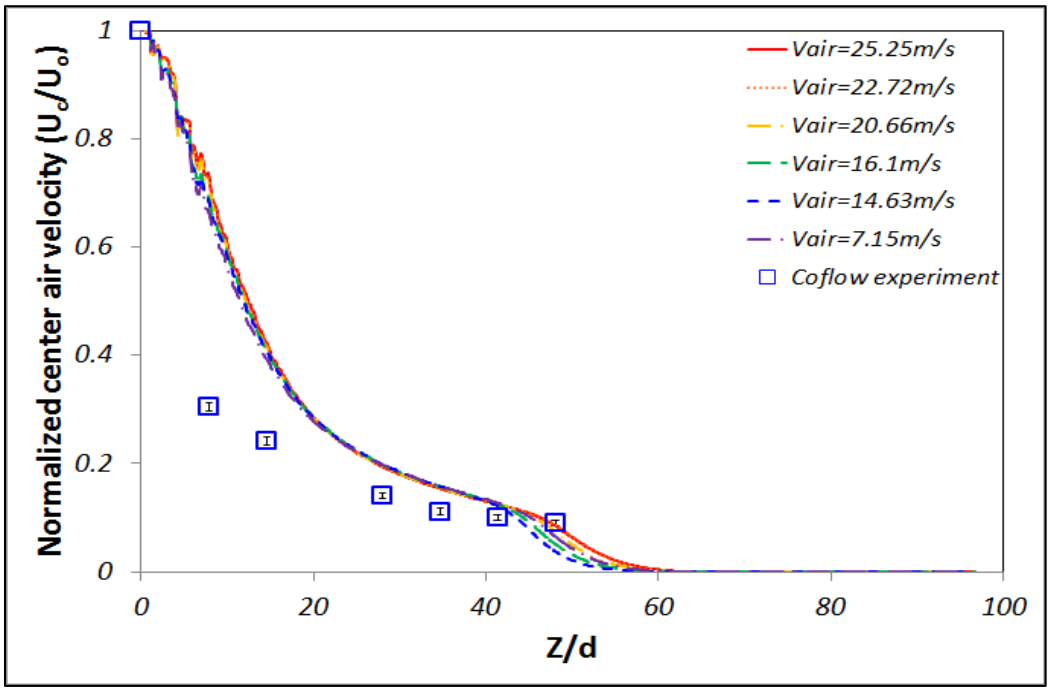

Figure 4.7 Normalized center air velocity along the air-axis

The flow characteristics of air inside the combustor are similar to co-flow conditions in previous streamline contour. For comparison between previous experimental result of confined

turbulent jet into co-flow and numerical result in current combustor, the normalized center air velocity along the air axis (U_c: Centerline air velocity, U_o: Initial fuel velocity at air inlet in figure 4.7) is plotted for the comparisons in figure 4.7. Although there are different geometry and conditions, previous experimental results and numerical results show a similar decay along the axial direction but with different decay rates. There is no stagnation location for the air flow except the one imposed by the furnace exit flow and bottom plate. There some of the air flows out through the exhaust ports and the rest moves back upward creating the larger recirculating region. Finally, the stagnation location happens on the fuel axis due to this back flow.

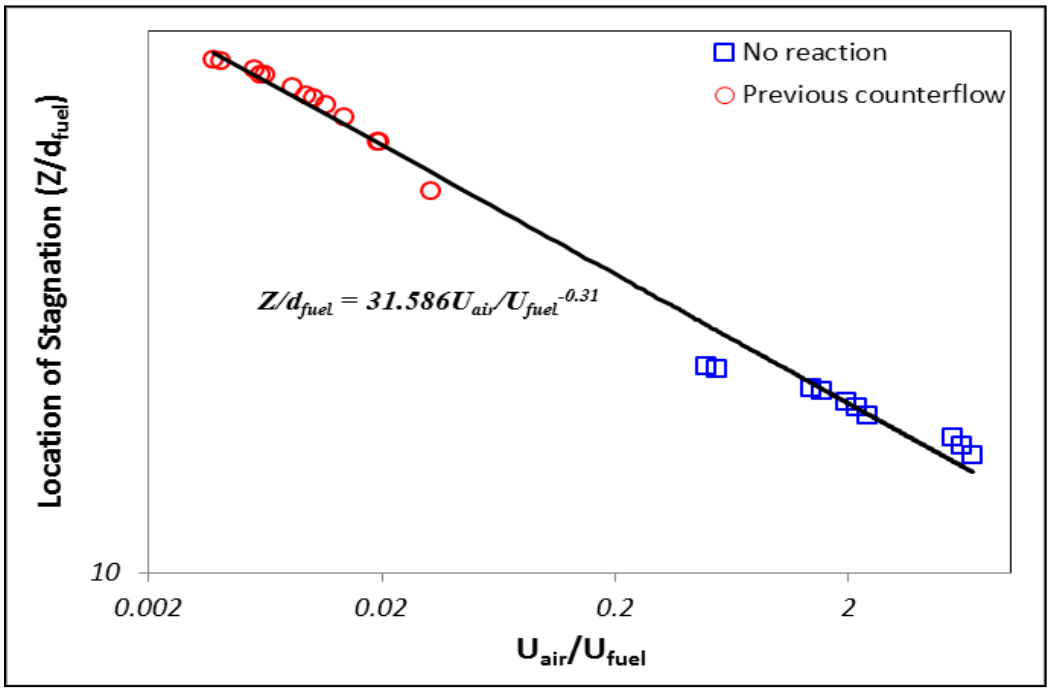

Figure 4.8 Location of stagnation point as function of air and fuel velocity ratios

To compare the location of stagnation between previous counter flow and numerical calculations inside combustor, the location of stagnation point as a function of air and fuel velocity ratio is plotted at figure 4.8. The empirical trend equation is correlated from the location of stagnation results and shown in equation 72. All of the results are reasonably approximated by

an empirical trend line equation. Usually, the stagnation location moves upward as air velocity increases.

$$\frac{Z}{d_{fuel}} = 31.586\left(\frac{U_{air}}{U_{fuel}}\right)^{-0.31} \tag{72}$$

Also, it is interesting to note that this curve fit for the equation of stagnation location is valid for the reacting flow case as shown in figure 4.9. The larger scale motion is not significantly affected by the heat release but is mainly a function of the momentum ratio between the air and fuel.

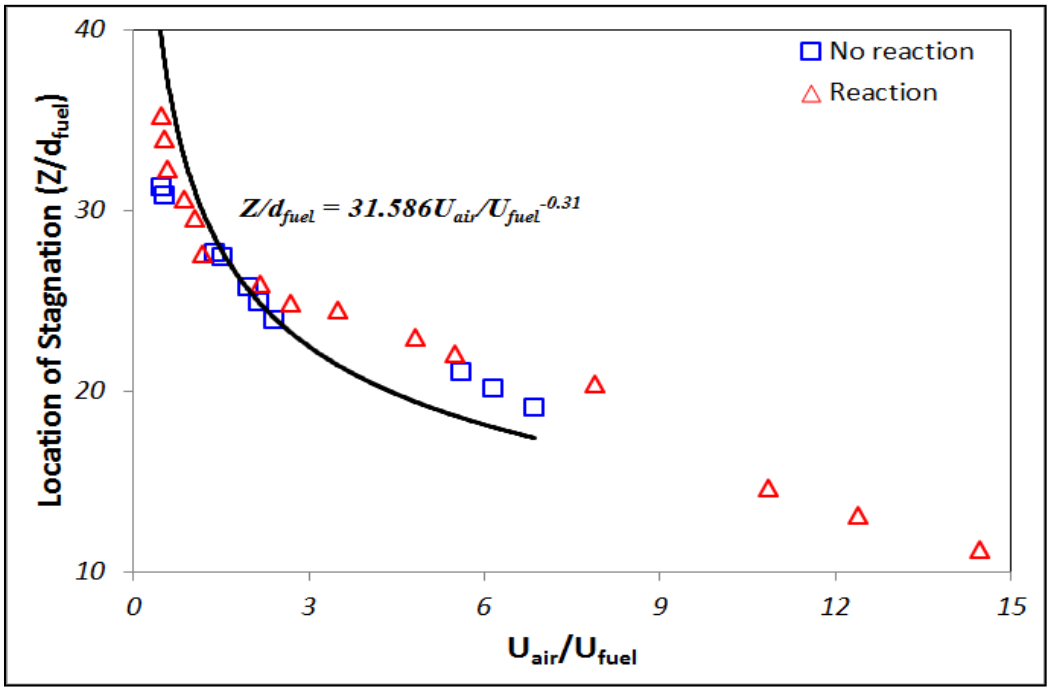

Figure 4.9 The comparison of location of stagnation location between non-reacting and reacting cases

4.2.3 Conclusion

Numerical studies were performed on the flow characteristics inside the combustor.

First, the flow is highly complex and 3-dimensional as illustrated by the streamline contour plots. A part of the flow has characteristics of counter-flow or co-flow and they are found along the fuel axis and air axis, respectively. The air jets extend nearly the full length of the furnace and flow out of the XZ plane into the YZ plane near the bottom and op towards the top to mix with the fuel jet. The recirculating zone then spreads the fuel further.

Second, the numerical result of normalized centerline fuel velocity is compared to previous counter-flow experimental results. These results are consistent along the axial direction in spite of different geometry and conditions. The stagnation location is found along the fuel axis due to the recirculating flow of high momentum air. Usually, the stagnation location moves up as the air flow velocity increases indicating the relative strength of the recirculating flow and the fuel jet.

Third, a previous counter-flow experiment of mass fraction of $\boldsymbol{CH_4}$ is well matched to numerical calculations along the axial direction. Usually, the mass fraction of $\boldsymbol{CH_4}$ drops more rapid near the stagnation location caused by the collision between the recirculating air zone and the fuel jet. As the recirculating air draws in some fuel near the top of the furnace and more mixing on its way down again (co-flowing with the fuel jet) this all results in a faster mixing as the air velocity increases. The 3-dimensional flow structures become crucial for the mixture preparation and promote the uniformity over the volume.

Fourth, location of the stoichiometric mixture fraction is an important parameter to predict the initial reaction location. Also, location of stoichiometric mixture fraction is closer to

jet inlet as air velocity increases due to faster mixing near the stagnation location and the strength of the recirculating region. Therefore, an initial reaction zone tends to be located near the upper zone of the combustor. This upper location provides the combustion products that enable the preheating and dilution of air and fuel in order to facilitate the homogeneous combustion.

Fifth, the characteristic of co-flow condition is found along the air axis. Numerical results of normalized air velocity along air axis are fairly similar to the previous co-flow results. Mostly, the normalized trend of air velocity along air-axis decays similarly despite different initial air velocities. Therefore, these results show that non-reacting confined turbulent jet flows have similar flow characteristics despite of different geometry and velocity conditions. Also, there is no stagnation location along air axis (except due to the bottom plate) due to the much higher momentum in the air jet as compared with the fuel jet.

Finally, the location of the stagnation point obtained by the previous counter flow and the numerical calculation inside combustor as function of air and fuel velocity ratio are compared. An empirical correlation for the stagnation location is found for the non-reacting flow and it provides a reasonable estimate for the reacting flow as well.

4.3 Numerical investigation of a reacting turbulent jet in a current furnace for homogeneous combustion

4.3.1 Validation of numerical model

The model of homogeneous combustion is illustrated against the previous experimental results obtained in the current experimental combustor [40].

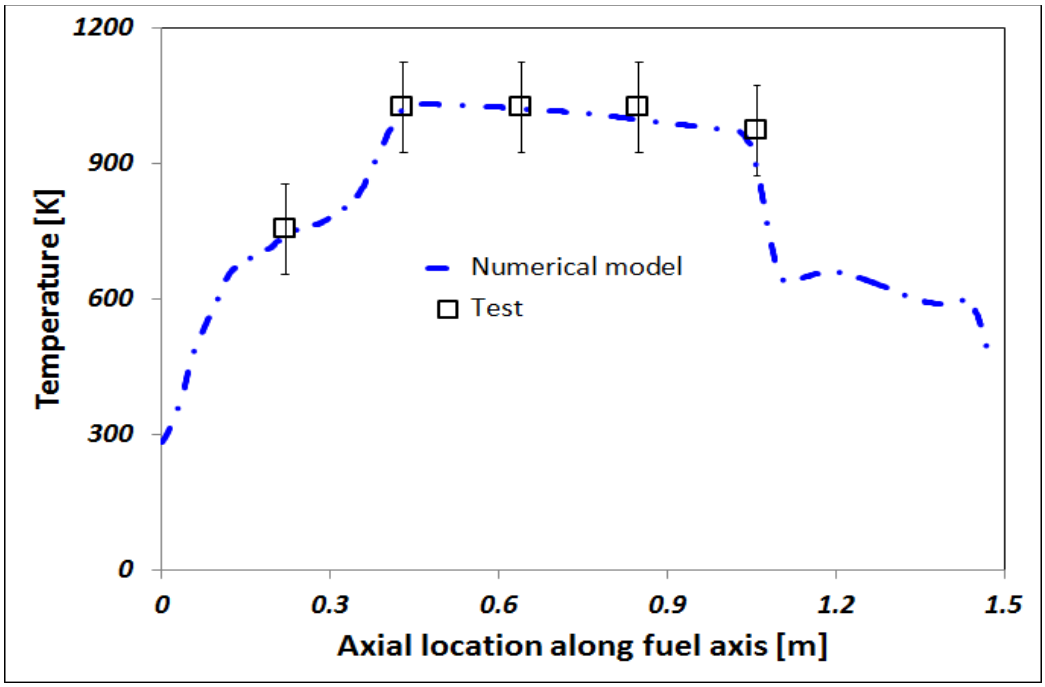

(a) Along fuel axis

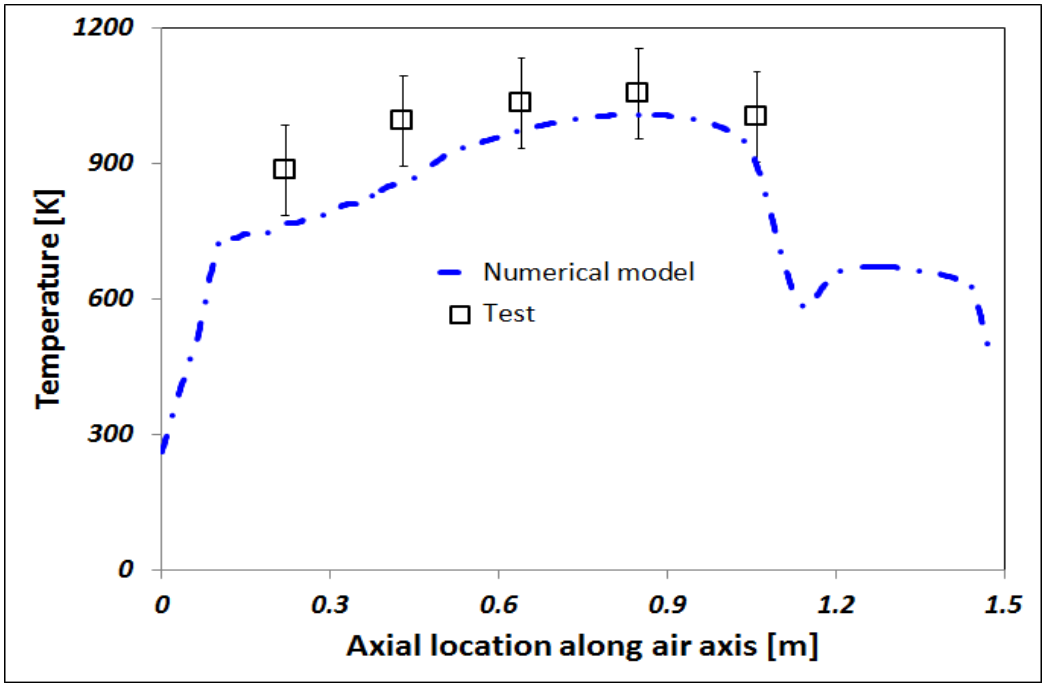

(b) Along air axis

Figure 4.10 The comparison between numerical and experimental temperature at run9 (X_{O2}=0.21, d_{O2}=15.9mm, Φ=1)

Figure 4.10 shows the comparison between the numerical and experimental temperature at axial location (***Z***) along the fuel and air axis for run 9. ***Z***=0 in each figure means fuel inlet and air inlet respectively. Moving from the inlet, the temperature inside combustor increases to about 1000K after which it is fairly constant along the axis. As the larger vortex near the bottom plate is approached the temperature drops to around 600K characteristic for that region, see also stream lines in fig 4.15. This is one of characteristics of homogeneous combustion. It is decreased by the effect of cooled bottom of the combustor and exhaust port as the axial location increases.

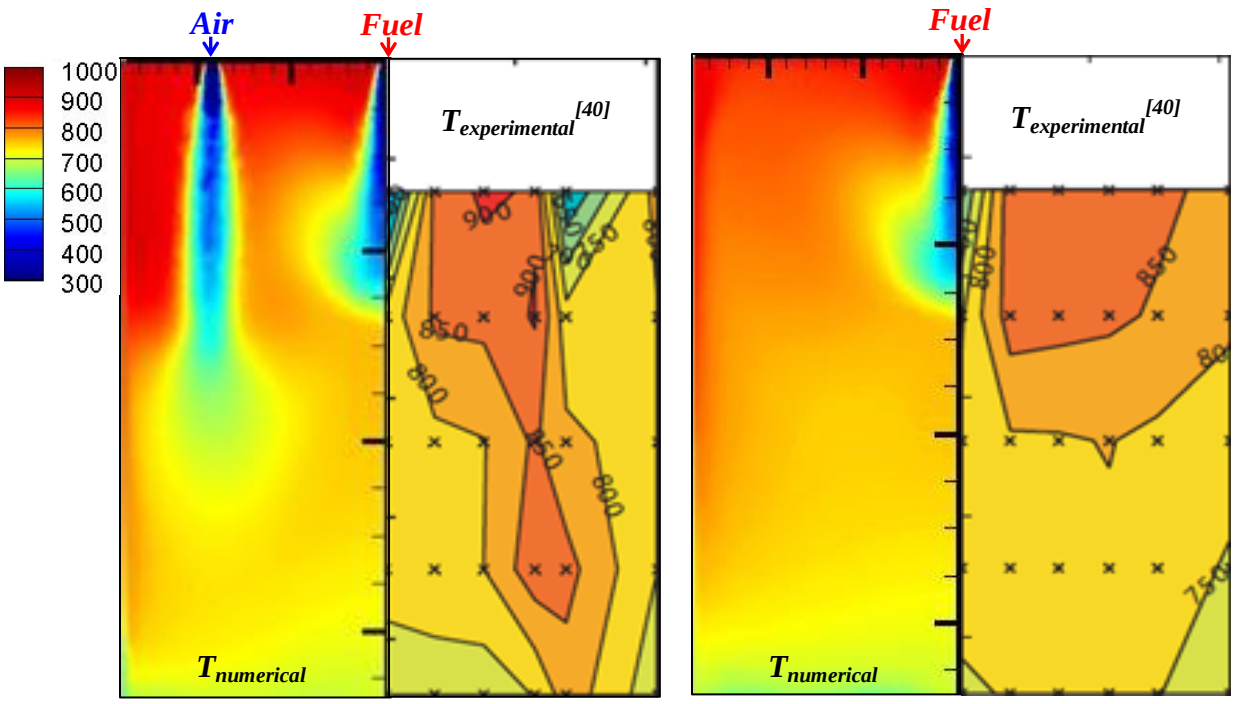

(a) *YZ* plane **(b) *XZ* plane**

Figure 4.11 The comparison between numerical and experimental temperature contour (°C) at run9 (X_{O2}=0.21, d_{O2}=15.9mm, Φ=1)

The temperature contours of ***YZ*** and ***XZ*** are shown in figure 4.11, respectively. Overall, the numerical results for the temperature (left-side in each figure) are reasonably similar to the experimental results (right-side in each figure) along all of the ranges of fuel, air axis as well as in the ***YZ*** and ***XZ*** planes.

4.3.2 The characteristics of homogeneous combustion

To find the characteristics of homogeneous combustion, air nozzle diameter (d_{air}), independent variables are changed; fuel nozzle diameter (d_f), equivalence ratio (Φ), oxygen concentration, gravity, different bottom temperature, separation distance and soot radiation. The characteristics of homogeneous combustion are found as follows. First, the main reaction occurs near the upper combustion wall in figure 4.12−(a) & (b). Also, the reaction spreads out in a larger volume inside the combustor as compared to the conventional diffusion flame combustion.

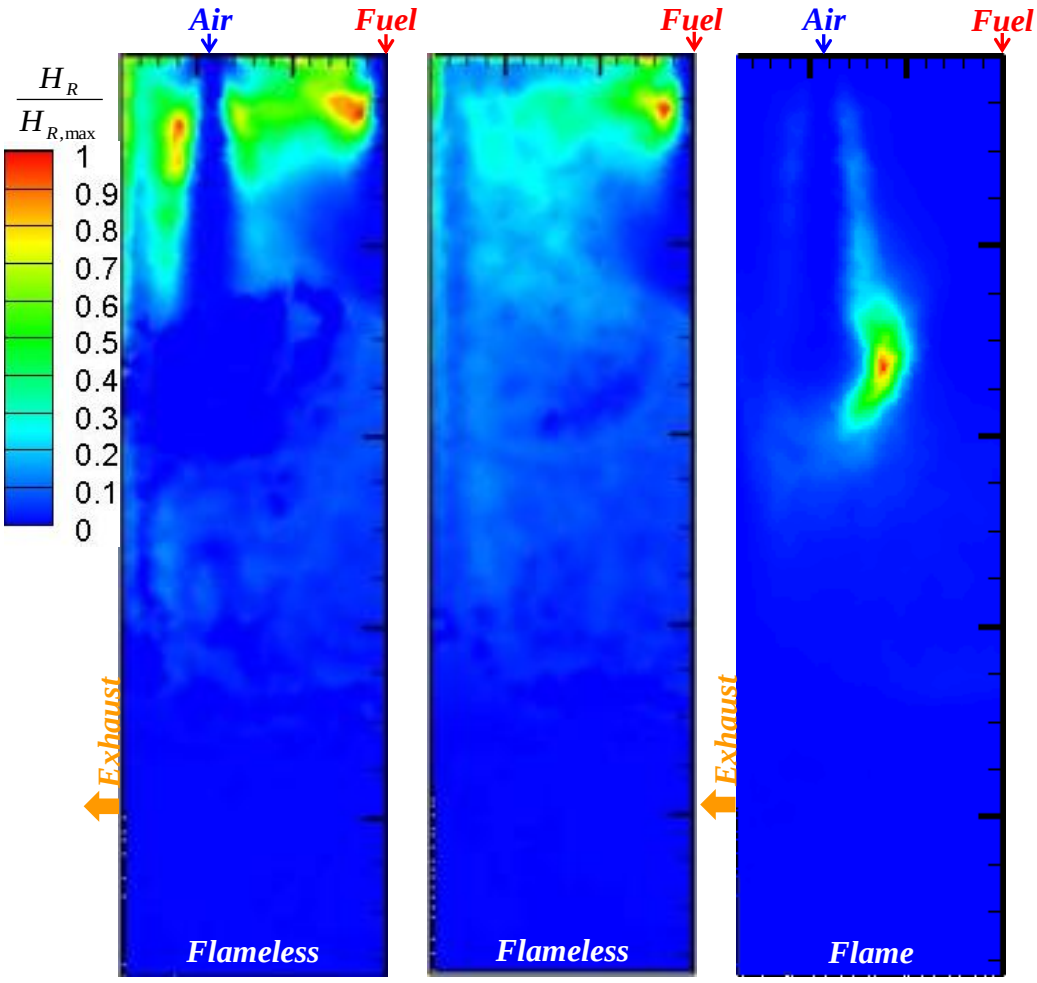

(a) *YZ* plane **(b) *XZ* plane** **(c) *YZ* plane**

Figure 4.12 The normalized heat of reaction ($H_R/H_{R,max}$, a & b at run9, c at run18)

***run9(X_{O2}=0.21, d_{O2}=15.9mm, Φ=1), run18(X_{O2}=0.40, d_{O2}=15.9mm, Φ=1)**

Conventional diffusion flame occurs between air and fuel as shown in figure 4.12−(c). $\boldsymbol{H_{R,max}}$ =0.023***kW(a)***, 0.022***kW(b)*** and 2.996***kW(c)*** are used in order to normalize to heat of reaction so the flaming combustion case does have a maximum reaction rate of about 130 times the maximum rate seen in cases (a) and (b). The flaming reaction location is further from the top plate so the air and fuel will not be preheated significantly before going into the reaction zone. In homogeneous combustion, air and fuel are preheated easier and earlier in the upper main reaction zone as they are mixed and diluted with hot combustion products. Accordingly, preheating and dilution of air and fuel are very important key factors in order to facilitate flameless combustion.

Second, homogeneous combustion has very uniform temperature distribution due to volumetric slow reaction. Figure 4.13 shows the comparison of temperature profiles between flameless and flame combustion along fuel and air axis respectively. The temperature in both flameless combustion and flame combustion is increased moving downstream as the jet mixes with hot products. In the case of flame combustion, the value of temperature increases up to ***Z***=0.6m which is the location close to the flame. After that, the temperature decreases. However, the temperature in flameless combustion has a different trend through comparing temperature profile at flame combustion. The temperature of flameless combustion along the fuel and air axis also increases. However, the increment of temperature is very small and almost uniform between ***A*** and ***B***. The difference between the highest temperature and lowest temperature is smaller in flameless combustion. To show the uniformity of temperature of homogeneous combustion inside the combustor, the three dimensional temperature distribution is plotted in figure 4.14-(b) by using the value of temperature between ***A*** (maximum temperature along fuel axis) and ***B*** (below 2.4% to temperature of ***A***).

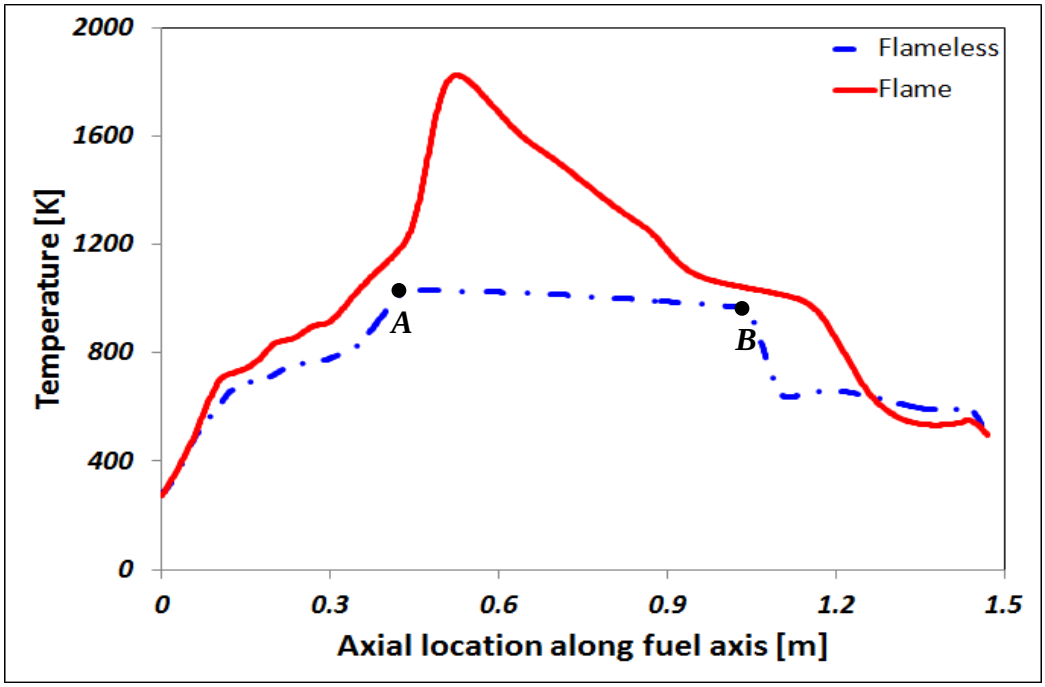

(a) Along fuel axis

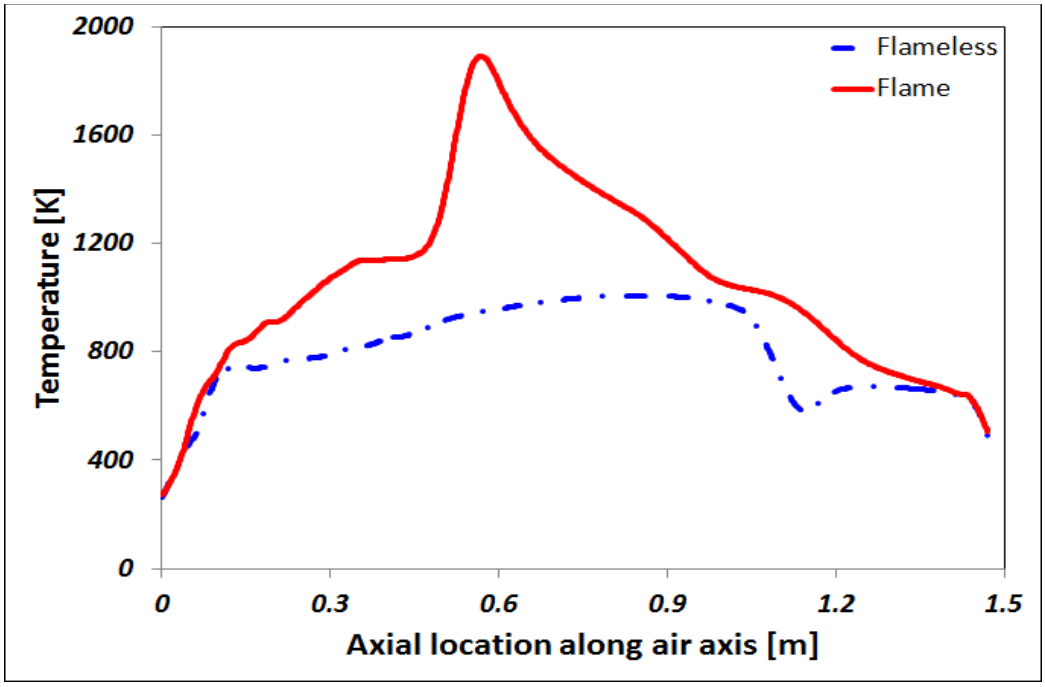

(b) Along air axis

Figure 4.13 The comparison of temperature between flameless and flame combustion (flameless at run9, flame at run 29)

***run9(X_{O2}=0.21, d_{O2}=15.9mm, Φ=1), run29(X_{O2}=0.40, d_{O2}=15.9mm, Φ=1, S=140mm)**

Most of the range of homogeneous combustion inside the combustor is placed between temperature of ***A*** and ***B***. A near uniform volumetrically temperature distribution of homogeneous combustion is observed again. This is the main characteristic of homogenous combustion which has already been found in previous studies. As a result, the flameless combustion can happen when there is significant dilution of both air and fuel jets to lower the chemical reaction rates and have a high rate of mixing.

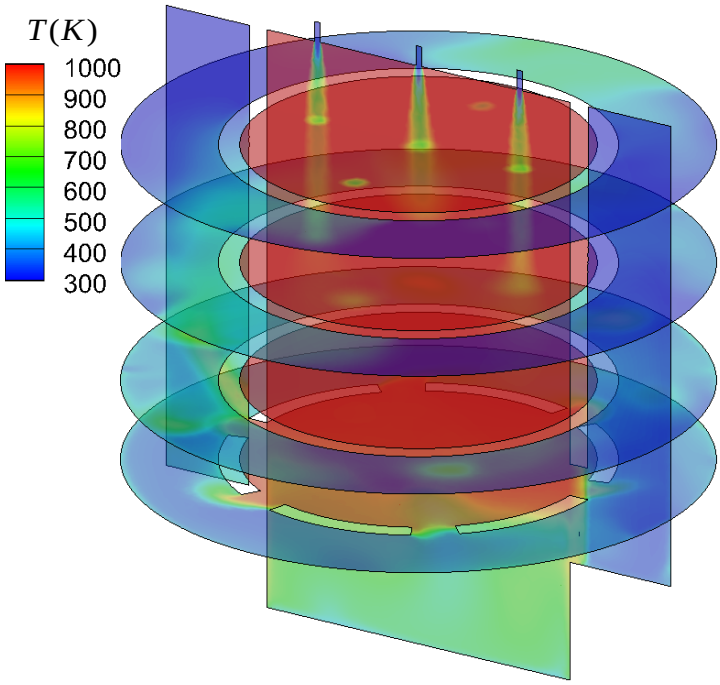

(a) *YZ* &*XY* at *Z*=0.2, 0.5, 0.8 &1.0

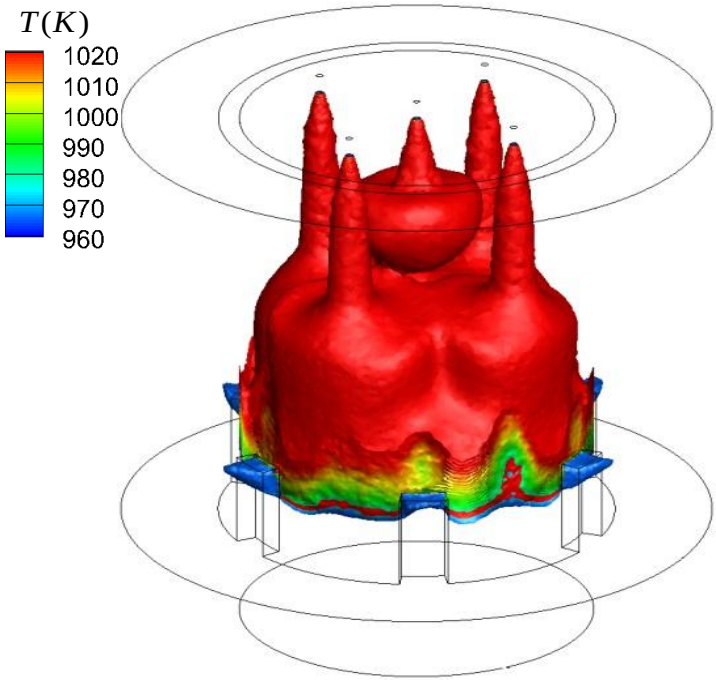

(b) Temperature distribution between T_A and T_B

Figure 4.14 Temperature (K) distribution of homogeneous combustion in 3D at run9 (X_{O2}=0.21, d_{O2}=15.9mm, Φ=1)

Third, the stagnation location is usually found at the fuel axis in homogeneous combustion through comparing non-homogeneous combustion (flame combustion) which has no stagnation location in figure 4.15. The stagnation location at the fuel axis is an important flow characteristic of homogeneous combustion because mixing between reactants and exhaust gas is finished at the stagnation location by the bigger recirculation zone between fuel axis and air axis as well as the collision of flows that forms a complex 3-dimesional flow field. The streamlines do show a flow field that is even more complex than the corresponding non-reacting flow field. Also several additional recirculating zones are present and the buoyancy keeps the burned gases near the top giving a slightly more complex flow out of the YZ plane to flow up towards the top in the XZ plane and mix with the burned gases. This recirculating flow generates a recirculating zone next to the fuel jet which cannot be seen in the YZ plane streamlines. To make flameless combustion, mixing between flows must be accomplished before the chemical reaction takes

place; otherwise it becomes a diffusion type flame. The Damköhler number ($\boldsymbol{D_a}$) is usually considered as a small value at homogeneous combustion. The stagnation location is a significant indicator of the large scale flow structures, their relative strength and the enhancing mixing they can produce to promote a diluted uniform combustible mixture. The specific flow characteristic inside the combustor is a result of the detailed geometry, the jet velocities (momentum) that forms the flow including the stagnation location, which is indicative of larger recirculating regions that allow for a fast mixing and dilution resulting in a low local Damköhler number. In this investigation the stagnation location and the larger recirculation regions are observed as unique flow characteristics under the conditions where homogeneous combustion can happen. This stagnation location can be used as an indicator for the possibility of homogeneous combustion. Actually, if the conditions result in a stagnation location that is too far away from the jet fuel origin the larger scale recirculating region near the fuel jet is no longer there and the result is a much lower mixing of fuel and air leading to flaming combustion, see Fig 4.17-(a) below. Therefore, the stagnation location of homogeneous combustion is investigated by using parameters such as the air and fuel velocity ratio, different fuel diameter and separation distances which have a significant effect on flow fields. The ***3D***-flow motion is illustrated by a few streamlines shown in figure 4.15-(d). This figure shows how the flow moves inside the combustor from each fuel and air inlet as a function of density to show preheating and dilution. Dilution and preheating occur earlier as shown in figure 4.15-(d). Fuel turns to the lateral direction by the stagnation location. Fuel starts to move rotationally to air-side. Finally, fuel and air collides and mixing between air and fuel occurs.

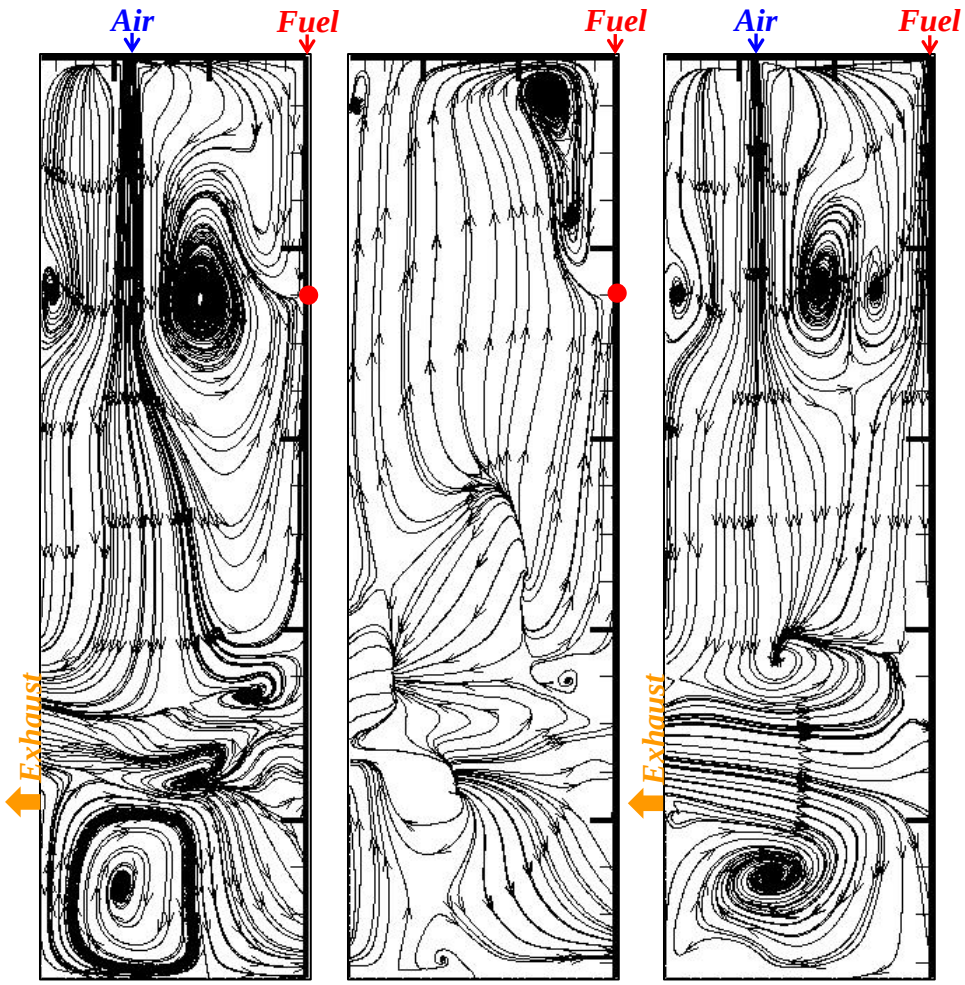

(a) *YZ* plane **(b) *XZ* plane** **(c) *YZ* plane**

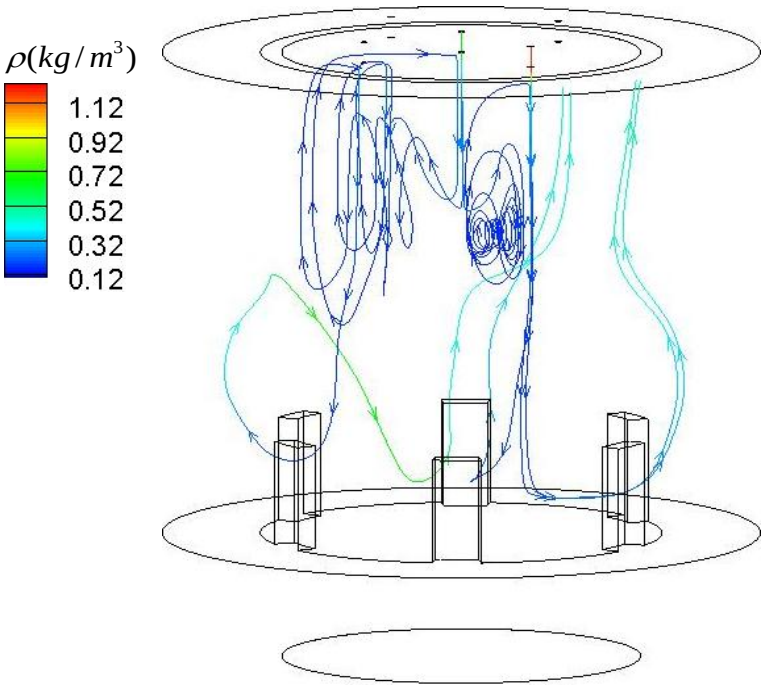

(d) *3D*

Figure 4.15. Streamline contour: flameless: (a) & (b) vs flame combustion −(c), (d) 3D-flameless (●: Stagnation location)

Stagnation location moves upward as air and fuel velocity ratio increases in figure 4.16. This means that high air velocity or air momentum increase back flow against fuel jet flow. Smaller air diameter is able to increase air velocity at fixed mass flow rate or fixed equivalence ratio. Therefore, smaller air diameter makes the stagnation location move upward. Different fuel diameters do not have significant effects on stagnation location. The stagnation location for different fuel diameters (d_f) such as 7.6 mm, 15.2 mm and 30.4 mm can be estimated by a single trend line shown in figure 4.16. However, the stagnation location is changed significantly by separation distance (S) between fuel and air inlet because separation distance has direct effect on the larger scale flow structures inside the combustor.

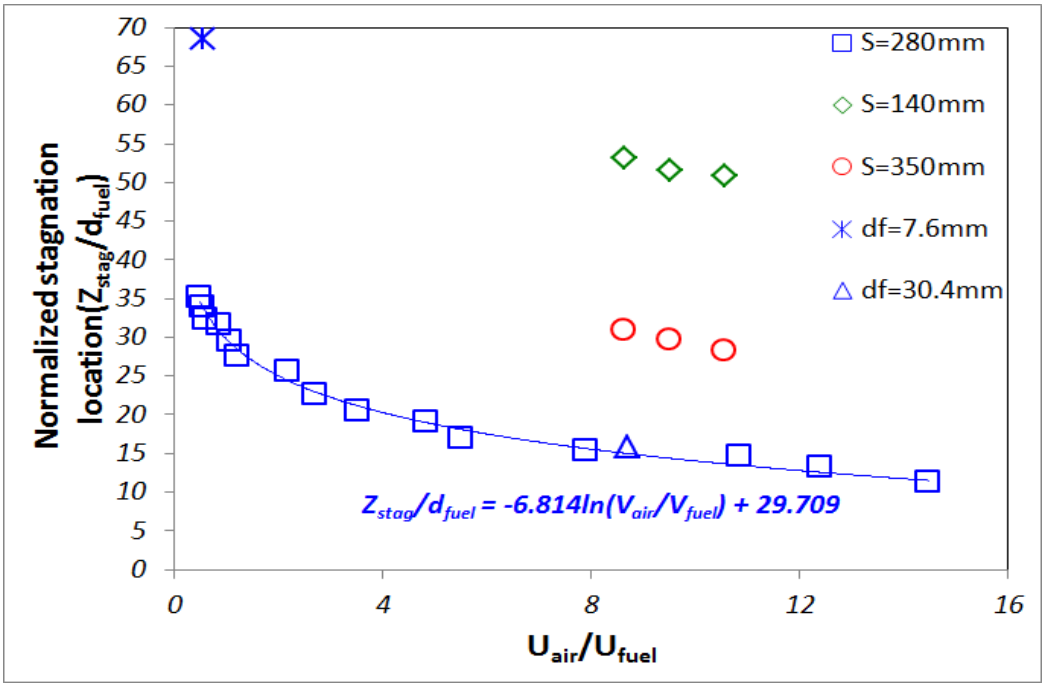

Figure 4.16 Normalized stagnation locations as function of air and fuel velocity ratios

The recirculation zone and shape changes by different separation distances are shown in figure 4.17. The stagnation location is the closest to the top at ***S***=280 mm and the largest distance from the top is at ***S***=140 mm among ***S***=140, 280 and 350mm. Generally, stagnation location is decreased or moved upward as separation distance increases up to 280mm. The recirculation zone between fuel at center and air is getting smaller but the recirculation zone between the air and side wall is enlarged as separation distance is decreased below ***S***=140mm.

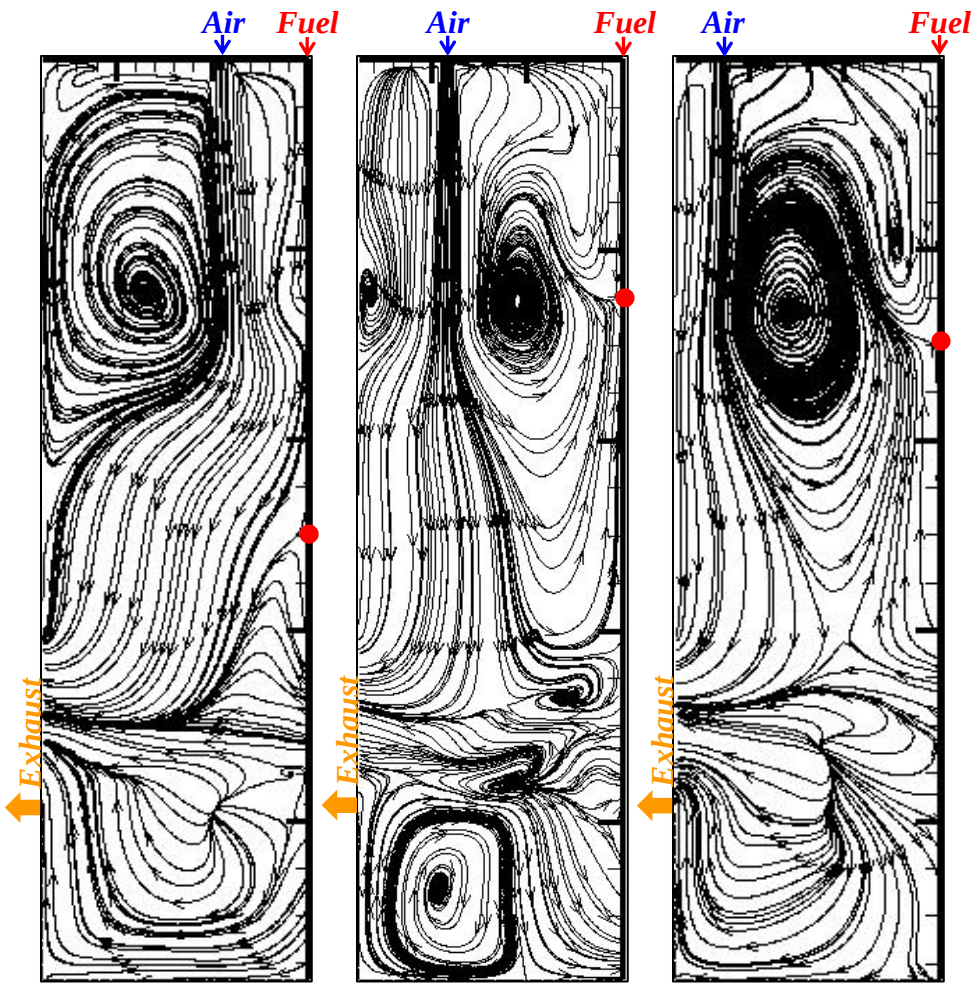

(a) *S*=140mm **(b) *S*=280mm** **(c) *S*=350mm**

Figure 4.17 Streamline contour of YZ at different separation distance

(X_{O2}=0.21, d_{O2}=15.9mm, Φ=1; ●:Stagnation location)

Finally, there is no recirculation zone between air and fuel at some critical separation distance. Also, this means that there is no stagnation location at fuel axis. Therefore, flaming combustion will be found at this critical separation distance due to insufficient and slow mixing between fuel and air. After ***S***=280mm, stagnation location is increased or moved downward. Similarly, the recirculation zone between fuel and air is increased but the recirculation zone between air and side wall is getting smaller as the separation distance is increased. Usually, the stagnation location and recirculation zone have an important role in making mixing fast and uniform.

Therefore, the shape and location of stagnation region as well as the recirculation zone are very important in order to estimate mixing. These results show that the separation distance has a significant influence on the shape and location of recirculation zones. Usually, the stagnation location has a role in making fast and uniform mixing or dilution, based on the counter flow experiments. Therefore, mixing is much faster at ***S***=280 mm than any other separation distances (***S***=140 and 350mm) because of the smallest stagnation location and the corresponding larger recirculating zone with the air. Also, when the combustor was designed and built, ***S***=280mm was selected, based on previous cold flow experiments shown to give better mixing. Therefore, ***S***=280mm is verified and considered as very unique optimal point to make a good degree of mixing in the current combustor geometry.

Fourth, air and fuel are diluted very well and uniformly by the exhaust gas. To show the degree of dilution by exhaust gas such as ***CO***, ***CO_2***, ***H_2O*** and ***NO***, the local dilution ratio (***$K_{v,local}$***) is defined in equation 73,

$$K_{v,local} = \frac{Y_{CO} + Y_{CO_2} + Y_{H_2O} + Y_{NO}}{Y_{CH_4} + Y_{O_2}} \tag{73}$$

Figure 4.18 shows that the local dilution ratio (***K_v***) is very uniform in all of the range in homogeneous combustion. Also, the air and fuel are diluted earlier and well along the fuel and air axis in homogeneous combustion because of the stagnation location along the fuel axis by the bigger recirculation zone between air and fuel. In homogeneous combustion, the stagnation location and bigger recirculation zone between air and fuel have strong effect on better mixing among flows. Therefore, local dilution ratio is more uniformly distributed inside the combustor

at homogeneous combustion. As a result, this is the key parameter to make flameless or homogeneous combustion. The local dilution ratio is below 1 from near exhaust port to bottom

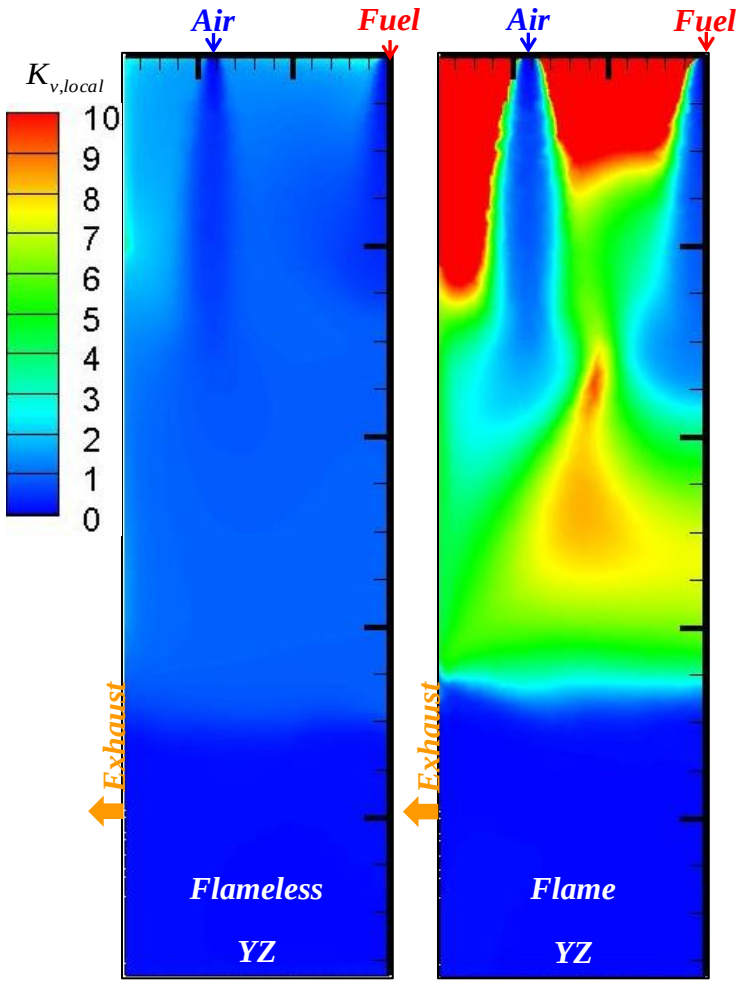

Figure 4.18 The contour of local dilution ratio: $K_{v,local}$ (flameless at run9, flame at run 18)

***run9 (X_{O2}=0.21, d_{O2}=15.9mm, Φ=1), run18 (X_{O2}=0.40, d_{O2}=15.9mm, Φ=1)**

plate due to some amount of oxygen which is coming from back flow through the exhaust ports as well as a very low mass fraction of product. The current combustor has some back flow through the exhaust ports which cannot be neglected; this is clearly demonstrated in the numerical results shown in Fig. 4.15 and 4.17. Notice the backflow is observed in Fig. 4.15 (b) XZ plane but not in the YZ plane so it is a 3-dimensional effect caused by the pressure distribution in the flow. This effect from the back flow is found not to have any significant

influence on the upper reaction zones which is the focus for the combustion zone. To minimize the effect of back flow, an approach with smaller size exhaust ports is studied in APPENDIX G.

Fifth, the reaction zone is spread out due to high dilution from the intense mixing as seen for run 9 (X_{O2}=0.21, d_{O2}=15.9mm, Φ=1) in fig 4.19 through comparing flaming combustion for run 18 (X_{O2}=0.40, d_{O2}=15.9mm, Φ=1) as shown in fig 4.19. This provides another proof (one of characteristics of homogeneous combustion) to show preheating and dilution of fuel by surrounding exhaust gas in homogeneous combustion. Most of the methane is decomposed at a diluted and preheated condition caused by the mixing with exhaust gas. In the case of flame combustion, the first step reaction (***CH₄***) occurs in a much smaller flame zone between air and fuel. Accordingly, the reaction zone of ***CH₄*** is located further downstream between air and fuel flows. However, in flameless combustion, the decomposition of ***CH₄*** is made closer to the top where the recirculating air/fuel is close to the hot combustion products and it much less local with lower rates.

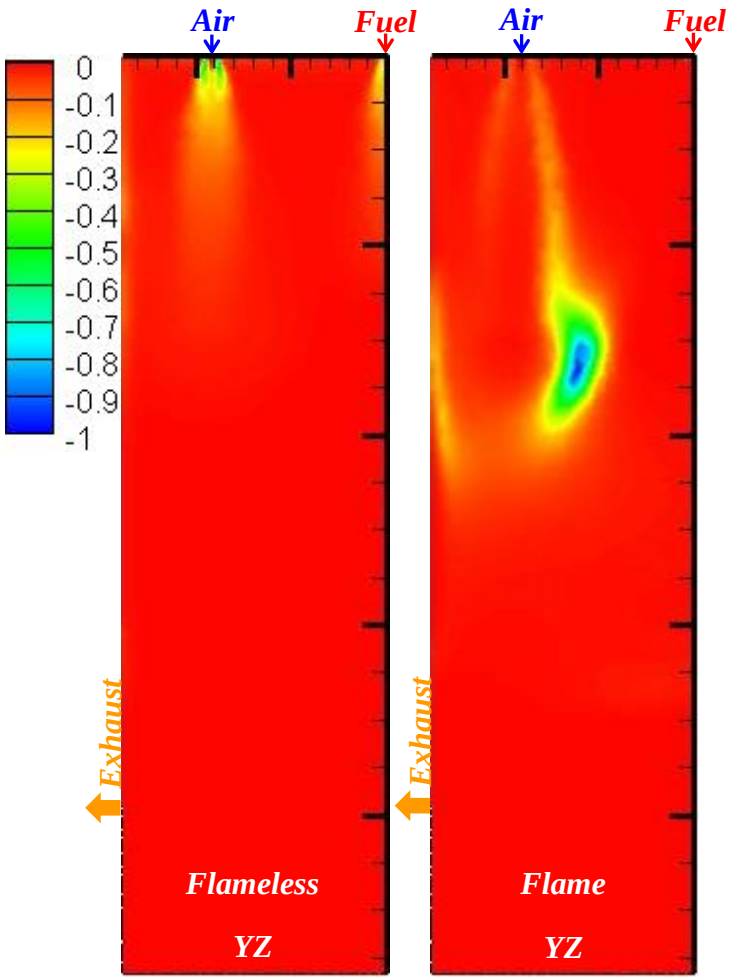

Figure 4.19 The normalized contour of $\frac{d[CH_4]/dt}{\left|d[CH_4]/dt\right|_{max}}$

(flameless at run9: X_{O2}=0.21, d_{O2}=15.9mm, Φ=1, flame at run 18: X_{O2}=0.40, d_{O2}=15.9mm, Φ=1)

Finally, the Damköhler number (***D*****$_a$**) is smaller in homogeneous combustion. Equation 74 shows the definition of Damköhler number (***D*****$_a$**).

$$D_a = \frac{\tau_{flow}}{\tau_{chem}} = \frac{2k/\varepsilon}{\rho(Y_{CH4}/\dot{w}_{CH4} + Y_{CO}/\dot{w}_{CO})} \tag{74}$$

Where ***k*** is turbulent kinetic energy, ***ε*** is turbulent dissipation rate, ***ρ*** is density, ***Y$_i$*** is mass fraction of species ***i*** and $\dot{w}_i$ is chemical reaction rate of species ***i***. Here, ***τ$_{flow}$*** is called to integral time scale of mixing. ***D$_a$*** is greater than 1 in the flaming combustion because the reaction time is

faster than the flow mixing time. However, D_a < 1 means that the chemical reaction is slower (time longer) than flow mixing scales caused by random turbulent flow motion. Therefore, the shape of the reaction zone is not a flame or thin reaction zone anymore. Chemical reactions distribute simultaneously over a large region of the combustor which is called the volumetric reaction. Here, one characteristics of homogeneous combustion classified as volumetric reaction requires a Damköhler number (D_a) below 1, which is seen for the whole region of combustor in flameless combustion in figure 4.20.

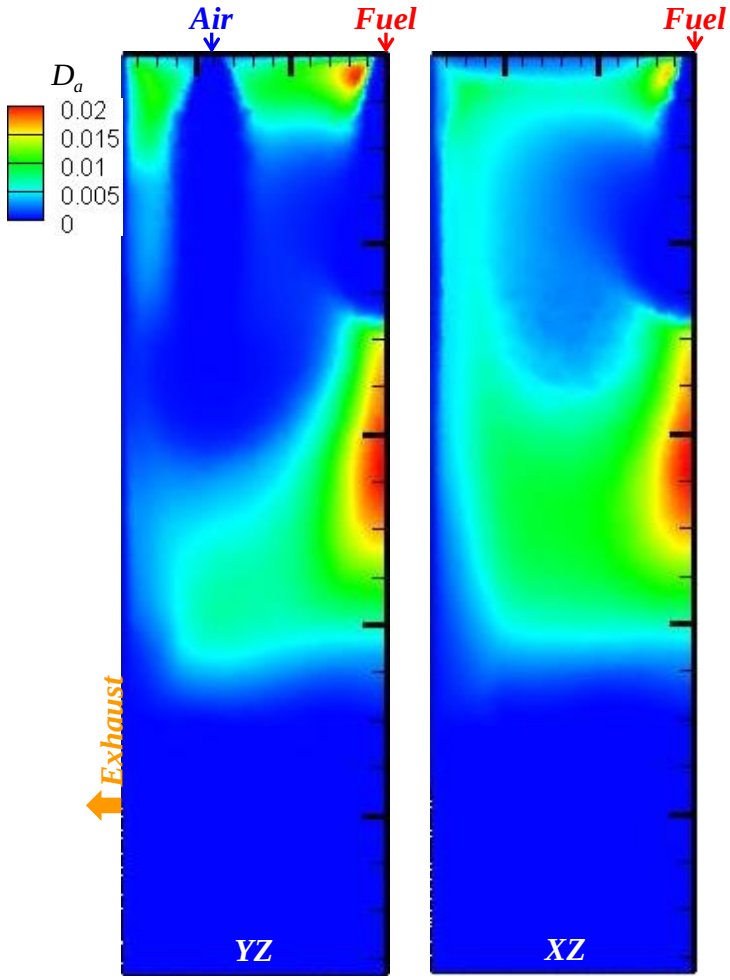

Figure 4.20 The contour of Damköhler number (D_a) in flameless combustion at run 9 (X_{O2}=0.21, d_{O2}=15.9mm, Φ=1)

4.3.3 The domain of homogeneous combustion

The limited domain of homogeneous combustion is shown with an equivalence ratio and air/fuel diameter ratio as parameters and also with equivalence ratio and air/fuel velocity ratio. These are based on the characteristics of homogeneous combustion from the numerical calculations and shown in figure 4.21. Usually, homogeneous combustion is not found at higher oxygen concentration (X_{O2} =0.30 and 0.40) or without gravity or at rich condition (Φ>1.1). Each reaction zone is defined at the condition of X_{O2}=0.21 and S=280mm in figure 4.21. '***A***' is a flaming combustion, '***B***' is an unstable combustion while '***C'*** is a flameless combustion or homogeneous combustion. The highest limit value of domain in homogeneous combustion is at Φ=1.1. The lowest domain is dependent on air/fuel diameter ratio, air/fuel velocity ratio or air/fuel momentum ratio. The lowest domain Φ value of homogeneous combustion is decreased as the air/fuel diameter ratio decreased. The domain of homogeneous combustion gets wider as the air/fuel diameter ratio is decreased. This means that air diameter gets smaller and air velocity gets higher. Higher air velocity induces more back flow or higher recirculation zone against fuel flow. The stagnation location along the fuel axis moves upward as air velocity increases. Therefore, the mixing among fuel, air and exhaust gas occurs earlier by the stagnation location. Upper stagnation location has significant effects on enhancing mixing. Mixing will get faster as air velocity increases. As a result, distributed reaction is easily caused by the fast mixing among flows inside the combustor (D_a<1). Also, the range of domain of homogeneous combustion as a function of air/fuel velocity ratio is wider as the equivalence ratio goes up to Φ=0.8. However, in Φ=0.7, the domain range of homogeneous combustion decreases due to the lean flammability limit. This means that a slightly higher air/fuel velocity ratio is needed in order to make stable and sufficient mixing by stagnation location or recirculation zone at below Φ=0.7. As a result,

X_{O2}=0.21 and smaller air diameter or higher air velocity at fixed fuel diameter and velocity is able to make homogeneous combustion in figure 4.21.

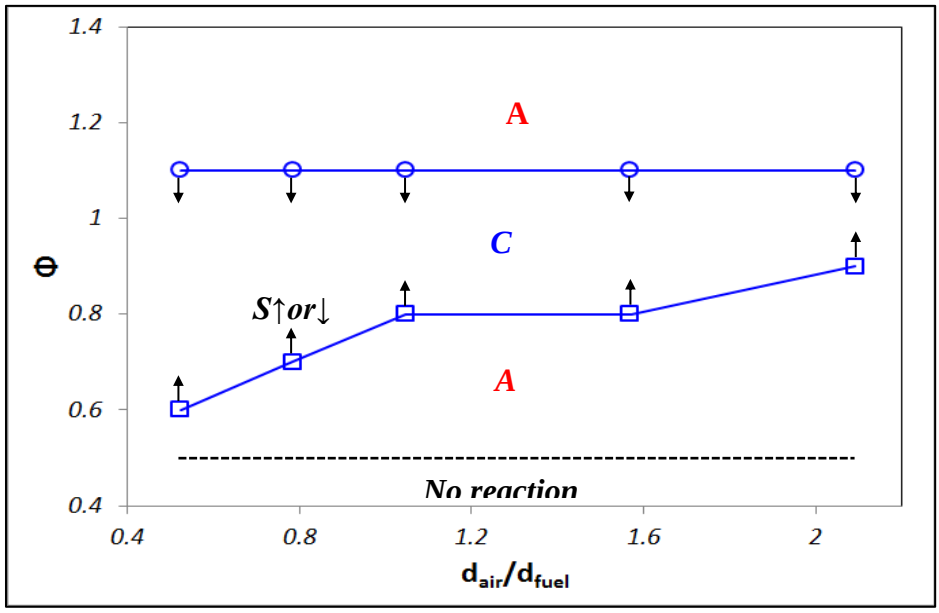

(a) Φ vs d_{air}/d_{fuel}

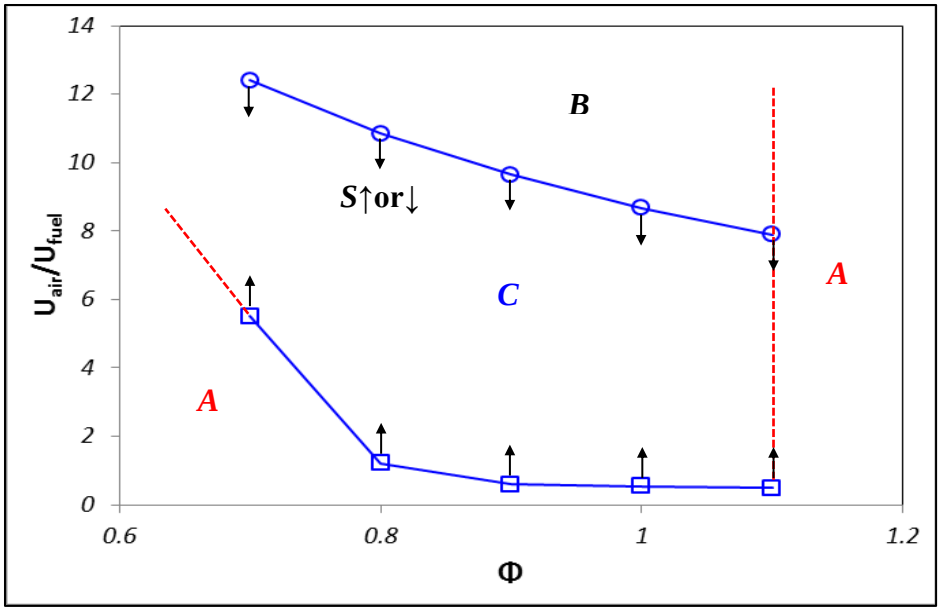

(b) U_{air}/U_{fuel} vs Φ

Figure 4.21 The domain of homogeneous combustion as function of Φ and d_{air}/d_{fuel} as well as U_{air}/U_{fuel} and Φ at X_{O2}=0.21 and S=280mm

Each reaction zone is defined at the condition of X_{O2}=0.21 and ***S***=280mm in figure 4.21. '***A***' is a flaming combustion, '***B***' is an unstable combustion while '***C'*** is a flameless combustion or homogeneous combustion. The domain of homogeneous combustion (***C***) will be smaller for the other separation distances (***S***=140 mm and ***S***=350 mm) due to lower mixing rates or dilution by different flow characteristics such as shape and location of stagnation and recirculation zone. To predict or define operating maps of homogeneous combustion well, experimental approach or detailed numerical approaches such as DNS with detailed chemical model is needed. Current few groups [62][63] are studying the homogeneous combustion by using DNS or a flamelet approach. However, the scale of the domain is very small and so it is impossible to estimate if the homogeneous combustion can be an average over a larger domain of small scale flamelets. Although this working domain of homogeneous combustion may not be estimated well to experimental working map of homogeneous combustion due to the limitation of numerical model in FLUENT, these results is valuable enough to show the trend of operating map of homogeneous combustion as function of the parameters such as separation distance, air and fuel velocity ratio, air and fuel diameter ratio and equivalence ratio.

4.3.4 The radiation effect on homogeneous combustion

To check the radiation effects on transition to homogeneous combustion, the soot radiation is considered by using two step model in FLUENT [43]. The two-step Tesner model estimate the generation of radical nuclei and then calculates the formation of soot on these nuclei. The effectiveness of soot radiation is investigated in this dissertation as it may be a possible way of transferring more heat directly to the bottom plate instead of indirectly from the top wall to the bottom plate. Usually the higher oxygen concentration is found to lead to flaming combustion. $\boldsymbol{X_{O2}}$=0.30, $\boldsymbol{d_{O2}}$=15.9mm and $\boldsymbol{\Phi}$=1(run 17) is selected in order to investigate the transition from flame combustion to flameless combustion. To check the effect of soot radiation, soot is introduced artificially by adding it through the fuel jet. 1% and 5% amount of soot of the mass flow rate of fuel are chosen, to investigate the possibility of homogeneous combustion ($\boldsymbol{\Phi}\leq 1.1$) in this dissertation. To cause an increase in radiation heat loss soot is added since the gas radiation from the products (water and carbon dioxide) is higher than for air but still insignificant compared to the total heat transfer. Figure 4.22 and 4.23 show the soot radiation effect through considering the heat of reaction and temperature distribution. Figure 4.22 shows that reaction zone moves from some downstream location between fuel and air to a location closer to the top. The soot addition spreads the reaction zone over a larger volume and the temperature also becomes more uniform. The upper reaction zone has significant effects on diluting and preheating of fuel and air by the hot combustion products. The transition from flame combustion to flameless combustion is facilitated. From figure 4.23, temperature distribution is more distributed uniformly and the highest temperature peak disappears as more soot is added into the fuel jet. Uniform temperature distribution is also another indication of homogeneous combustion. The Damköhler number (D_a), equation 74, is defined based on the large scale mixing time and

the chemical reaction time. For highly turbulent flows it can be done with the small scale mixing time (recall the EDC model) instead and shown in figure 4.24 where $D_{a,k}$ is Kolmogorov Damköhler number to define whether the reaction is fast or slow relative to the mixing rate. $D_{a,k}$ can explain the reaction at the finest scale by turbulent mixing & define as follows;

$$D_{a,k} = \frac{\tau_k}{\tau_{chem}} = \frac{0.4082(\nu/\varepsilon)^{1/2}}{\rho(Y_{CH4}/\dot{w}_{CH4} + Y_{CO}/\dot{w}_{CO})} \tag{75}$$

Here $\boldsymbol{\nu}$ is kinematic viscosity, $\boldsymbol{\varepsilon}$ is turbulent dissipation rate, $\boldsymbol{\rho}$ is density, $\boldsymbol{Y_i}$ is mass fraction of species $\boldsymbol{i}$ and $\dot{w}_i$ is chemical reaction rate of species $\boldsymbol{i}$.

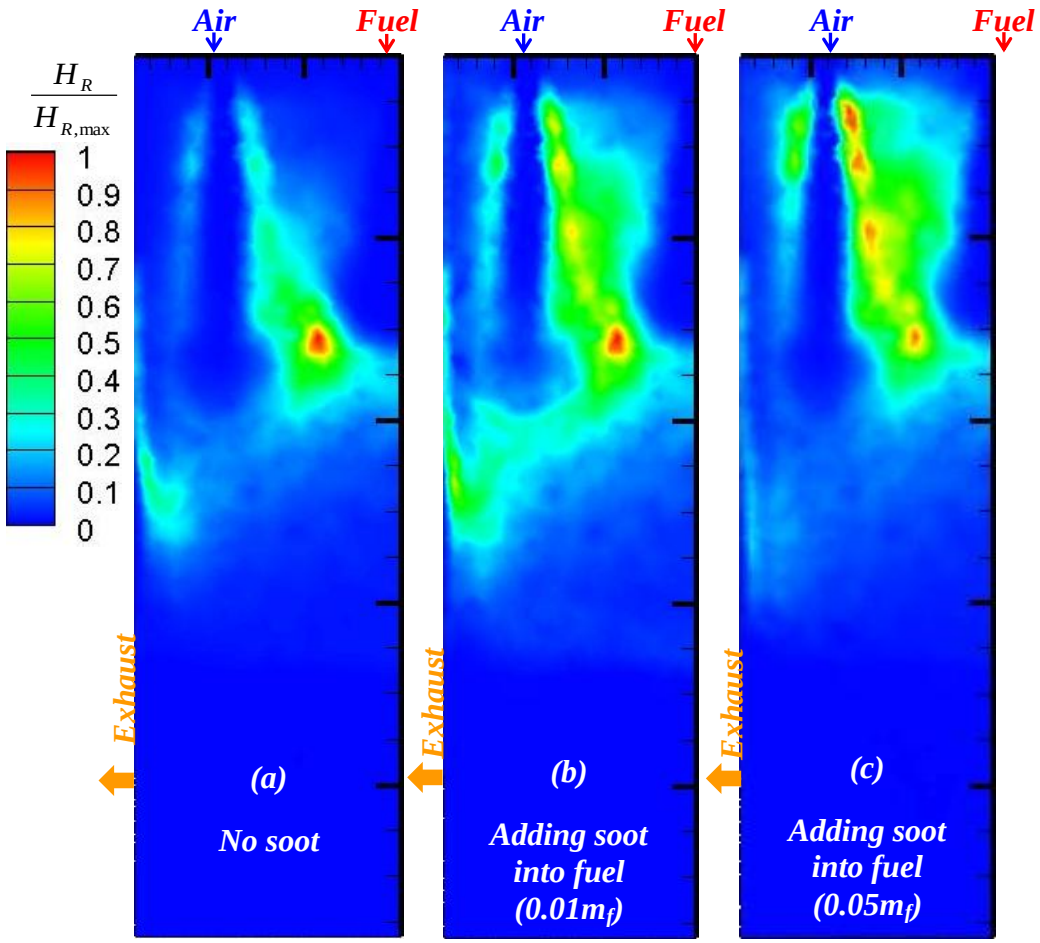

Figure 4.22 The normalized heat of reaction of *YZ* ((a) run17, (b) run27 and (c) run28) at X_{O2}=0.30, d_{O2}=15.9mm, Φ=1 ($H_{R,max}$=0.469kW)

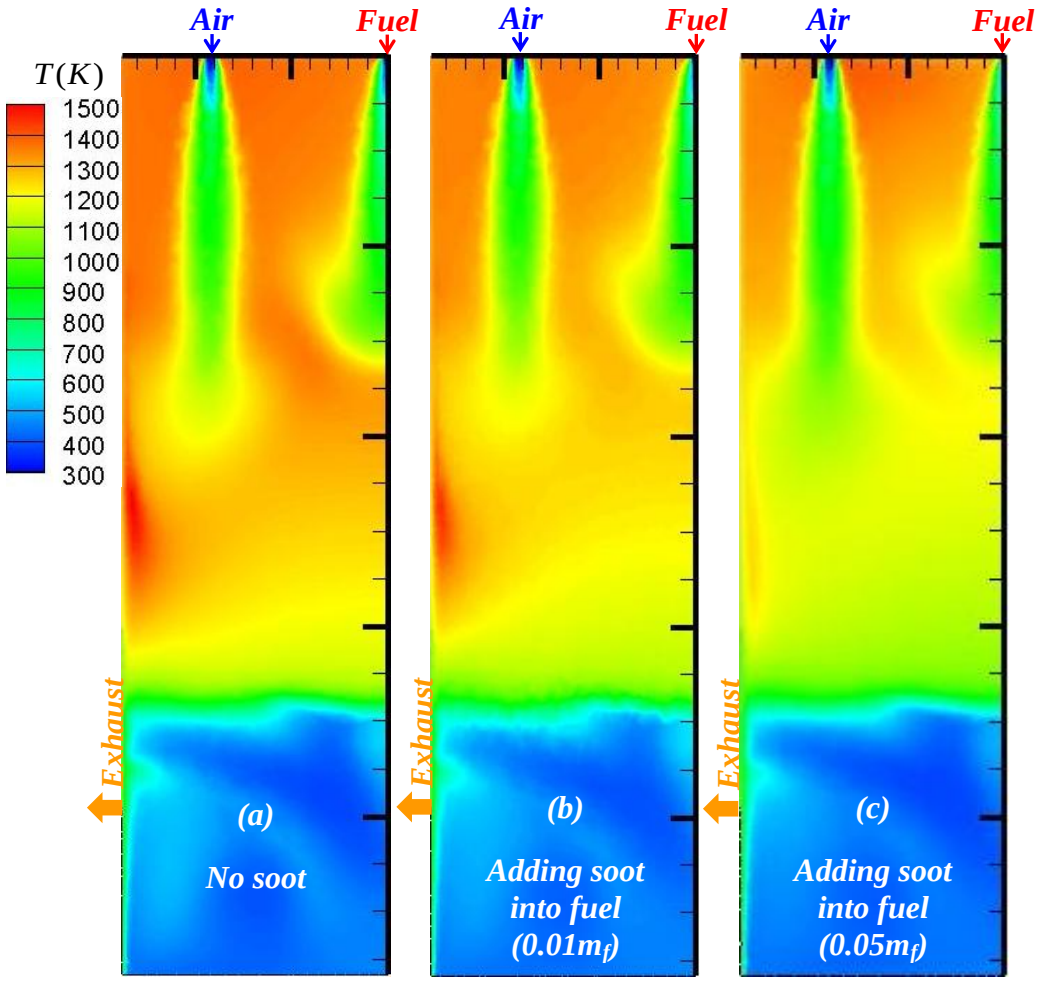

Figure 4.23 The temperature contour of *YZ* ((a) run17, (b) run27 and (c) run28) at X_{O2}=0.30, d_{O2}=15.9mm, Φ=1

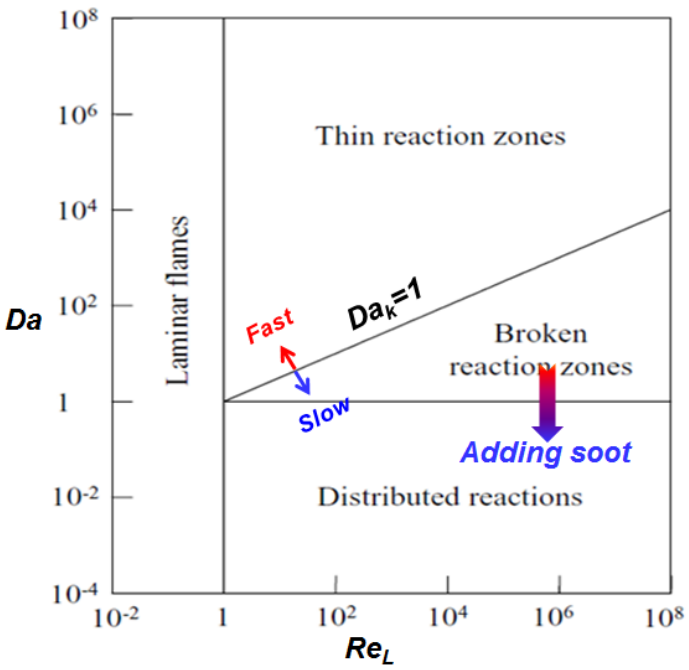

Figure 4.24 The regime diagram for non-premixed turbulent combustion[64]

Usually, the volumetric reaction or distributed reaction has the lower Damköhler number (Damköhler number: $D_a<1$) in figure 4.24. The Kolmogorove Damköhler number is less than 1 in all cases. These three cases have slow reaction regimes. To define zones between broken reaction zones and distributed reaction zones, the Damköhler number is plotted in figure 4.25. The maximum Damköhler number ($D_{a,max}$) from Fig 4.25 changes from 2.7 to 1.2 and 0.4 as more soot is added. Thus, the reaction zone moves from the ***Broken reaction*** region to the ***Distributed reaction region*** in region in figure 4.24. Also, other characteristics of homogeneous combustion like the existence of stagnation location, a uniform dilution ratio and a uniform CH_4 reaction rate are all checked and found to be satisfied confirming the proper conditions for homogeneous combustion. These results show that the flaming combustion is transformed into flameless combustion through adding soot into the fuel jet. It is therefore possible to use soot (or

other particles) to enhance the radiation and thus increase the operating range that makes homogeneous combustion possible.

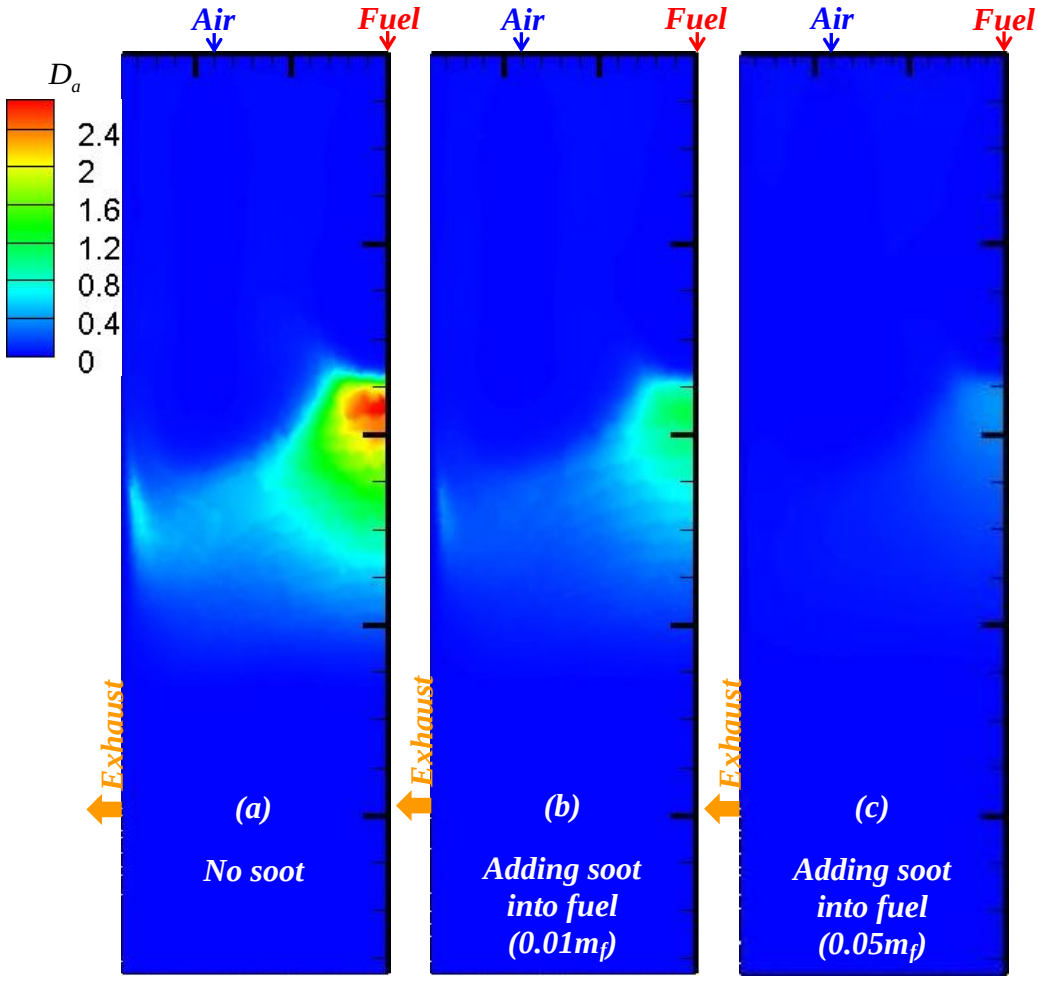

Figure 4.25 The Damköhler number contour of *YZ* ((a) run17, (b) run27 and (c) run28) at X_{O2}=0.30, d_{O2}=15.9mm, Φ=1

Also, temperature of upper and side wall combustor are checked by using area averaging in table 4.2. Side wall is defined in side surface area of combustor except side surface area below location of exhaust ports. Wall temperature does not change significantly. The ratio of temperature difference is only 0.3%. Therefore, soot radiation does not have a significant effect on heat transfer to the wall.

Run	Wall temperature (K)	
	Upper	Side
17	1341.3	1300.6
27	1338.8	1297.7
28	1336.7	1294.3

Table 4.2 Wall temperatures in the furnace

***Run 17(d_{air}=15.9mm,Φ=1, X_{O2}=0.30), Run 27(d_{air}=15.9mm,Φ=1, X_{O2}=0.30, 0.01m_f),**

Run 28(d_{air}=15.9mm,Φ=1, X_{O2}=0.30, 0.05m_f)

4.3.5. Heat balance in the furnace

The heat balance in the furnace is considered numerically and experimentally. The heat generated inside the combustor is transferred to cold bottom plate, the combustor walls, products and out of the combustor through the exhaust openings. The heat transfer rates absorbed into the cold bottom plate of combustor (main heat transfer rate in the furnace) are calculated numerically and experimentally in table 4.3 for various working conditions by using the heat transfer ratio in equation 76.

$$\text{Heat transfer ratio} = \frac{\dot{Q}_{cold}}{\dot{Q}_{in}} \tag{76}$$

Where $\dot{Q}_{cold}$ is the heat absorbed into cold bottom plate and $\dot{Q}_{in}$ is the mean heating value of combustion of fuel (63.8$\boldsymbol{kW}$).

Run	Heat transfer ratio	
	Experimental result	Numerical calculation
9	0.47	0.48
17	0.47	0.49
18	0.48	0.5

Table 4.3 Heat transfer ratio into cold bottom plate in the furnace

***Run 9(d_{air}=15.9mm,Φ=1, X_{O2}=0.21), Run 17(d_{air}=15.9mm,Φ=1, X_{O2}=0.30), Run 18(d_{air}=15.9mm,Φ=1, X_{O2}=0.40)**

From table 4.3, higher oxygen concentration induced relative higher heat transfer into cold bottom plate. However, approximately 48% of heat input (same amount) in all of cases including in the soot radiation (approximately 49%) is absorbed by the cold bottom plate. Therefore, soot radiation only has significant effect of facilitating near homogeneous combustion to be possible.

4.3.6. Conclusion

Numerical studies of homogeneous combustion were performed on the flow and the reacting characteristics such as main reaction zone, temperature distribution, stagnation location, the degree of dilution, $\boldsymbol{CH_4}$ reaction rate and Damköhler number ($\boldsymbol{D_a}$) as function of air nozzle diameter ($\boldsymbol{d_{air}}$), fuel nozzle diameter ($\boldsymbol{d_f}$), equivalence ratio ($\boldsymbol{\Phi}$), oxygen concentration, gravity, different bottom temperature and separation distance as well as soot radiation.

First, the main reaction zone occurs in the upper volume of the furnace when we have homogeneous combustion. A more uniform reaction is found in the volume at significant lower reactions rates (2 orders of magnitude) when homogeneous combustion happens. A conventional diffusion flame with a more local reaction between air and fuel happens due to less preheating and mixing of air and fuel before the reaction zone. In homogeneous combustion, the upper main reaction zone is created from the larger recirculating zones that promote mixing of air and fuel and brings it towards the combustion products to preheat and dilute the mixture before combustion takes place. As a result, the large scale motion of the air and fuel jets are considered key components of the flow that determine mixing/dilution and heating to make flameless combustion possible.

Second, the uniform temperature distribution is found in homogeneous combustion through comparing it to the case of flame. In flameless combustion, the increment of temperature along the fuel and air axis is very small and very uniform at 45% of the whole axial location. In the 3$\boldsymbol{D}$ figure of the temperature, the uniform distribution of temperature is verified.

Third, the homogeneous combustion usually has a stagnation location that indicates a strong recirculating air zone which enhances mixing and dilution between reactants and product

gases. Fast mixing of fuel and air, high dilution with hot products are two of the necessary characteristics of the flow to obtain homogeneous combustion. The mixing ensures uniformity and the high dilution leads to a low reaction rate but high enough temperature so the mixture can burn. As the stagnation location varies with different conditions it generally is because the size and or strength of the recirculating zones changes altering the very complex 3D-flow inside the combustor. Therefore, the stagnation location is analyzed as the function of air & fuel velocity ratio, different fuel diameter and separation distances. Usually, the location of stagnation moves up at the higher air and fuel velocity ratio due to the stronger air recirculation leading to higher back flow. This back flow enhances the mixing of air and fuel and brings that mixture towards the top of the furnace where it is diluted by the hot products and heated so $T \geq T_{auto\ ignition}$. The change of fuel diameter does not have any significant effect on the stagnation location nor the main flow characteristics. However, stagnation locations as well as flow characteristics of homogeneous combustion such as shape and location of recirculation zone, based on the streamline, are changed significantly by the separation distance. In current combustor, the location of the stagnation point is smallest at $\boldsymbol{S}$=280mm. This indicates a stronger air recirculation so the mixing is much faster at $\boldsymbol{S}$=280 mm than any other separation distance ($\boldsymbol{S}$=140 and 350mm).

Fourth, in homogenous combustion, air and fuel are diluted uniformly by exhaust gas which is described by a dilution ratio defined by $\boldsymbol{CO}$, $\boldsymbol{CO_2}$, $\boldsymbol{H_2O}$, $\boldsymbol{NO}$ air and $\boldsymbol{CH_4}$ inside the combustor. The real dilution cannot be calculated as the local products cannot be distinguished from the extra products mixed in, so this ratio is being used as a substitute. The dilution ratio confirms that the upper volume of the furnace has some products together with some fuel and oxygen, i.e. K_v is small. This is very different from the flaming combustion situation that show

high K_v values in the upper section (due to the absence of fuel and oxygen) and low values in other locations. The strong variation over the volume is a clear indication of a flaming combustion.

Fifth, the main reaction of $\boldsymbol{CH_4}$ is located in the upper part of the furnace. This is the result of the strong recirculation of both air and fuel bringing the mixture close to the combustion zone where it can be preheated and diluted. At the same time the high rate of mixing spreads the gases around most of the domain resulting in a near homogeneous combustion. Accordingly, the reaction rate of $\boldsymbol{CH_4}$ is distributed uniformly in a very large volume (and thus also low rate) showing near homogeneous combustion. This is in contrast to the flame combustion which has non-uniformity of the $\boldsymbol{CH_4}$ reaction rate because $\boldsymbol{CH_4}$ is mostly destroyed at a small flame zone between air and fuel like a diffusion flame with very high local value of the reaction rate.

Sixth, homogeneous combustion has to have fast mixing in order to make uniformly volumetric reaction. Therefore, the Damköhler number must be less than 1, based on the definition of the Damköhler number. In homogeneous combustion, the Damköhler number is found at values significantly below 1. This means that mixing is faster than the reaction, and the uniform volumetric reaction is possible. The Damköhler number is a necessary indicator to verify the homogenous combustion.

Seventh, the operating domain of homogeneous combustion is verified as function of equivalence ratio and air/fuel diameter ratio as well as equivalence ratio and air/fuel velocity ratio through considering the flow and reacting characteristics of the combustion domain. Usually, homogeneous combustion is not found at higher oxygen concentration ($\boldsymbol{X_{O2}}$ =0.30 and 0.40), without the gravity as well as rich condition ($\boldsymbol{\Phi}$>1.1). $\boldsymbol{\Phi}$=1.1 is highest limit value of

operation domain of homogeneous combustion. Air/fuel diameter ratio, air/fuel velocity ratio or air/fuel momentum ratio has the important effects on lowest operating domain value. Operation domain of homogeneous combustion is increased at low air/fuel diameter ratio, smaller air diameter or higher air velocity due to fast mixing or dilution by the stagnation location and higher recirculation zone. As a result, to facilitate near homogeneous combustion in the current furnace the following controllable conditions were found.

- ***Find optimal separation distance (S=280 mm is close to optimal).***
- ***X_{O2}=0.21 (No higher oxygen concentration with the current range of flow rates).***
- ***Higher velocity or smaller air diameter at fixed mass flow rate.***
- ***$\Phi \leq 1.1$.***

Finally, the effect of soot radiation is investigated through checking the heat of reaction, temperature distribution and the Damköhler number. The reaction zone moves towards the upper location as the amount of soot injected into the fuel jet increases. Temperature is distributed uniformly due to soot radiation emission/absorption by adding soot into the fuel jet. Finally, the Damköhler number is found to be below 1, verifying the proper condition for a volumetric reaction. As a result, the reaction mechanism is transferred from flame combustion to flameless combustion, based on heat reaction zone, temperature distribution, Damköhler number as well as other characteristics such as the existence of stagnation location, uniform dilution ratio and uniform CH_4 reaction rate. Also, soot radiation does not have any significant effect on energy balance. The significant effect of soot radiation is to extend the range of flameless combustion

with respect to other furnace conditions such as oxygen concentration, temperature, equivalence ratio etc.

CHAPTER 5

Future work

The main purpose of this dissertation is to computationally develop a fundamental understanding of flow and mixing characteristics of non-reacting and reacting confined turbulent jet flows for homogeneous combustion (***RHC***) and finds the operating ranges for ***RHC*** furnaces within some of the controllable parameters. We have first conducted numerical and experimental investigations of non-reactive confined turbulent jets injected into co- or counter-flowing streams by measuring and calculating the velocity, temperature, and tracer gas (***NO***) concentration profiles. The numerical study of reacting gas in the furnace is accomplished as function of air nozzle diameter (d_{air}), fuel nozzle diameter (d_f), equivalence ratio (Φ), oxygen concentration, gravity, different bottom temperature and separation distance as well as soot radiation, based on all of my previous and current results of flow and mixing characteristics of a confined turbulent jets flowing into co- and counter-flow as well as numerical calculations of non-reacting gas in the furnace. Therefore, the experimental approach will be needed for the validation of these numerical approaches of reacting gases. Also, detailed numerical approaches will be needed for better predictions.

1. The location of the main reaction zone could be verified with respect to its location in the combustor, based on the previous temperature measurement data and some residue of flame on the upper wall of combustor rather than enthalpy of reaction. Also, the reaction rate of CH_4 is found numerically to be distributed uniformly for the

higher flow velocities leading to homogeneous combustion. Therefore, the chemical reaction zone should be measured experimentally in order to check the location and uniformity of the reaction zone. It may need optical methods to measure the location and type of chemical reactions happening. Also, numerical results of temperature distribution show the uniformity in the homogeneous combustion inside the combustor. However, temperature must be measured at different planes to show and verify the uniformity of temperature map experimentally.

2. The stagnation location is found along fuel axis at homogeneous combustion. The stagnation location and the recirculation zones are very important characteristic to make faster mixing and more uniform as well as dilution and preheating of air and fuel (key essential to make homogeneous combustion). To show this stagnation location and recirculation zones experimentally, the velocity could be measured with either PIV or LDV.

3. For the numerical approaches, nozzle diameter ($\boldsymbol{d_{air}}$), fuel nozzle diameter ($\boldsymbol{d_f}$), equivalence ratio ($\boldsymbol{\Phi}$), oxygen concentration, different bottom temperature and separation distance as well as soot radiation are considered. These numerical results give us enough information about homogeneous combustion before starting experimental approach. Experimental approaches will be needed in order to verify and enlarge the operating domain of homogeneous combustion, guided by these numerical results.

4. Some important characteristics of homogeneous combustion are found by numerical investigation in this dissertation. These results are shown reasonably when considering averaging and macroscopic characteristics of homogeneous combustion.

However, the simple chemistry model and steady solver are used due to limited time and current computational capacity. Therefore, a more detailed numerical approach can be done by using more detailed chemistry mechanism model, different reaction model and turbulence model (for example, DNS), such computations will be pushing beyond current capabilities.

5. Soot radiation has some effects on making the homogeneous combustion possible as shown in this dissertation where they otherwise would not be possible. A more detailed investigation of soot radiation can be used for further refinements. For the experimental work, the fuel and air supply lines must be modified in order to add soot respectively. Also, size of soot particle is also another main parameter for such a study that was not part of the current work. To check the effect of size of soot particle, a soot model (to estimate soot movement, aggregation and destruction) must be developed and applied in this unique combustor based on previous works.

6. Current combustor has a back flow problem at exhaust ports due to the buoyancy. In this thesis, the effect of back flow through the exhaust ports does not have any significant effects on upper reaction zones where we are interested in but some effects on the bottom region of the furnace. This effect of the back flow causes a temperature change in the surface temperatures and thus influences the study of wall radiation. For further investigations of homogeneous combustion, this issue must be solved by changing the array/size of exhaust ports and the exhaust flow configuration.

APPENDIX A

Verification of two step reaction model in CHEMKIN

The two step reaction model is used for numerical calculation of homogeneous combustion in this dissertation. This model had been already verified by previous researchers. Many researchers use this model of their numerical calculation to reduce numerical calculation time. I verify the two step reaction model through comparing the calculation results with whole chemistry in ***CHEMKIN*** before I use numerical reaction calculation in my dissertation. Well stirred reactor (***WSR***) model such as very similar condition to homogeneous combustion (fast mixing) is used. Residence time (T_r) is selected 60s to make the complete reaction. Temperature inside the combustor ($T_{combustor}$) and inlet temperature (T_{inlet}) is 1200K and 298.15K in order to set up the similar condition respectively. Inlet pressure (P_{inlet}) is 1atm. Φ is selected, based on the working range of homogeneous combustion.

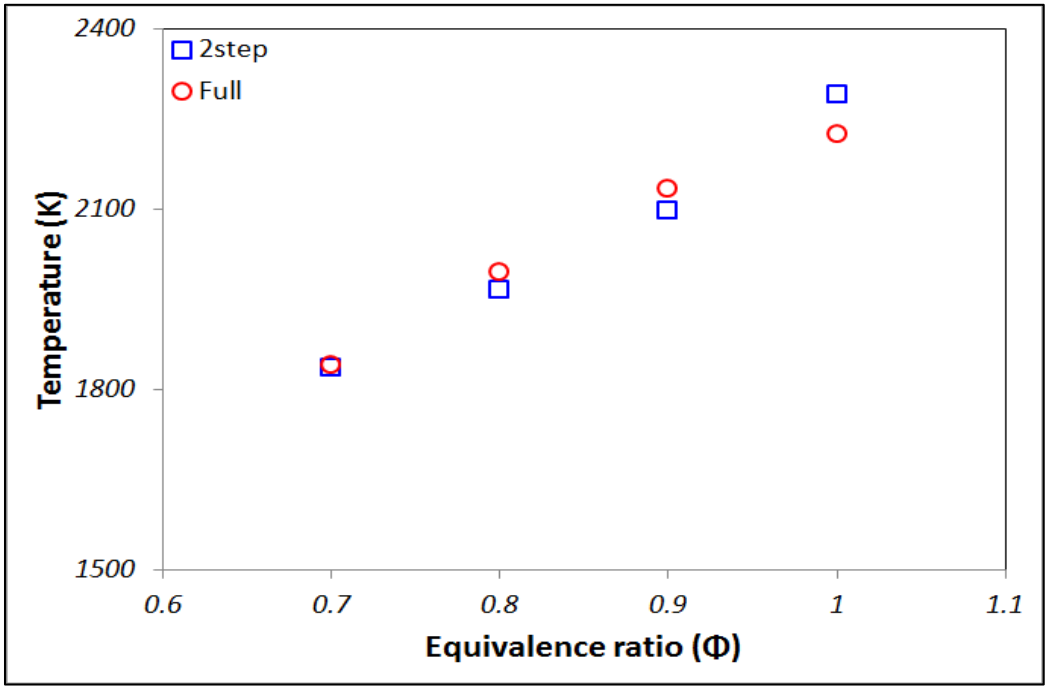

(a) Temperature

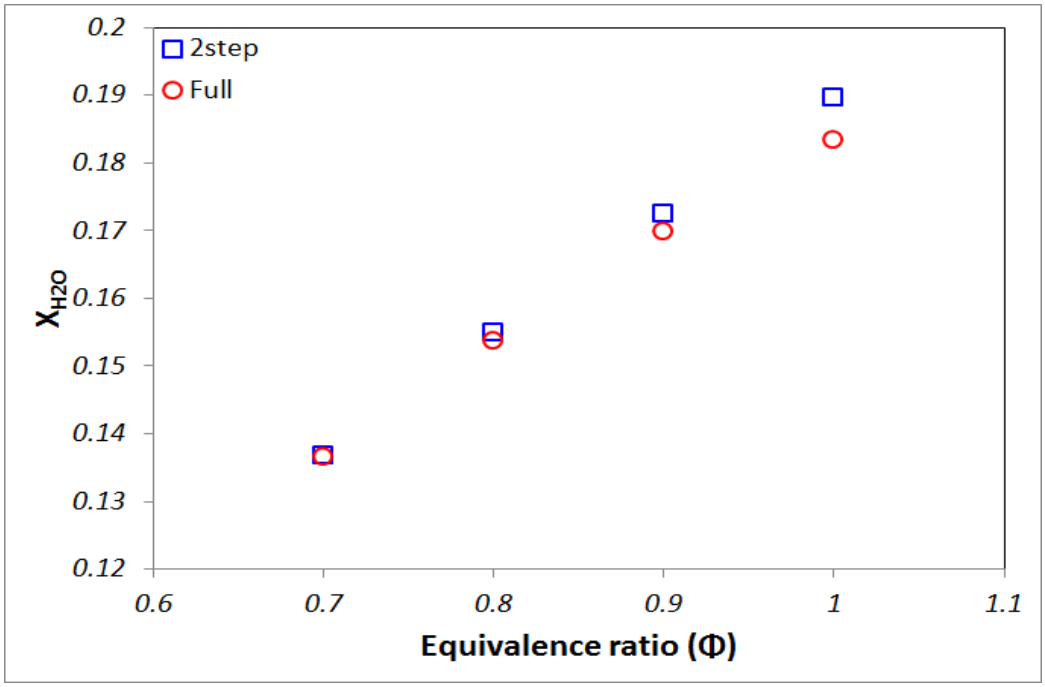

(b) Mole fraction of H_2O

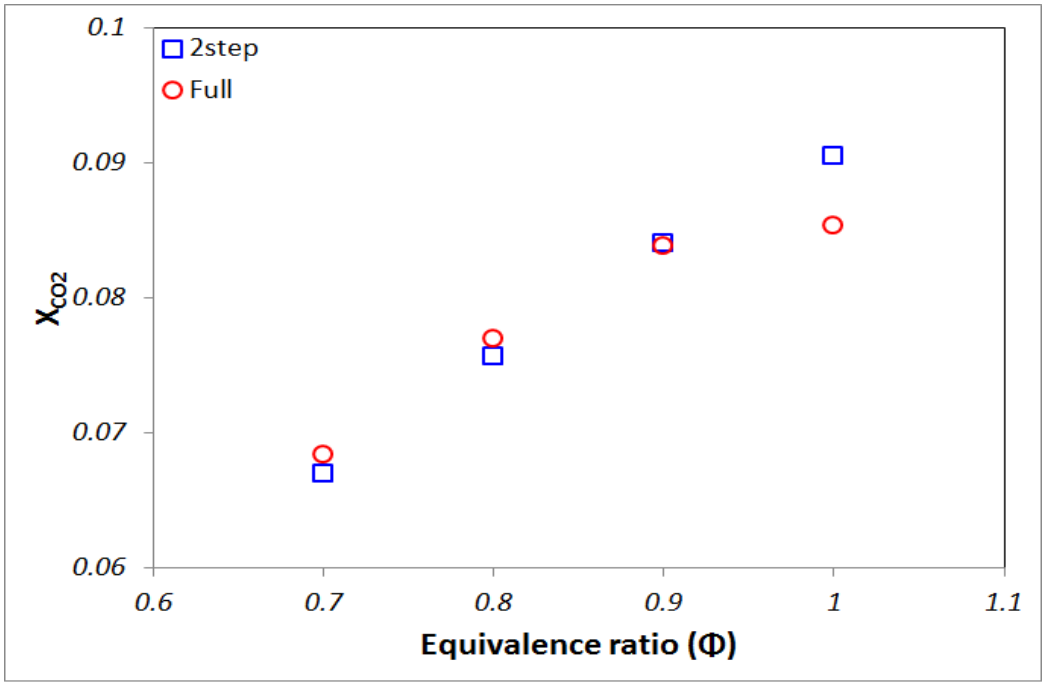

(c) Mole fraction of CO_2

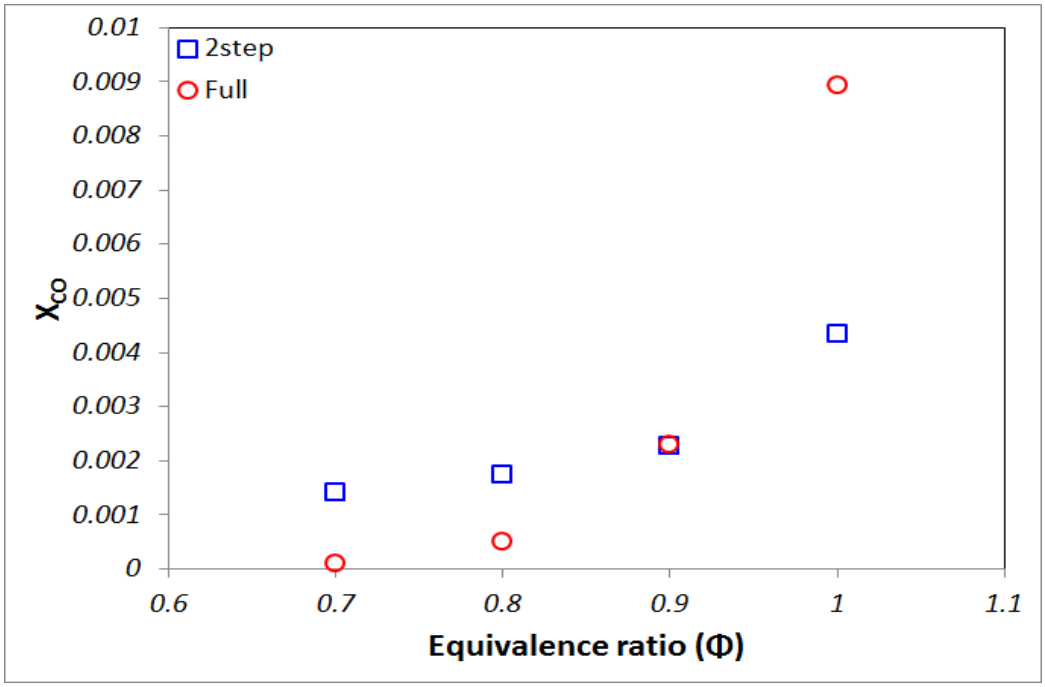

(d) Mole fraction of *CO*

Figure A.1 Comparison of temperature, X_{H2O}, X_{CO2} and X_{CO} between two step reaction model and whole chemistry model in *CHEMKIN*

Temperature, H_2O and CO_2 are well matched between the two step reaction model and whole chemistry model in ***CHEMKIN*** because the final products such as H_2O and CO_2 are well estimated by the total reaction mechanism. However, the deviation between the results of two reaction model and results of the whole chemistry reaction model is increased as equivalence ratio (Φ) increases because the two step reaction model is not well estimated to rich condition. To express the rich condition well, intermediate reaction mechanisms are needed to produce final products such as H_2O and CO_2. Also, there is a slight difference in the calculated result of mole fraction of ***CO*** because ***CO*** is intermediate species (not final product). ***CO*** needs detailed reaction mechanism. However, mostly, the difference between the results of the two step reaction model and results of whole chemistry model in ***CHEMKIN*** is negligible at the range of $0.7 \leq \Phi \leq 1.1$ which is the operating range of homogeneous combustion. Therefore, the two step

reaction model is verified in spite of the simple reaction mechanism for this study. Mechanism file of the two step reaction model is attached as below.

```
! two-step  CHEMKIN-II format

ELEMENTS

C H O N

END

SPECIES

CH4 O2 CO H2O CO2 N2

END

REACTIONS KCAL/MOLE

CH4+1.5O2=CO+2H2O 2.8E+9 0.00 48.4

FORD /CH4 -0.3/

FORD /O2 1.3/

CO+0.5O2<=>CO2 10.00E+14 0.00 40

FORD /H2O 0.5/

FORD /O2 0.25/

REV /5E+8 0.000 40/

END
```

Figure A.2 Mechanism file of the two step reaction model for *CHEMKIN*

APPENDIX B

Develop OPPF model in CHEMKIN for homogeneous combustion

The study of one-dimensional characteristics of homogeneous combustion is investigated by using CHEMKIN. Figure ***B***.1 shows the schematic of fuel and air jet configuration. The separation (***S***) distance between air and fuel jet is 280mm. The spray angle of turbulent air and fuel jet is considered to be 11.8°. The axial location of collision between fuel and air jet flow is Z_O (Virtual origin) + 67cm. In turbulent flow, Z_O is negligible. Therefore, fuel and air jet flow will collide at ***Z***=67cm. Then, flows are mixed and reacted finally. The reaction zone is expressed in red square symbol.

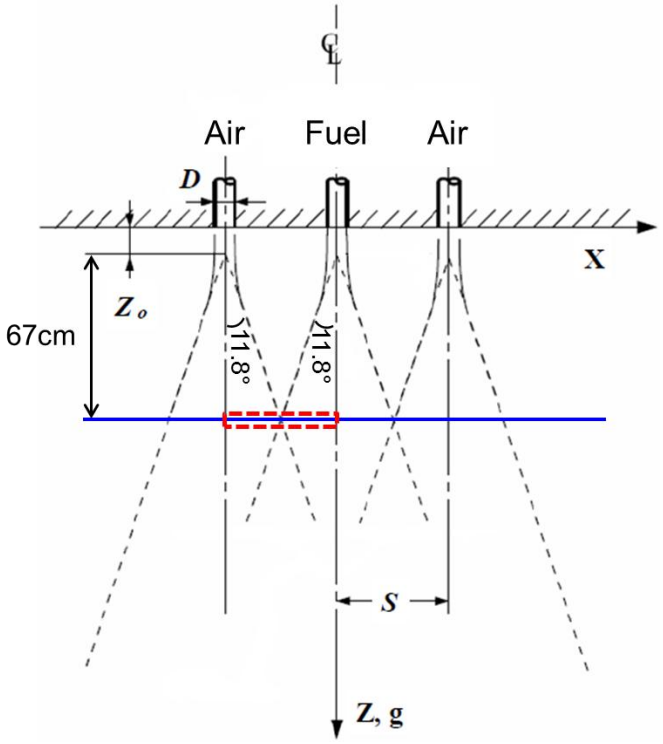

Figure B.1 The schematic of fuel and air jet configuration

Therefore, to simulate this reaction condition, ***OPPF*** model is selected. When the burner works in homogeneous combustion conditions, the fluid dynamic regime of the system can be roughly approximated as an isothermal nonreactive confined turbulent jet where a recycle of the burned gases takes place, increasing the dilution of jet by exhaust gas. Mild operative parameters map is shown as a function of recirculation rates ($\boldsymbol{K_v}$) of exhaust gases in figure 3. Recirculation rates ($\boldsymbol{K_v}$) of exhaust gases is defined as below.

$$K_v = \frac{\dot{m}_e}{\dot{m}_a + \dot{m}_f} \tag{A-1}$$

Where, $\dot{m}_e$, $\dot{m}_a$ and $\dot{m}_f$ are mass flow rate of exhaust gas, air and fuel respectively. From figure 3, homogeneous combustion requires recirculation rates ($\boldsymbol{K_v}$) of exhaust gases larger than about 4 for methane and combustion chamber temperature higher than 800~850°C. To check dilution effect of combustion, the value of $\boldsymbol{K_v}$ (the recirculation rate) is selected to 4.

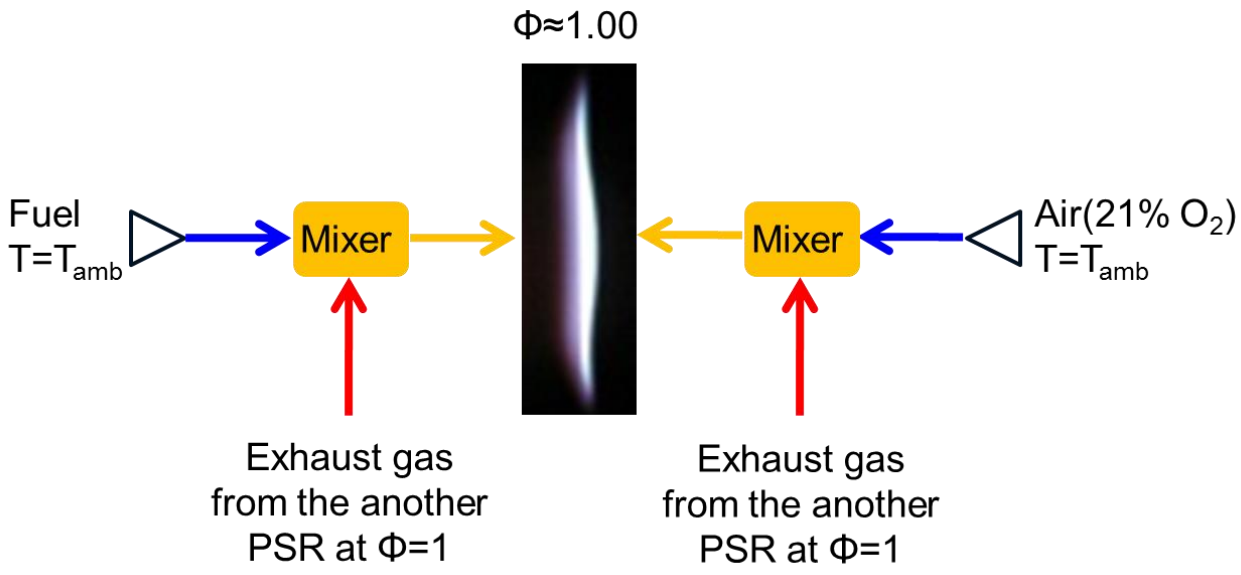

Figure B.2 The conceptual modeling of diluted combustion

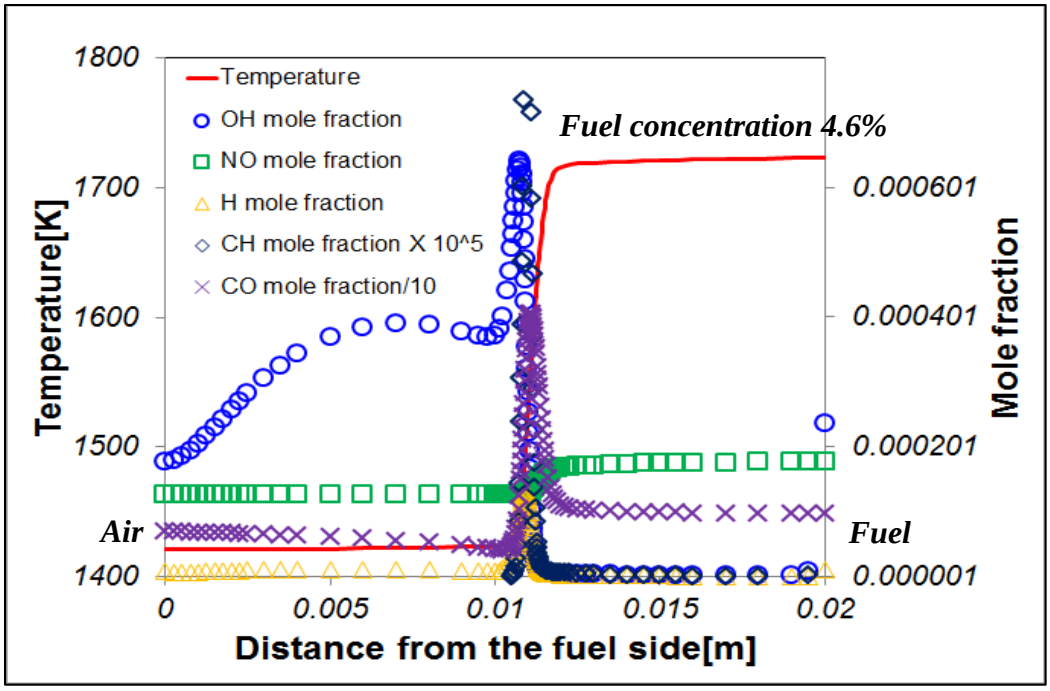

Figure B.3 The conceptual modeling of diluted combustion

In figure ***B***.3, this case (uniform temperature profile at K_v=4) is considered as homogeneous combustion through checking the extinction limit curve (based on strain rate as function of fuel concentration and temperature) as well as concentration of ***CH***, ***CO*** and ***H*** at reaction location. Also ***NO*** concentration does not have high jump in the reaction zone or the flame zone. The ***OH*** concentration is decreased before colliding between air mixture and fuel mixture.

APPENDIX C

The investigation of the possibility of simple geometry for the study of homogeneous combustion

The possibility of simple geometry is investigated for the study of homogeneous combustion. Figure ***C***.1 shows the schematic of simple geometry (2−***D*** axisymmetric plane). The simple geometry has following conditions; 1. Exact same fuel diameter to fuel diameter in whole geometry, 2. Exact same air mass flow rate to air mass flow rate in whole geometry, 3. Exact same area, location of exhaust port to the area and location of exhaust port in whole geometry and 4. Exact same shape and volume of combustor to the volume and shape of combustor in whole geometry. Only difference of area distribution of air and exhaust outlet ($\boldsymbol{Width}_{\boldsymbol{outlet}}$=0.0583m) in simple geometry is found against the whole geometry which is used for homogeneous combustion calculation in this dissertation. To investigate the possibility of simple geometry for the study of homogeneous combustion, $\boldsymbol{X}_{\boldsymbol{O2}}$=0.21, $\boldsymbol{d}_{\boldsymbol{air}}$=15.9mm, $\boldsymbol{\Phi}$=1 (run9) is used.

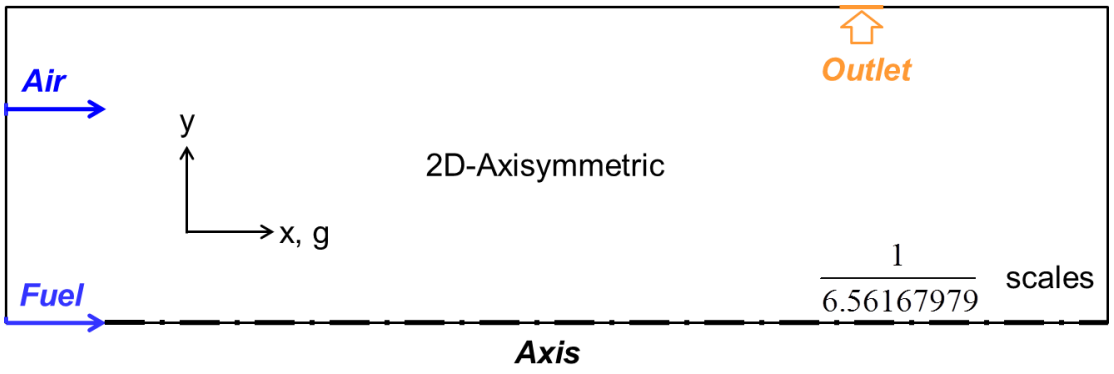

Figure C.1 The schematic of simple geometry

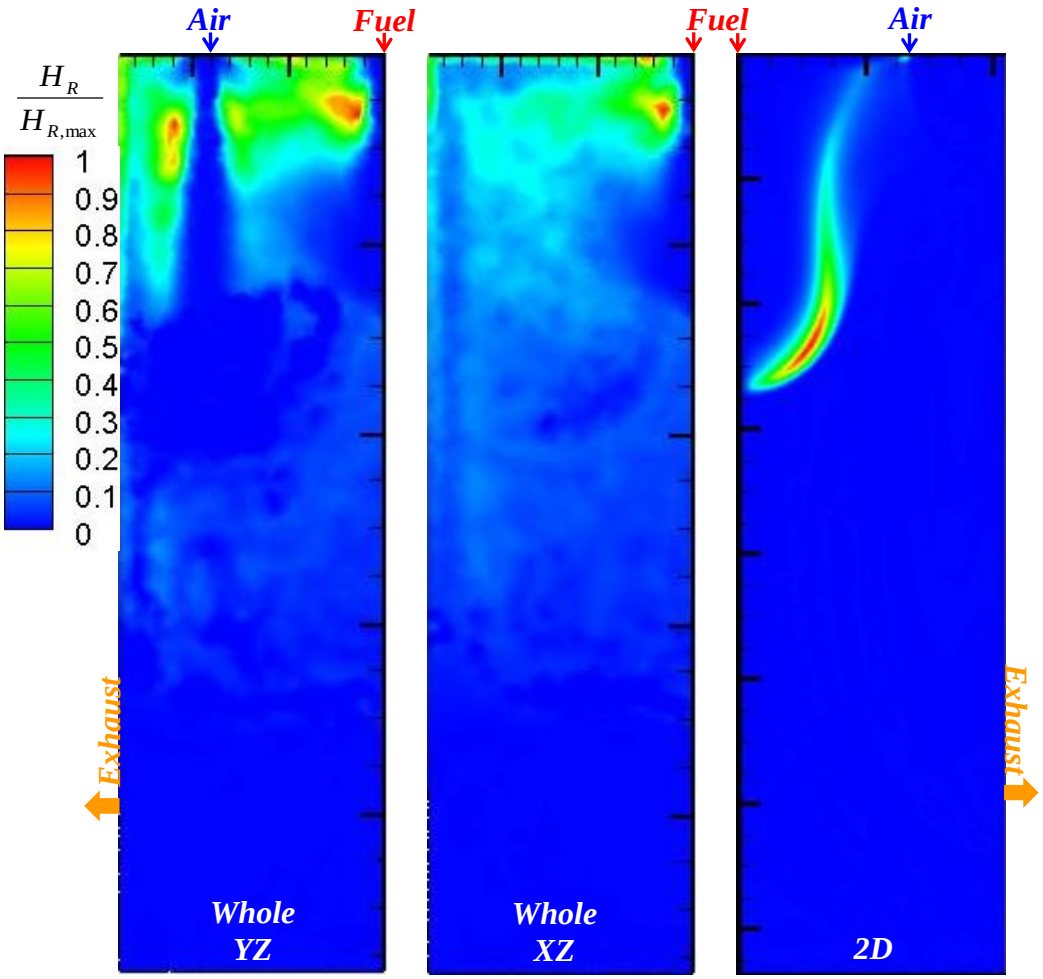

Figure C.2 The normalized heat of reaction

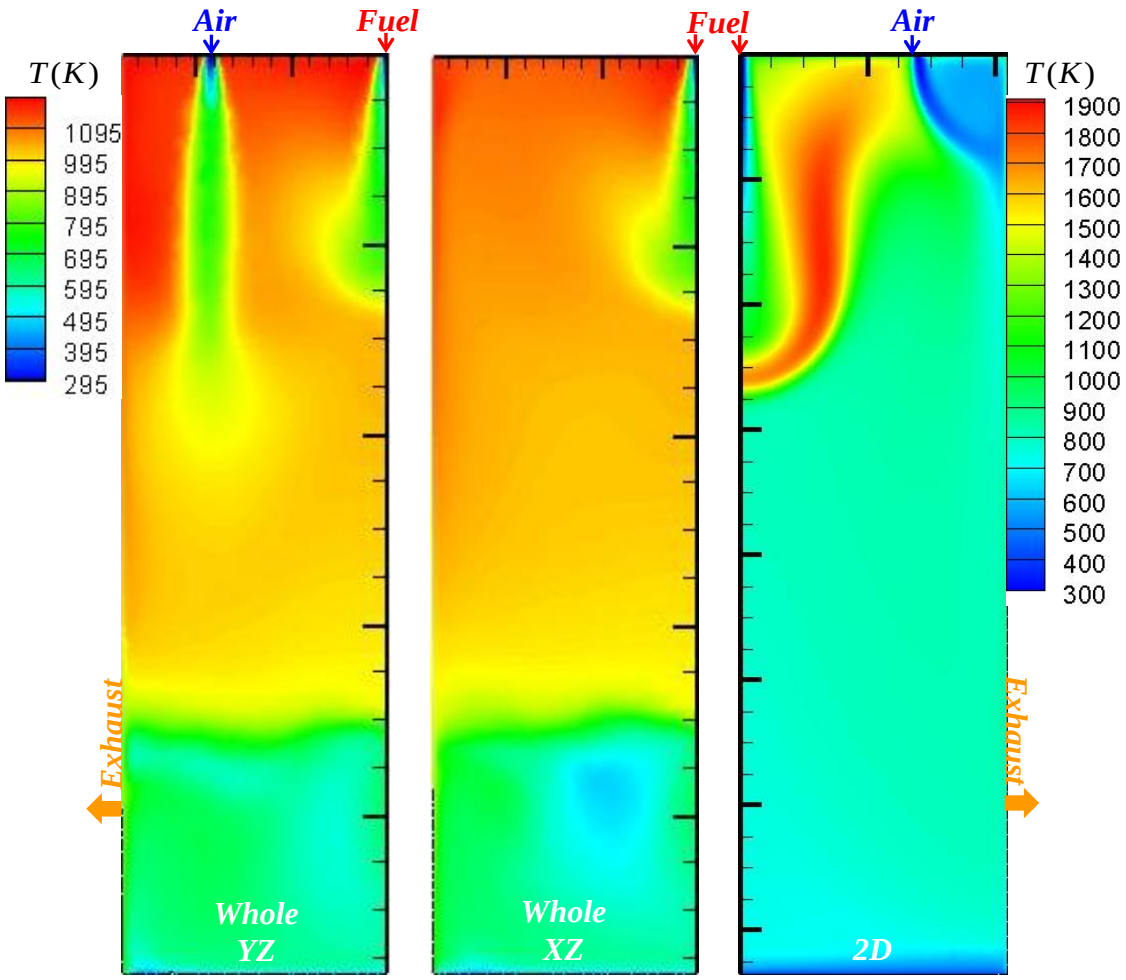

Figure C.3 The temperature (K) distribution

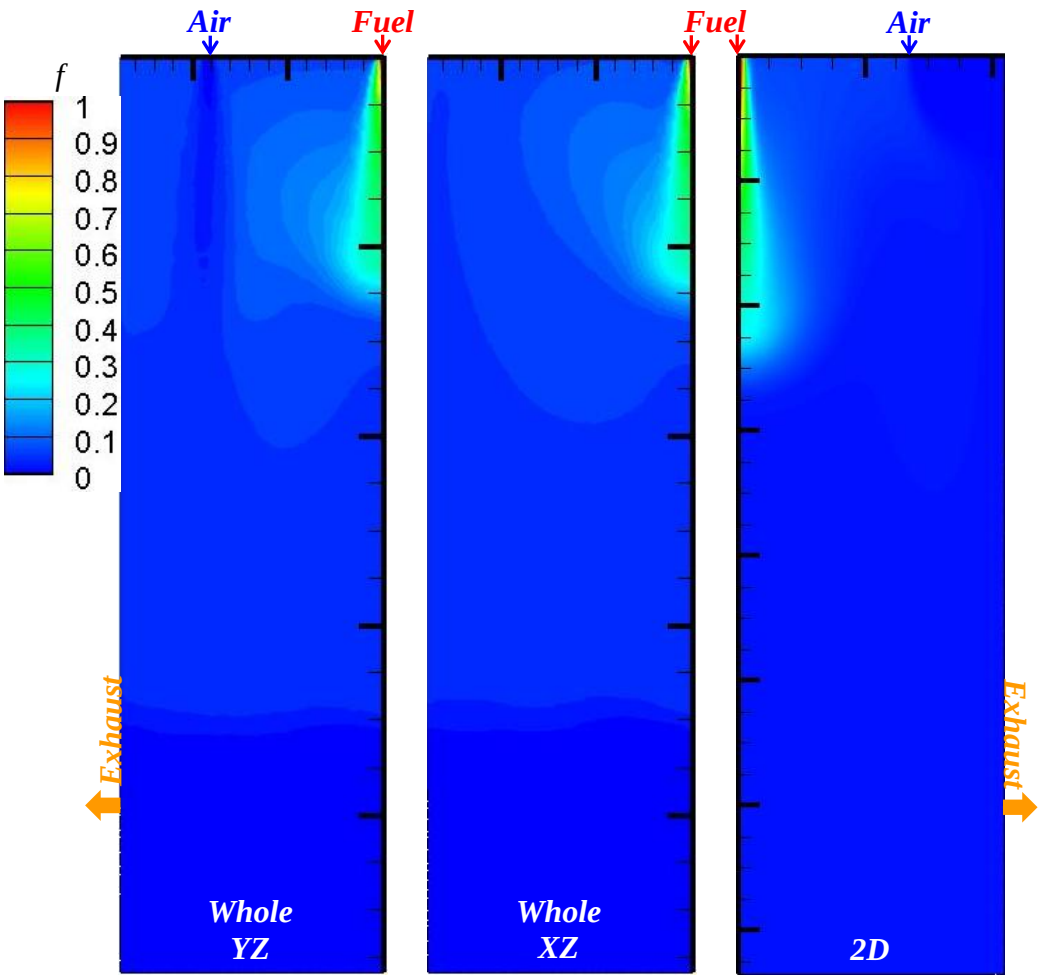

Figure C.4 The mixture fraction (*f*) distribution

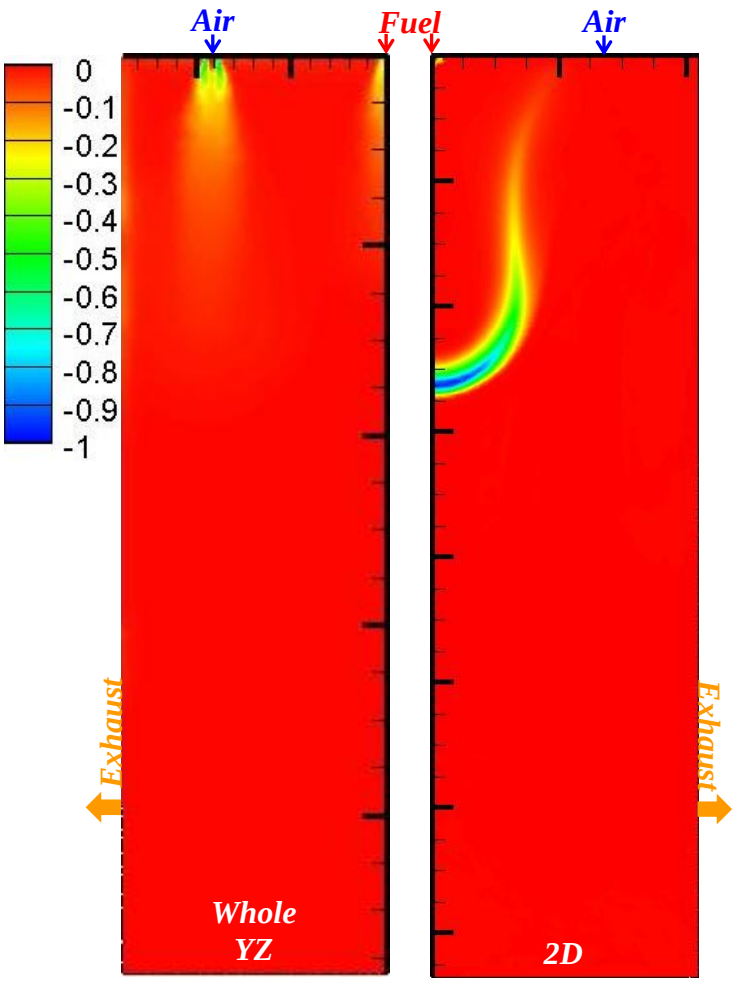

Figure C.5 The normalized distribution of $\dfrac{d[CH_4]/dt}{\left|d[CH_4]/dt\right|_{max}}$

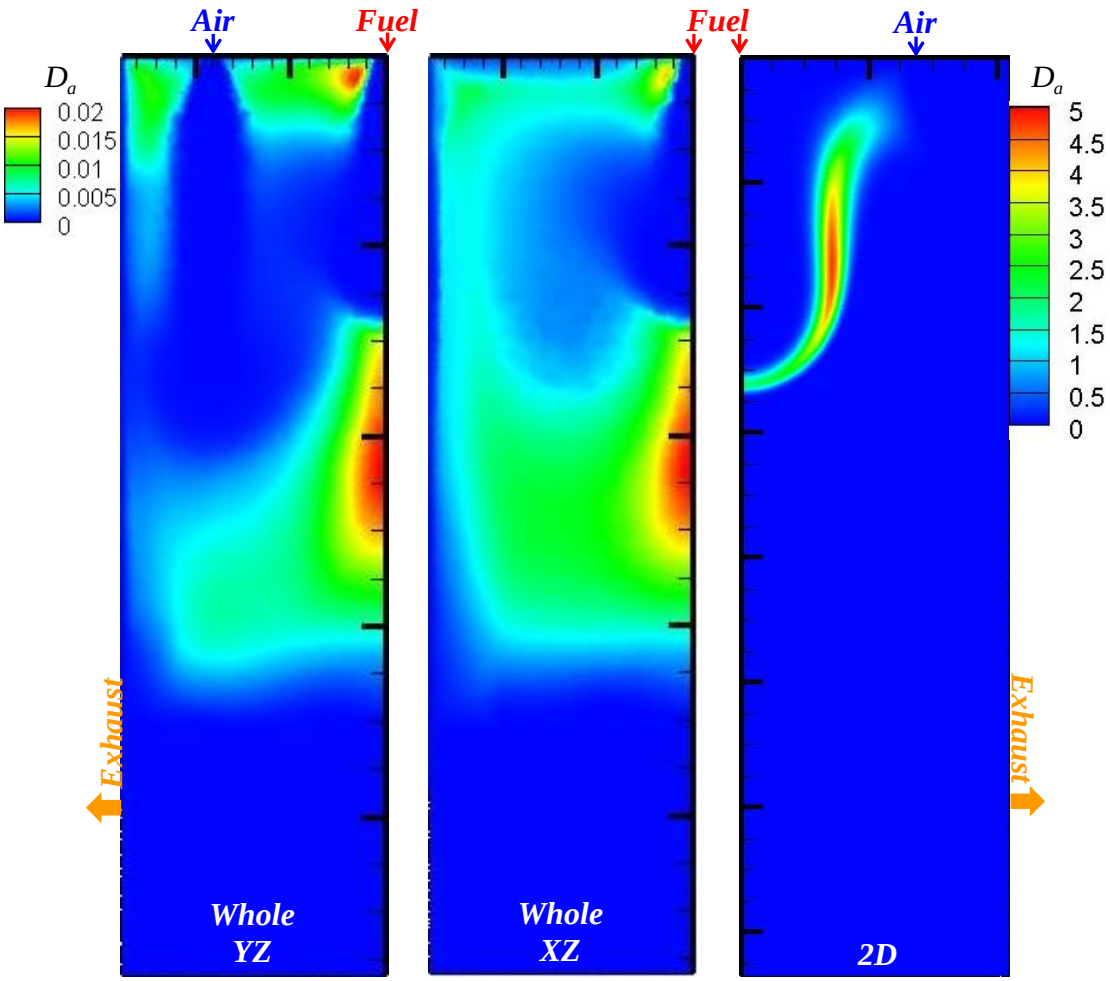

Figure C.6 The contour of Damköhler number (D_a)

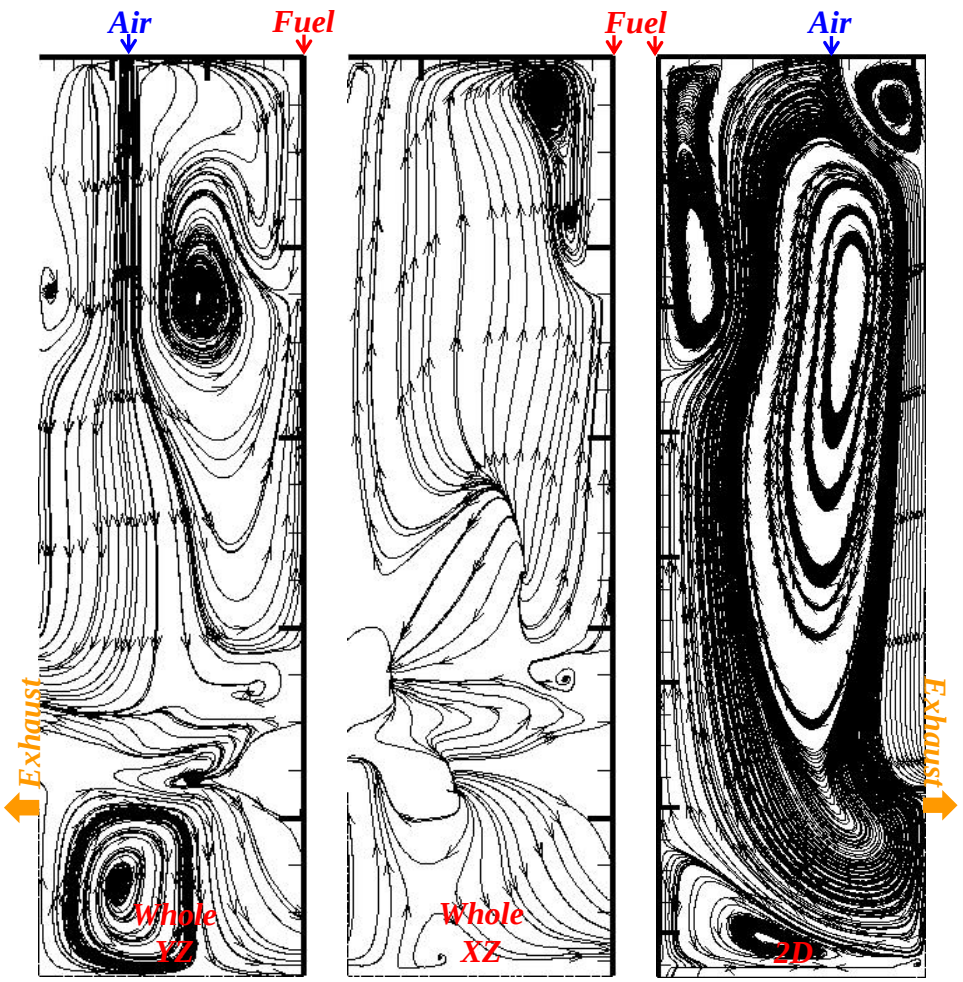

Figure C.7 The streamline

The condition of X_{O2}=0.21, d_{air}=15.9mm, Φ=1 (run9) is found at homogeneous combustion in the whole geometry. Same numerical condition applied into simple geometry which is almost similar geometry except area distribution of air and exhaust outlet. Although stagnation location is found along the fuel axis at both cases (This means that mixing time is enhanced), the characteristics of homogeneous combustion in this dissertation such as distributed heat reaction zone, uniform temperature distribution, distributed mixture fraction, uniform and distributed CH_4 reaction rate and low Damköhler number (D_a), D_a<1 is not found. Whole geometry is found to homogeneous combustion in spite of no adding external exhaust gas due to enough internal exhaust gas recirculation ratios by complex shape of exhaust port. However, in simple geometry,

there is no hindrance. That is, exhaust gas is going outside easily through exhaust port. There is very less internal exhaust gas recirculation in spite of bigger recirculation zone. In my dissertation, dilution and preheating are considered as very important parameters in order to make homogeneous combustion. Therefore, dilution is not enough to make homogeneous combustion even though mixing is enhanced by the recirculation zone. Internal $\boldsymbol{K_v}$ is estimated to $\boldsymbol{K_v}$ >>8 of whole geometry through comparing $\boldsymbol{D_a}$ number and Reynolds number of simple geometry in ***APPENDIX D***. This $\boldsymbol{K_v}$ ($\boldsymbol{K_v}$>>8 of whole geometry) is enough number to make flameless combustion on the basis of operating maps ($\boldsymbol{T_{combustor}}$ and $\boldsymbol{K_v}$) defined by Wünning [26].

APPENDIX D

The study of dilution ratio (K_v) in modified simple geometry

In ***APPENDIX C***, simple geometry which is made on the basis of whole geometry is not able to make homogeneous combustion due to less preheating and dilution by exhaust gas. Therefore, simple geometry needs to be modified in order to make homogeneous combustion through enough dilution by exhaust gas. For this approach, inlet is added to upper location of combustor. Inlet width ($\boldsymbol{Width_{intlet}}$=0.0583m) is selected by considering exactly same width of outlet and $\boldsymbol{X_{O2}}$=0.21, $\boldsymbol{d_{air}}$=15.9mm, $\boldsymbol{\Phi}$=1 (run9). This inlet flow results in fast mixing through colliding air and fuel in order to make homogeneous combustion.

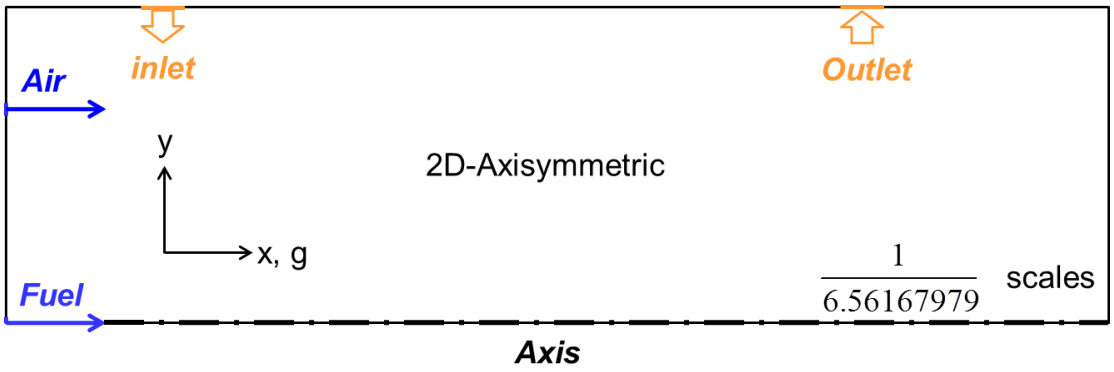

Figure D.1 The schematic of modified simple geometry

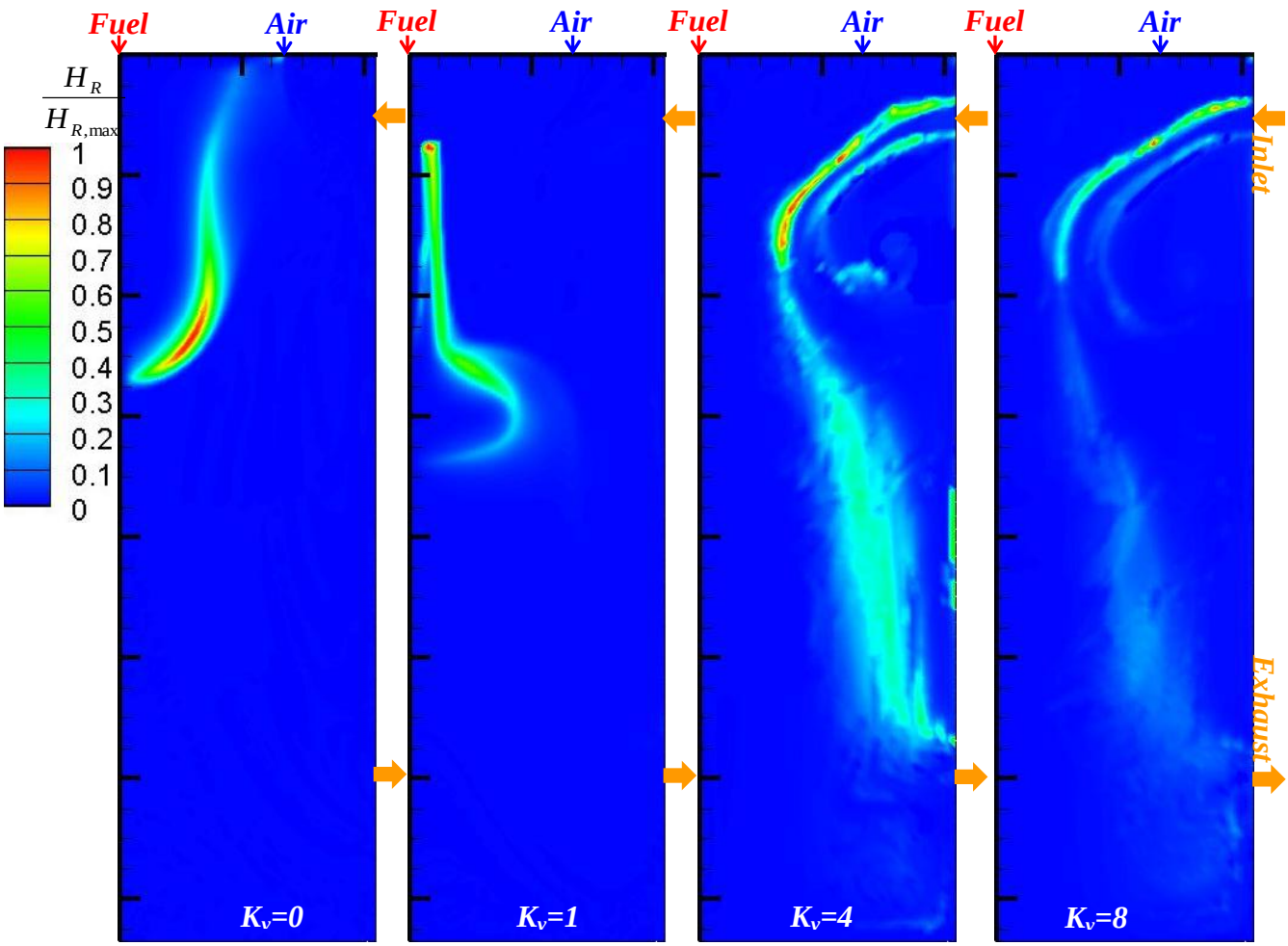

Figure D.2 The normalized heat of reaction

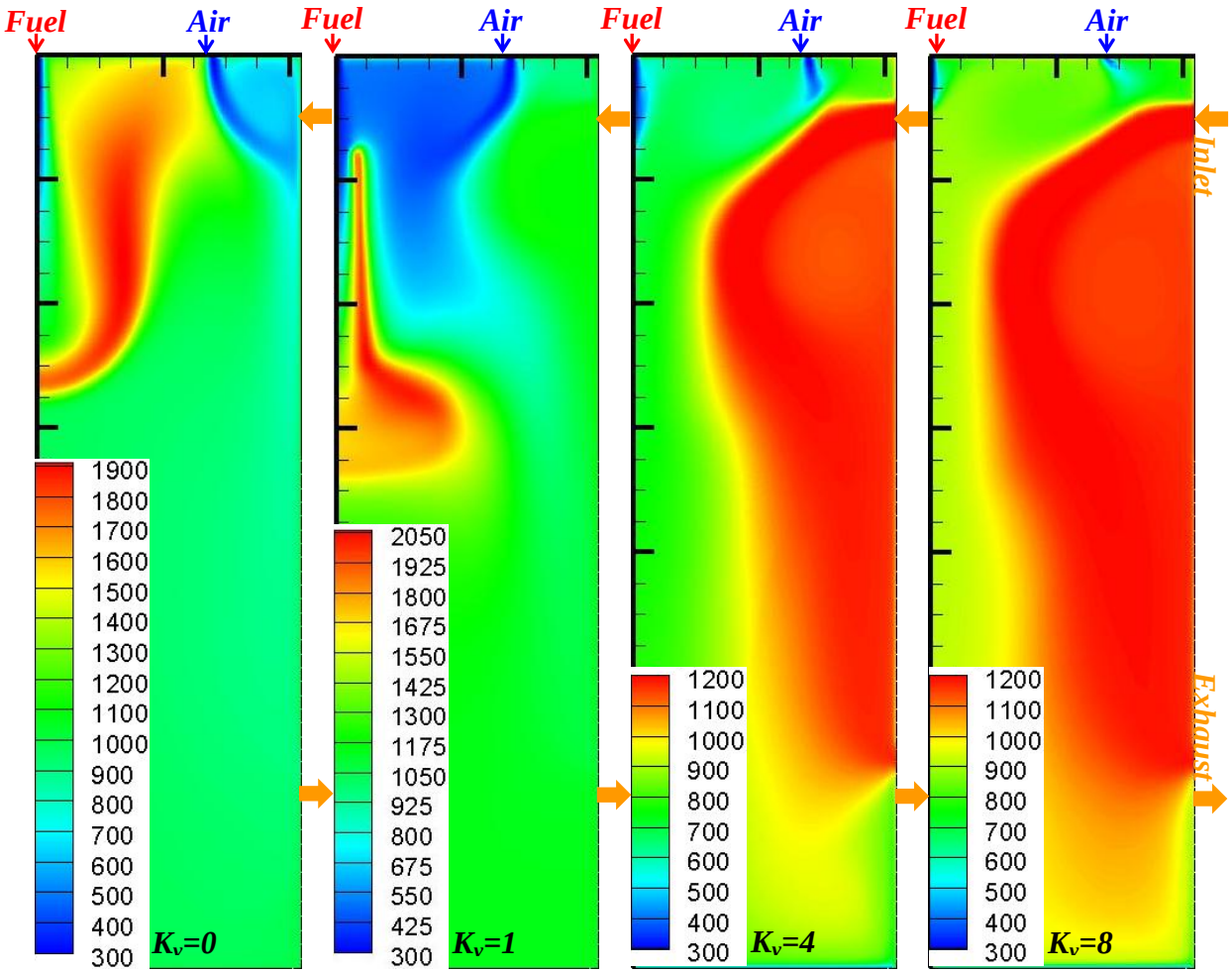

Figure D.3 The temperature (K) distribution

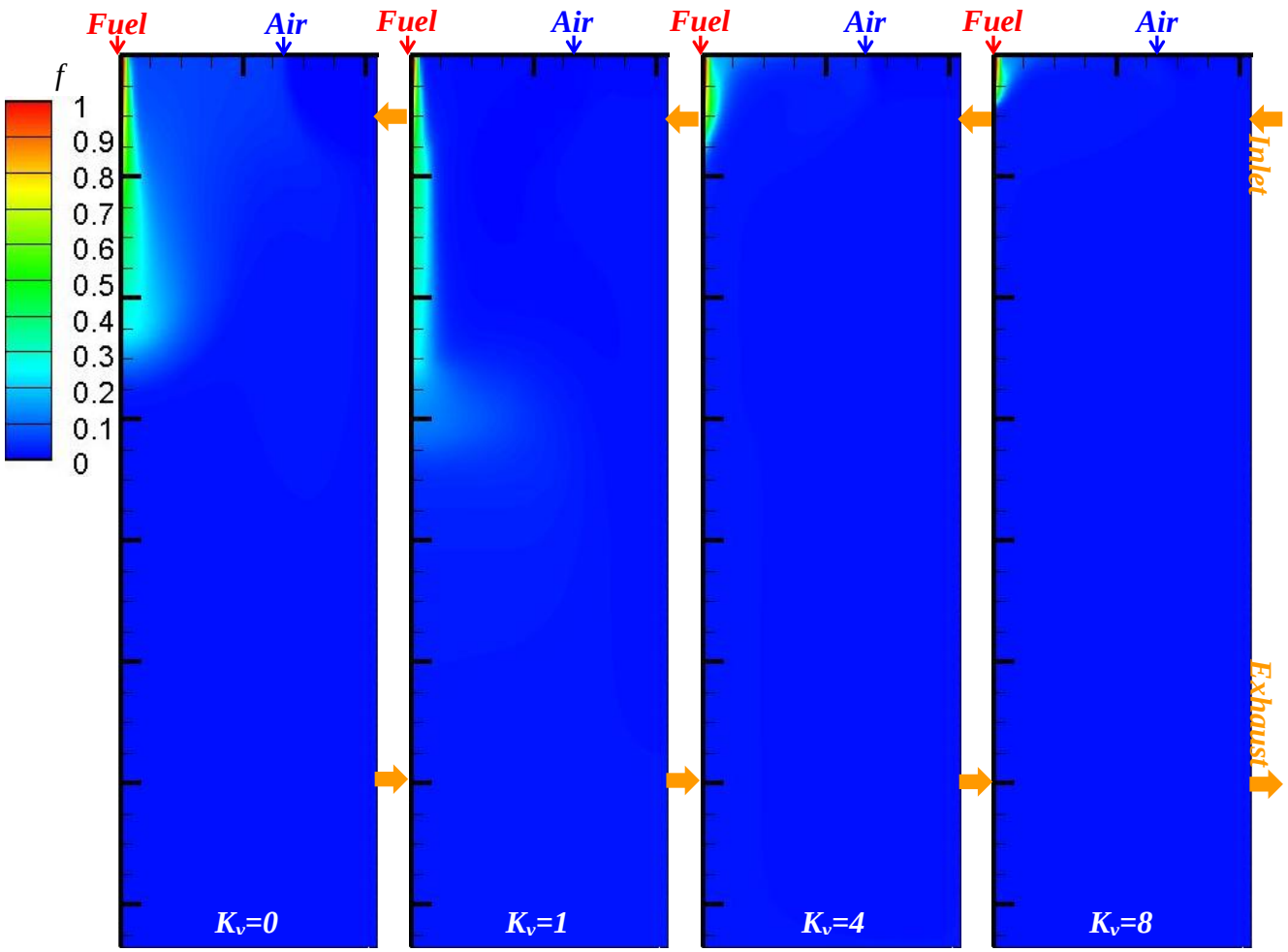

Figure D.4 The mixture fraction (*f*) distribution

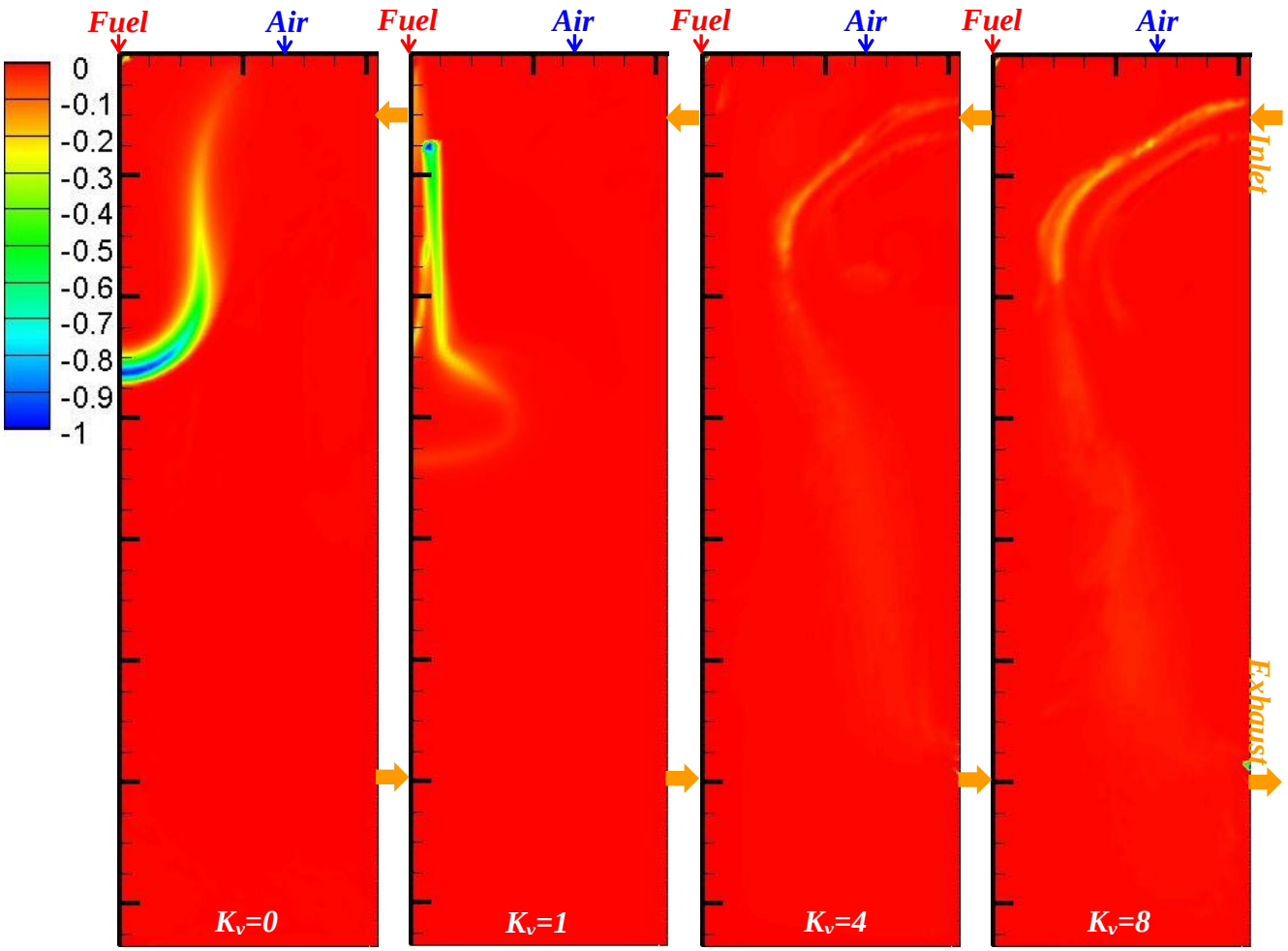

Figure D.5 The normalized distribution of $\dfrac{d[CH_4]/dt}{\left|d[CH_4]/dt\right|_{max}}$

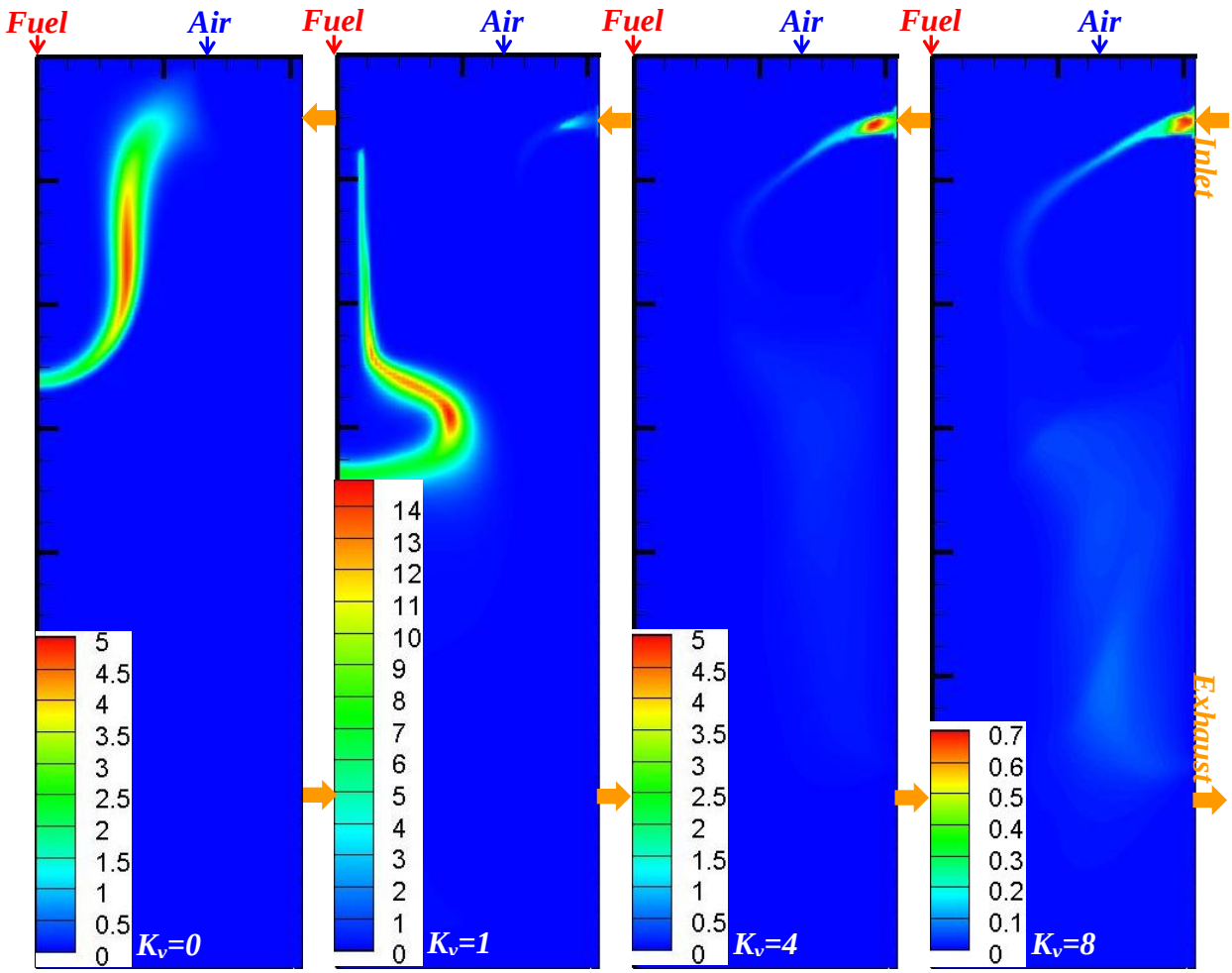

Figure D.6 The contour of Damköhler number (D_a)

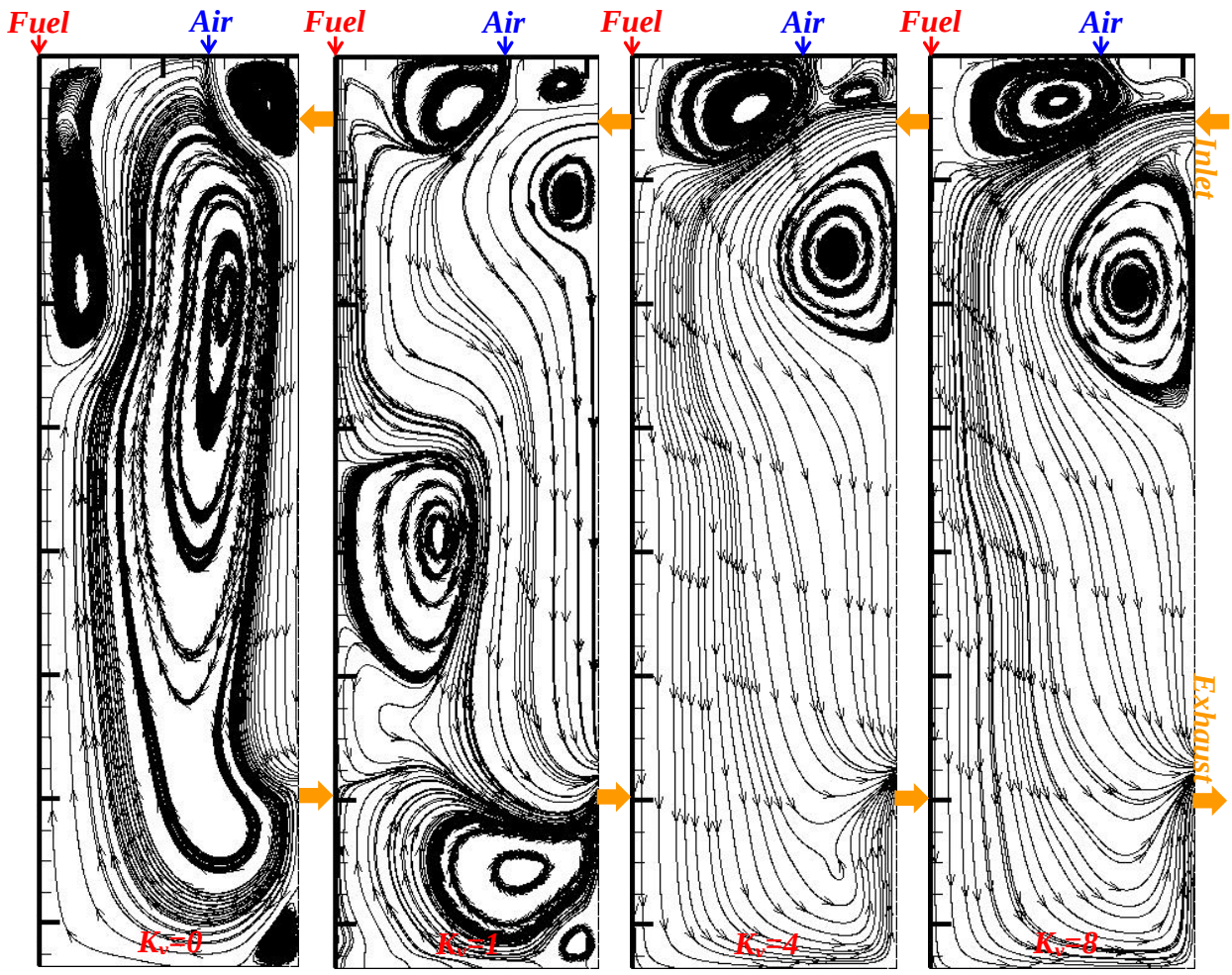

Figure D.7 The streamline

At K_v=1, exhaust gas through inlet collide with air and then, mixture of air and exhaust gas mixed with fuel. This unstable flow motion causes the two more recirculation zone at downstream. These recirculation zones also hinder to make stable combustion. Reaction zone is still shown as unstable diffusion flame at K_v=1. At higher K_v=4 and 8, air and fuel flow is blocked by higher exhaust gas flow momentum. Air and fuel recirculate at upper location. Therefore, air, fuel and exhaust gas are mixed near exhaust inlet by two recirculation zone. As a result, reaction zone moves near exhaust inlet. Reaction zone is distributed by exhaust gas flow motion. The characteristics of homogeneous combustion are checked in order to verify the effect of exhaust gas ratio. Distributed heat reaction zone, uniform temperature distribution, distributed

mixture fraction, uniform and distributed CH_4 reaction rate and D_a<<1 are found. From these conclusion, K_v>4 has significant possibility to make homogeneous combustion in this section as well as previous studies. Also, Internal K_v is considered as greater 8 in whole geometry through comparing D_a number and Reynolds number of simple geometry. This ratio of exhaust of gas (K_v>>8 of whole geometry) is enough value to produce homogeneous combustion. Adding exhaust gas through inlet in simple geometry has significant effects on reaction zone. To use simple geometry of the study of homogeneous combustion, the study of optimal design of simple geometry is needed for further approach.

APPENDIX E

The study of activation energy in reaction rate

The reaction rate of CH_4 is more uniform than that of CO in this dissertation. Usually, CO reaction rate is not uniform due to relatively fast reaction against CH_4 reaction rate.

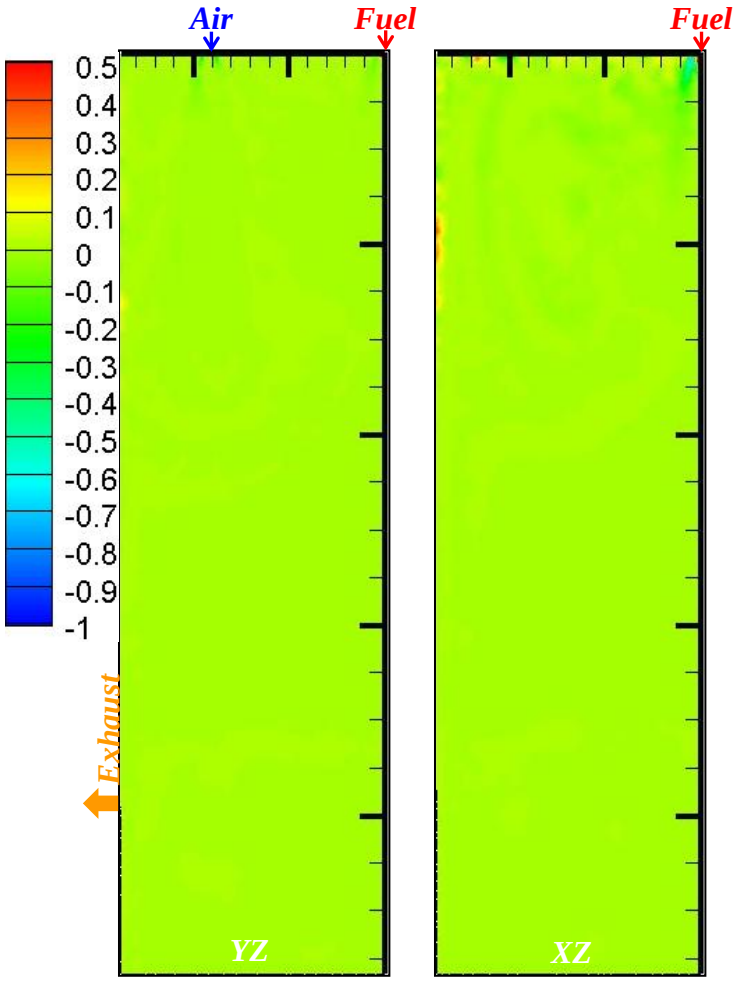

Figure E.1 The normalized contour of $\frac{d[CO]/dt}{\left|d[CO]/dt\right|_{max}}$ (run9)

The main reason is caused by the slow reaction of CH_4. To verify this assumption, CO reaction rate is decreased artificially by changing activation energy ($E_{a,CO}$) from $1.7e^{08}$ to $1.7e^{06}$ at X_{O2}=0.21, d_{air}=15.9mm, Φ=1 (run9). Figure E.1 shows the normalized contour of CO reaction

rate at ***YZ*** and ***XZ*** planes. After making a slow reaction of ***CO*** through changing the activation energy ($E_{a,CO}$), ***CO*** reaction rate obtains a uniform distribution. The following conclusion is found, ***"To make uniform distribution of any species reaction rate, the reaction time of any species must be slower".***

APPENDIX F

The study of wall emissivity

Wall radiation is considered through changing wall emissivity (ε_w) from 0.9 to 0.5. After reducing wall emissivity, reaction zone is changed on the basis of heat of reaction as well as a characteristic of temperature distribution is changed in figure ***F***.1 and ***F***.2. Although wall emissivity is decreased (wall radiation loss is decreased), reaction zone has very similar characteristics of homogeneous combustion, based on profile of heat of reaction and temperature.

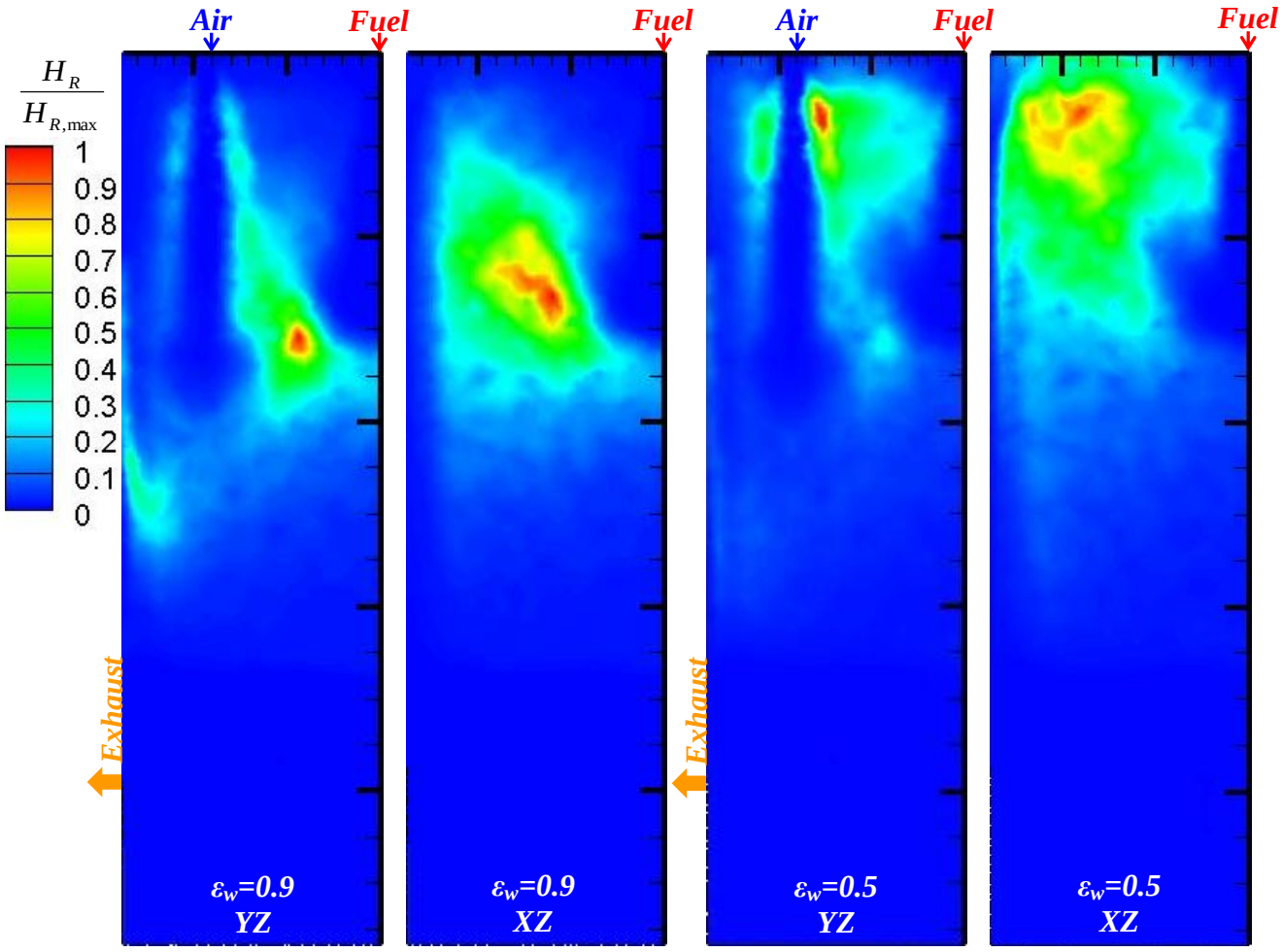

Figure F.1 The normalized contour of heat of reaction at different wall emissivity (ε_w) in *YZ* and *XZ* plane (run17)

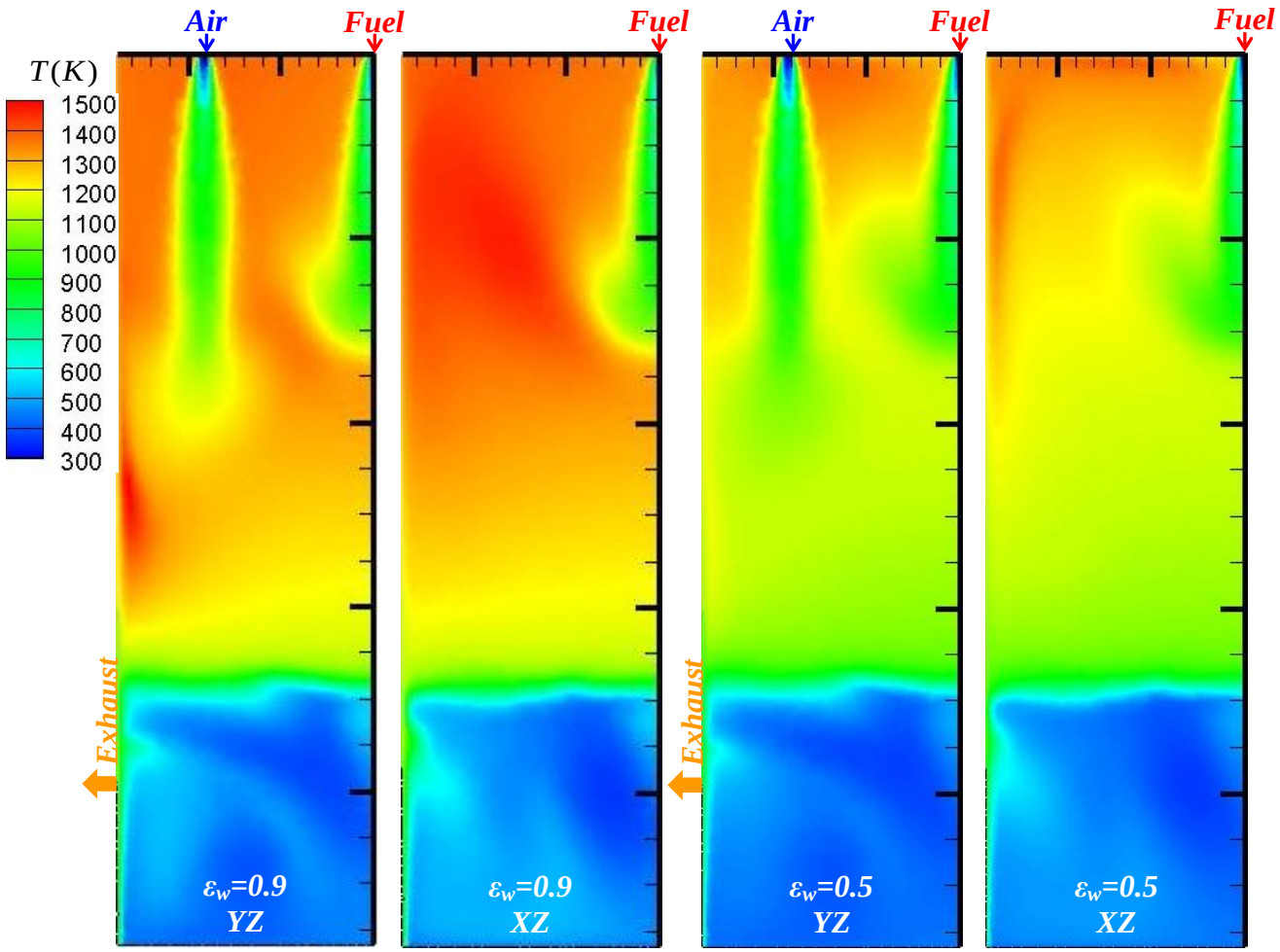

Figure F.2 The normalized contour of temperature at different wall emissivity (ε) in *YZ* and *XZ* plane (run17)

After changing wall emissivity of wall to 0.5, wall temperature at combustor increases 80K. Hot wall temperature is increased by the buoyancy effect. Finally, flow motion by buoyancy effect causes more air infiltration from exhaust port to inside combustor. Actually, air infiltration is increased up to 5.2%. Air infiltration makes the heat of reaction and temperature lower on considering energy balance.

APPENDIX G

The study of effect of half exhausts port

Air infiltration is found at wall radiation calculation. The effect of air infiltration on the result of homogeneous combustion is checked in this section. The total flow is coming into the combustor surrounded by exhaust duct. This exhaust duct is connected to the combustor by six exhaust ports. Six exhaust ports are distributed non-symmetrically to the location of fuel and air diameter distribution. Accordingly, to reduce air infiltration, exhaust duct diameter is reduced to ***d***/2 in figure ***G***.1-(a). Therefore, total flow is reduced to ½ half exhaust duct diameter (1/2***d***). The change of temperature at each port area is smaller at smaller exhaust duct area due to smaller inflow from ambient. Air infiltration is calculated at each exhaust port and temperature at each exhaust port is calculated in table ***G***.1.

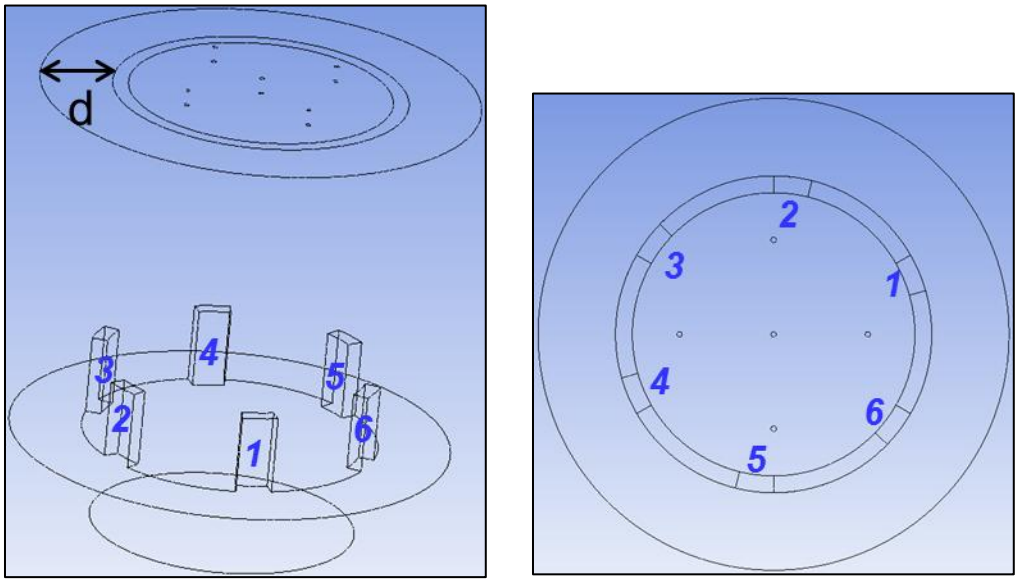

(a) 3*D* **(b) *XY* plane**

Figure G.1 The schematic of shape of exhaust duct and distribution of exhaust ports

'+' sign means inflow into combustor and '−' sign mean outflow from combustor in table ***G***.1.

Cases	Air infiltration (Kg/s)							
	1	2	3	4	5	6	(+)Total	Total
Original	-0.0057	0.008746	0.009543	-0.00206	-0.01194	-0.01263	0.018289	0.00566
Half exhaust duct	-0.00818	0.00731	0.002995	-0.00855	-0.00249	-0.0082	0.010305	-0.01465

(a) Air infiltration

Cases	Temperature (K)					
	1	2	3	4	5	6
Original	894.133	667.214	564.052	789.501	893.138	884.934
Half exhaust duct	945.115	952.67	838.132	732.364	953.006	947.486

(b) Temperature

Table G.1 Air infiltration and temperature at each exhaust port

Usually, flow is coming into the combustor through exhaust port 2 and 3. Flow is going out from exhaust port 1, 4, 5 and 6. The flow rate into combustor is reduced to almost 50% at half exhaust duct diameter. Total flow is coming into combustor with original duct at six exhaust ports but is going out from combustor with half exhaust duct at six exhaust ports. Therefore, flow is coming into the combustor with original exhaust duct more. Also, temperature is checked at six exhaust ports. The temperature is more constant at half exhaust duct than at original duct due to reduction of air flow coming into the exhaust duct. Moreover, this temperature is not cold such as ambient temperature in the location of exhaust port to combustor. Initially, flow is coming into exhaust duct. Inflow from ambient and hot flow from combustor is mixed inside exhaust duct. Some flow is coming into combustor. Then, others are going out ambient. Therefore, we estimated that there is complex flow motion inside the exhaust duct.

In original exhaust port, temperature is decreased somewhat near bottom place due to more cold air infiltration on the basis of result of table ***G***.1. However, the cold flow does not move upward due to the buoyancy effect. Mostly, heat transfer by convection occurs inefficiently near longitudinal locations of six exhaust ports. Therefore, in the zone of reaction at upper place of the combustor, there is no significantly different change of the temperature in the

reaction zone. Therefore, we conclude that this air infiltration has no significant effect on the reaction zone of current homogeneous combustion calculations in this dissertation.

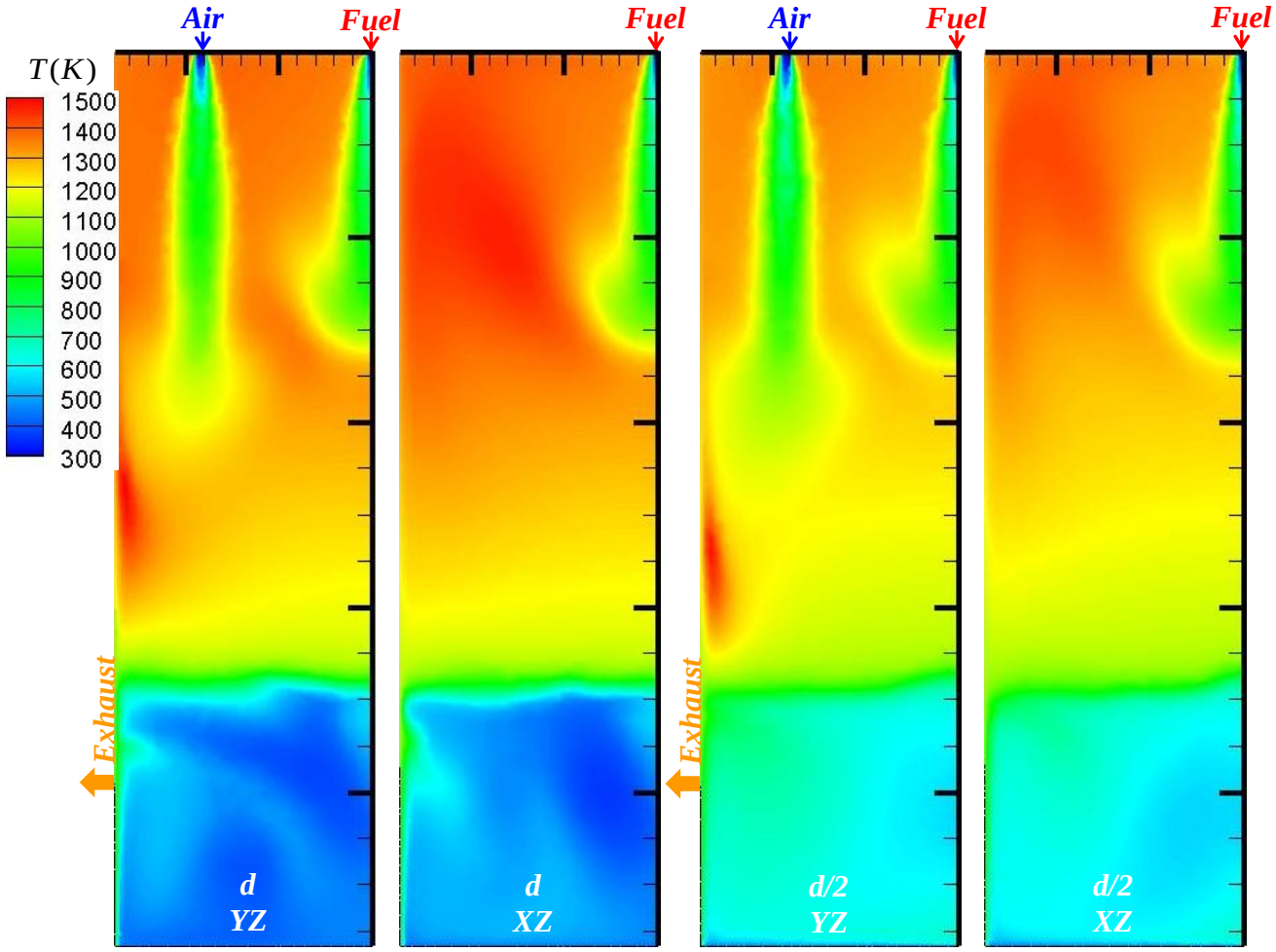

Figure G.2 The normalized contour of temperature at different exhaust duct in *YZ* and *XZ* plane (run17)

Bibliography

1. Thring M. W. and Newby M. P., Combustion length of enclosed turbulent jet flames, *Fourth Symposium institute on Combustion.* Williams and Wilkins (1953) 789–796.
2. Craya A. and Curtet R., On the spreading of a confined jet, *C. R. Acad, Sci. Paris* 241(1)(1955) 621–622.
3. Curtet R., Confined jets and recirculation phenomena with cold air, *Combustion and Flame.* 2(1958) 383–411.
4. Curtet R. and Ricou F. P., On the tendency to self-preservation in axisymmetric ducted jets, *Journal of Basic Engineering.* ASME Series D 86(4)(1964) 765–776.
5. Becker H. A., Hottel H. C. and Williams G. C., Mixing and flow in ducted turbulent jets, *Nineth Symposium institute on Combustion.* Academic Press(1963) 7–20.
6. Exley J. T. and Brighton J. C., Flow separation and reattachment in confined jet mixing, *Journal of Basic Engineering.* Transactions of the ASME (1971) 192–198.
7. Hill P. G., Turbulent jets in ducted streams, *Journal of Fluid Mechanics.* 22(1)(1965) 161–186.
8. Hill P. G., Incompressible jet mixing in converging-diverging axisymmetric ducts, *Journal of Basic Engineering.* Transactions of ASME (1966).
9. Nickels T. B. and A. E. Perry., An experimental and theoretical study of the turbulent coflowing jet, *Journal of Fluid Mechanics.* 309(1997) 157-182.
10. Dealy J. M., The confined circular jet with turbulent source, *Symposium on Fully Separated Flows ASME.* Newyork (1960).
11. Dealy J. M., Momentum exchange in a confined circular jet with turbulent source, *Ph.D thesis U of Michigan.* (1964).
12. Moeller W. G. and Dealy J. M., Backmixing in a confined jet, *The Canadian Journal of Chemical Engineering.* 48(1970) 356–361.

13. Razinsky E. and Brighton J. A., Confined jet mixing for nonseparating conditions, *Journal of Basic Engineering.* 93(3)(1971) 333–349.

14. Singh G., Sundararajan T. and Shet., Entrainment and mixing studies for a variable density confined jet, *Numerical Heat Transfer Part A Applications*. 35(2)(1999) 205–223.

15. Steward F. R. and Guruz A. G., Aerodynamics of confined jet with variable density, *Combustion Science and Technology*. 16(1977) 29–45.

16. Ricou F. P. and Spalding D. B., Measurement of entrainment by axis-symmetrical turbulent jets, *Journal of Fluid Mechanics*. 11(1960) 21-32.

17. Pritchard R., Guy J. J. and Connor N. E., Handbook of industrial gas utilization, *Van Nostrand Reinhold Company*. (1977).

18. Singh G., Sundararajan T. and Bhaskaran K. A., Mixing and entrainment characteristics of circular and noncircular confined jets, *Journal of Fluid Engineering*. 125(2003) 835-842.

19. Arendt J., Babcock H. A. and Schuster J., Penetration of a jet into a counterflow, *ASCE J. Hydr. Div.* 82(1956) 1038-8-11.

20. Oron A. and Abuaf N., Jet expanding into a uniform counterflow, *Isr. J. Tech.* 15(1977) 239-245.

21. Beltaos S. and Rajaratnam N., Circular turbulent jet in an opposing infinite stream, *Proc. 1st Canadian Hydrotechnical Conf.* (1973) 220-237.

22. Sekundov A. N., The propagation of a turbulent jet in an opposing stream, *Turbulent jets of air, plasma and real gas, G. N. abramovich, ed., consultants bureau, N. Y.* (1969) 99-109.

23. Morgan W. D., Brinkworth B. J. and Evans G. V., Upstream penetration of an enclosed counterflowing jet, *Ind. Eng. Chem. Fundam.* 15(1976) 125-127.

24. Lam K. M. and Chan C. H. C., Investigation of turbulent jets issuing into a counterflowing stream using digital image processing, *Exp. Fluids.* 10(1995)210-212.

25. Saghravani S. F. and Ramamurthy A. S., Penetration length of confined counter flowing free jets, *J.Hydr. Eng.* 136(2010)179-182.

26. Yoda M. and Fiedler H. E., The round jet in a uniform counterflow:flow visualization and mean concentration measurements, *Exp. Fluids.* 21(1996)427-436.

27. Bernero S. and Fiedler H. E., Application of particle image velocimetry and proper orthogonal decomposition to the study of a jet in a counterflow, *Experimentals in Fluids* (2000)S274-S281.

28. Bernero S., A turbulent jet in counterflow, *Ph.D thesis* Berlin: Technical University of Berlin (2000).

29. Lam K. M. and Chan C. H. C., Round jet in ambient counterflowing stream, *Journal of Hydraulic Engineering* 123(10)(1997)895-903.

30. Chan C. H. C. and Lam K. M., Centerline velocity decay of a circular jet in a counterflowing stream, *Physics of fluids* 10(3)(1998)637-644.

31. Chan C. H. C. and Lam K. M., The velocity field of a circular jet in a counterflow, *Environmental Hydraulics, J. H. W. Lee, A. W. Jayawardena and Z. Y. Yang, eds., Balkema Rotterdam* (1999)223-228.

32. Chan C. H. C., Lam K. M. and Bernero S., On the penetration of a round jet into a counterflow at different velocity ratios, *Environmental Hydraulics, J. H. W. Lee, A. W. Jayawardena and Z. Y. Yang, eds., Balkema Rotterdam* (1999)229-234.

33. Lam K. M. and Chan C. H. C., Time-averaged mixing behavior of circular jet in counterflow: velocity and concentration measurements, *Journal of hydraulic engineering* 128(9)(2002)861-865.

34. Tsunoda H. and Saruta M., Planar laser-induced fluorescence study on the diffusion field of a round jet in a uniform counterflow, *Journal of Turbulence* 4(1)(2003)13-21.

35. Luis A. T., Mohammad M., Briam A. F., David J. W. and David N., Mean concentration field of a jet in a uniform counter-flow, *Journal of Fluids Engineering* 134-1(2012).

36. Sivapragasam M., Ramamurthy S., Deshpande M. D. and Sridhara S. N., Computation of turbulent jets in annular counterflow, *11^{th} annual CFD symposium* (2009)1-8.

37. Wünning J. A. and Wünning J. G., Flameless oxidation to reduce thermal NO-formation. *Progress in Energy and Combustion Science*, 23(1997)81-94.

38. Katsuki M. and Hasegawa T., The science and technology of combustion in highly preheated air, *In Twenty-Seventh Symposium(International) on Combustion*, (1998)3135-3146.

39. Gavaliere A. and De Joannon M., Mild combustion, *Progress in Energy and Combustion Science* 30(2004)329-366.

40. Lee H. S., Experimental studies on mixing of multiple turbulent jets in non-reacting and reacting flows, *Ph.Dissertation Thesis, The university of Michigan,* 2007.

41. Shin S. J., Homogeneous combustion and its application to industrial furnaces, *Ph.Dissertation Thesis, The university of Michigan,* 2008.

42. Masahiro I. and Masaki T., Methods to calibrate a critical nozzle and flow meter using reference critical nozzles, *Flow Measurement and Instrumentation*. 11(2000) 293-303.

43. ANSYS FLUENT Theory Guide 14.5, *Ansys,Inc.* Oct.(2012).

44. Launder B. and Spalding D., Lectures in mathematical models of turbulence, *Academic press, London*. (1972).

45. Shih T. H., Liou W. W. Shabbir A. and Zhu J., A new k-ε eddy viscosity model for high Reynolds number flows-model development and validation, *Computers Fluids*. 24(3)(1995) 227-238.

46. Launder, B. E, Morse, A. P., Rodi, W., and Spalding, D. B., The prediction of free shear flows-a comparison of six turbulence models, *NASA SP-311*. (1972).

47. McGuirk, J.J. and Rodi, W., The calculation of three-dimensional turbulent free jets, *Symposium on Turbulent Shear Flows, Pennsylvania State University*. April(1977).

48. Morse, A. P., Axisymmetric turbulent shear flows with and without swirl, *Ph.D Thesis, London Univeristy, England*. (1977).

49. Christo, F.C. and Dally, B. B., Modeling turbulent reacting jets issuing into a hot and diluted coflow, *Combustion and flame*. 142(2)July(2005) 117-129.

50. Frassoldati, A., Sharma, P., Cuoci, A., Faravelli, T. and Ranzi, E., Kinetic and fluid dynamics modeling of a methane/hydrogen jet flames in diluted coflow, *Proceedings of the european combustion meeting*. (2009).

51. Chapman, S. and Cowling, T. G., The mathmatical theory of non-uniform gases: an account of the kinetic theory of viscosity, thermal condution, and diffusion in gases, *Cambridge University Press*. (1990).

52. Paul E. Dimotakis, The mixing transition in turbulent flows, *J. Fluid Mech*. 409 (2000).

53. C. J Chen and W. Rodi., Vertical turbulent buoyant jets- A review of experimental data, *The Science and Application of Heat and Mass Transfer Reports*. Pergamon Press.

54. Singh G., Sundararajan T. and Bhaskaran K. A., Mixing and entrainment characteristics of circular and noncircular confined jets, *Journal of Fluid Engineering*. 125(2003) 835-842.

55. Ricou F. P. and Spalding D. B., Measurement of entrainment by axis-symmetrical turbulent jets, *Journal of Fluid Mechanics*. 11(1960) 21-32.

56. H. J. Hussein, S. P. Capp. and W. K. George, Velocity measurements in a high-Reynolds number momentum conserving axisymmetric turbulent jet, J. Fluid Mech. 258(1994) 31-75.

57. T. Djeridane., Contribution à l'étude expérimentale de jets turbulents axisymétriques à densité variable. *Ph.D.Thesis, Université d'Aix-Marseille II, Marseille.* (1994).

58. Sivapragasam M., Deshpande M. D., Ramamurthy S. and White P., Turbulent jet in confined counterflow, *Indian Academy of Sciences39* (2014) 713-729.

59. Westbrook C. and Dryer F., Simplified reaction mechanisms for the oxidation of hydrocarbon fuels in flames, *Combust. Sci. and Tech.,* 27(1981)31−43.

60. A. Parente, E. Cresci, C. Galletti, M. Schiavetti, J. Riccardi and L Tognotti., Effect of H2 content in the fuel on the flameless combustion in industrial burners, *31th Combustion Meeting*, XII-7 1-6.

61. Bjørn F. Magnussen., The eddy dissipation concept, *ECCOMAS Thermatic Conference on Computational Combustion*, Lisboa, June(2005)21-24.

62. Y. Minamoto, N. Swaminathan, R. S. Cant & T. Leung., Reaction zones and their structure in MILD combustion, *Combust. Sci. and Tech.*, 10(2014)12−19.

63. M. Ihme and Y. C. See., LES flamelet modeling of a three-stream MILD combustor: Analysis of flame sensitivity to scalar inflow conditions, *Proceedings of the combustion institute*, 33(2011)1309−1317

64. C. K. Law, Combustion Physics, *Cambridge University Press*, 2010.